



EKTAM

A2M2C



1st International Conference on Advanced Materials and Advanced Manufacturing (A2M2C)

18-19-20 October 2023 ANKARA

Gazi University - Additive Manufacturing Technology Application and Research Center (EKTAM)



**1st International Conference on Advanced Materials and Advanced Manufacturing
(A2M2C-1)**

International Program Committee

General Chair:

Prof. Dr. Metin U. Salamci

Program Chair:

Prof. Dr. Yusuf Usta

Program Co-chair:

Prof. Dr. Olcay Ersel Canyurt

Conference Secretary:

Dr. Peyman Ansari

Text, Field, Language and Layout Editors:

E. Kıvanç Sadak

Murat Yıldız

Cover and Graphic Design:

Nurettin Akın

Organizing Committee

Mr. Muhammad Muteeb Butt

Mr. Ahmed Jawad

Dr. Can Barış Toprak

Mr. Yunus Yıldız

Mr. Anıl Emirlioğlu

Scientific Committee

Prof. Dr. Mehmet Arif Adli – Gazi University
Prof. Dr. O. Cenk Aktaş – Kiel University
Prof. Dr. Nizami Aktürk– Gazi University
Prof. Dr. Olcay Ersel Canyurt – Gazi University
Prof. Dr. Erdal Çelik - Turkish Aerospace Industries
Prof. Dr. Mustafa Güden – Izmir Institute of Technology
Prof. Dr. Y. Eren Kalay – Middle East Technical University
Prof. Dr. İrfan Kaymaz – Erzurum Technical University
Prof. Dr. Hüseyin Kızıl – Istanbul Technical University
Prof. Dr. Bahattin Koç – Sabanci University
Prof. Dr. Yogendra Kumar Mishra – University of Southern Denmark
Prof. Dr. Süleyman Özçelik – Gazi University
Prof. Dr. Fahrettin Öztürk - Turkish Aerospace Industries
Prof. Dr. Alper Taşdemirci - Izmir Institute of Technology
Prof. Dr. Yusuf Usta – Gazi University
Prof. Dr. Rahmi Ünal – Gazi University
Prof. Dr. Fatih Yıldız - Erzurum Technical University
Assoc. Prof. Dr. M. Fatih Aycan - Gazi University
Assoc. Prof. Dr. Havva Zeytin Kazdal – TUBITAK Marmara Research Center
Assoc. Prof. Dr. Sezer Özerinç - Middle East Technical University
Assoc. Prof. Dr. Bülent Özkan - Gazi University
Assoc. Prof. Dr. Elmas Salamcı - Gazi University
Assoc. Prof. Dr. Kürşad Sezer - Gazi University
Assoc. Prof. Dr. Ender Yıldırım - Middle East Technical University
Dr. Hüseyin Aydın - TUBITAK Marmara Research Center
Dr. Gustavo M. Castelluccio - Cranfield University
Dr. Andrea Cini – Carlos III Madrid University
Dr. Burcu Arslan Hamat - Turkish Aerospace Industries
Dr. İlhan Şen - Turkish Aerospace Industries
Dr. Evren Tan - ASELSAN
Dr. Hakan Yavaş - Turkish Aerospace Industries
Dr. Peyman Ansari - Gazi University
Sertaç Altınok - Turkish Aerospace Industries
Güray Akbulut - Tusaş Engine Industries
Deniz Demirci - SSB
Sami Duman - ASELSAN
Burak Karakaş – Ermaksan Co.
Orkun Umur Önem - Roketsan
Ahmet Özkayan – Ermaksan Co.

Keynote Speakers

Dr. Gustavo M. Castelluccio (Cranfield University)
Dr. Andrea Cini (Carlos III Madrid University)
Lars Langhans (FIT Additive Manufacturing Group)

Background

The Advanced Materials and Advanced Manufacturing Technologies Conference (A2M2C) is designed to foster dialogue and collaboration among researchers, academicians, and industry experts by exploring cutting-edge methods and innovative approaches in materials science and manufacturing technologies. The conference focuses on advancing value-added products and provides a platform for discussing a wide range of topics spanning engineering, interdisciplinary academic research, and industrial applications.

One of the highlights of the A2M2C conference is its emphasis on additive manufacturing methods, which have revolutionized manufacturing methodologies and continue to shape the future of the field. The conference serves as a meeting point for national and international participants, encouraging the exchange of ideas and knowledge that drive innovation.

The inaugural A2M2C conference also marks an important milestone for several high-impact projects, including the “Advanced Materials and Advanced Manufacturing Technologies (A2M2TECH)” project (www.a2m2tech), funded by the European Commission and TÜBİTAK, and the “New Generation 3D Printer Manufacturing Technologies Platform (3B-YIB)” (www.ektam.gaz.edu.tr) project, supported by TÜBİTAK. Attendees will gain insight into the breakthroughs achieved through these initiatives, as well as the latest research results derived from experiments conducted by leading academics in their respective fields. By bringing together diverse perspectives and expertise, the A2M2C conference aims to inspire collaborations that advance both academic research and industrial innovation, ensuring a brighter future for advanced materials and manufacturing technologies.



**1st International Conference on Advanced Materials
and Advanced Manufacturing**

(A2M2C-1)

18-20 October, 2023

EKTAM, Ankara

(10:00-16:00 hrs)

Organized by

**Gazi University
Additive Manufacturing Technologies Application
and Research Center
(EKTAM)**

Contents

A Solid Solution-Based Tough Polymer Electrolyte for Structural Energy Storage Applications	1
The Effect of Volumetric Energy Density on the Mechanical Behavior of AlSi10Mg Alloy Manufactured by Selective Laser Melting	6
Defect Analysis and Surface Roughness Characterization of Additively Manufactured Samples Using Computer Tomography	12
Effect of Post Heat Treatments on the Creep and Microstructural Characteristics of Inconel 939 Alloy Fabricated by Selective Laser Melting.....	19
A Study on Beam Shaping Effects on The Mechanical Properties and Residual Stresses in Parts Processed Using Selective Laser Melting.....	27
Effect of Surface Roughness on Fatigue Behavior of Ti6Al4V Produced by Selective Laser Melting.....	32
Additive Manufacturing of Molybdenum by Using Electron Beam Melting and Selective Laser Melting.....	37
Warpage at FDM Printed Composites: Case Study of A Thin-Walled Camera Holder.....	45
Wire-Arc Additive Manufacturing of Combustion Chamber	52
From Design to Smile: Leveraging AM and Topological Optimization for Jaw Implant Solutions.....	57
An Ex-Situ Energy Density Computation Method for Selective Laser Melting (SLM) System.....	63
Next Generation Eco-Materials Revolution: CO ₂ Emissions Reduction via Lattice-Structured Additive Manufactured Lever Arms	72
A Case Study in Deep Drawing Process: Numerical Simulation and Analysis of Material Behavior and Hardening Models	80
From Blueprint to Greenprint: A Case Study on CO ₂ Footprint Assessment in Product Design & Manufacturing (PDM).....	88
Synthesis of 2D MoS ₂ Polycrystalline for Electro-optical Applications.....	96
Defect Analysis of Additively Manufactured AlSi10Mg Samples Using Different Process Parameters in a Single Specimen	101
Corrosion Behavior in SLM-Produced AlSi10Mg Alloy: Evaluating Process Parameters Effect.....	107
Effect of Heat Treatment on the Energy Absorption and Ductility of the Imperfect BCC lattice Structures ..	113
Microstructural and Nano-mechanical Characterization of Gas Atomized IN738LC Powder	121
Standardization of High Temperature Fatigue Tests for AM Metals.....	129
Effect of The Orientation of The Trabecular Structure on The Comparison Strength of Bone for Future Studies	131
The Role of Dyes in Ceramic-Filled Acrylate Resin Composites for Ceramic Additive Manufacturing	139
A Study on Beam Shaping Effects on The Mechanical Properties and Residual Stresses in Parts Processed Using Selective Laser Melting.....	153
Enhancing Dimensional Precision for Complex Geometries in Additive Manufacturing Post-Processing through Advanced Computing.....	158
Additive Manufacturing Design with Overhang Constraint Based on Reliability-Based Topology Optimization Approach	162
Biodegradable Magnesium Bone Plates; Simulation Based Predictive Model for Controlled Degradation ...	171
Investigating the Impact of Recoater Speed on Micron-Sized Powder Dispersion on the Substrate in Selective Laser Melting (SLM) via DEM	176

Application of Micro Computed Tomography (μ -CT) method for Defect Detection in AlSi10Mg Parts Produced with SLM Technology	182
Numerical and Experimental Investigation of the Effect of Process Parameters on Mechanical Properties in Selective Laser Melting.....	189
An Experimental Study on Ultrasonic Atomized 316L Stainless Steel Powder for Additive Manufacturing.	198

A Solid Solution-Based Tough Polymer Electrolyte for Structural Energy Storage Applications

P. Teymoory^{*1}, Y. Chang¹, C. Shen¹

1. Department of Mechanical Engineering, University of Massachusetts Dartmouth 285 Old Westport Road, North Dartmouth, MA, USA, 02747 pteymoory@umassd.edu / 1-508-999-8449

Abstract

Multifunctional structural energy storage components that can replace existing structural components while providing additional energy storage capability can ease the power demands of various electrically powered systems. The serious trade-offs between the mechanical and electrochemical performance of structural electrolytes are a challenge to realizing practical structural energy storage components. In this research, a solid polymer electrolyte with hydrates was created using polylactic acid and lithium salt. One of the compositions achieved a significant ionic conductivity ($3.11 \mu\text{S}/\text{cm}$) with an excellent toughness ($15.4 \text{ MJ}/\text{m}^3$) that is one order higher than the base polymer. This study demonstrates the possibility of incorporating electrochemical functionality into structural composites while maintaining or even enhancing mechanical functionality, guiding the design of future structural energy storage components

Keywords: Structural energy storage; Supercapacitors; Solid polymer electrolyte; Multifunctionality.

Introduction

In electrically powered mobile systems, the heaviest components are energy storage devices and supporting structures. Taking an electric vehicle as an example, about 30% of the weight comes from the battery, and over 35% from structural components including frame, exterior, and interior. To further improve the operation time, travel range, and functionality of such systems, especially when the batteries are approaching their performance limit, one solution is to develop multifunctional structural energy storage components, which can replace existing structural components and provide extra energy storage capability. Researchers have demonstrated structural supercapacitors for this purpose¹. Most of these devices share the configuration of laminate fiber composites, in which two layers of carbon fiber electrodes are sandwiching a glass fiber separator and filled with an ion-conducting solid electrolyte as the matrix. The energy is stored through the electric double-layer capacitance effect at the carbon fiber-solid electrolyte interface. In almost all previous studies, the solid electrolytes are made of bi-continuous phase electrolytes (BPEs), which are simply the mixtures of liquid electrolytes and epoxy resins². The BPEs, however, have significant trade-offs between mechanical and electrochemical performance and poor electrochemical interfaces with electrode materials.

Our recent study demonstrated a solid polymer electrolyte incorporated with hydrates (denoted as SPE-H) that provides promising multifunctionality³. We used polyethylene terephthalate (PET) as the base polymer and melted it together with lithium perchlorate (LiClO_4) to produce an amorphous solid solution. The PET- LiClO_4 electrolyte was then hydrated under controlled humidity to convert the salt to its trihydrate ($\text{LiClO}_4 \cdot 3\text{H}_2\text{O}$). Unlike previous designs of BPEs, we found that the SPE-H provided significant ionic conductivity while retaining the base polymer's stiffness and toughness. Moreover, such electrolytes showed much better electrochemical interfaces with electrodes. In this research, we present another SPE-H system

made from a different base polymer, polylactic acid (PLA), and another salt, lithium bis(trifluoromethanesulfonyl)imide (LiTFSI). The new material system is easier to process and form desired shapes through various techniques. One of the compositions achieved a significant ionic conductivity ($3.11 \mu\text{S/cm}$) with an excellent toughness (15.4 MJ/m^3) that is one order higher than the base polymer after proper thermal treatment and controlled hydration.

This is the first evidence to show that it is possible to incorporate electrochemical functionality into structural composites while retaining or even enhancing their mechanical functionality. The mechanisms learned in this study can guide the design of better structural energy storage components in the future.

Experimental Set Up

Sample preparation: In a typical process, 2 grams of PLA and $x \text{ wt\%}$ ($x = 10$ to 50) of LiTFSI were mixed in 40 ml of dimethylformamide (DMF). The mixture was put on the hot plate and stirred vigorously under 110°C for 12 hours overnight to ensure the homogeneity of the solution. Then the solution was cast on a Teflon plate at 120°C for 6 hours. We denote the samples at this stage as “As-cast SE x ”, where SE stands for structural electrolyte and x reflects the wt% of the salt. The as prepared SE samples had residual DMF, so the cast film was then put into a convection oven at 165°C for one hour to evaporate the residual solvent as much as possible. The samples are denoted as “Dried SE x ” after this step. These dried samples can be melted and shaped through hot press, hot rolling, or injection molding. The shaped samples were then exposed to air with controlled humidity in an environmental chamber. The samples will absorb water molecules from the air because of the hygroscopic nature of the salt. The amount of water absorbed is self-limiting at fixed temperature (22°C in our laboratory) and relative humidity, as demonstrated in our previous studies^{3,4}. The samples are denoted as “Hydrated SE x ” after this step. Although it seems that the hydrated samples are only the results of replacing the DMF in as-cast samples with water, later tests show that the hydrated samples have both higher ionic conductivities and better mechanical properties than the as-cast ones.

Material characterizations: Fourier transform infrared spectroscopy (FTIR) testing was conducted on an Agilent Cary 630 to detect the presence of chemicals. Electrochemical impedance spectroscopy (EIS) was conducted using a Gamry Interface 1010 potentiostat to obtain the impedance of electrolyte samples for ionic conductivity calculation. Tensile tests were conducted using rectangular samples on an Instron 5569 testing machine to obtain their mechanical properties.

Results and Discussions

FTIR results:

The chemical compositions of the electrolyte samples are confirmed by FTIR analysis, which characterizes chemical bonds through the absorbance peaks of infrared light in resonant frequencies. The FTIR spectra of pure chemicals, including PLA, LiTFSI, DMF, and water are first tested and presented in Figure 1a. Pure PLA is featured by an absorption peak near 1749 cm^{-1} caused by C=O stretching, and many peaks in the range of 1500 cm^{-1} to 1250 cm^{-1} due to C-H stretching and 1250 cm^{-1} to 1000 cm^{-1} due to C-O stretching⁵. LiTFSI has strong feature peaks between 1500 cm^{-1} and 1000 cm^{-1} , but it is small peaks around 3600 cm^{-1} that distinguish it from other chemicals. DMF shows the strongest feature peak at 1665 cm^{-1} caused by C=O stretching. Liquid water is featured by a broad peak around 3300 cm^{-1} . The FTIR spectra of representative structural electrolyte samples are plotted in Figure 1b. The as-cast SE 40 sample

show two feature peaks at 1749 cm^{-1} and 1665 cm^{-1} , respectively, indicating the existence of both PLA and residual DMF. The DMF can be completely removed after the drying process, as the feature peak of DMF disappears in the dried SE 40 sample. The spectrum of the hydrated SE 40 sample, however, shows little difference from the dried sample. The absence of peaks around 3300 cm^{-1} indicates the absence of liquid water. A small rise of absorbance near 3600 cm^{-1} is caused by the interaction between LiTFSI and water.

Ionic conductivity results:

The ionic conductivities of as-cast SE samples with various compositions are first tested and shown in Figure 2a. The values increase by three orders of magnitude from $4.2 \times 10^{-4}\text{ }\mu\text{S/cm}$ to $8.7 \times 10^{-1}\text{ }\mu\text{S/cm}$ when the weight ratio of the salt increases from 10% to 50%. The increase of ionic conductivity is partially due to the increased amount of salt ions. More importantly, it is caused by the increased amount of residual DMF that is associated with the salt. When the DMF is completely removed, the ionic conductivity decreases sharply.

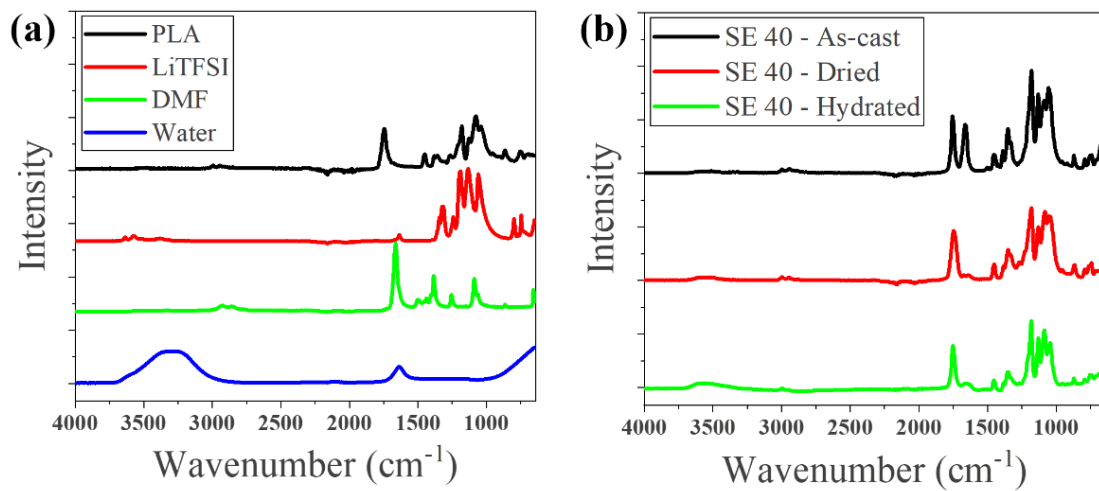


Figure 1. FTIR spectra of (a) pure chemicals used in the preparation of structural electrolyte samples and (b) representative structural electrolyte samples at different stages of processing.

For example, the ionic conductivity of SE 40 decreases from $4.8 \times 10^{-1}\text{ }\mu\text{S/cm}$ (as-cast, Figure 2a) to $1.1 \times 10^{-4}\text{ }\mu\text{S/cm}$ (dried, Figure 2b). The hydration process, on the other hand, will restore the ionic conductivity, as shown in Figure 2b. For SE 40, its ionic conductivity increases to $3.11\text{ }\mu\text{S/cm}$ when hydrated at a relative humidity of 70%, and it reaches $59.1\text{ }\mu\text{S/cm}$ when hydrated at 80% humidity. The hydration is self-limiting up to the humidity of 70% as indicated by the controlled weight gain (due to water absorption) measured in Figure 2c. However, the water absorption becomes out of control when the humidity reaches 80%, under which the salt will absorb too much water to form liquid solution. Liquid droplets were detected on samples, and the SE samples became gels with significantly reduced mechanical properties. Therefore, hydration under 70% humidity is considered as the optimized processing condition.

Tensile test results:

The stress-strain curves of as-cast SE samples with various compositions are presented in Figure 3a. As more LiTFSI is added to the polymer matrix, the samples show decreased elastic moduli and tensile strengths.

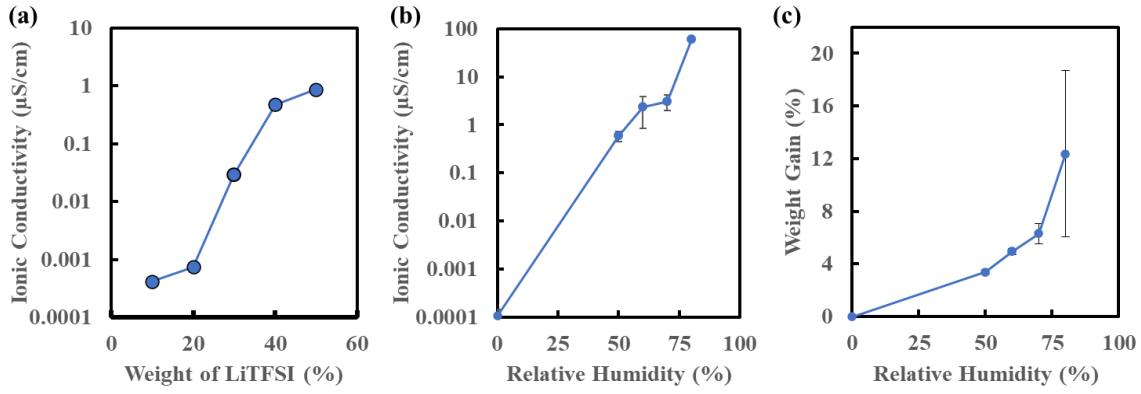


Figure 2. (a) The ionic conductivity of as-cast structural electrolyte samples with various weight ratios of LiTFSI. (b) The ionic conductivity of SE 40 samples hydrated at various relative humidity levels. (c) The weight change of SE 40 samples hydrated at various relative humidity levels.

However, the ductility of the samples increases greatly with more salts in them, resulting in very high toughness values as shown in Figure 3b. The significant increase in ductility indicates that the salt, together with the residual DMF, acts as a plasticizer in the material system. The toughness of the base polymer PLA is 1.83 MJ/m³, which is comparable to the values reported in the literature⁶. The toughness of as-cast SE 40, however, improves by one order of magnitude and achieves 18.5 MJ/m³. Then the mechanical properties of the SE 40 samples at different stages of processing are tested and shown in Figure 3c. The samples become stiffer and stronger after DMF is removed, while most of the ductility is preserved. As a result, the dried SE 40 presents a toughness of 30.0 MJ/m³. Hydration of the samples will decrease the elastic modulus and strength again, but they are still stiffer and stronger than the as-cast ones. The hydrated SE 40 (hydrated at 70% humidity) has a toughness of 15.4 MJ/m³, which is still one order of magnitude higher than that of pure PLA.

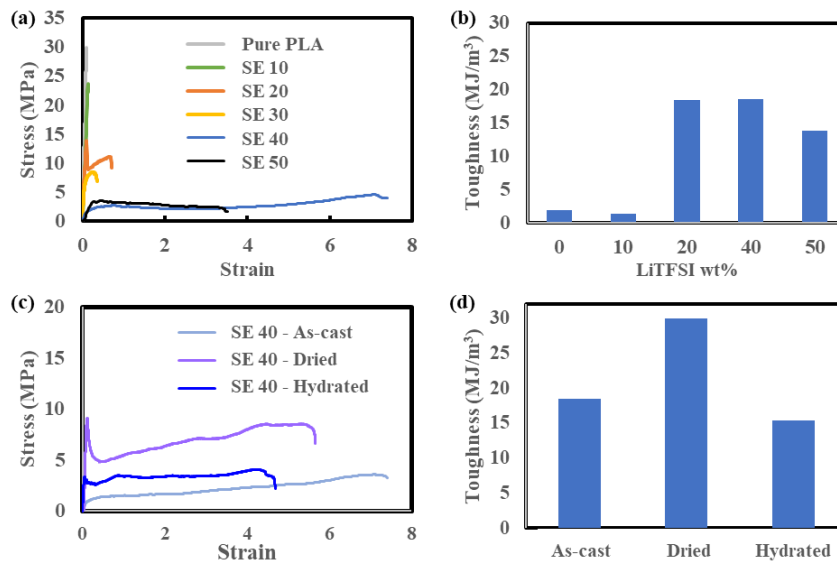


Figure 3. (a) The stress-strain curves of pure PLA and as-cast SE samples with various weight ratios of LiTFSI. (b) The average toughness values of pure PLA and as-cast SE samples with various weight ratios of LiTFSI. (c) The stress-strain curves of SE 40 at different stages of processing. (d) The average toughness values of SE 40 at different stages of processing.

Conclusions

We have demonstrated a solid polymer electrolyte incorporated with hydrates (SPE-H) using hydrated PLA-LiTFSI samples for potential structural energy storage applications. We found that the samples prepared by solution casting method have significant solvent residuals that greatly affect the ionic conductivity and mechanical properties of the electrolyte system. The samples can be processed and shaped through various techniques including hot rolling and injection molding after complete removal of the residual solvent. The final electrolyte prepared through proper hydration of the dried samples achieves a significant ionic conductivity ($3.11 \mu\text{S/cm}$) with an excellent toughness (15.4 MJ/m^3) that is one order higher than the base polymer. Future research will demonstrate the processing of such electrolyte through 3D printing and the combination with electrode materials for high-toughness multifunctional structural energy storage devices.

References

1. Xu, Y., Lu, W., Xu, G. & Chou, T.-W. Structural supercapacitor composites: A review. *Compos. Sci. Technol.* **204**, 108636 (2021).
2. Tu, V. *et al.* Performance of bicontinuous structural electrolytes. *Multifunct. Mater.* **3**, 025001 (2020).
3. Joyal, N., Chang, Y.-C., Shonar, M., Chalivendra, V. & Shen, C. Solid polymer electrolytes with hydrates for structural supercapacitors. *J. Energy Storage* **51**, 104459 (2022).
4. Anjum, N., Joyal, N., Iroegbu, J., Li, D. & Shen, C. Humidity-modulated properties of hydrogel polymer electrolytes for flexible supercapacitors. *J. Power Sources* **499**, 229962 (2021).
5. Li, D. *et al.* Preparation of plasticized poly (lactic acid) and its influence on the properties of composite materials. *PLoS One* **13**, 1–15 (2018).
6. Suttiruengwong, S., Pitak, S., Saedan, M., Wongpornchai, W. & Singho, D. Binary-additives toughened biopolymer for packaging application. *Energy Procedia* **56**, 431–438 (2014).

Acknowledgements

This research work is supported by UMass Dartmouth's Marine and Undersea Technology (MUST) Research Program funded by the Office of Naval Research (ONR) under grant N00014-20-1-2170, and also supported by National Science Foundation grant 2217172.

The Effect of Volumetric Energy Density on The Mechanical Behavior of AlSi10Mg Alloy Manufactured by Selective Laser Melting

Mian imran^{1,2}, Mustafa Güden¹, Çetin Bakıcı¹, Peyman Ansari^{2,3}, Metin U. Salamci^{2,3}, İlhan Şen⁴, AlperTaşdemirci¹

1. Dynamic Testing and Modeling Laboratory Department of Mechanical Engineering, Izmir Institute of Technology, Section of Materials Technology, Urla, Izmir 35430, Turkey

2. Additive Manufacturing Technologies Application and Research Center (EKTAM), Gazi University, No:6/1, 06560 Yenimahalle, Ankara, Turkey

3. Department of Mechanical Engineering, Gazi University, No:5, 06570 Maltepe, Ankara Turkey

4. Turkish Aerospace, Ankara, Turkey

Abstract

Additive manufacturing (AM) processes have wide applications in a variety of industries, especially aerospace, automobile, biomedical, marine, and other industries. The mechanical properties of these AM-manufactured parts are mostly affected by the process parameters. Volumetric energy density (VED) measures the cumulative effect of process parameters in this work, the relationship between VED and mechanical properties was established. Three different groups of AlSi10Mg samples having different values of VED in conduction, transition, and keyhole mode were manufactured using selective laser melting process. It was found that specimens having VED value in conduction mode exhibited higher tensile strength than the other two groups' specimens having VED value in transition and keyhole mode. However, the fracture strain of transition mode samples was reported to be higher than the other two groups of specimens.

Keywords: AlSi10Mg, Selective laser melting, Volumetric energy density, Tensile strength, Fracture strain

Introduction

Additive manufacturing (AM) or 3D printing is the process of joining materials in order to create objects from three-dimensional model data usually layer by layer upon layer. The 3-D printer performs similarly to a typical inkjet printer, however, rather than printing a layer of ink on paper, a 3-D printer utilizes materials to construct a three-dimensional part [1]. Powder bed fusion (PBF) and Direct Energy Deposition (DED) AM techniques are more suited for the manufacturing of metallic parts. AM procedures most utilized in powder bed fusion techniques include selective laser melting (SLM) and electron beam melting (EBM). In these AM techniques, a molten pool is formed by the interaction of a laser or electron beam with the feedstock powders, permitting rapid melting and re-solidification [2,3]. The Si-rich aluminum alloy AlSi10Mg is the most important of all aluminum alloys. The AlSi10Mg alloy is a hypoeutectic aluminum alloy. Because of its excellent castability, low density, and combination of remarkable mechanical properties, it is widely used in the automotive, aerospace, and military industries [4]. The process parameters of SLM-manufactured AlSi10Mg parts have a substantial impact on the part's eventual mechanical qualities. The most academic argument is over laser power, scan speed, hatch spacing, layer thickness, and scan method [5,6]. Lv et al. investigated the effect of scanning speed on the quasi-static elongation as well as the tensile strength of AlSi10Mg manufactured through the laser melting deposition process (LMD). Tensile strength increased initially and then decreased as scan speed increased, although elongation increased [7]. Wang et al. [8] researched on increasing the laser's power from 480 W to 1200 W. The highest tensile strength was obtained with a laser power of 910 W. However, as the laser's power increased, the total elongation increased considerably. Karan s. et al. [9] found that the tensile strength of aluminum alloy 5183 manufactured using wire arc additive manufacturing reduces as the deposition thickness increases. The effect of hatch

spacing was studied by Ilyas et.al [10]. They found that For Ti64 manufactured by SLM, the ultimate tensile strength values decreased as the hatch spacing increased; however, the elongation values showed a different trend. The elongation values rose to 67.5 μm and subsequently declined as the hatch spacing increased. Noriko. et.al[11] studied the effect of build direction on the static mechanical properties and concluded that tensile strength and elongation of SLM-manufactured AlSi10Mg parts alloy having horizontal built direction were higher than the vertically manufactured parts. Volumetric energy density (VED) is an important manufacturing parameter for melting powder raw materials. It indicates the energy transmitted by a laser beam to a unit volume of powder material and corresponds with numerous laser and scan characteristics. The most often used method of representing energy density is as follows.

$$E = \frac{P}{v \cdot h \cdot t} \dots\dots\dots(1)$$

Where P denotes laser power (w), v refers to scanning speed (mm/sec), h implies hatch space (mm), and t specifies layer thickness (mm) [12,13]. There are three types of SLM melting modes i.e., Conduction, transition, and keyhole. The VED is less than 50 J/mm³ in conduction mode and between 50 and 65 J/mm³ in transition mode. This is keyhole mode when VED exceeds 65 J/mm³ [14].

The current work aims to link the static mechanical behavior of AlSi10Mg produced via SLM to volumetric energy density. For that purpose, 3 groups of specimens having different VEDs were manufactured, and their static mechanical behavior was compared.

Material and Methods

Specimens manufacturing

Specimens were manufactured horizontally at Gazi University Additive Manufacturing Technology Application and Research Center (EKTAM) using a Concept Laser-M2 CUSING model-based 3D Printer. The following table shows the VED of each group sample manufactured.

Table 1. VED of fabricated specimens

Group No	Volumetric Energy density(J/mm ³)
Group 1	74.4
Group 2	56.81
Group 3	24.6

Tensile testing

Tensile testings were performed at the dynamic testing and modeling lab at Izmir Institute of Technology Turkey using Shimadzu AG-X 300 kN universal testing apparatus. The data from the device was further verified by using DIC (digital image correlation). For DIC MATLAB 2022b with ncorr was employed [15]. The strain rate during the tensile testing was 10⁻³ sec⁻¹. Figure 1 shows the arrangement of the testing machine.

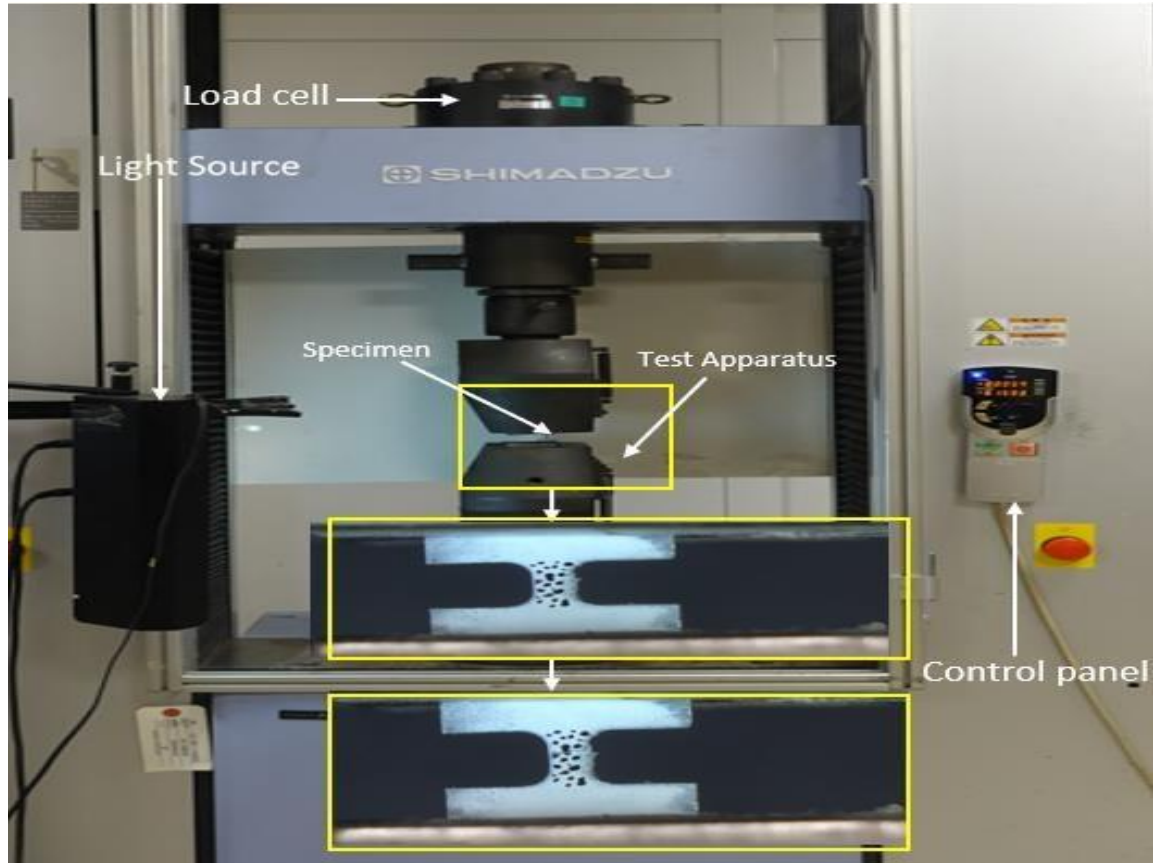


Figure 1. Tensile testing setup

Microstructure analysis

Surface and internal morphology was studied using a scanning electron microscope (SEM) at Izmir Institute of Technology Material Research Center.

Result and Discussion

Thermal Behavior

Four specimens from each group were tested and the behavior of samples within in group was almost similar. Figure 2 shows the fracture specimens after testing.

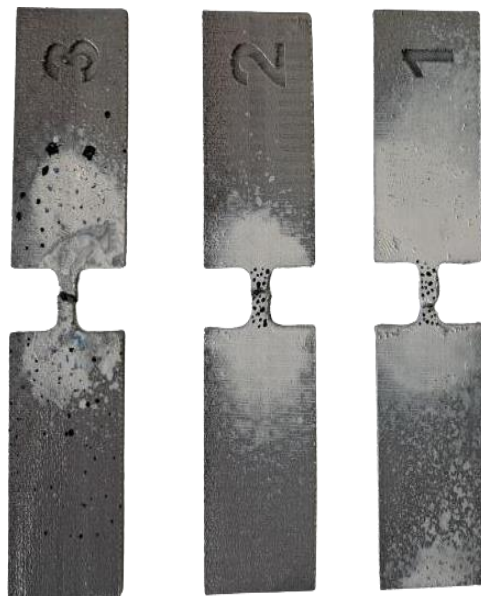


Figure 2. Fracture specimens

The true stress and true strain comparison of 3 groups samples are shown in the below figure.

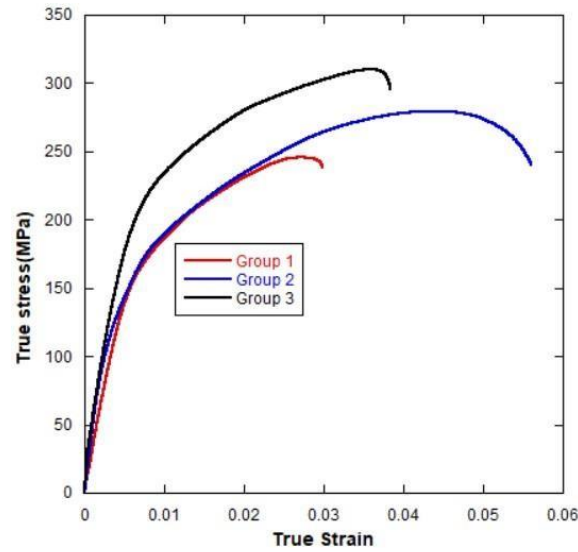


Figure 3. True stress vs True strain comparison

From the above figure, Group 3 samples having a VED value of 24.6 j/mm³ (conduction mode of melting) exhibited the highest tensile strength of 311.5 MPa while Group 1 samples having VED value of 74.4 J/mm³ (keyhole mode of melting) showed the lowest tensile strength of 246.01 MPa. Group 2 samples whose melting mode was transition (VED of 56.81 J/mm³) possessed a tensile strength of 279.15 MPa. It dictates that VED value and tensile strength have an inverse relationship. Increasing VED increases the temperature of molten metal because of which more hydrogen[H] is absorbed in the molten metal pool. During the solidification step the temperature is low and releases more [H] ultimately leading to more pores and due to these pores, the tensile strength and yield strength of samples drops [14,16]. Furthermore, from Figure 3 it is evident that the fracture strain initially increases from 0.038 to 0.056 as the VED is increased from 24.6 to 56.81 J/mm³ and then drops to 0.030 when the VED is further increased to 74.4 J/mm³. Increasing VED up to a certain value causes the slag to adsorb around the pores and produce a fine microstructure which produces a ductile condition. Further enhancement in VED does not keep this track and reduces the fracture strain [17]. So that is why fracture strain increased and then decreased when the VED value raised.

Microstructure analysis

The microstructure of each of the corresponding samples is depicted in the below figure 4. White spots represent the number of pores present in the specimen. The aforementioned figure elucidated that as the mode of melting changed from conduction to keyhole or the Value of VED increased the number of pores increased in the sample.

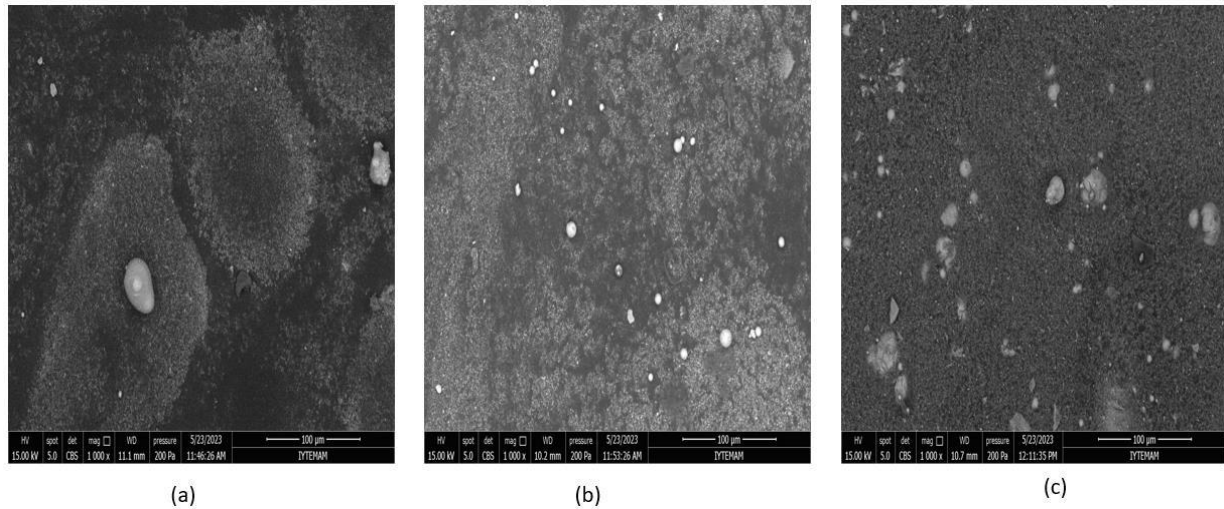


Figure 4. Pores content comparison: (a) Group 3 sample, (b) Group 2 sample, (c) Group 1 sample.

Conclusion

In this study, VEDs at different melting modes were correlated with the mechanical behavior of AlSi10Mg manufactured by SLM. Based on the experimental data and analysis the following conclusion can be made:

- (1). Tensile strength decreases as VED value increases. Samples having a VED of 24.6 J/mm³ showed tensile strength of 311.5 MPa. When the VED values increased to 56.81 and 74.4 J/mm³ the tensile strength dropped to 279.15 MPa and then 246.01 MPa.
- (2). Fracture strain(ductility) increases and then drops when the VEDs value increases. Initially, fracture strain increased from 0.038 to 0.056 as the VED increased from 24.6 to 56.81 J/mm³ and then dropped to 0.030 when the VED was further increased to 74.4 J/mm³ from 56.81 J/mm³.
- (3). The number of pores increases as the VED value rises in the samples. Group 3 samples having VED (24.6 J/mm³) in conduction possessed very few pores than Group 2 samples owing VED (56.81 J/mm³) in transition mode. Further, Group 2 sample pores are lesser than Group 1 samples possessing VED (74.4 J/mm³) in keyhole mode.

Funding

“This work has received funding from, the European Union’s Horizon 2020 research and innovation program under the Marie Skłodowska-Curie grant agreement No 101034425 for the project titled A2M2TECH. This study has also received funding from The Scientific and Technological Research Council of Türkiye (TUBITAK) with grant No 120C158 for the same A2M2TECH project under the TUBITAK’s 2236/B program.”

References

- [1] P. Witherell, J. Herron, and G. Ameta, “Towards Annotations and Product Definitions for Additive Manufacturing,” in *Procedia CIRP*, Elsevier B.V., 2016, pp. 339–344. doi: 10.1016/j.procir.2016.01.198.
- [2] L. Ladani and M. Sadeghilaridjani, “Review of powder bed fusion additive manufacturing for metals,” *Metals*, vol. 11, no. 9. MDPI, Sep. 01, 2021. doi: 10.3390/met11091391.
- [3] G. Gong et al., “Research status of laser additive manufacturing for metal: a review,” *Journal of Materials Research and Technology*, vol. 15. Elsevier Editora Ltda, pp. 855–884, Nov. 01, 2021. doi: 10.1016/j.jmrt.2021.08.050.
- [4] F. Trevisan et al., “On the selective laser melting (SLM) of the AlSi10Mg alloy: Process, microstructure, and mechanical properties,” *Materials*, vol. 10, no. 1. MDPI AG, 2017. doi: 10.3390/ma10010076.

- [5] T. Larimian, B. AlMangour, D. Grzesiak, G. Walunj, and T. Borkar, "Effect of Laser Spot Size, Scanning Strategy, Scanning Speed, and Laser Power on Microstructure and Mechanical Behavior of 316L Stainless Steel Fabricated via Selective Laser Melting," *J Mater Eng Perform*, 2021, doi: 10.1007/s11665-021-06387-8.
- [6] M. de Wild, T. Schollbach, R. Schumacher, E. Schkommodau, and T. Bormann, "Effects of laser parameters and scanning strategy on structural and mechanical properties of 3D NiTi implants fabricated with selective laser melting," *Biomedical Engineering / Biomedizinische Technik*, Oct. 2013, doi: 10.1515/bmt-2013-4088.
- [7] F. Lv, L. Shen, H. Liang, D. Xie, C. Wang, and Z. Tian, "Mechanical properties of AlSi10Mg alloy fabricated by laser melting deposition and improvements via heat treatment," *Optik (Stuttg)*, vol. 179, pp. 8–18, Feb. 2019, doi: 10.1016/j.ijleo.2018.10.112.
- [8] X. Wang, L. Li, J. Qu, and W. Tao, "Microstructure and mechanical properties of laser metal deposited AlSi10Mg alloys," *Materials Science and Technology (United Kingdom)*, vol. 35, no. 18, pp. 2284–2293, Dec. 2019, doi: 10.1080/02670836.2019.1674022.
- [9] K. S. Derekar et al., "Effects of Process Variants on Residual Stresses in Wire Arc Additive Manufacturing of Aluminum Alloy 5183," *Journal of Manufacturing Science and Engineering, Transactions of the ASME*, vol. 144, no. 7, Jul. 2022, doi: 10.1115/1.4052930
- [10] I. Hacısalıhoğlu, F. Yıldız, and A. Çelik, "The effects of build orientation and hatch spacing on mechanical properties of medical Ti–6Al–4V alloy manufactured by selective laser melting," *Materials Science and Engineering: A*, vol. 802, Jan. 2021, doi: 10.1016/j.msea.2020.140649.
- [11] N. Read, W. Wang, K. Essa, and M. M. Attallah, "Selective laser melting of AlSi10Mg alloy: Process optimisation and mechanical properties development," *Mater Des*, vol. 65, pp. 417–424, Jan. 2015, doi: 10.1016/j.matdes.2014.09.044.
- [12] T. Peng and C. Chen, "Influence of energy density on energy demand and porosity of 316L stainless steel fabricated by selective laser melting," *International Journal of Precision Engineering and Manufacturing - Green Technology*, vol. 5, no. 1, pp. 55–62, Jan. 2018, doi: 10.1007/s40684-018-0006-9.
- [13] Č. Donik, J. Kraner, I. Paulin, and M. Godec, "Influence of the energy density for selective laser melting on the microstructure and mechanical properties of stainless steel," *Metals (Basel)*, vol. 10, no. 7, pp. 1–19, Jul. 2020, doi: 10.3390/met10070919.
- [14] H. Wu et al., "Selective laser melted AlSi10Mg alloy under melting mode transition: Microstructure evolution, nanomechanical behaviors and tensile properties," *J Alloys Compd*, vol. 873, Aug. 2021, doi: 10.1016/j.jallcom.2021.159823.
- [15] C. Lim, Y. Jeong, S. Limkantanyu, and M. Kwon, "Strain Measuring of Composite Grid Using Digital Image Correlation," *Advances in Materials Science and Engineering*, vol. 2022, 2022, doi: 10.1155/2022/6041887.
- [16] P. Ansari and M. U. Salamci, "On the selective laser melting based additive manufacturing of AlSi10Mg: The process parameter investigation through multiphysics simulation and experimental validation," *J Alloys Compd*, vol. 890, Jan. 2022, doi: 10.1016/j.jallcom.2021.161873.
- [17] H. Wu et al., "Effect of laser parameters on microstructure, metallurgical defects and property of alsi10mg printed by selective laser melting," *J Micromech Mol Phys*, vol. 2, no. 4, Dec. 2017, doi: 10.1142/S2424913017500175.

Defect Analysis and Surface Roughness Characterization of Additively Manufactured Samples Using Computer Tomography

Muhammad Muteeb Butt^{1,2*}, Peyman Ansari^{2,3}, Hüseyin Kızıl^{1,2}

1. Department of Metallurgical and Materials Engineering, Istanbul Technical University, Istanbul, Turkey.

2. Additive Manufacturing Technologies Application and Research Center-EKTAM, Gazi University, Ankara, Turkey.

3. Department of Mechanical Engineering, Gazi University, 06570 Ankara, Türkiye.

Abstract

Additive manufacturing (AM) has revolutionized the production of complex components but poses challenges regarding quality assurance. This study delves into the interplay between surface roughness, density (reflecting the presence of defects), and AM process parameters in three uniquely fabricated samples. We delve into the density of specimens, which serves as a critical indicator of internal defects. The comprehensive understanding of surface roughness, density, and defect analysis achieved through characterization and experimental testing provides valuable insights. These insights empower us to optimize processing parameters to enhance surface finish, minimize defects, and improve the mechanical performance of AM produced components. The investigation capitalizes on advanced technique, X-ray Computer Tomography (XCT), and analysis, to provide a holistic view of AM part quality. While our initial findings suggest a promising relationship between the variables under study, we must acknowledge the need for more detailed experiments in our future scope. Further research will help solidify these relationships and refine our understanding of AM process optimization.

Keywords: Additive Manufacturing, Computer Tomography, Surface Roughness, Density, Defect Analysis.

Introduction

Additive manufacturing (AM), a technology that constructs intricate 3D objects by layering materials based on digital solid models, has evolved from its initial role in rapid prototyping to a groundbreaking method for producing functional and structural components. AM offers significant advantages in design flexibility, personalized product creation, and efficient low-volume production, making it a compelling alternative to conventional manufacturing techniques. Laser powder bed fusion (L-PBF) stands out among the various metal AM processes. In L-PBF, metallic powders are melted layer by layer using a heat source during fabrication, providing remarkable flexibility in manufacturing. This technique currently dominates the global metal AM market, accounting for 86.5% of all installed AM units 1.

One of the primary challenges associated with adopting AM technologies for functional and structural applications centers on the uncertainty surrounding their fatigue performance. The diminished fatigue strength and considerable variability in fatigue life observed in Laser Powder Bed Fusion (L-PBF) components can be traced back to the prevalence and irregularity of defects introduced during the L-PBF process. Within the context of L-PBF, distinct process characteristics, such as the dynamic nature of the melt pool, ultra-rapid solidification and cooling rates, and substantial thermal gradients, inevitably influence the microstructural features, leading to a spectrum of process-induced defects. These defects encompass entrapped gas and pores, incomplete fusion (Lack of Fusion or LOFs), and the formation of keyholes 2. Among these, defects represent a principal factor limiting the service life of L-PBF components under cyclic loads and serve as the predominant mechanisms for initiating fatigue cracks.

Notably, even after surface treatments are applied to eliminate significant surface roughness, these defects can affect the fatigue performance of L-PBF components, which act as sources of localized stress concentrations.

Extensive research has been conducted to investigate the influence of defects on the fatigue performance of Laser Powder Bed Fusion (L-PBF) specimens. These studies involve extracting defect characteristics, including type, size, aspect ratio, and distance from the surface, from fractography and X-ray computed tomography (CT) images. These extracted defect features are then integrated into established fatigue theories, such as fracture mechanics-based fatigue life prediction models, for comprehensive analysis 3. Additive Manufacturing (AM) presents a notable challenge in the form of inherently rough, as-built surfaces. These surfaces concentrate stress, leading to reduced fatigue life in AM-produced components. While the exterior surfaces of AM parts can be machined to achieve smoother finishes, the internal surfaces, which are often intricate and inaccessible, pose significant post-processing difficulties. AM's strength lies in its ability to create complex geometries with interior features, a characteristic frequently leveraged in design. Therefore, comprehending the quality of as-built surfaces is essential for the broader adoption of AM technology.

Greitemeier et al. 4 have demonstrated that surface finish plays a dominant role in fatigue failure, particularly in materials like Ti-6Al-4V. Surprisingly, no improvement in fatigue life was observed even with a reduction in internal porosity. It has been noted that certain features, such as valleys on additively manufactured surfaces, remain concealed from nondestructive surface roughness measurements. However, these hidden valleys are crucial when considering fatigue performance. Kantzos et al. 5 have shown that surface notches, rather than surface protrusions, are the primary contributors to stress concentration. Given the well-established link between stress concentrations and reduced fatigue life, it is reasonable to conclude that surface notches significantly influence the fatigue performance of components.

The textured surface of AM components arises due to the layer-by-layer nature of the manufacturing process. Surface measurements are typically categorized into line measurements, designated as 'R,' and area measurements, defined as 'S.' In 1995, Ippolito et al. emphasized the pivotal role of surface roughness as a 'crucial feature' in assessing the dimensional accuracy of AM processes. Numerous processing factors can influence the quality of AM surfaces. Among these, two key parameters, component height and component arrangement, have been subjects of prior investigation for their impact on surface roughness. Researchers have employed optical profilometry to measure surface roughness and have concluded that control over the surface quality of components manufactured through electron beam powder bed fusion can be achieved through judicious adjustments of process parameters and thoughtful arrangement of components on the build platform 6.

The reliance on R_a as the predominant metric for assessing surface roughness is questioned due to its unreliability, a sentiment echoed by numerous studies suggesting its inadequacy in characterizing the roughness of AM components. Investigations into the correlation between surface roughness and fatigue life have yielded consistent findings, highlighting the dominant influence of surface roughness on high-cycle fatigue properties.

For instance, Greitemeier et al., in their study of L-PBF specimens assessed using the total height of a line measurement (R_t), observed a pronounced impact of surface roughness on high-cycle fatigue life 7. In the study by Triantaphyllou et al., area average roughness (S_a) and area root mean squared height (S_q) emerged as suitable metrics for assessing areal surface roughness. Additionally, area height distribution skewness (S_{sk}) effectively distinguished upskin and downskin surfaces in Selective Laser Melting (SLM) components 8. Moylan reported that S_a , area maximum peak to valley (S_z), S_{sk} , and area height distribution kurtosis (S_{ku}) were the commonly reported metrics for surface roughness. It has been noted in powder bed AM that surface finish is influenced by powder particle size, and efforts to optimize surface topology have faced challenges in significantly improving part performance 9. However, gaining insight into the surface roughness of AM parts and the intricate process of optimizing this roughness remains an ongoing and complex area of research.

To tackle several of the challenges mentioned earlier, our study focused on the impact of process parameters on the surface roughness and defect attributes in L-PBF printed AlSi10Mg components. We have performed XCT of as built samples and collected information about the defects present in our samples, their morphology, location and impact on mechanical properties of parts will be evaluated. Subsequently, analysis will be done to assess the correlation between these defects and final mechanical properties by these process parameters.

Method

The following section will describe the material and geometry of a Selective Laser Melting (SLM) manufactured sample used for surface roughness evaluation, defect analysis and the chosen CT scan strategy.

Material and Method

Cylindrical fatigue bars of AlSi10Mg were printed having dimensions according to ASTM E466. The geometry of fatigue sample can be seen in Figure 1. Samples were printed through selective laser melting (SLM) process on Concept Laser M2 Cusing model. A total of 03 samples were printed with each having different parameters to study the PSPP relationship with samples having different defect and surface textures and were taken from study of Peyman et. al ¹⁰. Samples were produced through a combination of good and bad parameters so, some of the samples will have surfaces and defects worse than the typically printed parts. Laser power, spot diameter and scan speed were varied while keeping all other parameters constant as shown in Table 1.

Augmenting the laser power input introduces higher energy levels into the material, consequently expanding the size of the melt pool. This elevation in laser power settings progressively approaches what is known as the 'keyholing regime,' leading to a fundamental alteration in the physics governing the melt pool. Notably, it also leads to forming a gas pore near the base of the melt pool. Conversely, elevating the laser speed diminishes the energy imparted to the material and subsequently reduces the size of the melt pool. However, increased laser speed can introduce challenges such as unstable melt conditions and a phenomenon known as 'balling,' which results in an irregular weld bead formation. The variations in contour processing parameters can be effectively understood concerning a linear energy density metric, represented as Power/Speed, where a higher numerical value signifies a more significant infusion of energy into the material ¹¹.

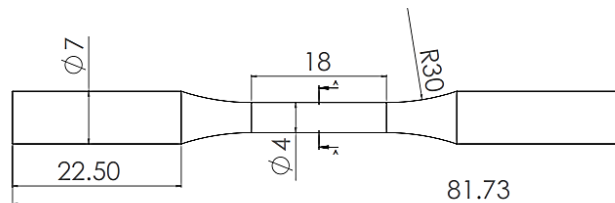


Figure 2. Fatigue test sample with dimensions in mm.

Table 1: Parameters for SLM printing of fatigue samples.

No.	Laser Power (W)	Laser Spot Diameter (μm)	Scanning Velocity (m/s)
1	225	140	1.4
2	350	140	1.1
3	400	140	0.8

Computed Tomography

All fatigue bars underwent comprehensive surface and volume analysis on the gage section employing a nondestructive technique. X-ray Computer Tomography (XCT) was used for characterizing the internal defects, surface properties and defect density of parts. This method was selected due to its ability to be executed before the mechanical testing phase, ensuring comprehensive assessment of the entire surface and volume could be achieved [12]. Figure 2 illustrates the configuration of an XCT scanning setup. The X-ray, emitted in a conical beam pattern by the X-ray tube, permeates the test sample and experiences partial absorption. The sample undergoes a full 360-degree rotation throughout the measurement process, enabling the detector to record multiple two-dimensional projected images. These images are the basis for reconstructing a three-dimensional dataset of volume elements (voxels) using specialized algorithms and high-capacity computer systems.

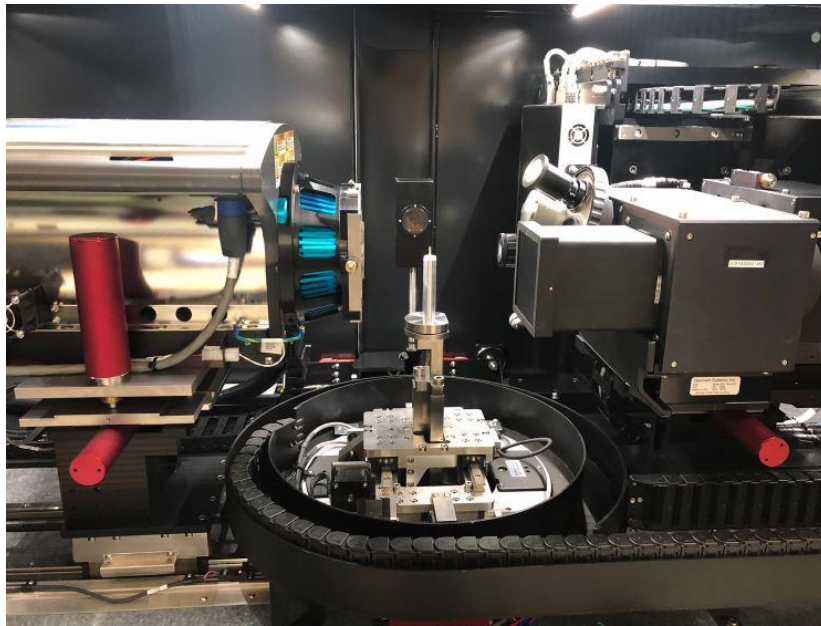


Figure 2. XCT setup of ZEISS XRadia 510 Versa

XCT of fatigue samples was performed using ZEISS XRadia 510 Versa system. This XCT system has source of 160 kV and maximum power of 10 W. The spatial resolution of the equipment can go up to 0.7 microns. The pixel size in our case was 21.90 μm . Detail of parameters used to perform XCT are given in Table 2. A software package provided by ZEISS was used to reconstruct the data.

The characterization of defects encompassed the assessment of both two-dimensional pore area and three-dimensional defect volume along with the density calculation. VG Studio software was used to analyse the defects in the material and to capture the reconstructed sample's cross-sectional images.

Table 2: Acquisition parameters for XCT.

Parameter	Value
Voltage	50 kV
Current	04 W
Exposure time	8 sec

To study the effect of process parameters on internal defects we estimated the density of our printed components and compared the values as shown in Table 3. Density of finished part is strongly effected

by the energy density being controlled by the process parameters 13. The density was calculated using the following relationship:

$$E = \frac{P}{vdt}$$

Where $E(J/mm^3)$, $P(W)$, $v(mm/s)$, $d(mm)$ and $t(mm)$ represent energy density, laser power, scanning velocity, laser beam sport diameter and powder layer thickness respectively.

Trend of energy density and component density is shown in Figure 3. A strong relation was observed between energy density and component density. For parameter 1 the energy density was low and inefficient melting was expected, this sample resulted in lower component density. Sample 2 had sufficient energy density and was expected to give minimum defects, resulting in the highest density of the component. Sample 3 had the highest energy density but some evaporation and excessive melting was anticipated at this high energy density due to which defects were observed in XCT, this sample gave a slightly lower component density than sample 2.

Each sample showed different surface roughness behavior which we were able to see visually through XCT images however specific image processing would be required to calculate surface roughness through those images which will then be verified through dedicated surface roughness measurement techniques like profilometry.

A further detailed study will be required considering other factors to develop a correlation which is the scope of our future work.

Table 3: Detail of process, energy density & component density.

Process No.	Energy Density (J/mm^3)	Est. Component density
1	28.69	94.65
2	56.81	99.92
3	89.28	99.62

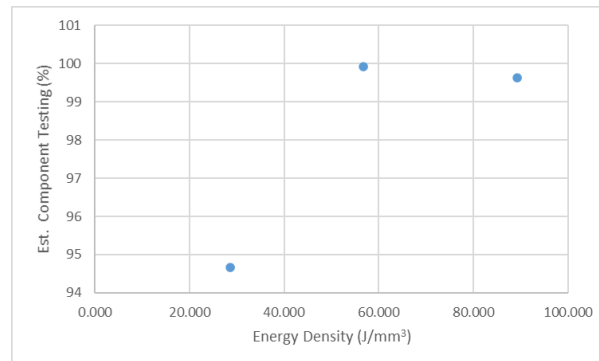


Figure 3. Relation between energy density and relative density.

Conclusions

Our study has explored the relationship between surface roughness, density, and AM process parameters in additive manufacturing. A direct relation has been observed between process parameters

and component density. While our preliminary findings show promise in optimizing AM processes for improved quality, we acknowledge that further detailed experiments are necessary to validate these results. This study represents a starting point for future research, aiming to provide more comprehensive insights into AM part quality and process optimization.

References

1. Li, A. et al. Defect criticality analysis on fatigue life of L-PBF 17-4 PH stainless steel via machine learning. Elsevier.
2. Ren, Y. et al. Low cycle fatigue properties of Ti-6Al-4V alloy fabricated by high-power laser directed energy deposition: Experimental and prediction. Elsevier.
3. Moon, S. et al. Impact of surface and pore characteristics on fatigue life of laser powder bed fusion Ti-6Al-4V alloy described by neural network models. *nature.com* S Moon, R Ma, R Attardo, C Tomonto, M Nordin, P Wheelock, M Glavicic, M Layman, R BilloScientific reports, 2021•nature.com.
4. Greitemeier, D., Dalle Donne, C., Syassen, F., Eufinger, J. & Melz, T. Effect of surface roughness on fatigue performance of additive manufactured Ti-6Al-4V. *Materials Science and Technology (United Kingdom)* 32, 629–634 (2016).
5. Kantzos, C. A., Cunningham, R. W., Tari, V. & Rollett, A. D. Characterization of metal additive manufacturing surfaces using synchrotron X-ray CT and micromechanical modeling. *Comput Mech* 61, 575–580 (2018).
6. Jamshidinia, M., Metrology, R. K.-S. T. & 2015, undefined. The influence of heat accumulation on the surface roughness in powder-bed additive manufacturing. *iopscience.iop.org* M Jamshidinia, R KovacevicSurface Topography: Metrology and Properties, 2015•iopscience.iop.org 3, 14003 (2015).
7. Ippolito, R., Iuliano, L., annals, A. G.-C. & 1995, undefined. Benchmarking of rapid prototyping techniques in terms of dimensional accuracy and surface finish. Elsevier.
8. Triantaphyllou, A., ... C. G.-S. topography & 2015, undefined. Surface texture measurement for additive manufacturing. *iopscience.iop.org* A Triantaphyllou, CL Giusca, GD Macaulay, F Roerig, M Hoebel, RK Leach, B TomitaSurface topography: metrology and properties, 2015•iopscience.iop.org.
9. Fox, J., Moylan, S., Cirp, B. L.-P. & 2016, undefined. Effect of process parameters on the surface roughness of overhanging structures in laser powder bed fusion additive manufacturing. Elsevier.
10. Ansari, P., Compounds, M. S.-J. of A. and & 2022, undefined. On the selective laser melting based additive manufacturing of AlSi10Mg: The process parameter investigation through multiphysics simulation and. Elsevier.
11. Gockel, J., Sheridan, L., Koerper, B. & Whip, B. The influence of additive manufacturing processing parameters on surface roughness and fatigue life. *Int J Fatigue* 124, 380–388 (2019).
12. Tamas-Williams, S., Withers, P., reports, I. T.-S. & 2017, undefined. The influence of porosity on fatigue crack initiation in additively manufactured titanium components. *nature.com*.

13. Calta, N., Wang, J., Kiss, A., ... A. M.-R. of S. & 2018, undefined. An instrument for in situ time-resolved X-ray imaging and diffraction of laser powder bed fusion additive manufacturing processes. pubs.aip.org.

Funding

This work has received funding from, the European Union's Horizon 2020 research and innovation program under the Marie Skłodowska-Curie grant agreement No 101034425 for the project titled A2M2TECH. This study has also received funding from The Scientific and Technological Research Council of Türkiye (TUBITAK) with the grant No 120C158 for the same A2M2TECH project under the TUBITAK's 2236/B program.

Effect of Post Heat Treatments on the Creep and Microstructural Characteristics of Inconel 939 Alloy Fabricated by Selective Laser Melting

Fatih Guler^{1,5}, Aylin Sahin Kahraman², Merve Canbolat³, Guney Mert Bilgin⁴, Ozgul Keles⁵, Huseyin Aydin⁶

1,2,6. Metallic Materials Technologies Research Group, TUBITAK MAM, Kocaeli, Türkiye.

1,5. Department of Metallurgical and Materials Engineering, Istanbul Technical University, Istanbul, Türkiye.

3. Department of Materials Science and Engineering, Gebze Technical University, Kocaeli, Türkiye.

4. TUSAS Engine Industries, Inc. (TEI), Eskisehir, Türkiye.

Abstract

This study focuses on examining the creep behavior and microstructural properties of heat-treated Inconel 939 alloy produced through additive manufacturing. Inconel 939 is a critical alloy in high-temperature applications, yet the impact of additive manufacturing and post-processing on its mechanical behavior and microstructure remains not fully understood. The research involves creep rupture tests on selectively laser melted Inconel 939 alloy that has undergone post-processing through hot isostatic pressing (HIP) and/or vacuum heat treatments (VHT). Heat-treated alloy microstructure is also examined in detail using optical microscopy (OM) and scanning electron microscopy (SEM). The study's findings indicate that all conducted heat treatment recipes improved rupture times compared to the as-built condition. However, there are considerable differences in rupture time and Creep% between HIP and/or VHT. This study represents a small yet significant step towards optimizing the use of this alloy in high-temperature applications and contributing to engineering applications.

Keywords: Creep, Inconel 939, HIP, SLM, VHT.

Introduction

Nickel-based superalloys are widely used in aviation and energy industries due to their remarkable resistance to oxidation and superior creep properties at high service temperatures. However, conventional manufacturing techniques have limitations regarding component complexity, costs, and production time, reducing efficiency. Hence, new manufacturing processes like selective laser melting (SLM) have been researched for nickel-based superalloys to expand design possibilities, and reduce time and costs [1,4].

Selective Laser Melting (SLM) is a 3D printing method that involves using a high power-density laser to melt and fuse metallic powders. Despite its many advantages over conventional techniques, manufacturing nickel-based superalloys with the SLM technique can pose several challenges. The microstructural heterogeneity due to nature of this method also leads to mechanical insufficiency. Therefore, post-processes such as hot isostatic pressing (HIP) and vacuum heat treatments (VHT) become necessary to achieve the desired microstructure [5,6].

Inconel 939 is a superalloy primarily composed of nickel, which results in the FCC crystal structure matrix. It is highly resistant to corrosion and oxidation at high temperatures, making it an ideal material for use in environments as hot as 850°C. The high resistance to corrosion and oxidation is due to the high percentage of chromium, which facilitates the formation of a protective Cr₂O₃ oxide layer. This property is particularly beneficial in the construction of turbines, especially industrial gas turbines where hot corrosion from gas is a significant concern when selecting materials. It is also worth noting that the mechanical properties of the alloy can differ based on its processing history due to its precipitation-

hardening nature. The properties of as-built material will vary from those of solution-treated or aged hardening material. Furthermore, exposure to high temperatures can cause changes in the alloy's properties over time as the γ' precipitates become coarser, and other thermodynamically stable phases form in the microstructure [4,7,8].

This research thoroughly examines the effects of post heat treatments, namely HIP (hot isostatic pressing) and VHT (vacuum heat treatments), on the microstructure and creep properties of additively manufactured Inconel 939 superalloys.

Materials and Experimental Procedures

Gas-atomized Inconel 939 powder supplied from EOS GmbH (Nickel Alloy IN939) was used for the SLM process. The nominal chemical composition of the powder measured by the ICP-combustion method, is given in **Table 2**.

Table 2. Nominal chemical composition of the IN939 powder (in wt%)

<i>Cr</i>	<i>Co</i>	<i>Al</i>	<i>Ti</i>	<i>Ta</i>	<i>Ni</i>
22.5	19.3	1.9	3.7	1.4	
<i>Nb</i>	<i>W</i>	<i>Zr</i>	<i>B</i>	<i>C</i>	balance
1.0	2.0	0.1	<0,01	0.15	

An EOS M 290 metal 3D printer was used to fabricate cylindrical bar specimens from Inconel 939 powder. To analyze the microstructure of the specimens, optical and scanning electron microscopy (SEM) techniques were utilized. The optical micrographs were captured and processed using the Olympus BX53M inverted microscope. Electron microscopy was conducted through a HITACHI SU7000 equipped with an Energy-Dispersive X-ray Spectroscopy (EDX) detector.

In order to determine the appropriate post heat treatment parameters, DSC and Thermo-Calc simulation techniques were utilized. DSC analysis was performed using the Setaram Setsys Evolution, and the measurements were carried out in an argon atmosphere, with a flow rate of 20 mL min⁻¹. The heat flux was recorded as the samples were heated at a rate of 10°C min⁻¹ from room temperature to 1450°C before cooling back to room temperature at the same rate (Figure 1). Scheil Gulliver solidification simulation of Inconel 939 was conducted using the Calphad-based Thermo-Calc program and its TCNI10 Nickel-based Superalloys Database, to match the temperature-dependent properties of the samples with the DSC and microstructure analyses as well (**Figure 2**) [9].

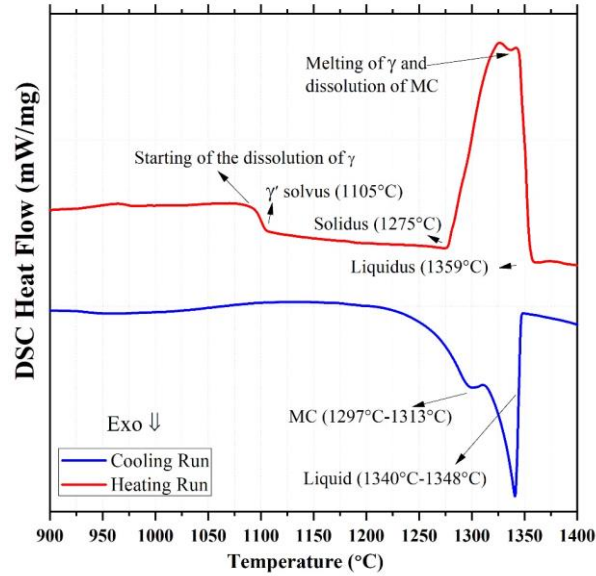


Figure 1. DSC graphs for cooling and heating runs

Three different routes were conducted on the as-built samples for heat treatment studies. HT1 involved solutionizing with both high temperature and high pressure via Quintus QIH-21 hot isostatic press (HIP), and then two-stage aging. HT2 involved solutionizing without pressure and two-stage aging in a TAV brand vacuum heat treatment furnace. HT3 involved a combination of the first two processes. Detailed heat treatment recipes are given in **Table 2**.

After the heat treatment processes, cylindrical bar samples were machined in accordance with ASTM E139 standards (*Standard Test Methods for Conducting Creep, Creep-Rupture, and Stress-Rupture Tests of Metallic Materials*). Creep rupture tests were conducted at 750°C and 350 MPa using an ATS 2330 model creep testing system that employs the lever arm working principle.

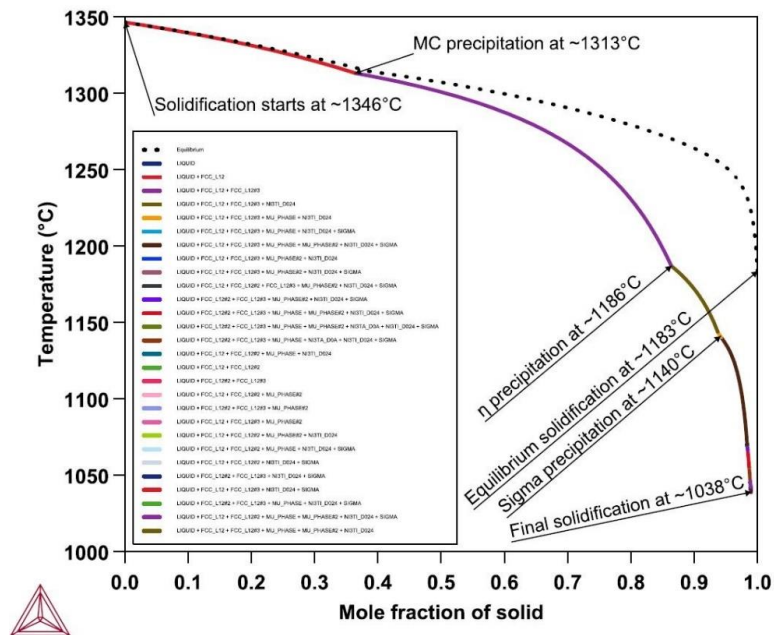


Figure 2. Scheil Gulliver solidification simulation of Inconel 939

Table 3. Detailed recipes for the heat treatments

<i>Recipe</i>	<i>Temp.</i> (°C)	<i>Pressure</i> (MPa)	<i>Hold Time</i> (hour)	<i>Cooling</i>
<i>HT1 (HIP)</i>	1190	170	4	Argon
	1000	-	6	Argon
	800	-	4	Argon
<i>HT2 (VHT)</i>	1190	-	4	Argon
	1000	-	6	Argon
	800	-	4	Argon
<i>HT3</i> <i>(HIP+VHT)</i>	1190	170	4	Argon
	1190	-	4	Argon
	1000	-	6	Argon
	800	-	4	Argon

Results and Discussion

Microstructural Characterization

The micrographs presented in Figure 3 illustrate the as-built condition of SLM-processed samples. One can clearly observe the arch-shaped molten pool boundaries that result from the layer-by-layer processing (Figure 3a). Upon closer inspection, Figure 3b reveals the dendritic and interdendritic structure, showcasing the significant impact of heat flux during layer-wise manufacturing on the microstructure of SLM material. As a result, anisotropic microstructural features are prevalent [10].

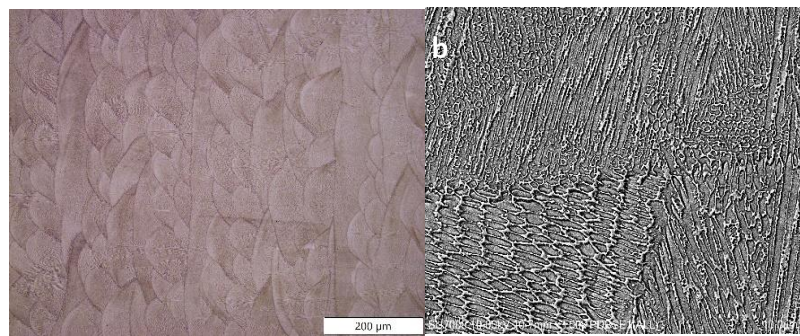


Figure 3. Micrographs for the as-built condition: (a) optical microscope and (b) scanning electron microscope.

Figure 4 showcases the SLM-processed samples under heat treated conditions. As anticipated, the melt pools that were present in the as-built specimens were not found in any of the heat treated samples. Upon closer examination, it was observed that the microstructure in each heat treated condition was remarkably

similar, with fine grains that retained their columnar shape and remained aligned parallel to the building direction. Additionally, small equiaxed grains that formed between the columnar grains were estimated to be recrystallized grains [7].

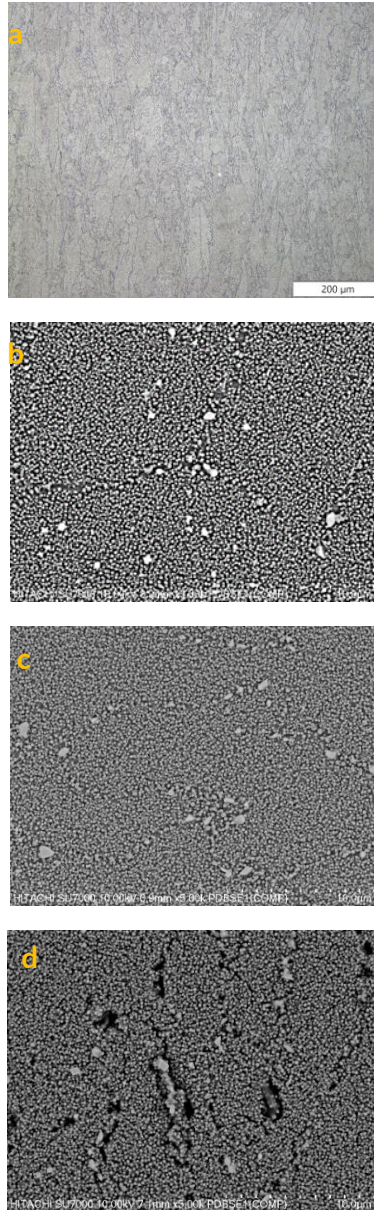


Figure 4. Micrographs for the heat treated conditions: OM images of (a) HT1 (HIP), and SEM images of (b) HT1 (HIP), (c) HT2 (VHT), and (d) HT3 (HIP+VHT).

Further analysis revealed the formation of spherical gamma prime precipitates, as well as the larger carbides that were Ti and Ta rich and present at the grain boundaries and intergranular areas (as shown in Figure 5). It is worth noting that no plate-like phases were observed in the microstructures.

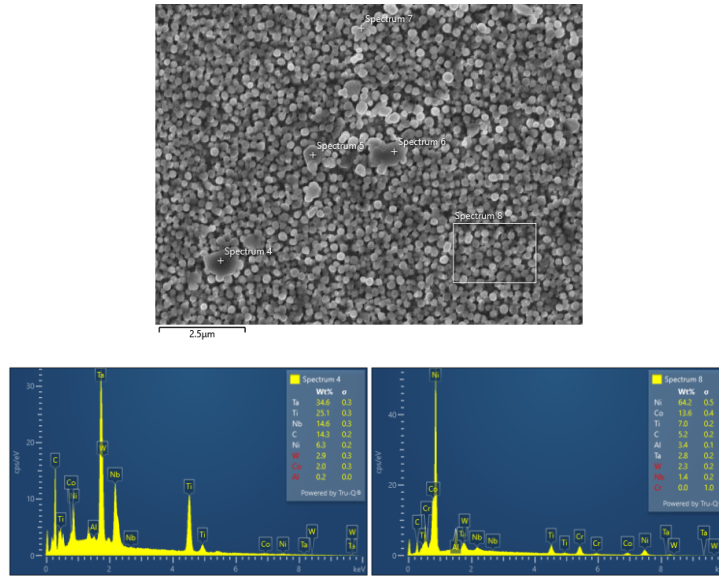


Figure 3. Gamma prime precipitates and metal carbides, rich in Ti and Ta, present at the grain boundaries and intergranular areas

Creep Properties

Figure 6 shows the creep curves of the as-built and heat treated samples at 750°C and 350 MPa. It can be observed from the creep curves that both HT1 and HT2 have improved rupture times compared to the as-built condition. On the other hand, HT3 rupture time did not exhibit any difference from the as-built condition and had a relatively lower %Strain. It should be stated that, HT2 (VHT) condition demonstrated more prolonged %Strain and rupture time than the other heat treated samples.

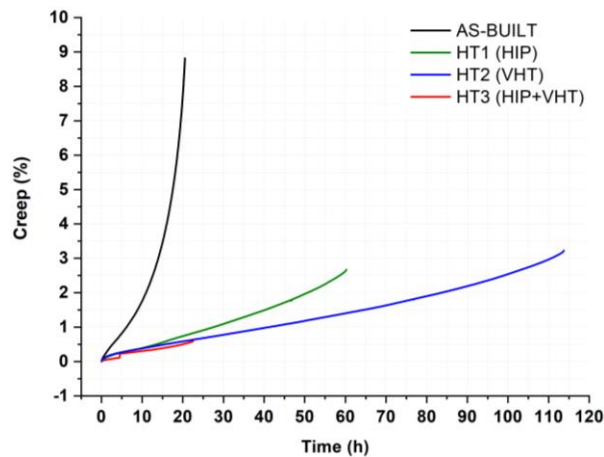


Figure 6. Creep curves of SLM-processed Inconel 939 specimens at 750°C under 350 MPa

Observations from **Figure 7** reveal microstructural changes near the creep-fractured surface. The gamma prime precipitate in the HT1 (HIP) changed from a spherical to a plate-like shape after creep tests, as directional coarsening or rafting occurred (Figure 7a). Previous studies suggest that this rafting behavior can result in material softening, leading to an increase in plastic strain within the corresponding γ channels and nearby γ/γ' interfaces [11]. As a result, the rafting of the gamma prime precipitates could reduce the rupture time in the HT1 (HIP) when compared to the HT2 (VHT). Furthermore, HT2 and HT3 both showed gamma prime coalescence, which was distributed in different areas within the microstructure. This may indicate reduced ductility and creep strength. Lastly, HT3 exhibited the lowest

creep resistance due to a more brittle structure that resulted from increasing secondary gamma prime formation.

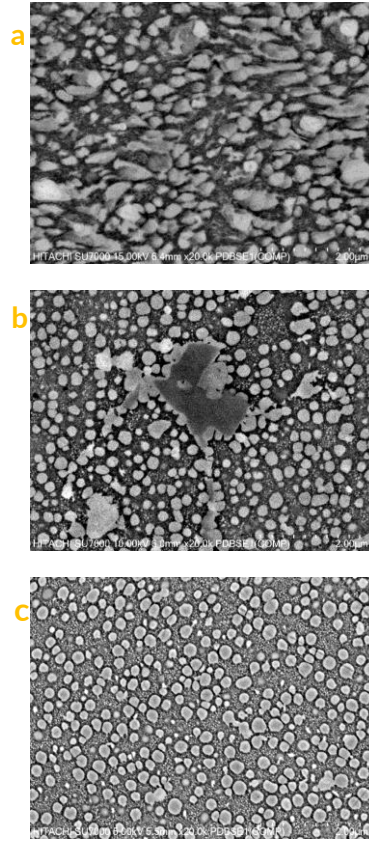


Figure 7. Microstructure images taken from near the creep-fractured surface: (a) HT1 (HIP), (b) HT2 (VHT), and (c) HT3 (HIP+VHT).

Conclusions and Future Studies

This study searched the impact of post heat treatment processes on the microstructure and creep properties of selectively laser-melted Inconel 939 superalloy. The findings demonstrate that both HT1 and HT2 post-treatment processes resulted in improved rupture times during creep testing when compared to the as-built condition. Among the heat-treated samples, HT2 exhibited the most significant increase in rupture time. Additionally, the rafting of gamma prime precipitates was found to reduce the rupture time in HT1 when compared to HT2. Conversely, HT3 displayed the lowest creep resistance due to a more brittle structure that resulted from increasing secondary gamma prime formation.

To gain a better understanding of the alloy's behavior in service, further research will be conducted. This will involve implementing modified heat treatment procedures and conducting mechanical tests and advanced microstructural characterization studies.

Acknowledgments

TUBITAK TEYDEB supported the study with project code 3219504. The authors would like to express their sincere appreciation to the Metallic Materials Research Group for their invaluable assistance. The authors extend their gratitude to TUSAS-TEI for their generous in-kind contribution.

References

- [1] P. Kanagarajah, F. Brenne, T. Niendorf, and H. J. Maier, "Inconel 939 processed by selective laser melting: Effect of microstructure and temperature on the mechanical properties under static and cyclic loading," 2013. doi: 10.1016/j.msea.2013.09.025.
- [2] Randy Bowman, "Superalloys: A Primer and History," in *Superalloys: A Primer and History*, [Online]. Available: <https://www.tms.org/meetings/specialty/superalloys2000/superalloyshistory.html>
- [3] M. Doi, D. Miki, T. Moritani, and T. Kozakai, "Gamma/gamma-prime microstructure formed by phase separation of gamma-prime precipitates in a Ni-Al-Ti alloy," in *Proceedings of the International Symposium on Superalloys*, 2004. doi: 10.7449/2004/superalloys_2004_109_114.
- [4] W. Philpott, M. A. E. Jepson, and R. C. Thomson, "Comparison of the effects of a conventional heat treatment between cast and selective laser melted IN939 alloy," 2016.
- [5] N. J. Harrison, "Selective Laser Melting of Nickel Superalloys : solidification , microstructure and material response," 2016.
- [6] J. Risse, "Additive Manufacturing of Nickel-Base Superalloy IN738LC by Laser Powder Bed Fusion," 2019.
- [7] S. Banoth, C. W. Li, Y. Hiratsuka, and K. Kakehi, "The effect of recrystallization on creep properties of alloy in939 fabricated by selective laser melting process," 2020.
- [8] G. Sjöberg et al., "Evaluation of the IN 939 alloy for large aircraft engine structures," in *Proceedings of the International Symposium on Superalloys*, 2004. doi: 10.7449/2004/superalloys_2004_441_450.
- [9] M. Jahangiri, "Study on incipient melting in cast Ni base IN939 superalloy during solution annealing and its effect on hot workability," *Mater. Sci. Technol.*, vol. 28, pp. 1402–1413, Jun. 2012.
- [10] A. Formenti, A. Eliasson, A. Mitchell, and H. Fredriksson, "Solidification sequence and carbide precipitation in Ni-base superalloys IN718, IN625 AND IN939," *High Temp. Mater. Process.*, vol. 24, Jun. 2005, doi: 10.1515/HTMP.2005.24.4.239.
- [11] Z. Yu, X. Wang, F. Yang, Z. Yue, and J. C. M. Li, "Review of γ' rafting behavior in nickel-based superalloys: Crystal plasticity and phase-field simulation," *Crystals*. 2020.

A Study on Beam Shaping Effects on The Mechanical Properties and Residual Stresses in Parts Processed Using Selective Laser Melting

Ahmad Reshad Bakhtari^{1,2}, Hüseyin Kürşad Sezer³, Olcay Ersel Canyurt^{1,2}

1. Mechanical Engineering, Gazi University, Ankara, Türkiye.

2. Additive Manufacturing Technology Application and Research Center (EKTAM), Gazi University, Ankara, Türkiye.

3. Industrial Engineering Design, Gazi University, Ankara, Türkiye.

Abstract

Selective Laser Melting (SLM) has emerged as an innovative technique for additive manufacturing, offering unparalleled freedom in design and precision in the fabrication of complex metallic components. An important aspect that influences the laser-material interaction and, eventually, the quality and performance of SLM-produced parts is the laser beam profile utilized during the process. In this study, COMSOL Multiphysics is employed to simulate the laser-material interaction in SLM, aiming to understand the effect of varying beam shapes on the generation of residual stresses in the fabricated components. The on-hand research begins with a comprehensive analysis of the physical processes involved in SLM, including laser energy absorption, heat transfer, and solidification dynamics. By varying the laser beam profile, such as the Gaussian to Top-Hat, the paper systematically explores their impact on laser-material interaction, melting and solidification, and, most importantly, the generation of residual stresses within the parts. The findings of this study are expected to provide valuable insights into optimizing SLM processes for improved mechanical performance and reduced defects in additively manufactured components. Understanding these effects is pivotal for optimizing SLM processes to enhance mechanical properties and reduce defects, bridging theory and practical applications in additive manufacturing.

Keywords: Selective Laser Melting, Residual Stresses, Beam Shaping, Beam Profile, Numerical Modelling.

Introduction

Additive manufacturing (AM) stands as a disruptive technology pivotal to realizing Industry 4.0 [1], revolutionizing traditional manufacturing methods by directly translating CAD models into components, reducing costs, time, and material waste [2]. Laser-Powder Bed Fusion (L-PBF), a key AM process, employs laser energy to melt metallic powders precisely, yielding custom components with fine grain structures and excellent mechanical properties [3]. However, the conventional Gaussian laser beam shape has inherent drawbacks, causing localized overheating, evaporation, and spattering during L-PBF due to its irradiance distribution [4,5]. As a result, it adversely affects melt pool dimensions, stability, and product quality [4,6].

To address these issues, researchers have explored alternative beam shapes from laser welding processes, known for their impact on weld quality and performance [7,8]. Insights from these studies offer promising strategies to enhance L-PBF [4–6]. In this context, the on-hand research aims to perform thermomechanical modelling using COMSOL Multiphysics to analyze the effects of beam shaping on residual stress generation in the Selective Laser Melting (SLM) process. It seeks to investigate how alternative beam shapes, developed initially for laser welding and related techniques, impact thermal

and mechanical behaviour within the SLM process. By simulating and comprehensively evaluating the resulting residual stresses, we aim to gain deeper insights into the potential benefits and challenges associated with adopting alternative beam shapes in L-PBF, contributing to the advancement of this transformative manufacturing technology.

Thermomechanical 3D FEM Model

In this study, a comprehensive continuum-based thermomechanical model was developed to investigate the effects of alternative beam shapes on the generation of residual stresses during the SLM process. The approach considers the powder layer, composed of discrete particles, as a continuum medium with equivalent properties, facilitating an accurate representation of thermal and mechanical behaviour.

The domain considered for the 3D FEM model has a length of 5 mm, a width of 2.5 mm, and a layer thickness of 25 μm , as shown in Figure 1. The model incorporates temperature-dependent material properties to capture the evolving behaviour of the Ti6Al4V alloy during the SLM process with precision. Specifically, consideration is given to temperature-dependent elasticity and plasticity, along with isotropic hardening, while kinematic hardening effects are disregarded. The mechanical properties of Ti6Al4V used in the simulation are taken from [9]. To accurately represent the phase change from powder to solid, the latent heat of fusion, phase change temperature, and temperature-dependent material properties are incorporated [10]. In contrast to some prior studies [11,12] that assume a lower density and thermal conductivity for the powder compared to the solid material, these properties are considered to be similar for both the powder and solid material in this study. This choice is made to prevent abrupt changes in material properties, which can lead to convergence issues in the numerical scheme or analysis. Maintaining similar properties is intended to ensure the stability and accuracy of the simulations. Table 1 shows the process parameters used for this study.

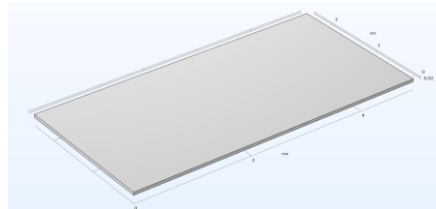


Figure 1. Thermomechanical 3D FEM model.

Table 1: Process parameters

Parameter	Value
Laser scanning speed (v)	1100 mm/s
Laser power (P)	190 W
Absorption coefficient (A)	0.3
Laser spot radius (r)	70 μm
Hatch space (H_s)	70 μm
Emissivity (ϵ)	0.35
Optical penetration depth (δ)	65 μm
convective heat transfer coefficient (h_c)	10 W/m ² K

Governing Equations, Initial and Boundary Conditions

The thermomechanical model consists of two governing equations: the heat balance equation for the transient thermal analysis and Hook's law for the thermal stress analysis. The heat balance equation is expressed as follows:

$$\rho C_p \frac{\partial x}{\partial y} + \rho C_p u \nabla T = \nabla(k \nabla T) + Q \quad (1)$$

where ρ is density, C_p is specific heat capacity, k is thermal conductivity, u is the laser velocity, T is temperature, and Q is the heat absorbed (i.e., heat source). An exponentially decaying volumetric heat source, adapted from [11], is used and further modified to accommodate different beam shapes (e.g., Top hat and Donut).

$$Q(x, y, z) = \frac{2AP}{\pi \delta r^2} \exp\left(-\frac{2((x-ut)^2 + y^2)}{r^2}\right) \exp\left(-\frac{|z|}{\delta}\right) \quad (2)$$

A is absorption coefficient, P is laser power, r is laser spot radius, $|z|$ is the absolute value of the z -coordinate, and δ is the optical penetration depth of the laser for Ti6Al4v.

The whole domain is considered to be at ambient temperature (i.e., $T_0 = 293$ K at $t = 0$), and a heat loss due to convection and radiation at the surface of the domain takes place during the laser and material interaction and can be expressed as follows:

$$-k \frac{\partial T}{\partial n} = h_c(T - T_0) + \varepsilon \sigma(T^4 + T_0^4) \quad (3)$$

The (-) sign shows the heat loss from the domain surface (n), h_c is the convective heat transfer coefficient, ε is the surface emissivity coefficient, and σ is the Stefan-Boltzmann constant.

For the thermal stresses analysis, Hook's law of elasticity considering an ideal elastic-plastic body, which goes under elastic and plastic deformation due to the cyclic loading behaviour of the SLM process is used:

$$\{\sigma\} = [D]\{\epsilon^e\} \quad (4)$$

$$\{\epsilon^e\} = \{\epsilon\} - \{\epsilon^p\} - \{\epsilon^t\} \quad (5)$$

$\{\sigma\}$ is the stress vector, $[D]$ is the elasticity matrix, $\{\epsilon^e\}$ is the elastic strain vector, $\{\epsilon\}$ is the total strain vector, $\{\epsilon^p\}$ is the plastic strain vector, $\{\epsilon^t\}$ is the thermal strain vector.

Results and Discussion

You may include color simulation images. Please export your simulation images such that the final resolution of your figures is at least 300 DPI.

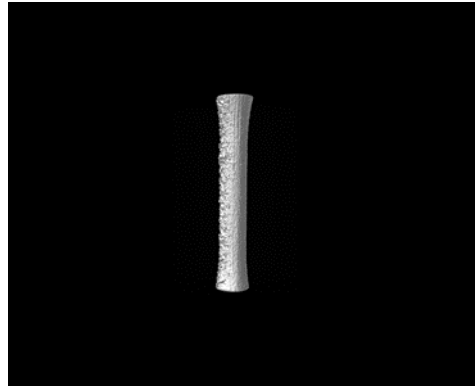


Figure 2. The caption should be centered underneath the figure and set in 9-point font.

Conclusions

You may include any implications or conclusions obtained from your work. You may include plans for future work.

References

- [1] Bakhtari AR, Waris MM, Sanin C, Szczerbicki E. Evaluating Industry 4.0 Implementation Challenges Using Interpretive Structural Modeling and Fuzzy Analytic Hierarchy Process. *Cybern Syst* 2021. <https://doi.org/10.1080/01969722.2020.1871226>.
- [2] Gibson I, Rosen D, Stucker B. Additive manufacturing technologies. Springer; 2010.
- [3] Thijs L, Kempen K, Kruth J-P, Van Humbeeck J. Fine-structured aluminium products with controllable texture by selective laser melting of pre-alloyed AlSi10Mg powder. *Acta Mater* 2013;61:1809–19. <https://doi.org/10.1016/j.actamat.2012.11.052>.
- [4] Wischeropp TM, Tarhini H, Emmelmann C. Influence of laser beam profile on the selective laser melting process of AlSi10Mg. *J Laser Appl* 2020;32:022059. <https://doi.org/10.2351/7.0000100>.
- [5] Grünwald J, Gehringer F, Schmöllner M, Wudy K. Influence of Ring-Shaped Beam Profiles on Process Stability and Productivity in Laser-Based Powder Bed Fusion of AISI 316L. *Metals (Basel)* 2021;11:1989. <https://doi.org/10.3390/met11121989>.
- [6] Gusarov A V., Grigoriev SN, Volosova MA, Melnik YA, Laskin A, Kotoban D V., et al. On productivity of laser additive manufacturing. *J Mater Process Technol* 2018;261:213–32. <https://doi.org/10.1016/j.jmatprotec.2018.05.033>.
- [7] Hansen KS, Kristiansen M, Olsen FO. Beam Shaping to Control of Weldpool Size in Width and Depth. *Phys Procedia* 2014;56:467–76. <https://doi.org/10.1016/j.phpro.2014.08.150>.
- [8] Rasch M, Roider C, Kohl S, Strauß J, Maurer N, Nagulin KY, et al. Shaped laser beam profiles for heat conduction welding of aluminium-copper alloys. *Opt Lasers Eng* 2019;115:179–89. <https://doi.org/10.1016/j.optlaseng.2018.11.025>.
- [9] Li Z, Xu R, Zhang Z, Kucukkoc I. The influence of scan length on fabricating thin-walled components in selective laser melting. *Int J Mach Tools Manuf* 2018;126:1–12. <https://doi.org/10.1016/j.ijmachtools.2017.11.012>.

- [10] Fu CH, Guo YB. Three-Dimensional Temperature Gradient Mechanism in Selective Laser Melting of Ti-6Al-4V. *J Manuf Sci Eng* 2014;136. <https://doi.org/10.1115/1.4028539>.
- [11] Liu S, Zhu H, Peng G, Yin J, Zeng X. Microstructure prediction of selective laser melting AlSi10Mg using finite element analysis. *Mater Des* 2018;142:319–28. <https://doi.org/10.1016/j.matdes.2018.01.022>.
- [12] Shi Q, Gu D, Xia M, Cao S, Rong T. Effects of laser processing parameters on thermal behavior and melting/solidification mechanism during selective laser melting of TiC/Inconel 718 composites. *Opt Laser Technol* 2016;84:9–22. <https://doi.org/10.1016/j.optlastec.2016.04.009>.

Acknowledgements

Funding: This work has received funding from the European Union’s Horizon 2020 research and innovation program under the Marie Skłodowska-Curie grant agreement No [101034425] for the project titled A2M2TECH. This study has also received funding from The Scientific and Technological Research Council of Türkiye (TUBITAK) with grant No [120C158] for the same A2M2TECH project under the TUBITAK’s 2236/B program.

Effect of Surface Roughness on Fatigue Behavior of Ti6Al4V Produced by Selective Laser Melting

Hilmi Tekdir^{1*}, Gürkan Kaya¹, A. Fatih Yetim¹, Fatih Yıldız¹, İsmail Hakkı Korkmaz¹, İrfan Kaymaz¹, Tuba Yetim²

¹Dept. of Mechanical Eng., Erzurum Technical University, 25050 Erzurum, TÜRKİYE

²Dept. of Chemical Eng., Erzurum Technical University, 25050 Erzurum, TÜRKİYE

*Corresponding author: hilmi.tekdir@erzurum.edu.tr

Abstract

This study investigates the effect of surface roughness on the fatigue behavior of Ti6Al4V produced by Selective Laser Melting (SLM). The study used Ti6Al4V-ELI powder material and electrochemical polishing to reduce surface roughness. The results showed that the electrochemical polishing process significantly improved the fatigue behavior of the alloy, with an improvement of approximately 18% in the fatigue limit value. The study also found that surface irregularities and voids in the samples produced by the SLM method caused ready areas on the surface that would cause fatigue crack initiation. The study concludes that the electrochemical polishing process has a significant effect on the fatigue behavior of the alloy.

Keywords: Selective laser melting, Ti6Al4V, Surface Roughness, Fatigue

Introduction

Additive Manufacturing (AM) technology has expanded across industries like electronics, biomedical, automotive, and aerospace [1]. Selective Laser Melting (SLM), developed in the 90s, is a popular technique used for products by melting metal powder layers using a high-energy laser beam. The research study focuses on the SLMed Ti6Al4V alloy, which is highly corrosion resistant, has a high specific strength, is bio-compatible, and has better fracture toughness [2-3]. It is a preferred alloy for investigation due to its wide applications in 3D-printed components like compressor modules, aircraft fuel nozzles, and aero-engine fans [4]. However, the SLM-AM process has many disadvantages, it presents certain manufacturing challenges, including higher costs, a high thermal stress gradient, and inferior surface quality [5-7]. The fatigue behavior of SLM-AM Ti6Al4V alloy has been studied by many researchers in recent publications [8-10]. However, the effect of surface roughness on the fatigue properties of additively produced Ti6Al4V alloy has rarely been studied. Therefore, this study focused on the effect of surface roughness on the fatigue properties of samples produced by SLM. Electrochemical polishing was applied to the samples and the effect of this process on fatigue life was investigated. Samples were subject to fatigue tests under axial loading conditions. Also, the structural properties, fracture surfaces, and surface roughness of the samples were evaluated by using XRD, SEM, and a 3D optical profilometer, respectively.

Experimental Details

In this study, Ti6Al4V-ELI (Grade 23) powder material ($D_{50} \approx 28 \mu\text{m}$) was used, which was fabricated by gas atomization. Additive manufacturing operations were carried out using the Concept Laser MLab-R SLM system, using a bidirectional scanning strategy and continual laser mode. In order to prevent oxidative reactions, all production was carried out in a protective argon gas atmosphere. In production

with SLM, the laser power was chosen as 80 W, scanning speed as 1125 mm/s, layer thickness as 25 μm , and hatch distance as 45 μm . The dimensions of fatigue test samples were determined according to ASTM E466–96. Fatigue tests were performed with the Instron 8872 axial universal testing machine at a frequency of 10 Hz. The fatigue (endurance) limit was accepted as 1×10^6 cycles and the device was stopped automatically either reaching this value or the fracture of test samples. Bi-linear type S–N curve was applied to show the test results. In this method, the S–N curve consists of two parts: linear and horizontal. By determining 5 stress levels in the linear part, 3 repetitions were performed at each stress level. The curve fitting was performed according to the JSME S 002–1981 standard. The staircase method was used for the horizontal part.

Electrochemical polishing was applied to the samples to reduce surface roughness. The content of the solution used in the electrochemical polish process; is ethyl alcohol (700 ml/L), isopropyl alcohol (300 ml/L), aluminum chloride (60 g/L), and zinc chloride (250 g/L). The parameters used in the polishing process are set as follows: voltage at 20 V, current at 1.5 A, and polishing time at 20 minutes.

XRD measurements were performed with the GNR Explorer X-Ray Diffraction device and a Cu-K α anode X-ray source with a wavelength of 1.5405 \AA . The fracture surface images of the samples were obtained using the QUANTA-FEG 250 scanning electron microscope (SEM). Surface roughness measurements were conducted by Bruker-Contour GT 3D optic profilometer.

Results and Discussion

Fig. 1 shows XRD patterns of Ti6Al4V powders and SLMed Ti6Al4V. The peaks of the Ti6Al4V powder material and the As-Built sample show the martensitic α' phase [7], which can be explained as the rapid cooling in the production process with cooling rates of 10^3 – 10^6 K/s resulting from the laser interaction with the powder material in the SLM method. The images taken before and after the electrochemical polishing process of the fatigue samples are provided in Figure 2, and the effect of the process is clearly visible.

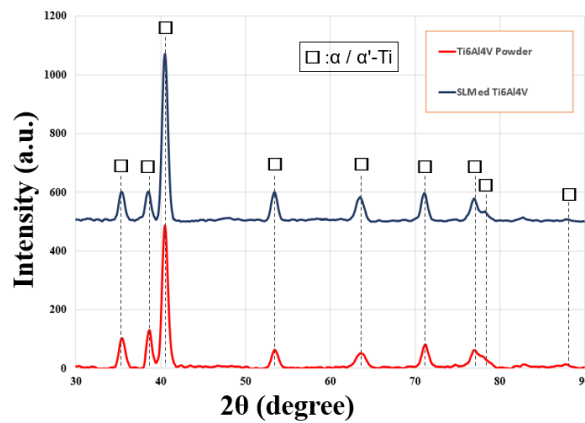


Figure 1. XRD patterns of Ti6Al4V powder and SLMed Ti6Al4V samples



Figure 2. The appearance of fatigue samples before and after the electrochemical polishing process.

3D optical profilometer images of As-built and polished Ti6Al4V surfaces are shown in Fig.3a and b. In the samples produced by SLM, the surface roughness value of the unpolished surface is $5.411 \mu\text{m}$, while the surface roughness of the polished surface is $0.504 \mu\text{m}$. According to scientific literature, The roughness of the surface on SLM product parts results from two independent mechanisms, uneven solidification of the molten material caused by melt pool turbulences and unintended melting of powder particles to the part contour caused by high local energy input [8], [11]. A rough surface is undesirable in terms of fatigue loading because notch-like features act as stress raisers and therefore crack initiation sites that significantly reduce fatigue strength [9].

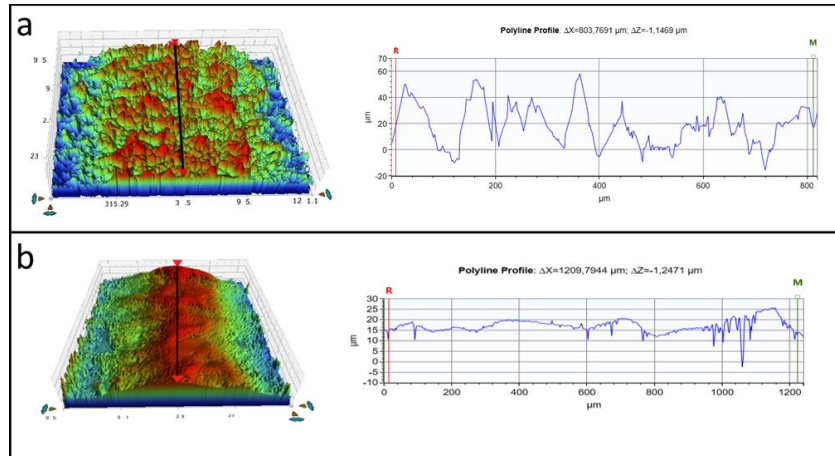


Figure 3. 3D optical profilometer images; (a) as-built and (b) polished Ti6Al4V

S-N curves of As-built and polished Ti6Al4V samples are shown in Fig. 4. While the fatigue limit of the as-built SLM Ti6Al4V alloy was 220 MPa, after the polishing process, the fatigue limit reached 260 MPa. It has been determined that the electrochemical polishing process has a significant effect on the fatigue behavior of the alloy. After the polishing process, an improvement of approximately 18% was achieved in the fatigue limit value of the alloy.

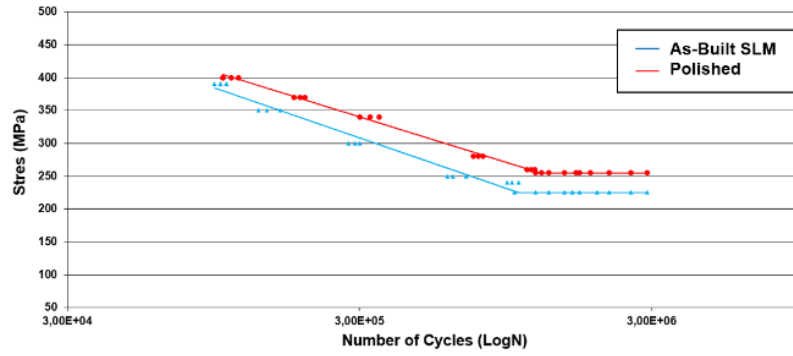


Figure 4. *S-N curves of as-built and polished Ti6Al4V alloy*

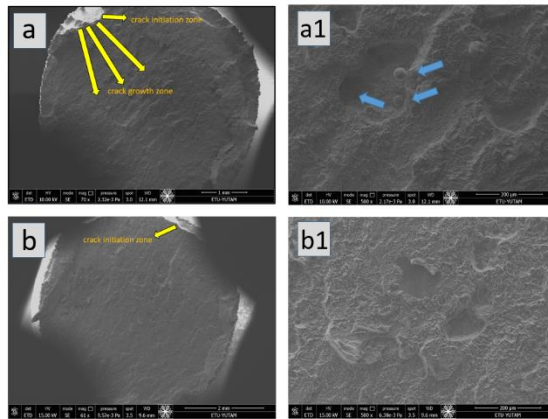


Figure 5. *SEM images of the fatigue fracture surfaces; (a) as-built and (b) polished Ti6Al4V*

SEM images of the fracture surface of SLMed Ti6Al4V alloy are given in Figure 5. In samples obtained by the SLM method, surface irregularities (increase in roughness) resulting from the nature of the production method cause the formation of ready areas on the surface that will cause fatigue crack initiation. In addition, since the samples produced by the SLM method contain more voids compared to the samples obtained by traditional methods, these voids cause both local crack initiation and easier propagation of the crack that starts on the surface [12]. In Figure 5b, unmelted powder particles and voids are shown with arrows. Cracks that started on the surface propagated more easily in these areas and caused damage to the samples.

Conclusions

According to the XRD results of the Ti6Al4V alloy produced by the SLM method using the selected optimum parameter set, a martensitic α' phase was formed. In the samples produced by SLM, the surface roughness value of the unpolished surface is $5.411 \mu\text{m}$, while the surface roughness of the polished surface is $0.504 \mu\text{m}$. Since a cylindrical cathode was used in the electrochemical polishing process, a homogeneous polishing was achieved. Polishing the sample surfaces reduced the notch effect that causes crack initiation. After the polishing process, an improvement of approximately 18% was achieved in the fatigue limit value of the alloy.

Acknowledgements

This study is supported by the Scientific and Technological Research Council of Turkey (TÜBİTAK) with the project code 20AG048. We would like to thank TÜBİTAK for their contributions. We also

thank Erzurum Technical University High Technology Research and Application Center (ETÜ-YÜTAM) for its support in experimental studies.

References

- [1] H. Lee, C. H. J. Lim, M. J. Low, N. Tham, V. M. Murukeshan, and Y. J. Kim, “Lasers in additive manufacturing: A review,” *Int. J. Precis. Eng. Manuf. - Green Technol.*, vol. 4, no. 3, pp. 307–322, 2017.
- [2] N. Rahulan, S. S. Sharma, N. Rakesh, and R. Sambhu, “A short review on mechanical properties of SLM titanium alloys based on recent research works,” *Mater. Today Proc.*, vol. 56, pp. A7–A12, 2022.
- [3] Q. Chao et al., “On the enhanced corrosion resistance of a selective laser melted austenitic stainless steel,” *Scr. Mater.*, vol. 141, pp. 94–98, 2017.
- [4] A. Emiralioglu and R. Ünal, “Additive manufacturing of gamma titanium aluminide alloys: a review,” *J. Mater. Sci.*, vol. 57, no. 7, pp. 4441–4466, 2022.
- [5] D. Gu et al., “Densification behavior, microstructure evolution, and wear performance of selective laser melting processed commercially pure titanium,” *Acta Mater.*, vol. 60, no. 9, pp. 3849–3860, 2012.
- [6] C. Galy, E. Le Guen, E. Lacoste, and C. Arvieu, “Main defects observed in aluminum alloy parts produced by SLM: From causes to consequences,” *Addit. Manuf.*, vol. 22, no. May, pp. 165–175, 2018.
- [7] B. Vrancken, L. Thijs, J. P. Kruth, and J. Van Humbeeck, “Heat treatment of Ti6Al4V produced by Selective Laser Melting: Microstructure and mechanical properties,” *J. Alloys Compd.*, vol. 541, pp. 177–185, 2012.
- [8] M. Benedetti et al., “The effect of post-sintering treatments on the fatigue and biological behavior of Ti-6Al-4V ELI parts made by selective laser melting,” *J. Mech. Behav. Biomed. Mater.*, vol. 71, no. February, pp. 295–306, 2017.
- [9] D. B. Witkin, D. N. Patel, H. Helvajian, L. Steffeney, and A. Diaz, “Surface Treatment of Powder-Bed Fusion Additive Manufactured Metals for Improved Fatigue Life,” *J. Mater. Eng. Perform.*, vol. 28, no. 2, pp. 681–692, 2019.
- [10] E. Brandl, U. Heckenberger, V. Holzinger, and D. Buchbinder, “Additive manufactured AlSi10Mg samples using Selective Laser Melting (SLM): Microstructure , high cycle fatigue , and fracture behavior,” *J. Mater.*, vol. 34, pp. 159–169, 2012.
- [11] T. Persenot, A. Burr, G. Martin, J. Y. Buffiere, R. Dendievel, and E. Maire, “Effect of build orientation on the fatigue properties of as-built Electron Beam Melted Ti-6Al-4V alloy,” *Int. J. Fatigue*, vol. 118, no. August 2018, pp. 65–76, 2019.
- [12] Z. H. Jiao, R. D. Xu, H. C. Yu, and X. R. Wu, “Evaluation on Tensile and Fatigue Crack Growth Performances of Ti6Al4V Alloy Produced by Selective Laser Melting,” *Procedia Struct. Integr.*, vol. 7, pp. 124–132, 2017.

Additive Manufacturing of Molybdenum by Using Electron Beam Melting and Selective Laser Melting

T. Göynük^{1,2}, E. Yasa³, İ. Karakaya², O. Önem¹

1. ROKETSAN Missiles INC., P.K. 30 Elmadağ 06780 Ankara – Turkey

2. Middle East Technical University, Üniversiteler, Dumlupınar Bulvarı No:1, 06800 Çankaya/Ankara

3. University of Sheffield Advanced Manufacturing Research Centre, Factory of the Future Advanced Manufacturing Park Wallis Way, Catcliffe Rotherham S60 5TZ

Abstract

Refractory metals are used in parts that are exposed to high temperatures in applications requiring high strength. Molybdenum, one of the refractory metals is frequently used in such applications due to its high melting temperature and mechanical properties [1,2]. Process parameters of additive manufacturing of molybdenum will be examined to determine the relationships between processing, microstructure, and mechanical properties. At the same time, an integrative study will be carried out by dealing with the modeling and subsequent processes of the additive manufacturing process.

Keywords: Refractory metals, electron beam melting, molybdenum additive manufacturing, selective laser melting

Experimental Set Up

Powder and Powder Characterization

Molybdenum metal powder -75+38 μ in size was supplied from TEKNA Plasma Europe. Powder characterization test results are shared below.

Properties	TEKNA	Roketsan
Hall Flow Test (g/s)	9,1	8,75
Tap Density (g/cm ³)	6,4	6,03
Apparent Density (g/cm ³)	5,8	5,725
Chemical Composition (wt%)		
Mo	>99,95	*Remaining
Al	0,004	N/A
Fe	<0,001	N/A
Ni	<0,001	N/A
O	0,025	N/A
Ti	0,003	0,0004
V	0,003	N/A
W	0,019	0,022

EBM Experiments

EBM experiments were done by ARCAM A2X machine. Initially, molybdenum base plate was melted without molybdenum powder, to check selected parameters and to investigate the material response.

After that, powderless production trials were moved to ARCAM A2X electron beam melting equipment. Two different parameters (scan speed and current) with 8 and 3 factors were tested without preheating. Scan speeds were chosen as 500, 1000, 1500, 2000, 2500, 3000, 3500 and 4000 mm/s, while 10, 20 and 30 mA current values were applied.

Design Summary

Factors: 2 Replicates: 1

Base runs: 24 Total runs: 24

Base blocks: 1 Total blocks: 1

Then, 1050°C and 1250°C preheating temperatures were applied to powderless single track experiments.

Finally single track experiments were conducted by stainless steel base plate rather than molybdenum substrate in which smoking of molybdenum powder problem remained unsolved using 75 μ layer thickness.

SLM Experiments

In this study, Renishaw AM400 Selective Laser Melting machine was used. This SLM equipment utilizes a Yb-Fiber pulsed-wave laser with a wavelength of 1064 nm and a maximum power of 400 W. The experiments were conducted in argon environment. With a fixed layer thickness of 50 μ , experiments were conducted on AISI 1040 substrate using power levels of 240, 300, and 360 W, line energies of 0.66, 0.72, and 0.78 J/mm, and point distance parameters of 50, 75, and 100 μ . Subsequently, based on the results obtained from the single-track experiments, thin-walled geometries with a height of 3 mm were produced and examined microstructurally.

Design Summary

Factors: 3 Replicates: 1

Base runs: 27 Total runs: 27

Base blocks: 1 Total blocks: 1

Results and Discussion

EBM Experiment Results

-Single Track Experiments on Molybdenum Baseplate

There was not sufficient melting to investigate in the tests performed without preheating parameters, as it can be examined in the following figure.



Figure 1. Picture Showing Powderless Single Track Experiment Without Preheating

Since successful melting was not achieved in the previous experiment, a new sample was tested by using the parameters in the design of experiment table by providing a preheating of 1050°C. Successful melting has been achieved from this experiment. The scanned surface at the preheating stage and single-track melting can be seen on the molybdenum base plate.

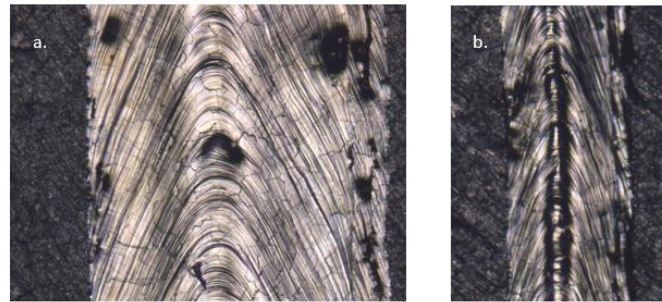


Figure 2. Optical Image of Powderless Single Track Experiment employing 1050°C Preheating a. 500 mm/s, 30 mA, b. 500 mm/s, 10 mA

By increasing the current from 30 mA to 40 mA during the preheating phase, a preheating temperature of 1250°C was obtained. However, more serious cracks were observed both on the molybdenum substrate and on the single-track lines.

- Single Track Experiments with Powder

Molybdenum powder was placed onto a 75-micron-wide groove opened on the molybdenum substrate, and single track experiments were planned to be conducted with the same parameters. However, as soon as the electron beam hit the substrate, the molybdenum powder started to become airborne, causing a smoking effect. The necessary literature review has been carried out and two possibilities emerged:

- Oxidation of powders
- Excessive preheating parameters [3,4]

First of all, the preheat current was reduced to 20 mA, but powders showed the tendency to smoke again. The same problem occurred when ball milled powder was placed on a molybdenum substrate having a diameter of 80 mm and a wall thickness of 10 mm. Therefore, the substrate size was changed to 170x170x10 mm stainless steel to reduce the energy of the preheat on base plate. The smoking phenomenon continued on the stainless steel substrate as well. After that, the possibility of oxidation of the powders gained weight. To break the oxide layer on the metal powders, the powders were ball-milled using the following parameters.

Table 1. Ball Milling Parameters

Ball Milling Parameters	
Speed (rpm)	500
Time (min)	8
Pause (min)	1
Cycle	2
Reverse	On

XPS analysis of both virgin powders and ball-milled powders are shared below.

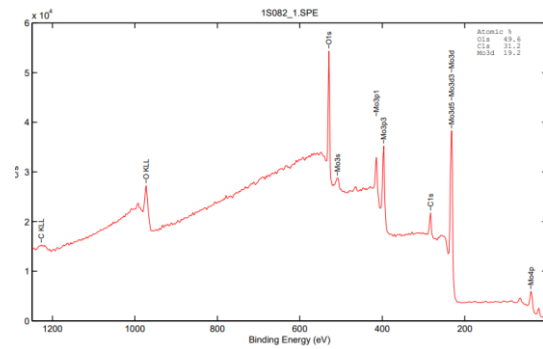


Figure 3. XPS Analysis of Virgin Molybdenum Powder

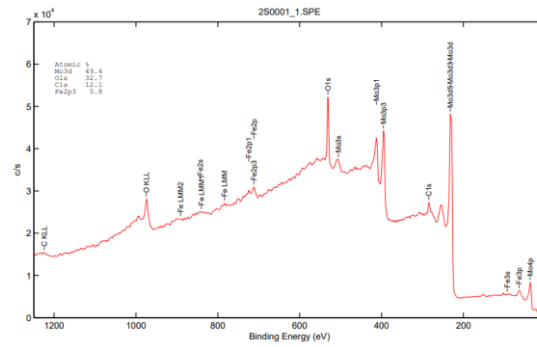


Figure 4. XPS Analysis of Ball Milled Molybdenum Powder

Scanning electron microscope (SEM) images of powders before and after ball mill are shared below.

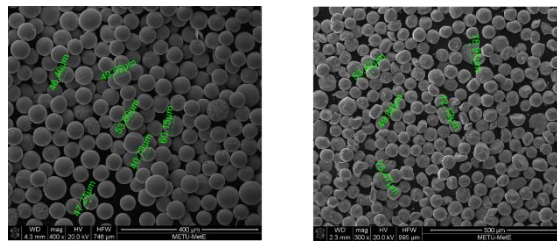


Figure 5. SEM Images of Virgin (Left) and Ball Milled (Right) Powder

A successful single-track production was achieved with low preheating parameters (20 mA), 170x170x10 mm stainless substrate and ball milled powder. Due to low current values, 930°C preheat temperature was achieved.

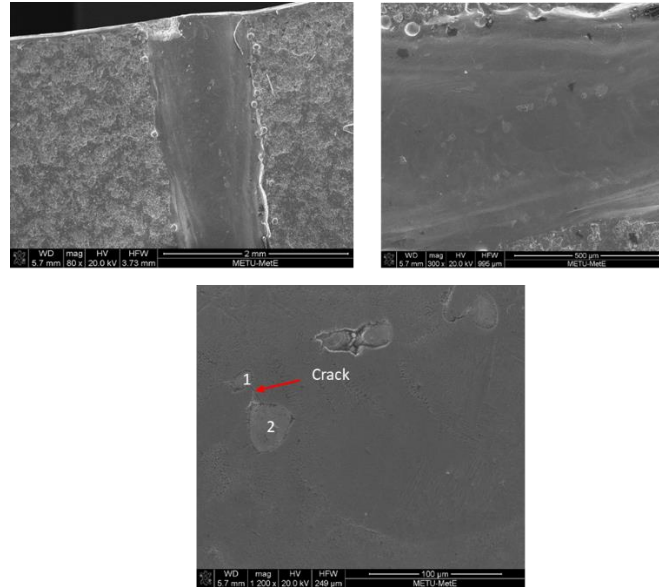


Figure 6. SEM Images of parts formed by the Single-Track Experiment at 500 mm/s, 20 mA

The EDS analysis results of the regions shown as 1 and 2 labelled on the SEM image are shared below.

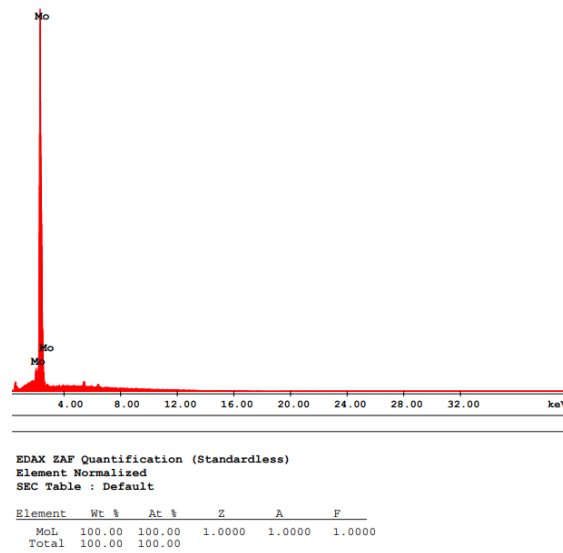


Figure 7. EDS Analysis of the Region Labelled as 1 on Figure 6

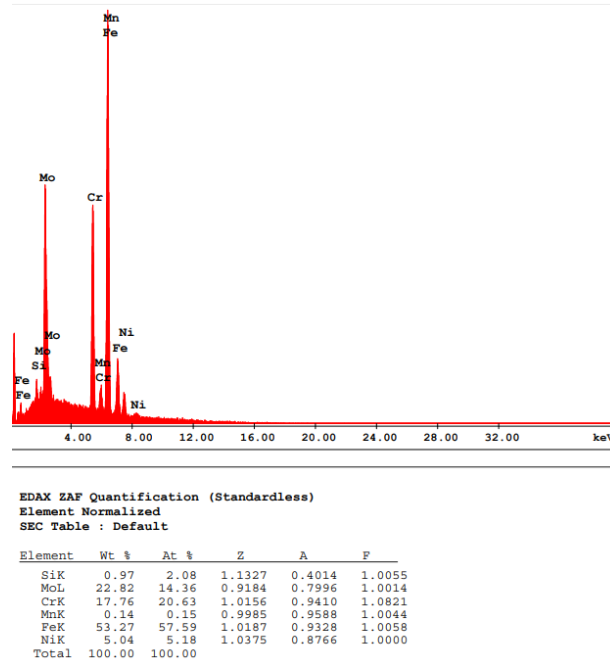


Figure 8. EDS Analysis of the Region Labelled as 2 on Figure 6

SLM Experiment Results

-Single Track Experiments

Initially, single-line experiments were conducted using the parameters described in the experimental setup section. The visuals of the single-line experiments can be seen below.

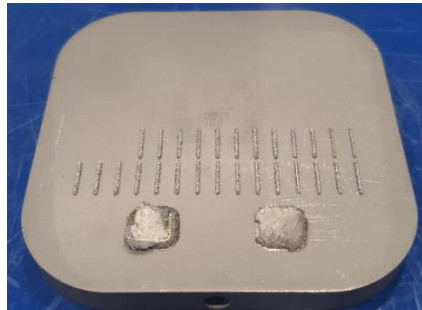


Figure 9. Single track experiments of molybdenum by SLM

The results of the single-track experiment were subjected to metallographic examinations. After grinding and polishing, they were etched by ASTM E407-98c. Following optical microscope examinations, thin-walled multi-layer structures were constructed using the selected parameters given below.

Table 2. SLM parameters of thin wall structures

Layer Thickness (μ)	Line Energy (J/mm)	Point Distance (μ)	Power (kW)
50	0,66	100	360
50	0,66	50	300
50	0,72	100	240
50	0,78	50	360

Optical images are shown in the following figures. It was observed that cracks continue to form in the molybdenum microstructure during the SLM process.

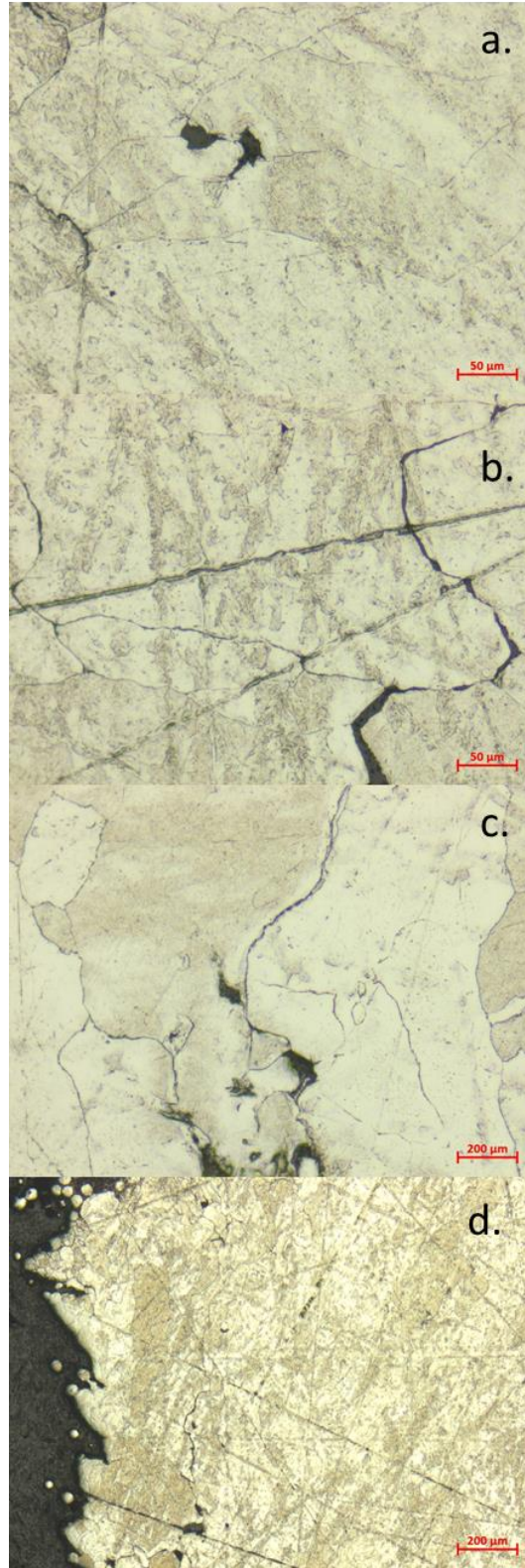


Figure 10. Optical images of SLM of molybdenum material with a parameter of a. 0,78 J/mm line energy, 50μ point distance, 360kW power, b. 0,72 J/mm line energy, 100μ point distance, 2400kW power,

c. 0,66 J/mm line energy, 100 μ point distance, 360kW power, d. 0,66 J/mm line energy, 100 μ point distance, 300kW power

As can be seen from Figure 10d, there are no visible cracks in the overall microstructure; only delamination has occurred in the final layer. Thinner wall structures will be attempted using this parameter in the future. Additionally, SEM and EDS analyses of these structures produced by SLM will also be carried out.

Conclusions

Single track experiments with molybdenum powder and powderless experiments were conducted using the EBM method. Some modifications to the equipment are required to create parts using the EBM method, and work on this is ongoing.

Based on the results of the single-track experiments conducted using the SLM method, thin-walled structures have been constructed.

In future works, an integrative study will be carried out by dealing with the modeling and subsequent processes of the additive manufacturing process.

References

- [1] J. Braun et al., International Journal of Refractory Metals & Hard Materials 84 (2019) 104999
- [2] L. Kaserer et al., International Journal of Refractory Metals & Hard Materials 84 (2019) 105000
- [3] W. Sames, “Additive Manufacturing Of Inconel 718 Using Electron Beam Melting: Processing, Post-Processing, & Mechanical Properties,” May 2015, PhD Thesis, Submitted to the Office of Graduate and Professional Studies of Texas A&M University
- [4] A. Chiba, Y. Daino, K. Aoyagi, K. Yamanaka, Smoke Suppression in Electron Beam Melting of Inconel 718 Alloy Powder Based on Insulator–Metal Transition of Surface Oxide Film by Mechanical Stimulation, Materials 2021, 14, 4662. <https://doi.org/10.3390/ma141646>

Warpage At FDM Printed Composites: Case Study of A Thin-Walled Camera Holder

Ş. Sirtlı¹, H. Tanabi¹, M. Ghazizni¹

1. Mechanical Engineering, University of Turkish Aeronautical Association, Ankara, Turkey.
2. Mechanical Engineering, University of Turkish Aeronautical Association, Ankara, Turkey.
3. Mechanical Engineering, University of Turkish Aeronautical Association, Ankara, Turkey.

Abstract

Fused Deposition Modeling (FDM) technology is applied across diverse industries, including aerospace and aviation, where addressing warpage issues stemming from temperature variations is of paramount importance. This research endeavors to identify optimal printing parameters, distinct from temperature adjustments, specifically tailored to carbon fiber-reinforced thermoplastic materials in order to mitigate this critical concern. The investigation into printed part warpage delves into infill percentage and infill pattern as key variables. Remarkably, the research findings reveal that the warpage can be minimized using a balanced infill pattern like Linear and Triangle patterns. Using unbalanced patterns results in higher warpage especially at higher concentrations.

Keywords: FDM, warpage, composite materials, carbon fiber reinforcement

Introduction

Additive manufacturing (AM) has become one of the most widespread manufacturing techniques that allows producing high-performance parts with ease and affordable cost. Among the AM processes, Fused Deposition Modelling (FDM) is more attractive because of its accessibility, low-cost production, and being able to produce parts with different materials [1].

In FDM production the part is constructed by layer-by-layer extrusion of a filament. Thermoplastic polymers such as Acrylonitrile butadiene styrene (ABS), Poly Lactic Acid (PLA), and nylon are well-known filament materials. However, these filaments are not generally eligible for engineering applications due to a lack of structural functionality and strength. Short fiber reinforced filaments are classified as engineering filaments for FDM and the fabricated parts show a higher mechanical properties than those fabricated using pure thermoplastic polymers [2] [3].

Lightweight and durable design is an extensively explored and utilized concept in many industries, especially in aerospace applications. In addition, the parts must meet requirements for dimensional accuracy. Residual stress and warpage are known as the main issue of the FDM printed thin-walled parts. Warpage occurs due to the temperature difference. In the printing process, the extrusion nozzle is heated around 280 °C degrees where the build plate is 60 °C and the chamber temperature is generally lower than 30 °C. Also, the gradient air around the part to be printed is the main reason for the warpage [4] [5].

Together with process parameters, the warpage is affected by material properties and part geometry. In previous studies, simulations and analytical models have been developed to estimate the warpage in a part depending on the geometrical properties and thermomechanical job. [6].

This ongoing study investigates the effect of infill pattern and density on the warpage on a camera holder (Figure 1) for a gimbal integrated into an unmanned aerial vehicle (UAV) using DIGIMAT AM.

This case study aims to determine the deviation angle between the camera itself and the camera holder based on geometric printing properties.

Experimental Set-Up

Sample Preparation

The samples were printed using Raise3D Industrial PA12-CF carbon fiber-reinforced composite filament based on Polyamide 612 (PA612, Nylon 612). This filament consists of 15% carbon fiber with optimum length distribution. The part was created in SolidWorks and was exported to a stereolithography (STL) file. The model was fabricated with RAISE3D's E2CF double-nozzle 3D printer. Due to the abrasive nature of fiber-reinforced filaments, a hard steel nozzle diameter of 0.4 mm was used as the extruder. The printing speed is set to 70 mm/s with a layer height of 0.1 mm for infill layer where shell thickness is 0.8mm. The printing nozzle temperature is 280 °C, the build plate temperature is 60 °C and the measured chamber temperature is 28 °C. There was no adhesive used in the printing process. The arrangement of the models using the slicing software IDEAMAKER 4.3.1. After the process parameters and experiment parameters were made to match in IDEAMAKER 4.3.1, the G-codes were uploaded to the printer, and the samples were printed. The dimensions of the part and printing orientation are shown in Figure 2

In this study, the warpage of the printed part is investigated in terms of infill percentage and infill pattern. The process parameters and assigned values are shown in **Hata! Başvuru kaynağı bulunamadı..**

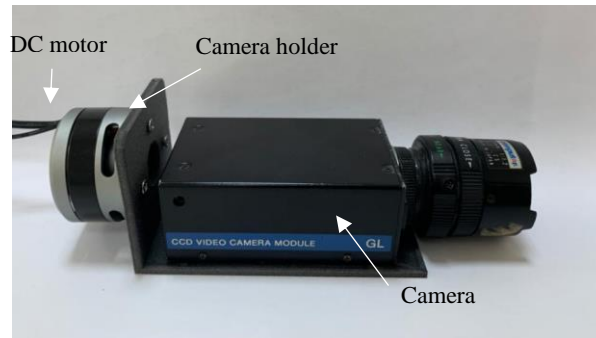
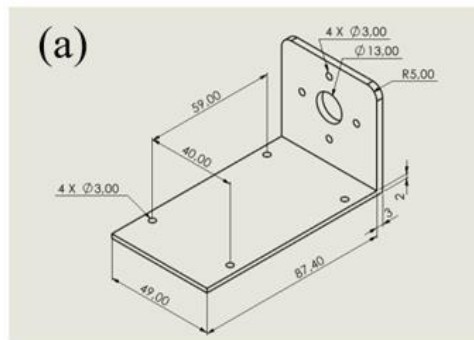


Figure 1. Desired assembly orientation



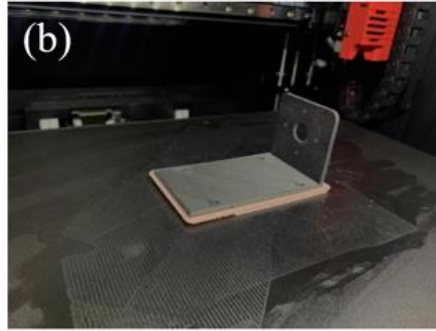


Figure 2. Camera holder, a) dimensions b) printed on flat orientation

An experimental design matrix was established for four factors with multiple levels (see Table 2) using general factorial design approach. Based on the design matrix 9 tests were performed. Designing the experiment and analyzing the results were done via statistical software MINITAB 21.1.0.

Simulation Process

For the warpage simulation, the STL model was sliced using ULTIMAKER slicer the obtained G-code was exported Using the imported G-code part regenerated in DIGIMAT AM considering the orientation of filaments at each layer. In addition, the materials features such as fiber reinforcement percentage and its orientation, and FDM process parameters which are the extruder and chamber temperature while printing.

The analyses were conducted with a mesh size coefficient of 0.855 and 30566 voxels. The meshed part is shown in Figure 3.

The orientation of the carbon fibers data has been obtained from [7] as $a_{11} = 0.0911$, $a_{22} = 0.1081$ and $a_{33} = 0.8006$.

Table 1. Fabrication Parameters

	Parameters	
	Infill Density (%)	Infill Pattern
Levels	25	Lines
	50	Concentric
	90	Triangles

Table 2. Design matrix

Exp.	Infill Density (%)	Infill Pattern
1	25	Lines
2	25	Concentric
3	25	Triangles
4	50	Lines
5	50	Concentric
6	50	Triangles
7	90	Lines
8	90	Concentric
9	90	Triangles

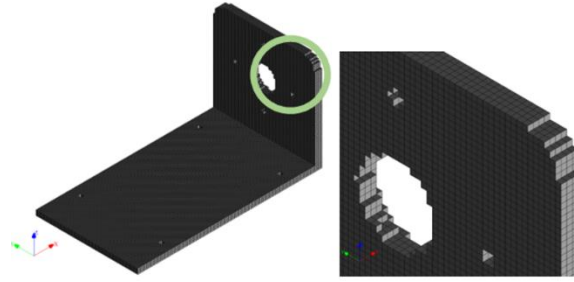


Figure 3. Meshed version of the model

Table 3. Digimat AM Simulation Results

Exp.	Deflection (mm)	Exp.	Deflection (mm)
1	1.446	6	2.294
2	1.055	7	1.066
3	1.958	8	4.518
4	2.041	9	1.189
5	2.816		

Results and Discussion

Simulations were run to obtain the deflection at all axes of the model. The simulation result for the RUN 1 is shown in Figure 4. When the data was collected including the most and least deflected parts in all axes and three random parts were selected. The selection is shown in Table 3. The effect of the main parameters and their interactions are shown in Figure 5. The lowest deflections are measured as 1.055 and 1.066 at RUN 2 and RUN 7 respectively. On the other hand, the highest deflection was measured at RUN 8. Considering Figure 5, Line and Triangle patterns are shown very similar pattern at various concentrations. This can be described as both patterns having $\pm 45^\circ$ orientations. Each layer of the Triangle pattern involves $\pm 45^\circ$ orientations, while for the Line pattern 45° orientation is followed by a -45° layer. The infill patterns at 25% density are shown at Figure 6. Thus both patterns have a balanced structure. On the other hand, in Concentric pattern, infill filaments are aligned with the outer shell direction at all layers. Therefore, the Concentric pattern is an unbalanced pattern and due to this fact, the deflection is increased as the concentration increased.

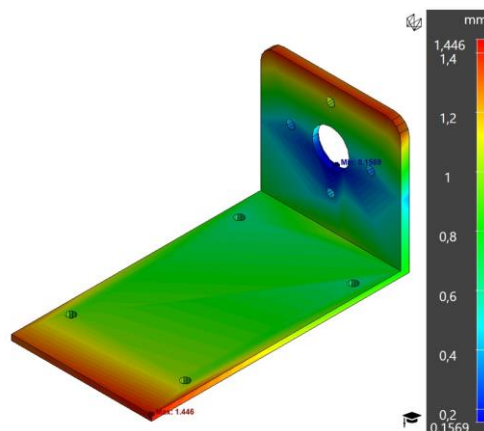


Figure 4. The simulation result of the Run 1

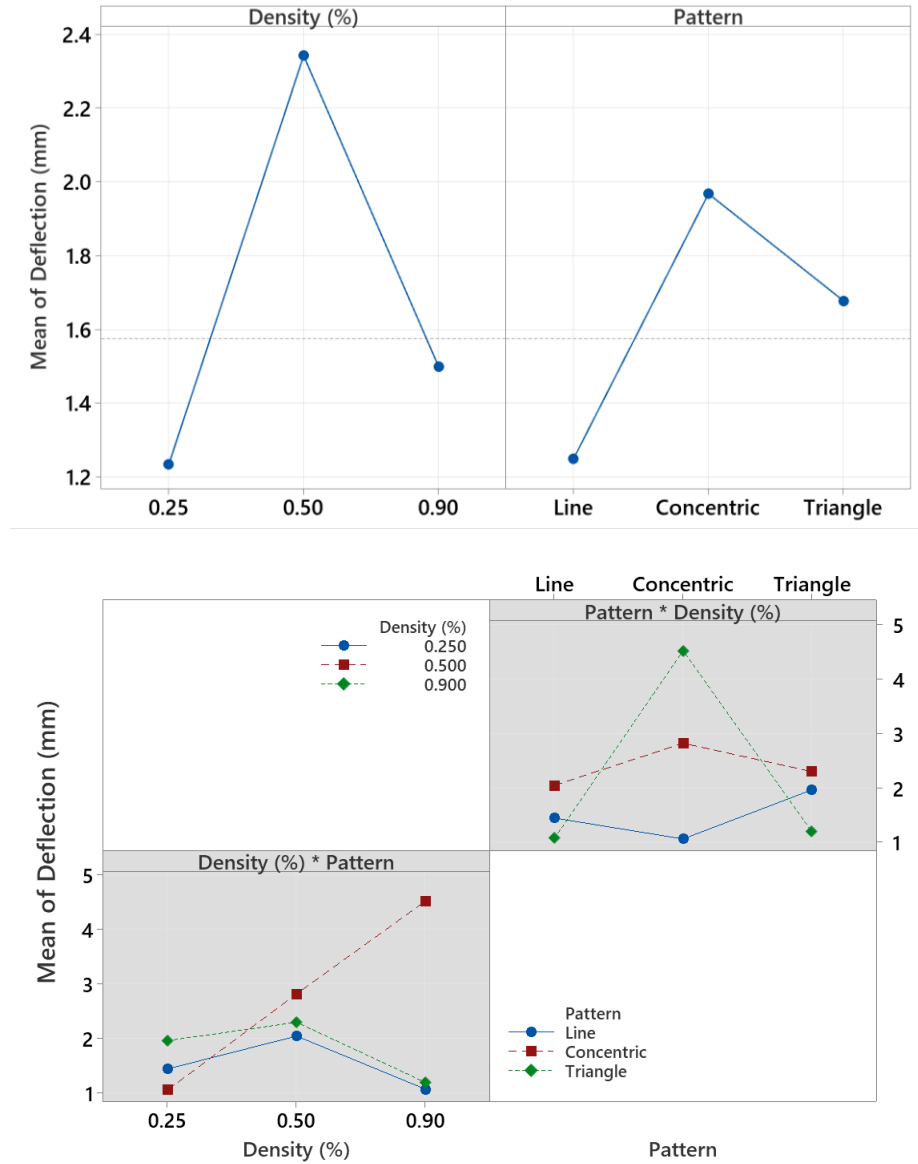


Figure 5. Effect of the a) main factors, and b) interactions on deflection

Conclusions

In this study, the effect of infill pattern and infill density on the warpage of a thin-walled FDM printed carbon fiber reinforced filament was investigated. The simulations were conducted at DIGIMAT software, considering process temperatures, material thermal properties, and slicing G-codes. It was found that the warpage can be minimized using Line or Triangles patterns which are balanced patterns, while unbalanced patterns such as concentric was resulted in a higher warpage, especially at the higher concentrations.

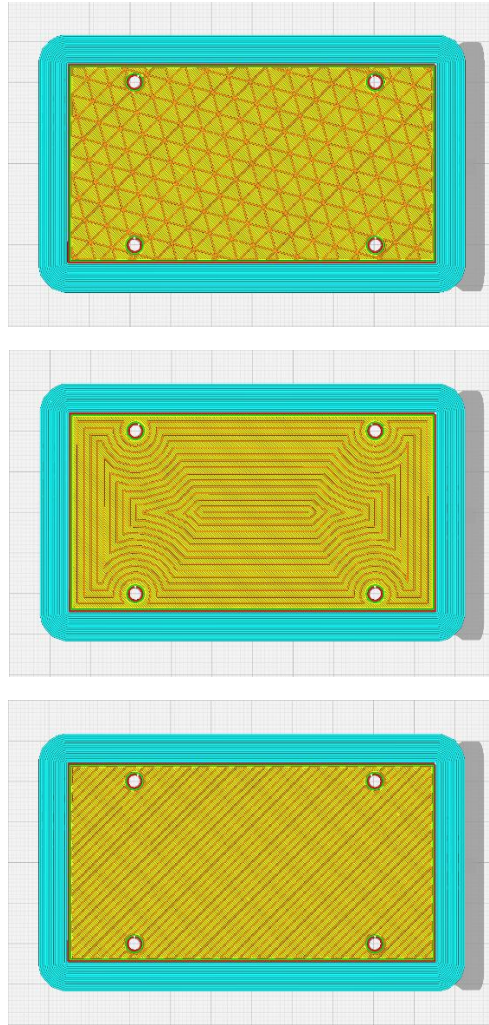


Figure 6. In fill patterns at 25% concentration, a) linear, b) Triangle, and c) Concentric

References

- [1] Ł. Pejkowski, J. Seyda, K. Nowicki and D. Mrozik, "Mechanical performance of non-reinforced, carbon fiber reinforced and glass bubbles reinforced 3D printed PA12 polyamide," *Polymer Testing*, vol. 118, p. 107891, 2023.
- [2] T. Hamed, "Investigation of the shear properties of 3D printed short carbon fiber-reinforced thermoplastic composites," *Journal of Thermoplastic Composite Materials*, pp. 2178-2193, 2022.
- [3] E. Yasa and K. Ersoy, "Dimensional accuracy and mechanical properties of chopped carbon reinforced polymers and produced by material extrusion additive manufacturing," *Materials*, vol. 12, no. 23, p. 3885, 2019.
- [4] H. Tanabi, "Investigation of the temperature effect on the mechanical properties of 3D printed composites," *INTERNATIONAL ADVANCED RESEARCHES and ENGINEERING JOURNAL*, vol. 05, no. 02, pp. 188-193, 2021.
- [5] A. Armillotta, M. Bellotti and M. Cavallaro, "Warpage of FDM parts: Experimental tests and analytic model," *Robotics and Computer-Integrated Manufacturing*, pp. 140-152, 2017.

- [6] C. Casavola, A. Cazzato, V. Moramarco and G. Pappaletta, "Residual stress measurement in Fused Deposition Modelling parts," *Polymer Testing*, vol. 58, pp. 249-255, 2017.
- [7] S. Yu, Y. H. Hwang, J. Y. Hwang and S. H. Hong, "Analytical study on the 3D-printed structure and mechanical properties of basalt fiber-reinforced PLA composites using X-ray microscopy," *Composites Science and Technology*, pp. 18-27, 2019.

Acknowledgments

This study was supported by the University of Turkish Aeronautical Association Office of Scientific Research Projects Coordination (BAP) through the project "Investigation of the mechanical properties of FDM printed carbon fiber reinforced thermoplastic composites under static and dynamic loadings".

Wire-Arc Additive Manufacturing of Combustion Chamber

G. Can¹, M. Yücel¹, O. Önem¹

1. ROKETSAN Missiles INC., P.K. 30 Elmadağ 06780 Ankara – Turkey

Abstract

Wire-arc additive manufacturing (WAAM) is increasingly gaining popularity in aerospace applications due to its cost-reduction capabilities and short lead times. Aerospace applications encompass many components that are expensive to manufacture using conventional methods. One significant example of expensive products produced through traditional methods is the combustion chambers of rocket engines. These parts are roughly machined from bulk geometry and subsequently machined to their final thickness. By employing WAAM technology, material waste and CNC machining time can be reduced, thereby drastically decreasing the overall part cost. This paper focuses on the design of an experiment (DOE) to produce combustion chambers for aerospace applications using WAAM. To meet the high-quality and low-weight requirements of aerospace applications, welding parameters should be optimized. The optimized parameters are current, voltage, travel speed (TS), wire feed speed (WFS), waiting time between passes, distortion, and stacking strategy. In this project, the inspected properties are tensile strength, yield strength, porosity, elasticity modulus, and elongation. The DOE comprises three stages. First, a number (n) of single beads with distinct parameters are created, and through geometrical macro inspection, most of the single bead parameters are eliminated. Using the remaining parameter sets, thin walls are generated, and specimens are taken from these walls to assess mechanical properties. Destructive and non-destructive tests are then applied. Finally, parameter sets that offer the highest mechanical quality are employed in the additive manufacturing of the combustion chamber for aerospace applications.

Keywords: Additive Manufacturing, Wire-Arc Additive Manufacturing, Welding Parameter Optimization, Design of Experiment, Combustion Chamber of a Rocket Engine

Introduction

This paper focuses on the DOE application for manufacturing a combustion chamber for the aerospace industry via WAAM. Three main stages are depicted for the DOE application. Firstly, the necessary welding parameter sets are created, and through single-bead experiments, parameter sets that can provide low-quality welds are eliminated. Single beads are inspected via geometrical macro inspection, and the ones with better penetration into the build plate, a cross-section shape, and a desired constant height are found eligible to move on to the next experimental stage.

In the second step, parameter sets that found eligible are used to manufacture thin walls. These walls are cut to obtain specimens to be inspected via tensile tests. In the final stage, the parameter set that shows higher performance compared to others is used for WAAM. After the thin walls are created and the parameter sets are determined, toolpath generation for the combustion chamber becomes a concern because the welding torch angles during manufacturing significantly affect the weld quality. The welding torch is intended to be directed at a point close to the base of the previous bead, and the collision of the welding torch with the built plate is prevented by the mobility of the tilt table.

Desing of Experiment

Experimental Variables

Controlled, independent, and dependent variables of the experiments are set. Controlled variables are filler material, welding type (CMT), shielding gas type and flow rate, wire diameter, and substrate temperature. Independent variables are WFS, TS, voltage, and current. Dependent variables are layer width, layer thickness, penetration depth, penetration cross-section, and layer cross-section.

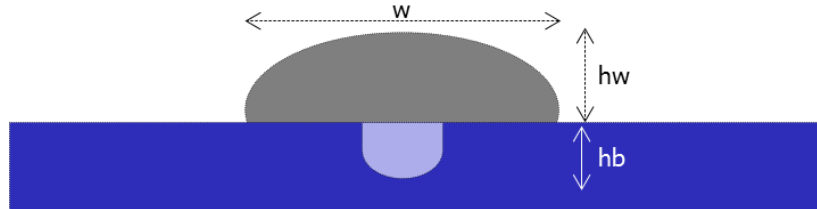


Figure 1. Single bead geometry. Demonstrating layer width(w), layer height (hw), and penetration depth (hb).

For decreasing the overall manufacturing time, the height value hw shown in Fig. 1 should be maximized while maintaining a proper geometry of the weld seam. In the preliminary study, samples produced with a WFS of 7 m/min and a TS of 20 mm/min were visually distorted, so these values are used as boundaries for the optimization parameter range. This way, the range of WFS and TS is determined as 4 to 7 m/min and 20 to 50 mm/min, respectively, as shown in Table 1 with other independent variables.

Table 1. Experimental parameter sets including WFS, TS, voltage and current values in m/min, mm/min, V, and A respectively.

WFS(m/dk)	TS(mm/dk)	V(V)	I(A)
5	35	11,5	145
4	20	12,2	122
7	35	14,8	184
6	50	12,3	152
5	50	12,7	140
4	35	10,7	111
6	35	13,7	162
4	50	11,5	116
6	20	13,7	165
5	20	12,8	142
7	50	13,7	177
7	20	14,2	180

Parameter Optimization Process

Optimization of the independent variables is conducted on the optimization plot depicted in Fig. 2. The range of material deposition is determined as 4 m/min WFS and 20 mm/min TS for the lowest, and 7 m/min WFS and 50 mm/min TS for the highest material deposition rate. Single bead experiment results are analyzed, and microstructure examination is applied to the samples. The parameter set that provides the highest layer height and penetration depth while using material efficiently is selected, and the microstructure of this parameter set is found acceptable. The optimum layer thickness value for a considerably high deposition rate is obtained at 6 m/min WFS and 35 mm/min TS.

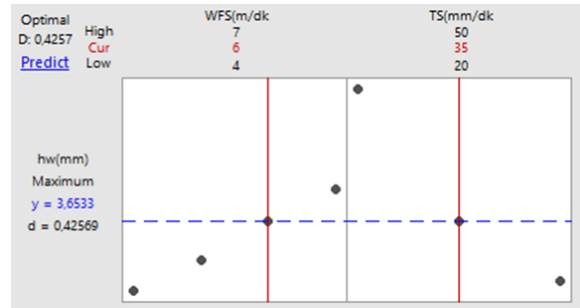


Figure 2. Optimization plot for the given parameter ranges. Maximum hw value of 3.65mm is attained for 6m/min WFS and 35mm/min TS.

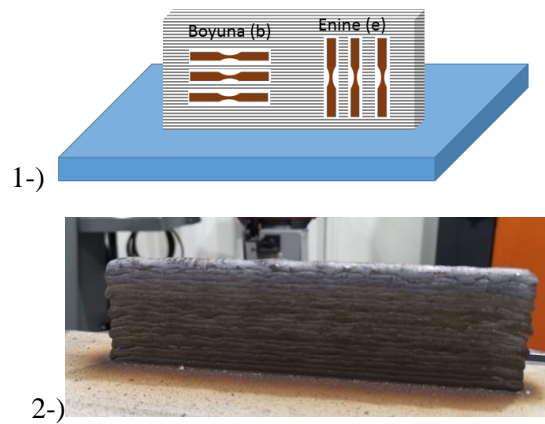


Figure 3. 1-) Horizontal and vertical test specimens taken from thin wall. 2-) Thin wall manufactured via WAAM.

A thin wall is produced via WAAM with 18 passes. Tensile test specimens are cut from the manufactured single pass thin wall and machined to be tested in tensile test setup as shown in Fig 3.

Combustion Chamber Production via WAAM

Autodesk Powermill and Netfabb software are utilized to generate the toolpath for the WAAM process. Since the combustion chamber has curves with changing angles, it is a common practice to edit the toolpath after it is first generated. Being able to select tool-axis angle, retraction and approach point during manufacturing, and orientation towards the previous layer are crucial for this process since the tool should be oriented differently during manufacturing due to the curvy part on the combustion chamber.

During simulations, when the tilt angle is not used, a collision with the build table is observed. To prevent collision, both the rotating and tilt axes of the positioning device are used. Also, while using 8 axes, a pause problem is observed in the Powermill simulation, and the software company has acknowledged that kinematic calculations cannot be made when there is a transition between concave and convex surfaces. Since offline programming errors originate from the software, manual programming becomes a reasonable approach. During the process, the Fronius TPS 400i CMT MAG is used with a 1.2 mm diameter ER316LSi wire. As the shielding gas, Cronigon gas consisting of 98% argon and 2% oxygen is selected. As a welding strategy, PMC (Pulse Multi Control) is preferred compared to CMT and CMT mix since it can offer a more stable welding seam. To obtain identical welding seams in each layer, a pyrometer is used to measure the temperature of the last layer, and the process is interrupted until a predetermined temperature value is attained. By setting the starting temperature of the last layer constant,

layer height and layer width are precisely controlled, and the first combustion chamber is additively manufactured.

Results and Discussion

Tensile tests are conducted on the test specimens cut from the thin walls, and the results are presented in Table 2. Maximum load, tensile stress at maximum load, tensile stress at yield, and tensile strain at break are provided for horizontal specimens. For vertical specimens, the tensile stress at maximum load is found to be 485 MPa, the tensile stress at yield is found to be 170 MPa, and the tensile strain at break is found to be 30-50%.

Table 2. Tensile test results of the specimens taken from thin wall manufactured via WAAM.

	Maximum Load (kN)	Tensile stress at Maximum Load (MPa)	Tensile stress at Yield (Offset 0.2 %) (MPa)	Tensile strain at Break (Standard) (%)
1	11.16	603	332	33.1
2	11.48	620	334	32.9
3	11.21	605	339	34.0
4	10.95	591	332	34.4
5	11.11	600	331	34.5
6	10.91	589	332	35.0
7	10.51	568	295	38.9
8	10.20	551	302	39.4
9	10.19	551	291	44.2
10	10.21	552	299	39.4
11	10.05	543	290	40.3
12	10.38	561	302	40.1

In the experiment, it is observed that hw and hb values are directly proportional to WFS and inversely proportional to TS. The microstructures of the resulting samples had an impact on the selection of the process parameters in addition to the WFS and TS parameters. Test results showed that the mechanical properties of WAAM products are superior to those manufactured using conventional methods. Better mechanical properties indicate that there is no critical porosity or other welding defects in the structure. Statistical analysis of the test results yielded acceptable p-values, chi-square values, and residual plots. The statistical analysis results for hw and hb are shown in Fig. 4 and Fig. 5, respectively.

Analysis of Variance

Source	DF	Adj SS	Adj MS	F-Value	P-Value
Model	5	5,88615	1,17723	112,92	0,000
Linear	5	5,88615	1,17723	112,92	0,000
WFS (m/dk)	3	1,07910	0,35970	34,50	0,000
TS (mm/dk)	2	4,80705	2,40352	230,55	0,000
Error	6	0,06255	0,01043		
Total	11	5,94870			

Model Summary

S	R-sq	R-sq(adj)	R-sq(pred)
0,102103	98,95%	98,07%	95,79%

Figure 4. Statistical analysis results for hw depicting R-sq value of 98.07%.

Analysis of Variance

Source	DF	Adj SS	Adj MS	F-Value	P-Value
Model	5	0,8337	0,16674	7,74	0,014
Linear	5	0,8337	0,16674	7,74	0,014
WFS (m/dk)	3	0,5845	0,19483	9,05	0,012
TS (mm/dk)	2	0,2492	0,12461	5,79	0,040
Error	6	0,1292	0,02153		
Total	11	0,9629			

Model Summary

S	R-sq	R-sq(adj)	R-sq(pred)
0,146733	86,58%	75,40%	46,34%

Figure 5. Statistical analysis results for hb depicting R-sq value of 75.40%.

Conclusions

In conclusion, this paper presents the design of an experimental approach to manufacture a combustion chamber for aerospace applications via WAAM. One of the most important aspects of the WAAM process, namely selecting a proper welding parameter set, is addressed in the design of the experimental approach. The methodology created through this study is found to be fairly beneficial for determining a proper welding parameter set in a time-efficient manner. After applying destructive and nondestructive tests, the best parameter set is obtained, which appears to have high mechanical properties sufficient for use in aerospace applications. Using this parameter set, a combustion chamber is successfully manufactured.

From Design to Smile: Leveraging AM and Topological Optimization for Jaw Implant Solutions

Muhammad Hassan RAZZAQ^{1,2}, Cenk AKTAŞ³, Yogendra Kumar MISHRA⁴, Mehmet Fatih AYCAN^{1,2}

1. Gazi University, Mechanical Engineering Department, Ankara, Türkiye
2. Additive Manufacturing Technologies Research and Application Center- EKTAM, Gazi University, Ankara 06560, Türkiye
3. University of Kiel, Institute of Materials Science, Kiel, Germany
4. University of Southern Denmark (SDU), Odense, Denmark

Abstract

The jaw implants support dental prostheses to replace missing teeth. Speech, bone loss prevention, aesthetics, preservation of neighboring teeth and jaw fractures, comfort, and oral health are improved with these implants. Ti-64 and CoCr alloys are used in dentistry for biocompatibility, corrosion resistance, biostability, osseointegration, durability, and clinical success. In orthopedics and reconstructive surgery, 3D-printed bone implants are common. Thanks to digital technologies, additive manufacturing, and topological optimization are accelerating biomedical research and development like never before. Their key benefits include patient-specific implants, intricate geometries, faster production and operation, good bone and reconstructive integration, and patient comfort. This ongoing research employs a custom-made jaw model to study its mechanical properties under chewing stresses. The model was then subjected to topological simulation, as a part of DfAM. We used 3D printing simulations to investigate dimensional inaccuracies caused by thermal stresses and support structure removal. Although chewing loads were below the yield strength, substantial dimensional distortion suggested using compensated geometry to manufacture the implant. This study seeks to provide researchers with helpful advice for future research.

Keywords: Bone & dental implants, additive manufacturing, 3D printing, topology optimization, Ti64, CoCr.

Introduction

Additive manufacturing, often known as 3-D printing, redefines creativity and is a technical revolution of the contemporary day. The fabrication of three-dimensional products layer by layer during this transformational process constitutes a departure from centuries-old subtractive manufacturing procedures. Additive manufacturing (AM) has grown in popularity recently because of its design flexibility, high production liberalization, reduced material waste, and superior forming precision [1].

This technology can transform the healthcare industry, particularly bone and dental implantology. The accuracy and customization of AM might lead to a shift toward patient-centered therapy. Clinicians and engineers may design customized implants that match each patient's anatomical and therapeutic needs, breaking free from previous constraints [2]. These implants are tailored to encourage easy integration and long-term efficacy, resulting in higher patient happiness and welfare. Customizing additive manufacturing (AM) may result in complex, porous designs that improve osseointegration and help integrate bone tissues (Figure 1). This technology would enhance patient outcomes, healing times, and the quality of life when considering additive manufacturing (AM) in healthcare [3] [4].

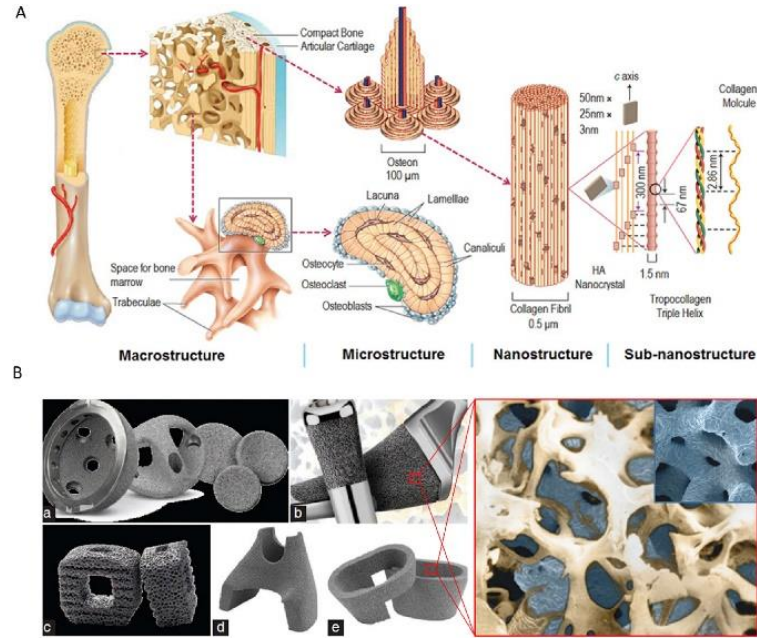


Figure 1. Additive Manufacturing of Bone Implants [5]

Edentulism is a prevalent condition on a global scale, particularly among the elderly population. Natural teeth's profound and permanent absence substantially influences individuals' overall health, leading to functional and social constraints. The incidence of bone disorders and fractures is increasing steadily over time. A mandibular issue may arise due to an accident or illness affecting the mandible, the most significant and robust bone in the human facial structure [6]. A bone grafting treatment is employed to expedite the recovery of patients due to the protracted duration of the inherent healing process of mandibular bones.

The use of biomaterials in bone replacement by 3D printing is being investigated as an alternative to conventional bone grafting procedures such as autographs, allografts, and xenografts, all of which have inherent limitations. The bone scaffold may be effectively manufactured utilizing additive manufacturing or 3D printing, allowing for rapid production and material customization. Recently, many alternative additive manufacturing methods have been explored for bone tissue creation. SLA, FDM, DMLS, 3DP, SLM, Poly-Jet Technology, and EBM are the methods employed in the sector [7]. In recent years, there has been a steady increase in research on mandibular bone replacement surgery.

The initiation of the CAD design process for mandibular jaw implants often involves the acquisition of high-resolution CT (Computed Tomography) scan data of the patient's mandible in DICOM format [8]. This 3D volumetric data is then imported into one of the commercially available specialized medical imaging software and serves as the foundation for the subsequent CAD modeling steps [9]. The mandibular implant is methodically built using computer-aided design tools, resulting in a highly detailed virtual model (Figure 2).

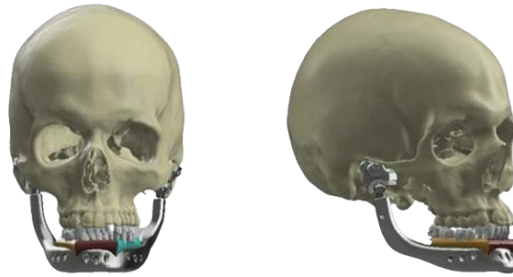


Figure 2. *Mandibular Jaw Implant [10]*

Materials and Methods

This study prefers Ti64 (titanium alloy Ti-6Al-4V) for implants such as orthopedic and dental devices because of its biocompatibility, corrosion resistance, and high strength-to-weight ratio. The material's Young's modulus and Poisson ratio were set to 116 GPa and 0.31, respectively, and the yield strength value of 880 MPa was used [11].

The .STEP file of the CAD model was obtained from publicly accessible free libraries online (Figure 3). Subsequently, finite element analysis (FEA) simulations were employed using the Altair Inspire Software to evaluate the implant's stress distribution and load-bearing characteristics under physiological conditions. Topological optimization and 3D printing simulations were also performed in the same software.

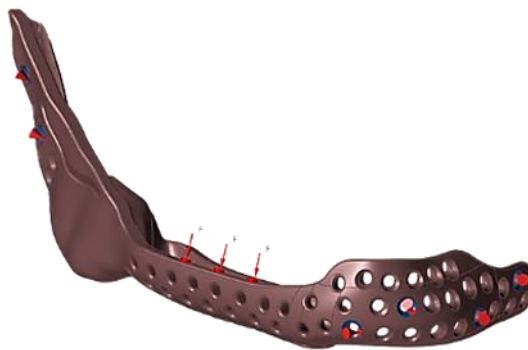


Figure 3. *CAD model of Mandibular Jaw Implant used.*

The chewing patterns of the patients recovering from implant surgery and the chewing requirements of a typical meal (where a maximum force is not used in every chew) were both attempted to be reflected by the two load scenarios employed in this study. Forces of 240N and 450N were applied in the 1st and 2nd load cases, assuming 1st as the regular chewing force and 2nd under severe conditions, respectively [12]. The implant was constrained in 6 positions, replicating the actual scenario of being implanted in any patient.

In all loading scenarios, the resultant forces were exerted on the three posts, replicating the transfer of stresses from the denture to the whole metal structure of the implant. These were followed by topological optimizations, with 'maximum stiffness' as the TO method. 3D printing simulations enabled us to evaluate the dimensional errors that could occur due to thermal stresses inherent in the process [4] and the removal of support structures during the additive manufacturing of these implants.

Results and Discussion

For regular and extreme chewing cases, i.e., the maximum displacements for 1st and 2nd load cases were less than 0.05mm and 0.1mm, respectively. Similarly, the maximum von Mises stresses were less than 300MPa and 500MPa, respectively. The displacement is insignificant, and the stresses are much lower than the yield strength of titanium, which is approximately 880MPa.

For topological optimization, 62% of the mass was reduced when compared with the original model, as shown in Figure 4, while the objective of the topological optimization was set to “Maximize Stiffness.” The optimized part was again subjected to the 2nd load case, and the maximum displacement and von Mises stresses were less than 0.1mm and 300MPa, respectively.



Figure 4. *Topologically optimized part*

Following the topological optimization, the 3D printing simulations were performed on the original model to get the residual stresses and maximum spring back displacement when the supports were removed. The maximum residual stress was approximately 950 MPa at one of the supports (Figure 5), while the maximum displacement was more than 1.5 mm after removing the supports (Figure 6). So, the compensated geometry should be used while printing the part.

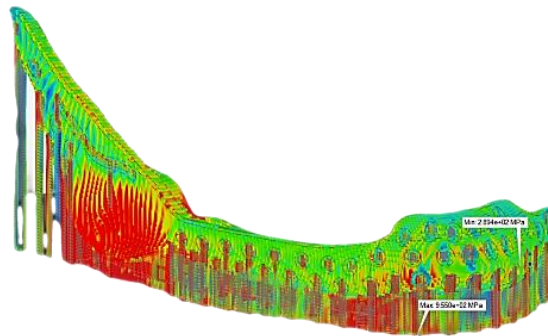


Figure 5: *Residual Stresses after printing*

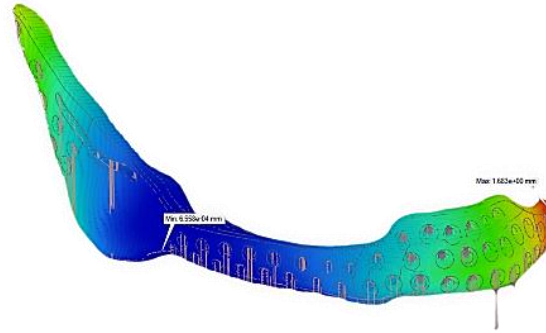


Figure 6: *Springback Displacement*

Conclusions

The study demonstrates that employing these computational tools before in-vivo tests and actual surgeries enhances the comfort and quality of life for edentulous patients who may benefit from sub-periosteal jaw-fastened implant systems in the future. These simulations also assisted us in gaining a better knowledge of the implant's function and stability and identifying potential improvement areas. This study will be the foundation for data-driven improvements in mandibular jaw implant design and implantology.

References

- [1] A. Nouri, A. Rohani Shirvan, Y. Li, C. Wen, Additive manufacturing of metallic and polymeric load-bearing biomaterials using laser powder bed fusion: A review, *J Mater Sci Technol.* 94 (2021) 196–215. <https://doi.org/10.1016/j.jmst.2021.03.058>.
- [2] R. Koppunur, K.K. Dama, U. Rokkala, B. Thirupathi, N.V.S.S. Sagar, B. Gugulothu, Design and Fabrication of Patient-Specific Implant for Maxillofacial Surgery Using Additive Manufacturing, *Advances in Materials Science and Engineering.* 2022 (2022). <https://doi.org/10.1155/2022/7145732>.
- [3] A.A. Raheem, P. Hameed, R. Whenish, R.S. Elsen, G. Aswin, A.K. Jaiswal, K.G. Prashanth, G. Manivasagam, A review on development of bio-inspired implants using 3d printing, *Biomimetics.* 6 (2021). <https://doi.org/10.3390/biomimetics6040065>.
- [4] D. Martinez-Marquez, M. Jokymaityte, A. Mirnajafizadeh, C.P. Carty, D. Lloyd, R.A. Stewart, Development of 18 quality control gates for additive manufacturing of error free patient-specific implants, *Materials.* 12 (2019). <https://doi.org/10.3390/ma12193110>.
- [5] J. Li, X. Cui, G.J. Hooper, K.S. Lim, T.B.F. Woodfield, Rational design, bio-functionalization and biological performance of hybrid additive manufactured titanium implants for orthopaedic applications: A review, *J Mech Behav Biomed Mater.* 105 (2020). <https://doi.org/10.1016/j.jmbbm.2020.103671>.
- [6] A.A. Raheem, P. Hameed, R. Whenish, R.S. Elsen, G. Aswin, A.K. Jaiswal, K.G. Prashanth, G. Manivasagam, A review on development of bio-inspired implants using 3d printing, *Biomimetics.* 6 (2021). <https://doi.org/10.3390/biomimetics6040065>.
- [7] E. DEMİRALP, G. DOĞRU, H. YILMAZ, Additive Manufacturing (3D PRINTING) Methods and Applications in Dentistry, *Clinical and Experimental Health Sciences.* 11 (2021) 182–190. <https://doi.org/10.33808/clinexphealthsci.786018>.

- [8] E. DEMİRALP, G. DOĞRU, H. YILMAZ, Additive Manufacturing (3D PRINTING) Methods and Applications in Dentistry, Clinical and Experimental Health Sciences. 11 (2021) 182–190. <https://doi.org/10.33808/clinexphealthsci.786018>.
- [9] E. De Moor, S.E.F. Huys, G.H. van Lenthe, M.Y. Mommaerts, J. Vander Sloten, Mechanical evaluation of a patient-specific additively manufactured subperiosteal jaw implant (AMSJI) using finite-element analysis, *Int J Oral Maxillofac Surg.* 51 (2022) 405–411. <https://doi.org/10.1016/j.ijom.2021.05.011>.
- [10] F.A. Govoni, N. Felici, M. Ornelli, V.A. Marcelli, E. Migliano, B.A. Pesucci, R. Pistilli, Total mandible and bilateral TMJ reconstruction combining a customized jaw implant with a free fibular flap: a case report and literature review, *Maxillofac Plast Reconstr Surg.* 45 (2023). <https://doi.org/10.1186/s40902-023-00374-w>.
- [11] J. Liu, Q. Sun, C. Zhou, X. Wang, H. Li, K. Guo, J. Sun, Achieving Ti6Al4V alloys with both high strength and ductility via selective laser melting, *Materials Science and Engineering: A.* 766 (2019). <https://doi.org/10.1016/j.msea.2019.138319>.
- [12] A. Carnicero, A. Peláez, A. Restoy-Lozano, I. Jacquott, R. Perera, Improvement of an additively manufactured subperiosteal implant structure design by finite elements based topological optimization, *Sci Rep.* 11 (2021). <https://doi.org/10.1038/s41598-021-94980-1>.

Fundings

This work has received funding from the European Union’s Horizon 2020 research and innovation program under the Marie Skłodowska-Curie grant agreement No 101034425 for the project titled A2M2TECH. This study has also received funding from The Scientific and Technological Research Council of Türkiye (TUBITAK) with grant No 120C158 for the same A2M2TECH project under the TUBITAK's 2236/B program.

Conflict Of Interests

The authors declare that they have no competing interests.

An Ex-Situ Energy Density Computation Method for Selective Laser Melting (SLM) Systems

Ahmet Hakan Karakurt¹, Cem Batur¹, Peyman Ansari¹, Metin Uymaz Salamci^{1,2,3}

1. Additive Manufacturing Technologies Application And Research Center-EKTAM, Gazi University, Ankara 06560, Turkey

2. Manufacturing Technologies Center of Excellence- URTEMM A.S., Ankara 06980, Turkey

3. Department of Mechanical Engineering, Gazi University, Ankara 06570, Turkey

Abstract

The parameters such as laser power, spot diameter and scanning velocity used during the selective laser melting (SLM) process affect the temperature variation between layers. On the other hand, in practical applications the temperature variations between layers cannot be measured directly. In this study, the diode intensity values obtained from the Melt Pool monitoring features of Concept Laser M2 Cusing machine were utilized to reveal applied Energy Density values on layers. By establishing a correlation between these values and theoretically calculated energy density values, a mathematical model has been derived. This study presents a multiphysics numerical model with the aim of investigating the influencing factors in the Selective Laser Melting (SLM) process for part production. In this context, mathematical relationships among these factors are established while utilizing aluminum alloy AlSi10Mg powder as the material of interest. The research thoroughly examines the effects of laser power and laser spot diameter on the temperature of the melt pool at various scanning velocities. Consequently, mathematical expressions that establish correlations between process parameters and melt pool temperature are derived.

Keywords: Energy density; diode intensity; additive manufacturing; selective laser melting (SLM); process parameter; AlSi10Mg aluminum alloy; finite element method (FEM)

Introduction

Additive manufacturing (AM) is the process of constructing 3D structures by fusing layers of material powder together. The AM methods are becoming an alternative manufacturing technology rapidly replacing traditional manufacturing counterparts. It reduces the need for traditional methods such as casting and drilling and allows complex parts to be produced directly. It also reduces the need for large assemblies and allows a more liberal approach to design than traditional manufacturing. In metal additive manufacturing technology, one of the most prominent methods is the Powder Bed Fusion (PBF) process. In the PBF process, material powder is selectively fused together layer-by-layer into a 3D structure. The PBF can be broadly classified as[1-6]:

1. direct metal laser sintering (DMLS)
2. electron beam melting (EBM)
3. selective heat sintering (SHS)
4. selective laser melting (SLM)
5. selective laser sintering (SLS)

Among the above mentioned production schemes, SLM method is the most preferred one. SLM is a powder-bed process whereby a high-density-focused laser beam selectively scans a powder bed. The scanned and solidified layers are stacked upon each other to build a fully functional three-dimensional part, tool, or a prototype. PBF technologies, in which either laser, heat or electron beam is used as the energy source to fuse the powder particles together to form a three-dimensional object, can be used for a diverse range of applications [7-14]. Unlike conventional manufacturing processes, pre-processing starts directly with the CAD model converted to a special file format to represent the geometry with triangles and special algorithms are used to slice the 3D model into thin layers, typically of about 20–40 μm in the SLM process. After setting process parameters such as scan strategy, laser power, hatch distance, and scan speed for the material to be processed, a suitable (commercially available) software embedded to the SLM machine slices the 3D object down to a 2D production file and the SLM device scans every layer on top of each other until the part geometry is completely built [15-20]. This method has advantages and disadvantages compared to other production methods. The production time is usually much longer than conventional manufacturing techniques. In addition, more support structure is needed in the SLM method compared to the EBM production method. On the other hand, it provides better surface quality compared to production methods such as EBM. In the SLM method, -depending on the SLM device- some of the parameters can be changed to have certain expected microstructure and/or mechanical properties. Indeed, parameters such as laser power, scanning speed, layer thickness and laser spot diameter directly affect the energy density. Before starting the production of the part, the energy density is calculated and the laser power, scanning speed, Laser Spot Diameter and layer thickness suitable for the material to be used are determined. Then, the determined parameters are given to the SLM system as inputs before starting the production. However, in general, information about the energy density value or layer temperature cannot be obtained directly from the SLM systems. Therefore, various numerical models are developed and the theoretical energy density is calculated with the input parameters. By the energy density equation(s), it is found that there is a direct proportion between energy density and laser power, and an inverse proportion with scanning speed, layer thickness and Laser Spot Diameter. For the experimental investigations, the layer temperature can be measured using a thermal camera. However, in some studies [21-28], the temperature was calculated without using a thermal camera. On the other hand, some SLM devices are equipped with diode sensors to monitor melt pool features. These kinds of sensors take images of the production at certain periods during operation. Then the light intensity is determined from the pictures and is recorded into a file. Once the operation is completed, both the pictures taken during production and the diode intensity values are recorded.

In this study, an ex-situ energy density computation method is introduced by correlating diode intensity obtained from some of SLM devices. For this purpose, the theoretically calculated energy density and the diode densities obtained from the SLM machine were compared. The variations between the layers are calculated and a numerical model is investigated.

Experimental Setup and Controlling Layer Properties

Layer properties can be controlled by changing various parameters [29]. For example, the laser power can be changed according to the material that will be used in printing. A parameter set suitable for production can be created by optimizing some of the process parameters. It is known that process parameter changes adversely affect the final results. For instance, if the material is exposed to a temperature higher than the melting temperature of the material, the part may have some defects or the melting powder may vaporize. On the other hand, when the temperature is lower than the temperature

required for the material to melt, the melt pool characteristics, such as melt pool life, area, may not be enough to produce the desired geometry.

The effects of parameter changes can be estimated for a single layer. However, since there is energy transfer between the layers, the estimations and the measurements made during the production might not agree. Therefore, the transfer between layers should be considered as well. This is not necessarily straightforward. This is why the data recorded by the SLM machine during production are fed into the simulations performed. The diode density data may be used to provide information about the energy density. Using the data, energy and temperature changes between layers can be calculated.

In this study, the following assumptions were taken into consideration while making correlation [30]:

I. The speed of the laser beam is constant, and the focused laser spot is circular. The deposited layer geometry is taken as elliptical because the energy distribution in the laser beam cross-section is considered to be Gaussian. This type of energy distribution yields a convex shaped deposited layer, along the cross-section that can be correlated with an “elliptical” profile.

II. The surface tension can be determined via the microscopic structure of the liquid near the surface. At the liquid–vapor interface, the density changes radically from a high value in the liquid state to a very low value in the gas phase. Surface atoms experience an “attraction” toward the liquid phase, which originates from the surface tension. In this study measurements were conducted via post-processing techniques because in-situ layer deposition could not be monitored. Thus, the surface tension of the melt flow was neglected. The thickness of the powder layer is known to be an input in the LPBF process.

The laser beam energy dissipation by the powder granules is assumed to be constant, and the powder particle mean size is considered. While forming a powder bed, the overlapping of the powder particles are ignored.

Table 1. *AlSi10Mg LPBF printing experimental parameters*

Sample No.	Laser Power (W)	Layer Spot Diameter (μm)	Scanning Velocity (m/s)
1	75	140	0.6
2	225	140	1.4
3	275	140	0.6
4	350	140	1.1
5	400	140	0.8
6	110	150	0.8
7	110	120	1.1
8	110	100	0.6
9	110	75	1.1
10	110	50	1.4

In this study, AlSi10Mg Aluminium powder was used. The production was carried out with multiple sets of parameters. The parameter sets that were used are given in Table.1. Between the runs, laser power, scanning speed and laser diameter were varied and layer thickness was kept constant. The layer thickness is set to 25 μm. With these parameter sets, it was possible to observe the change in energy density and the change between layers. All of the parameter sets used in this study were prepared considering the aluminum material in order to ensure production was carried out smoothly.

Method

In this section, the correlation study between diode density and energy density is described. The values obtained for the study were converted into real data by applying a normalization process. Firstly, 10 different parameter sets were defined for each part to be produced. Then, volumetric energy density values were calculated for each run using the parameter sets entered before production. The volumetric energy density can be calculated as follows [25].

$$VED = P / (\omega H d)$$

where VED is volumetric energy density (J/mm^3), P is laser power (W), ω is scan rate (mm/s), H is scan depth (mm) and d is spot diameter (mm).

Volumetric energy density value was calculated for each part and parameter set. Diode density and melt pool area values were taken from the Concept Laser M2 Cusing device. The volumetric energy density values obtained were used to calculate the differences between the layers. The change in the result of each layer was calculated as a percentage. The change between the layers was obtained as a result of the change of parameter sets. Also, the change in diode intensity values obtained from the SLM machine was calculated for each layer. The energy density and diode intensity values were compared and a correlation between the values was found. Then it was possible to come up with a formula using parameters such as laser power, laser spot diameter and scanning velocity. The developed formula is suitable for all SLM machines and its suitability was tested for different parameters.

Experimental Results and Discussion

For the study, 10 parameter sets of 30 specimens each were prepared. As a result, the relationship between diode intensity and energy density was derived. It is also observed that the percentage of change of these variables between layers is close to each other. In addition, a relationship was derived by using linear regression between the two values. The experimentally calculated margin of error was used in the formula obtained at the end of the study. Also all variants of specimens achieved the default assumed error rate. This condition was met by all the specimens produced by SLM production method.

The correlation between the theoretically obtained energy density value of the 9th sample and the diode density values obtained in the SLM machine can be seen in Figure 1. When the same data is normalized, the amount of percentage change between them converges.

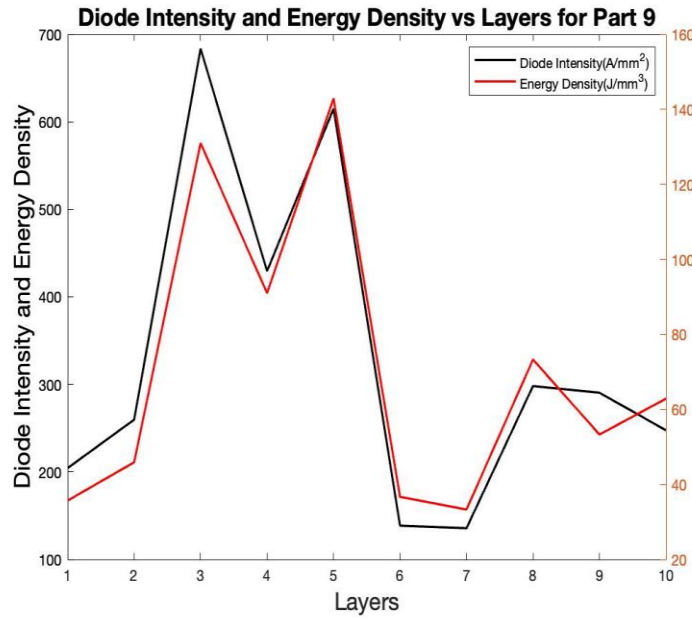


Figure 1. Diode Intensity and Energy Density through layers for Part 9

It can also be seen in Figure 2 that a similar relationship was observed in the 12th sample where the parameter set order was different from the other samples. As a result, the error rate between experimental and theoretical data was used as a coefficient variable.

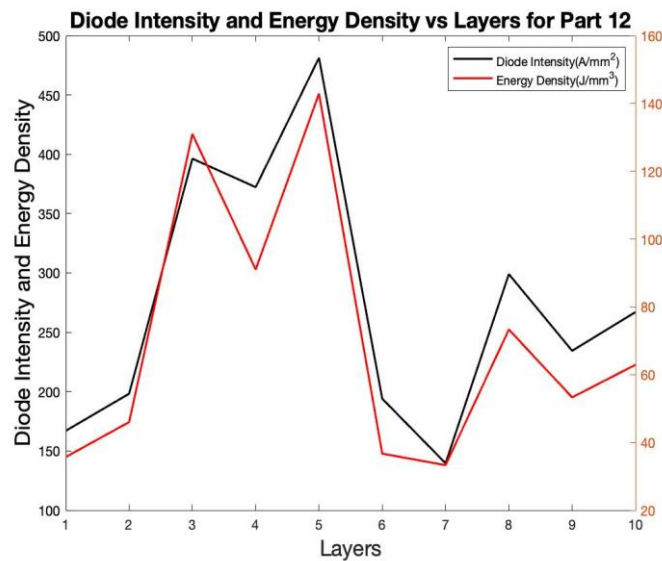


Figure 2. Diode Intensity and Energy Density through layers for Part 12

The empirical relationship derived using the data sets obtained between diode intensity and energy density was valid through all samples. The cosmetic differences (like outer texture, surface reflectivity) between different samples can be observed in Figure 3. These differences are due to the laser power, laser spot diameter and scanning velocity values. The differences between the parts could also be observed in diode intensity maps of the parts. In addition, with some specific parameters it was observed that the support structures were separated from the production table. It was found that the separation was also caused by the parameter choice such as scanning speed. There is no significant difference in the

parts produced with parameter sets that are similar. However, the difference between samples could also be observed in the internal structure of the sample and the values obtained from the SLM machine.



Figure 3. Image of the manufactured part

As a result of the study, formulas were developed to predict the interlayer energy exchange for any part to be produced with the SLM production method.

Conclusions

In this study, the variation between layers as a result of parameter changes is investigated experimentally and theoretically. It was observed that diode intensity and energy density are correlated with each other. This relation could be utilized in the control of temperature throughout a layer and in between layers. In other words by the help of the relation found, heat transfer between layers can be calculated before production and necessary changes can be made. This would ensure the printed part to be optimized in desired characteristics. This study deals with all layers and the parametric variation of each point position. Previous studies [31-34] have generally studied a single layer. Therefore, this study proposes a novel approach to verify the applied Energy Density during the SLMed parts by using Diode Intensity data recorded by some of SLM systems.

Acknowledgements

Funding

This work is supported by The Scientific And Technological Research Council Of Türkiye (Tübitak) under the 1004 Program for the project number 20AG008.

References

- [1] Galarraga, H., Warren, R. J., Lados, D. A., Dehoff, R. R., Kirka, M. M., & Nandwana, P. (2017). Effects of heat treatments on microstructure and properties of Ti-6Al-4V ELI alloy fabricated by electron beam melting (EBM). *Materials Science and Engineering: A*, 685, 417-428.
- [2] Lekurwale, S., Karanwad, T., & Banerjee, S. (2022). Selective laser sintering (SLS) of 3D printers using a 3D printer composed of IR/red-diode laser. *Annals of 3D Printed Medicine*, 6, 100054.
- [3] Kurzynowski, T., Stopyra, W., Gruber, K., Ziółkowski, G., Kuźnicka, B., & Chlebus, E. (2019). Effect of scanning and support strategies on relative density of SLM-ed H13 steel in relation to specimen size. *Materials*, 12(2), 239.

- [4] Singh, D. D., Mahender, T., & Reddy, A. R. (2021). Powder bed fusion process: A brief review. *Materials Today: Proceedings*, 46, 350-355.
- [5] Shahbudin, N., Lee, T. C., & Ramlan, R. J. P. M. (2019). An overview on 3D printing technology: Technological, materials, and applications. *Procedia Manufacturing*, 35, 1286-1296.
- [6] Gupta, N., Weber, C., & Newsome, S. (2012). *Additive manufacturing: status and opportunities*. Science and Technology Policy Institute, Washington.
- [7] Bourell, D. L., Beaman, J. J., & Wohlers, T. (2020). History and evolution of additive manufacturing.
- [8] Wong, K. V., & Hernandez, A. (2012). A review of additive manufacturing. *International scholarly research notices*, 2012.
- [9] Francois, M. M., Sun, A., King, W. E., Henson, N. J., Tourret, D., Bronkhorst, C. A., ... & Abdeljawad, F. (2017). Modeling of additive manufacturing processes for metals: Challenges and opportunities. *Current Opinion in Solid State and Materials Science*, 21(4), 198-206.
- [10] Bahnini, I., Rivette, M., Rechia, A., Siadat, A., & Elmesbahi, A. (2018). Additive manufacturing technology: the status, applications, and prospects. *The International Journal of Advanced Manufacturing Technology*, 97, 147-161.
- [11] Vayre, B., Vignat, F., & Villeneuve, F. (2012). Designing for additive manufacturing. *Procedia CIRP*, 3, 632-637.
- [12] Negi, S., Dhiman, S., & Sharma, R. K. (2013). Basics, applications and future of additive manufacturing technologies: A review. *Journal of Manufacturing Technology Research*, 5(1/2), 75.
- [13] Yakout, M., Elbestawi, M. A., & Veldhuis, S. C. (2018). A review of metal additive manufacturing technologies. *Solid State Phenomena*, 278, 1-14.
- [14] Horn, T. J., & Harrysson, O. L. (2012). Overview of current additive manufacturing technologies and selected applications. *Science progress*, 95(3), 255-282.
- [15] Calignano, F., Manfredi, D., Ambrosio, E. P., Biamino, S., Lombardi, M., Atzeni, E., ... & Fino, P. (2017). Overview on additive manufacturing technologies. *Proceedings of the IEEE*, 105(4), 593-612.
- [16] Vaezi, M., Seitz, H., & Yang, S. (2013). A review on 3D micro-additive manufacturing technologies. *The International Journal of Advanced Manufacturing Technology*, 67, 1721-1754.
- [17] Ford, S. L. (2014). Additive manufacturing technology: potential implications for US manufacturing competitiveness. *J. Int'l Com. & Econ.*, 6, 40.
- [18] Williams, C. B., Mistree, F., & Rosen, D. W. (2008, January). A Functional Classification Framework for the Conceptual Design of Layered Manufacturing Technologies. In *International Design Engineering Technical Conferences and Computers and Information in Engineering Conference* (Vol. 43291, pp. 35-48).
- [19] Manzhairov, A. V. (2017). Advances in the theory of surface growth with applications to additive manufacturing technologies. *Procedia Engineering*, 173, 11-16.
- [20] Zalameda, J. N., Burke, E. R., Hafley, R. A., Taminger, K. M., Domack, C. S., Brewer, A., & Martin, R. E. (2013, May). Thermal imaging for assessment of electron-beam freeform fabrication

(EBF3) additive manufacturing deposits. In *Thermosense: Thermal Infrared Applications XXXV* (Vol. 8705, pp. 174-181). SPIE.

[21] Khanzadeh, M., Tian, W., Yadollahi, A., Doude, H. R., Tschopp, M. A., & Bian, L. (2018). Dual process monitoring of metal-based additive manufacturing using tensor decomposition of thermal image streams. *Additive Manufacturing*, 23, 443-456.

[22] Khanzadeh, M., Chowdhury, S., Bian, L., & Tschopp, M. A. (2017, June). A methodology for predicting porosity from thermal imaging of melt pools in additive manufacturing thin wall sections. In *International Manufacturing Science and Engineering Conference* (Vol. 50732, p. V002T01A044). American Society of Mechanical Engineers.

[23] Myers, A. J., Quirarte, G., Ogoke, F., Lane, B. M., Uddin, S. Z., Farimani, A. B., ... & Malen, J. A. (2023). High-resolution melt pool thermal imaging for metals additive manufacturing using the two-color method with a color camera. *Additive Manufacturing*, 103663.

[24] Li, J., Jin, R., & Hang, Z. Y. (2018). Integration of physically-based and data-driven approaches for thermal field prediction in additive manufacturing. *Materials & Design*, 139, 473-485.

[25] Francis, J., & Bian, L. (2019). Deep learning for distortion prediction in laser-based additive manufacturing using big data. *Manufacturing Letters*, 20, 10-14.

[26] Farshidianfar, M. H., Khajepour, A., & Gerlich, A. (2016). Real-time control of microstructure in laser additive manufacturing. *The International Journal of Advanced Manufacturing Technology*, 82, 1173-1186.

[27] Compton, B. G., Post, B. K., Duty, C. E., Love, L., & Kunc, V. (2017). Thermal analysis of additive manufacturing of large-scale thermoplastic polymer composites. *Additive Manufacturing*, 17, 77-86.

[28] Hanzl, P., Zetek, M., Bakša, T., & Kroupa, T. (2015). The influence of processing parameters on the mechanical properties of SLM parts. *Procedia Engineering*, 100, 1405-1413.

[29] Ur Rehman, A., Mahmood, M. A., Ansari, P., Pitir, F., Salamci, M. U., Popescu, A. C., & Mihailescu, I. N. (2021). Spatter formation and splashing induced defects in laser-based powder bed fusion of AlSi10Mg alloy: a novel hydrodynamics modeling with empirical testing. *Metals*, 11(12), 2023.

[30] Kurzynowski, T., Stopyra, W., Gruber, K., Ziółkowski, G., Kuźnicka, B., & Chlebus, E. (2019). Effect of scanning and support strategies on relative density of SLM-ed H13 steel in relation to specimen size. *Materials*, 12(2), 239.

[31] He, Y., Gardy, J., Hassanpour, A., & Bayly, A. E. (2020). A digital-based approach for characterizing spread powder layer in additive manufacturing. *Materials & design*, 196, 109102.

[32] Luo, Z., Yang, F., Dong, G., Tang, Y., & Zhao, Y. F. (2016, August). Orientation optimization in layer-based additive manufacturing process. In *International Design Engineering Technical Conferences and Computers and Information in Engineering Conference* (Vol. 50077, p. V01AT02A039). American Society of Mechanical Engineers.

- [33] Williams, C. B. (2008). Design and development of a layer-based additive manufacturing process for the realization of metal parts of designed mesostructure. Georgia Institute of Technology.
- [34] Hirsch, M., Patel, R., Li, W., Guan, G., Leach, R. K., Sharples, S. D., & Clare, A. T. (2017). Assessing the capability of in-situ nondestructive analysis during layer based additive manufacture. Additive Manufacturing, 13, 135-142.

Next Generation Eco-Materials Revolution: CO₂ Emissions Reduction via Lattice-Structured Additive Manufactured Lever Arms

M. Usman Sikandar¹, Roozbeh Neshani²

1. Additive Manufacturing Technologies Application & Research Center-EKTAM, Gazi University, Ankara, Turkey

2. Department of Mechanical Engineering, METU, Ankara, Turkey

Abstract

Environmental sustainability necessitates a profound reevaluation of materials engineering. This paper introduces an innovative approach to eco-materials design, leveraging lattice structures with the potential to transform the sustainable materials landscape. Drawing inspiration from nature's efficient designs, these geometric patterns offer mechanical efficiency, durability, and recyclability. Our research focuses on assessing the environmental advantages presented by these pioneering lattice structures. We explore various lattice designs, including Simple Cubic, Diamond Cubic, Octet, Kelvin, Tesseract lattices, and a hybrid SC-BCC lattice. We quantify their sustainability impact, specifically in terms of CO₂ reduction, when applied to additive manufacturing of an AlSi10Mg lever arm. The lattice structures used in our study featured a cell size of 10 by 10 mm with strut dimensions of 1.5 mm. Employing Altair Inspire 2022 for lattice design and Ansys Workbench 2023 R2 for analysis, we assigned the AlSi10Mg material to CAD models. Our analysis reveals compelling results: The Octet lattice achieves an 8.31% CO₂ reduction, while the Tesseract lattice attains 11.78%, the SC-BCC lattice achieves an impressive 18.94%, Kelvin lattice reaches 19.86%, Diamond Cubic lattice achieves 20.09%, and Simple Cubic lattice leads with a substantial 20.32% CO₂ reduction compared to a full solid model. Furthermore, we conducted failure analysis, finding that the solid model can withstand forces up to 10,300 N before yielding, whereas the cubic lattice begins to yield at 1,550 N. This indicates that the application of lattices under load conditions of 1,550 N can significantly reduce CO₂ emissions. Our findings underscore the promise of lattice structures in advancing sustainable materials engineering, demonstrating their potential to enhance environmental performance in automotive.

Keywords: Lattices, BCC, Cubic, Sustainability, Lever Arm

Introduction

Additive manufacturing (AM) empowers the creation of robust yet lightweight constructions featuring intricate lattice designs that are beyond the capabilities of conventional manufacturing techniques [1]. A lattice structure is a regular and porous arrangement formed by systematically combining fundamental units in a specific periodic fashion [2]. Gradient formations are prevalent in nature, manifesting in the microstructures of various organisms, including animals, plants, and even human bones. For instance, consider the microstructure of bamboo, which exhibits a porous gradient pattern characterized by heightened porosity on the outer surface encompassing the bamboo's circular structure and diminishing porosity as it approaches the inner surface [3]. Nevertheless, a significant distinction between uniform lattice structures (ULS) and gradient lattice structures (GLS) lies in their response to external forces. When subjected to force, ULS tend to experience layer-by-layer deterioration. Conversely, GLS can confer specific strength to particular regions within the structures by modulating density variations throughout the volume [4].

Next Generation Materials

Lattice Structures

Emerging polymer 3D-printing technologies are enabling the design and fabrication of mechanically efficient lattice structures with intricate structures

[5]. Polymer lattices are a type of cellular material that is made up of a network of interconnected struts. They have a number of unique properties, including high strength, stiffness, and energy absorption. They are also very lightweight, which makes them ideal for a variety of applications. The lattices below are very diverse in terms of their shape, size, and material. This demonstrates the versatility of AM for printing polymer lattices. In areas of safety equipment, polymer-printed lattices achieve efficient energy absorption with a rapid fabrication process that bypasses the supply chain limitations of bulk manufacturing [6][7].

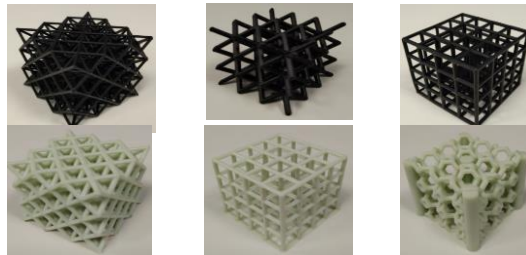


Figure 1. Polymer Lattices Nano-Mechanics lab-ODTU [8]

Similarly, the metal additive manufacturing techniques can be used for the development of the metallic lattices.

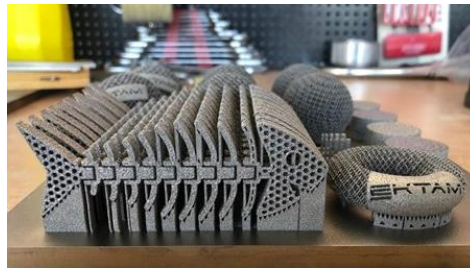


Figure 2. Lattice Structures Applications-EKTAM [9]

Gradient Structures & Generative Design

We employ ntopology and Gen 3D software for the generation of lattice structures, while also utilizing Autodesk Inventor's generative design feature to create lattices within parts and optimize them according to specific requirements [10].

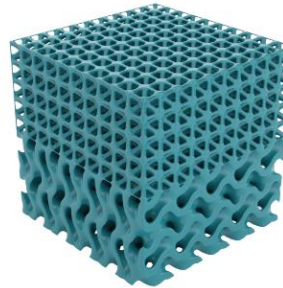


Figure 3. *Hybrid Lattices [11]*

Metallized Structures

Polymers inherently lack metal-like properties such as electrical and thermal conductivity, light absorption and reflectivity, magnetism, and high durability. Consequently, researchers have directed their efforts towards metallizing polymers, a process that empowers the development of structures featuring augmented properties bridging the gap between polymers and metals [12]. We employ a variety of techniques to metallize polymers, including physical vapor deposition, electroless plating, vapor phase deposition, electroplating, lithography for metal patterning, screen printing for metal patterning, direct writing methods, electrohydrodynamic printing, and ion beam milling [13].

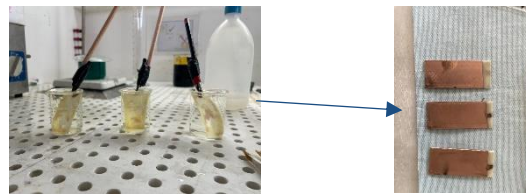


Figure 4. *Thermochemical and Electrochemical Materials Processing Laboratory-ODTU ABS Coating [14]*



Figure 5. *Thermochemical and Electrochemical Materials Processing Laboratory-ODTU Honeycombs [15]*

Harnessing Environmental Sustainability

Incorporating lattice structures into product design offers a significant advantage by facilitating the development of lighter-weight products. This approach directly translates into reduced material usage,

which, in turn, contributes to a noteworthy decrease in the carbon dioxide (CO₂) footprint associated with the production and use of the product. By optimizing the structural design through these innovative lattice patterns, we not only achieve weight reduction but also align our efforts with sustainability goals by minimizing resource consumption and environmental impact.

In the image, the lever arm is the long, thin metal rod that is attached to the top swivel and the steering arm. It is responsible for transferring the rotational force from the steering wheel to the steering knuckles, which turn the wheels as shown in figure below.

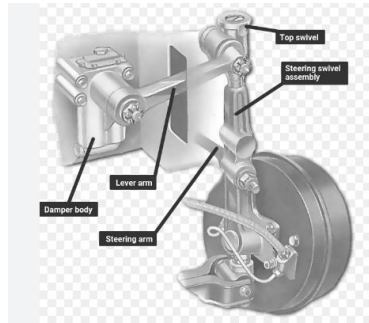
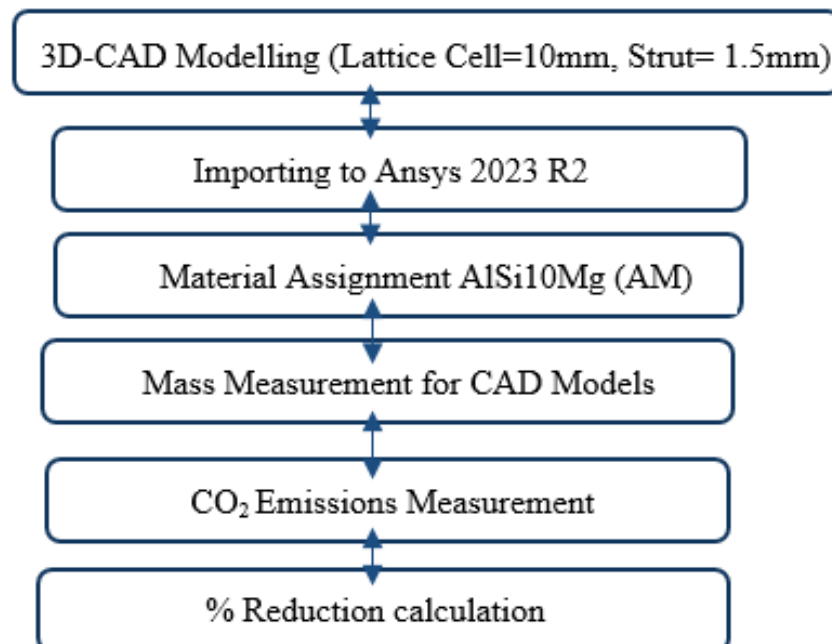


Figure 6. *Lever Arm Application [16]*

Here, different lattices are introduced in a solid lever arm (Length X=236.82 mm, Height Y=40mm, Width Z=50mm) & CO₂ reduction is investigated using Ansys 2023 R2.

Methodology



CAD Models

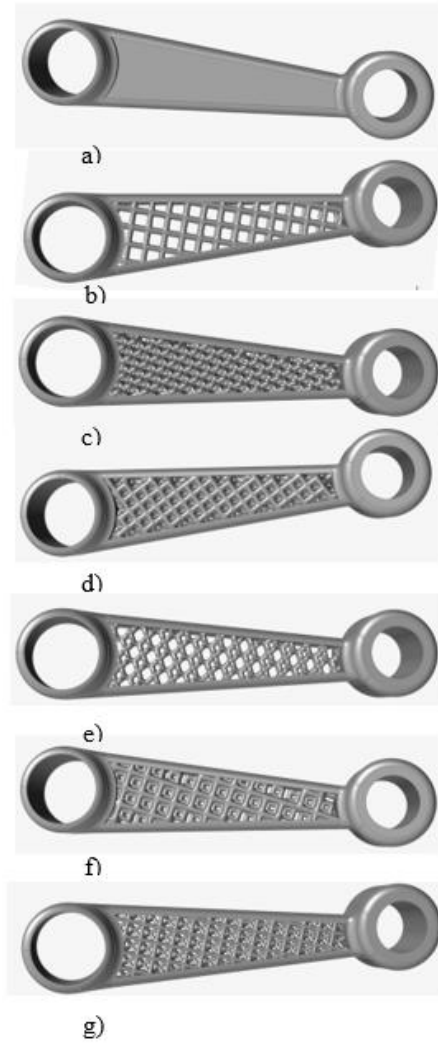


Figure 7. a) Solid b) Simple Cubic c) Diamond Cubic d) Octet e) Kelvin f) Tesseract g) SC-BCC

CO₂ Emissions Reduction

Table 4. Comparative CO₂ Emissions Reduction

Comparative CO ₂ Emissions Reduction			
1Kg AlSi10Mg =296.39Kg [17]			
Single Lattice Cell=10×10 mm, Strut= 1.5mm			
Design	Mass Kg	CO ₂ Emission Kg	% CO ₂ Reduction
Solid	0.433	128.34	
Simple	0.345	102.25	20.32
D. Cube	0.346	102.55	20.09
Octet	0.397	117.67	8.31
Kelvin	0.347	102.85	19.86
Tesseract	0.382	113.22	11.78
Hybrid Lattice Cell=10×10 mm, Strut= 1.5mm			
SC-BCC	0.351	104.03	18.94

Insights from Failure Analysis

Furthermore, we conducted failure analysis, finding that the solid model can withstand forces up to 10,300 N before yielding (250MPa), whereas the cubic lattice begins to yield at 1,550 N. This indicates that the application of lattices under load conditions of 1,550 N, can significantly reduce CO₂ emissions.

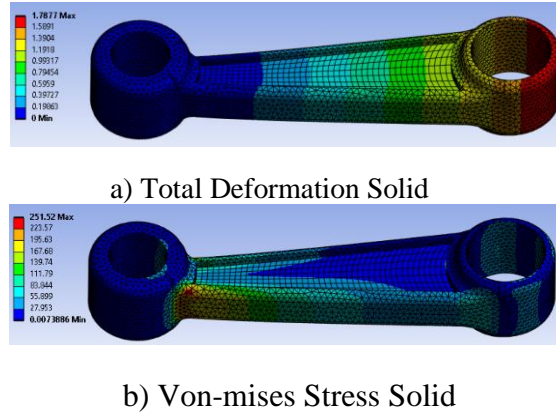


Figure 8. Failure Analysis Solid Model

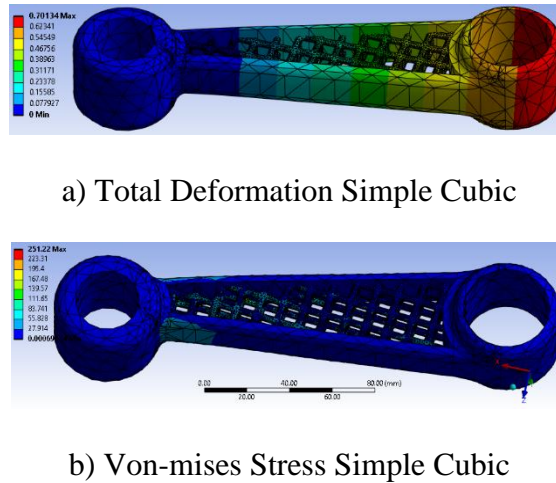


Figure 9. Failure Analysis Cubic Lattice

Conclusions & Recommendations

In conclusion, our exploration of lattice structures within the realm of eco-materials design has revealed a promising path toward a more sustainable future. The results showcased in this paper underscore the significant environmental benefits that can be achieved through the adoption of these innovative structures across various industries, including automotive.

Our findings on different lattices clearly demonstrate substantial weight reductions compared to traditional solid structure, resulting in noteworthy CO₂ emissions reductions. These reductions not only contribute to a more environmentally responsible approach to materials engineering but also align with the urgent global need to combat climate change. The work will be extended for complete failure analysis of all these lattices.

As we look to the future, it's evident that thick metallization of polymer lattices holds the potential for substantial economic benefits as substitute to metal additive manufacturing. This innovative approach not only enhances the structural integrity of polymer lattices eco-materials but also introduces new opportunities for industries to reduce costs and environmental impact simultaneously. The comparative assessment of failure analysis is needed between LPBF & metallized polymer lattice-engineered structures.

In the coming years, we anticipate continued advancements in eco-materials design, with a focus on refining and expanding the utilization of lattice structures.

Funding

Author is working under a co-funded project that has received funding from European Union's Horizon 2020 research and innovation program under the Marie Skłodowska-Curie grant agreement no. 10103442 that is co-funded by the Scientific and Technological Research Council of Türkiye (TUBITAK) with grant no.120C158 for the A2M2TECH project under the TUBITAK's 2236/B program.

References

- [1] Hao, L., Raymont, D., Yan, C., Hussein, A., & Young, P. (2011, September). Design and additive manufacturing of cellular lattice structures. In *The International Conference on Advanced Research in Virtual and Rapid Prototyping (VRAP)*. Taylor & Francis Group, Leiria (pp. 249-254).
- [2] Yin, H., Zhang, W., Zhu, L., Meng, F., Liu, J., & Wen, G. (2022). Review on lattice structures for energy absorption properties. *Composite Structures*, 116397.
- [3] Tan, T., Rahbar, N., Allameh, S. M., Kwofie, S., Dissmore, D., Ghavami, K., & Soboyejo, W. O. (2011). Mechanical properties of functionally graded hierarchical bamboo structures. *Acta biomaterialia*, 7(10), 3796-3803.
- [4] Seharing, A., Azman, A. H., & Abdullah, S. (2020). A review on integration of lightweight gradient lattice structures in additive manufacturing parts. *Advances in Mechanical Engineering*, 12(6), 1687814020916951.
- [5] Egan, P. F., Khatri, N. R., Parab, M. A., & Arefin, A. M. (2022). Mechanics of 3D-Printed Polymer Lattices with Varied Design and Processing Strategies. *Polymers*, 14(24), 5515.
- [6] Erickson, M. M., Richardson, E. S., Hernandez, N. M., Bobbert II, D. W., Gall, K., & Fearis, P. (2020). Helmet modification to PPE with 3D printing during the COVID-19 pandemic at Duke University Medical Center: a novel technique. *The Journal of arthroplasty*, 35(7), S23-S27.
- [7] Provenzano, D., Rao, Y. J., Mitic, K., Obaid, S. N., Pierce, D., Huckenpahler, J., ... & Loew, M. H. (2020). Rapid prototyping of reusable 3D-printed N95 equivalent respirators at the George Washington University.
- [8] <http://nanomechanics.me.metu.edu.tr/>
- [9] <https://ektam.gazi.edu.tr/view/page/288670/research>

[10] <https://www.ntop.com/>

[11] <https://gen3d.com/sulis-lattice/>

[12] Melentiev, R., Yudhanto, A., Tao, R., Vuchkov, T., & Lubineau, G. (2022). Metallization of polymers and composites: State-of-the-art approaches. *Materials & Design*, 110958.

[13] Perera, A. T. K., Song, K., Umezu, S., & Sato, H. (2023). Recent progress in functionalized plastic 3D printing in creation of metallized architectures. *Materials & Design*, 112044.

[14] <https://mete.metu.edu.tr/research-laboratories/thermochemical-and-electrochemical-materials-processing-laboratory>

[15] <https://catalog.library.metu.edu.tr/search~S15/a?Neshani+Roozbeh>

[16] <https://www.howacarworks.com/suspension/replacing-lever-arm-dampers>

[17] Weiss, Christian & Bödger, Christian & Ekkehard, Schiefer & Heußen, Daniel & Häfner, Constantin. (2022). Evaluation of the Ecological Footprint for Parts from AlSi10Mg manufactured by Laser Powder Bed Fusion.

A Case Study in Deep Drawing Process: Numerical Simulation and Analysis of Material Behavior and Hardening Models

M. Usman Sikandar¹, Muhammad Usama²

1. Additive Manufacturing Technologies Application & Research Center-EKTAM, Gazi University, Ankara, Turkey

2. Department of Mechanical Engineering, METU, Ankara, Turkey

Abstract

This case study employs Abaqus software to conduct a numerical simulation of the deep drawing process. Four crucial components, including the blank, blank holder, die, and punch, are meticulously assembled within the Abaqus environment. The investigation involves the application of three distinct hardening models, encompassing isotropic, kinematic, and combined approaches, as well as the utilization of two yielding functions: isotropic Von-Mises and anisotropic Hills function. The plasticity parameters, crucial for accurate material representation, are derived from data obtained in a comprehensive uniaxial tensile test. The material under examination is DKP 6112, and precise friction coefficients are determined to characterize interactions between the blank, blank holder, die, and punch. Concurrently, blank holding forces are fine-tuned to mitigate instability risks, while the velocity of the punch is systematically adjusted to explore its impact on blank deformation. This investigation also delves into the theoretical foundations of plasticity, providing a comprehensive backdrop for the Abaqus simulations. The empirical data gathered from a tensile test, encompassing stress-strain values at varying loads, contributes to engineering stress-strain and true stress-true strain graph development. Employing Ludwick's equation, stress values are extrapolated from true plastic strain data. Subsequently, these stress-strain profiles, along with residual stress assessments during unloading, are incorporated into the Abaqus simulations. Notably, the research reveals that the combined hardening model yields superior and more precise results when compared to the isotropic and kinematic hardening models. The study concludes by identifying a punch displacement of 20 mm as a key parameter influencing the deep drawing process.

Keywords: Deep Drawing Process Simulation, Abaqus, Hardening Models, Isotropic, Kinematic, Hills function

Introduction

Deep drawing is characterized as a sheet forming process that involves the transformation of a flat sheet into a hollow component, either with one side open (direct drawing) or by shaping an open hollow part into a smaller cross-sectional hollow part (re-drawing) [1]. The deep drawing process involves essential components, including a blank, punch, die, and optionally, a blank holder with or without draw beads positioned along the die's edges. The punch exerts radial downward pressure on the sheet metal, compelling it to take the shape of the die cavity [2-3].

Deep drawing can be performed in multiple stages. While single-stage deep drawing processes can benefit from preconditioning to widen their processing windows, the presence of hardening effects

imposes constraints on multi-stage forming processes, which are essential for manufacturing complex components [4].

Throughout the deep drawing process, sheet metal frequently experiences various stress conditions during plastic deformation. These conditions primarily encompass uniaxial tension, equiaxial biaxial tension, and shear stress states [5].

In this case study, we conduct a simulation of the deep drawing process. The study entails the utilization of three different hardening models, including isotropic, kinematic, and combined models, in conjunction with two yielding functions: isotropic Von-Mises and anisotropic Hills function.

Methodology & Results

In this simulation, the model comprises four distinct components, namely a die, a punch, a blank holder, and a blank, as previously described. To facilitate computational efficiency, a quarter model is created within the Abaqus environment. The blank is represented as a 3D deformable sheet, while the die, punch, and blank holder are modeled as 3D discrete and rigid entities. Subsequent simulations are conducted for all hardening models, employing both yielding functions. Detailed methodologies employed within Abaqus are expounded upon in this section.

Table 1. Dimensions & Data

Blank dimensions (mm)	280 X 260
Punch dimensions (mm)	200 X 180
Punch shoulder radius (mm)	14
Punch corner radius (mm)	35
Die dimensions (mm)	203 x 183
Die shoulder radius (mm)	12
Die corner radius (mm)	38
Sheet thickness (mm)	1.2
Material	DKP6112

In the first simulation, we utilize the isotropic hardening model with an isotropic Von Mises yielding function in the SI mm system. Material properties, including density, Young's modulus, yield strength, and Poisson's ratio, are defined. Density data is sourced from Dizaji [6], while Young's modulus and yield strength are extracted from the tensile test data, with Poisson's ratio also obtained from Dizaji [6].

Table 2. Elasticity Parameters

Elasticity Parameters	
Density (tonnes/mm ³)	7.83*10 ⁻⁹
Young's Modulus (MPa)	141394
Poisson's ratio	0.32
Yield Stress (MPa)	245

In the plasticity analysis, we begin by constructing an engineering stress vs. engineering strain curve based on the provided tensile data. Subsequently, we transform this curve into a true stress vs. true strain representation using appropriate equations. From this curve, plastic strains are obtained. Since the values before the yield point are negative hence they are converted to positive values. For the plasticity

parameters, the data required is obtained by using Ludwick's equation. The values of H and n are determined by curve fitting in MATLAB and given as $H=537.5$ and $n=0.6191$ and yield stress is given as 245 MPa. The Ludwick's curve is provided below:

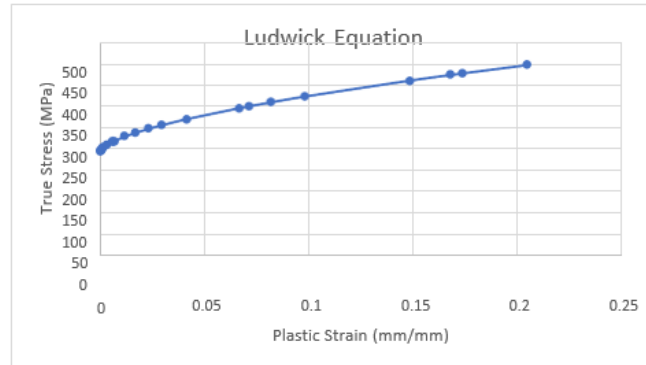


Figure 1. *Ludwick's Curve*

The plasticity parameters inputted in the software. After defining material properties, we assign them to the blank. To assess the forces acting on the blank holder, an inertia value of 5 is assigned to it. Subsequently, all components are assembled in Abaqus, and surfaces involved in the deep drawing process are designated, including those between the blank and die, blank and holder, and blank and punch. We establish two steps: loading, to observe blank deformation, and unloading, to study springback and residual stresses. Both steps span 0.1 seconds. Next, we define interaction properties for the interacting surfaces using the penalty method and a friction coefficient of 0.05 [1]. Boundary conditions are applied to all parts, including two for the blank, one for the holder, and two for the punch (one specifying punch velocity, determined as 200 mm/s). The load on the blank holder is set at 30 MPa to maintain contact with the die while allowing blank deformation. After several simulations, this pressure value was determined as optimal, while the pressure required to secure the blank holder was found to be 10 MPa. The figures below illustrate pressure distribution and the model assembly.

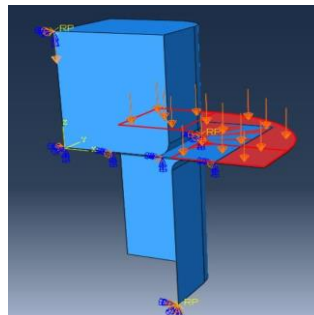


Figure 2. *Blank Holder Pressure*

The subsequent step, meshing the components, posed challenges due to a 1000-node limitation. To address this, the blank was assigned a global size of 8, yielding 646 nodes and 288 elements (C3D8R type). Other parts were meshed with a global size of 30 due to node restrictions. The die featured 77 nodes and 60 elements (60 linear quadrilateral elements of R3D4 type), the holder had 12 nodes and 5 elements (R3D4 type), and the punch utilized 158 nodes, 156 elements, and 156 quadrilateral elements (R3D4 type).

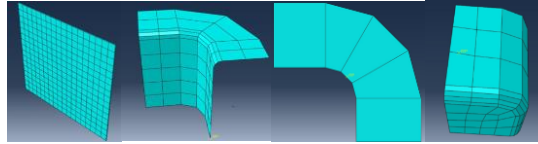


Figure 3. Meshed Components

In the case of isotropic hardening with a Von-Mises yielding function, the loading step employs a blank holder force of 30 MPa and a punch velocity of 200 mm/s. During the unloading step, the blank holder force gradually decreases from 30 MPa to 10 MPa, while the punch unloading velocity is set at 400 mm/s.

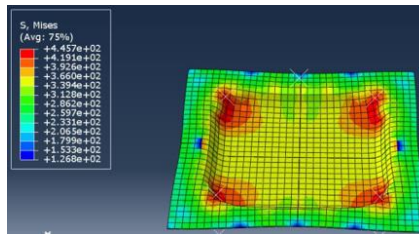


Figure 4. Deformation Loading Step (Isotropic)

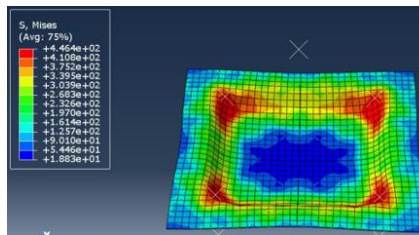


Figure 5. Deformation Unloading Step (Isotropic)

The next selected hardening type is linear kinematic hardening, which introduces two sets of plasticity parameters while keeping other parameters consistent with the previous isotropic hardening case. Loading and unloading forces and velocities remain identical to the isotropic hardening scenario. The primary distinction between isotropic and kinematic hardening lies in their respective behaviors: isotropic hardening entails yield surface expansion, while kinematic hardening involves the translation of the yield surface's center. Additionally, kinematic hardening introduces the Bauschinger effect, where material is initially loaded beyond the yield point and subsequently reloaded in the reverse direction, resulting in a lower yield point in the reverse direction.

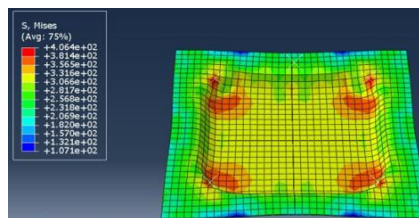


Figure 4. Deformation Loading (Kinematic)

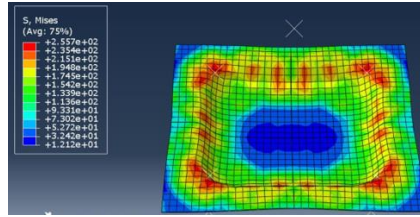


Figure 5. Deformation Unloading (Kinematic)

After unloading the blank, we analyze residual stresses and springback. Residual forces are lower than those during loading. Furthermore, the subsequent section will cover the discussion of kinetic and internal energy graph results for all cases.

In the case of combined hardening, plasticity parameters are derived from the Ludwick's curve, with the remaining values matching those of the isotropic hardening scenario. Half cycle data is utilized, and a single back stress is considered. The deformation results are illustrated in the following figures:

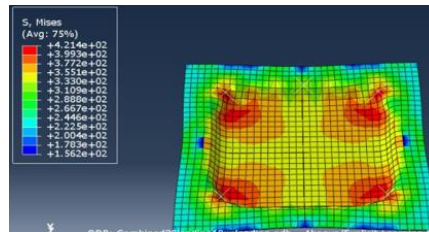


Figure 6. Deformation Loading Step (Combined)

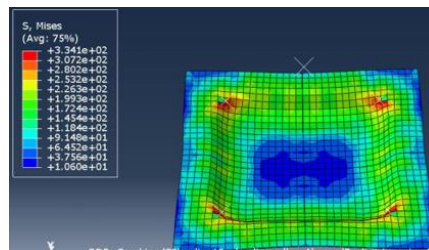


Figure 7. Deformation Unloading Step (Combined)

Anisotropic modeling, utilizing Hill's potential function, is applied to all three hardening models. In this approach, a local datum is established mirroring the global datum, and material orientation for anisotropy is defined. All other parameters remain consistent. Below, the deformed blank condition at the end of the loading step is depicted for the isotropic hardening case employing Hill's potential function. The figure below reveals unexpected stresses in the blank caused by anisotropies.

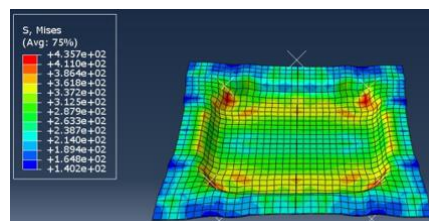


Figure 8. Deformation Loading (Hill's Isotropic)

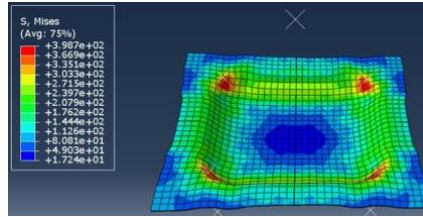


Figure 9. Deformation Unloading (Hill's Isotropic)

Similarly, for linear kinematic hardening using Hill's potential function, figures for both loading and unloading steps are provided below:

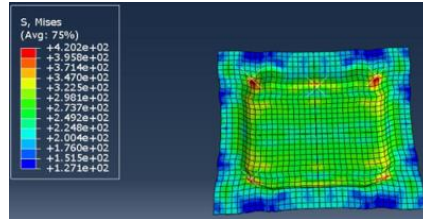


Figure 10. Deformation Loading (Hill's Kinematic)

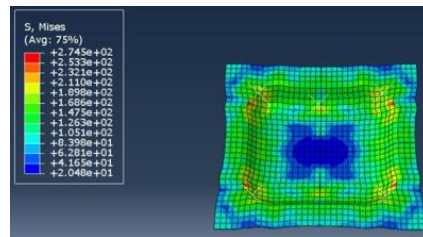


Figure 11. Deformation Unloading (Hill's Kinematic)

Additionally, for the combined hardening case with Hill's potential function, the loading and unloading steps are shown below:

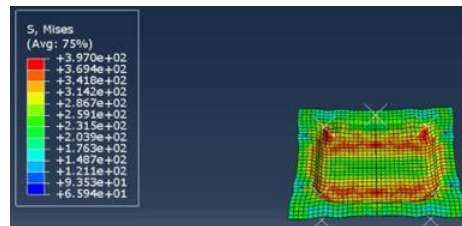


Figure 12. Deformation Loading (Hill's Combined)

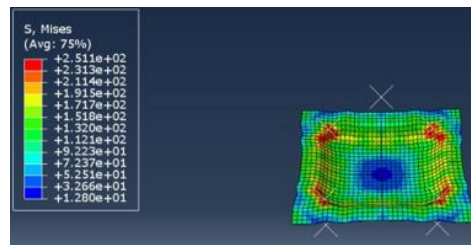


Figure 13. Deformation Unloading (Hill's Combined)

Kinetic and internal energies for all three cases were identical, as shown in the following figures.

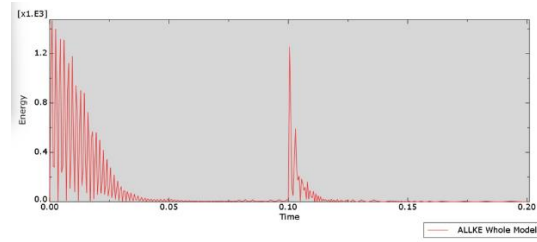


Figure 14. Kinetic Energy (All Cases)

The internal energy plot follows, revealing values over 10 times greater than the kinetic energy of the model.

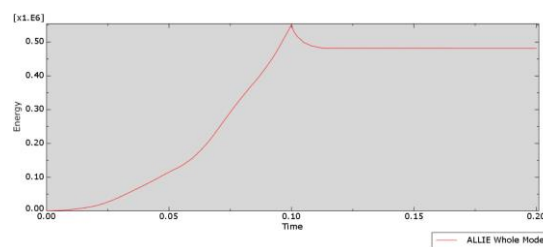


Figure 15. Internal Energy (All Cases)

Conclusion & Recommendations

This study involved a thorough analysis of the deep drawing process through experimental data and finite element simulations in Abaqus. Key findings include:

1. **Material Characterization:** A tensile test yielded stress-strain data used to construct engineering and true stress-strain curves. Ludwick's equation was applied to determine stresses from true plastic strain.
2. **Hardening Models:** Three hardening models (isotropic, kinematic, and combined) with two yielding functions were employed. The combined hardening model outperformed the others, reducing residual stress during unloading.
3. **Punch Displacement:** A critical parameter, the punch displacement, was found to be 20 mm.

Recommendations & Future Work:

1. **Advanced Simulation:** Investigate advanced simulation methods, including adaptive meshing and multi-scale modeling, to address meshing challenges.
2. **Process Optimization:** Study additional process parameters such as blank holder force and friction coefficients for optimization.
3. **Validation Studies:** Conduct experimental validation to validate simulation results.

In summary, this study offers valuable insights into the deep drawing process and hardening models, providing a foundation for future research and improvements in deep drawing simulations.

Funding

Author is working under a co-funded project that has received funding from European Union's Horizon 2020 research and innovation program under the Marie Skłodowska-Curie grant agreement no. 10103442 that is co-funded by the Scientific and Technological Research Council of Türkiye

(TUBITAK) with grant no.120C158 for the A2M2TECH project under the TUBITAK's 2236/B program.

References

- [1] Singh, C. P., & Agnihotri, G. (2015). Study of deep drawing process parameters: a review. *International Journal of Scientific and Research Publications*, 5(2), 1-15.
- [2] Lim, Y., Venugopal, R., & Ulsoy, A. G. (2008). Advances in the control of sheet metal forming. *IFAC Proceedings Volumes*, 41(2), 1875-1883.
- [3] Das, P., Panda, S. K., & Pratihari, D. K. (2013). Modification of initial blank shape to minimize earing in deep drawing process. *International Journal of Advanced Materials Manufacturing and Characterization*, 3(1), 99-104.
- [4] Günzel, J., Hauß, J., & Groche, P. (2023). Opportunities, Challenges, and Influencing Factors in the Forming of Preconditioned Semi-Finished Products Made of EN AW-6082 and-7075. *Advanced Engineering Materials*, 2201799.
- [5] Zhang, Y., Duan, Y., Fu, P., Qi, S., & Zhao, J. (2023). Constitutive modeling based on non-associated flow rule for anisotropic sheet metals forming. *Materials Today Communications*, 107086.
- [6] Abbasnejad Dizaji, S. (2014). An investigation of ductile fracture criteria for sheet metal forming.

From Blueprint to Greenprint: A Case Study on CO₂ Footprint assessment in Product Design & Manufacturing (PDM)

M. Usman Sikandar¹, M. Saad²

1. Additive Manufacturing Technologies Application & Research Center-EKTAM, Gazi University, Ankara, Turkey

2. Seakeepers (Pvt.) Ltd., Karachi, Pakistan

Abstract

This conference paper presents a meticulous eco-audit of a controllable pitch propeller, performed with the aid of ANSYS Granta software. The study's inception involved defining crucial dimensions and establishing a comprehensive set of general and specific requirements, categorically divided into structural and environmental considerations. Employing the Ashby method for material selection, an exhaustive process was conducted to carefully choose materials aligning with these stringent requirements, while concurrently identifying suitable suppliers. The research also encompassed the development of detailed technical drawings, comprehensive manufacturing processes for each propeller component, assembly procedures, and a precise assessment of associated equipment costs. Subsequently, this extensive dataset formed the basis for an eco-audit, entailing a thorough analysis of carbon footprint, energy consumption, and costs (CEE). The study's findings unveiled a total CO₂ footprint of 1.4×10^5 kg, with materials emerging as a prominent contributor, constituting a substantial 75% of this footprint. Furthermore, it was evident that the integration of recycling measures held the potential to achieve a notable reduction in the carbon footprint, with the possibility of up to a 30% decrease.

Keywords: Ansys Granta, Controllable Pitch Propeller (CPP), Circular economies, Ashby Method

Introduction

The marine propeller constitutes a vital component within the traditional ship propulsion system, comprising the primary engine, transmission shaft, and propeller. Its primary role is to propel the vessel, harnessing power generated and conveyed by the main engine [1]. The process of selecting an appropriate propeller holds paramount importance, hinging upon the stern hull configuration, directly influencing ship velocity, and ensuring sustained propeller performance throughout the vessel's operational lifespan. The choice of propeller also exerts a significant impact on the operational parameters of the engine, encompassing speed, power output, and fuel consumption [2]. These factors, in turn, play a pivotal role in shaping the ship's energy efficiency index, with the ultimate goal of reducing carbon dioxide (CO₂) emissions. This index may manifest as the energy efficiency design index (EEDI) for new ships or the energy efficiency existing ship index (EEXI) for vessels in current operation, as defined in [3].

The primary thrust mechanism employed in ships is the controllable pitch propeller, which can dynamically alter both the thrust force and direction by adjusting the pitch of its blades. This adjustment allows for precise control of the vessel's speed and facilitates smooth transitions between forward and reverse motion. In contrast to fixed pitch propellers, controllable pitch propellers offer superior maneuverability and energy efficiency, making them the preferred choice for a wide range of maritime applications [4]. According to Wartsila, a prominent global manufacturer, "Approximately 20,000 vessels worldwide operate using Controllable Pitch Propellers (CPP) [5].

Methodology

Controllable Pitch Propeller Main Dimensions

The main dimensions of CPP are the hub diameter, the propeller diameter, and the number of blades.

Table 5. Main Dimensions

Hub Diameter	600-2200 mm
Number of Blades	4-5
Propeller Diameter	>1200 mm

General & Specific Requirements

Table 6. General Requirement

Strength	Flexural resistance & Torsion resistance (rotating blades)
Corrosion Resistance	Corrosion to sea water
Fluid Sealing	Sealing to high pressure water

Table 7. Specific Requirement

Component	Specific Requirements & Environment
1.Blade	Flexural, Cavitation, Corrosion resistance <u>Beam in bending, high corrosive</u>
1.Hub	Corrosion Resistance <u>Beam in bending, high corrosive</u>
1.Camdisc	Corrosion Resistance <u>Beam in bending, high corrosive</u>
2.Piston Cam	High-pressure resistance <u>Beam in Bending, low corrosive</u>
3.Supporting disc	High-pressure resistance <u>Compressed gasket, low corrosive</u>
4.Cover	High pressure yielding resistance <u>Column in compression, high corrosive</u>
5.Stop	High pressure yielding resistance <u>Column in compression, low corrosive</u>
6.Seal	Sealing to high pressure, Corrosion resistance <u>Compressed Seal, high corrosive</u>

The specified criteria give rise to 6 distinct categories. These proposed groups serve the purpose of delineating particular material attributes that can be visualized and sorted using Ansys Granta. This enables the compilation of a roster of materials best suited for the intended application. Moreover, this initial list will undergo further refinement, considering factors related to processability to facilitate the selection of appropriate manufacturing methods. Ultimately, the decision for the definitive material for each component within the group will also be influenced by its cost per kilogram.

Materials Selection (Ashby Method)

Ansys Granta EduPack will be used to conduct materials selection as it has used in various studies earlier with effective use [6]. This tool follows the rational materials selection methodology by Ashby et al. [7], illustrated schematically in the diagram below. Ashby's method[8] for material selection is well-suited for use in optimization with many design variables, because of its simplicity [9].

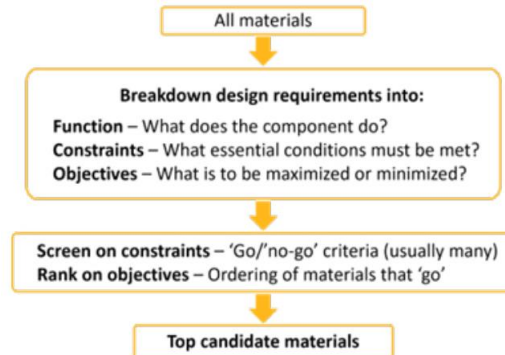


Figure 16. Systematic Materials Selection Methodology[6]

Prof. Ashby at Cambridge University developed the Ashby method using CES software to create material property charts [10]. These charts, known as Ashby charts, use logarithmic scales to graphically represent two material properties, aiding in material selection for engineering applications. This approach serves as an efficient initial screening method for candidate materials and integrates seamlessly with mechanical design for quick performance evaluation [11]. The materials and suppliers for the 6 different groups are selected and given below.

Table 8. Materials Selection & Suppliers

Group	Materials & Suppliers (to EU Fr)
1.Blade	Brass, C86550 Supplier:Shree Extrusions,India
1.Hub	Brass, C86550 Supplier:Shree Extrusions,India
1.Camdisc	Brass, C86550 Supplier:Shree Extrusions,India
2.Piston	ASTM CE30,cast,H ₂ O quenched Supplier:Magsen Foundry,China
2. Cam	ASTM CE30,cast,H ₂ Oquenched Supplier:Magsen Foundry,China
3.Supporting disc	ASTM CE30,cast,H ₂ Oquenched Supplier:Magsen Foundry,China
4.Cover	Brass, CuZn40Mn3Al2Fe2 Suppliers:Shree Extrusions,India
5.Stop	ASTM CE30,cast,H ₂ Oquenched Supplier:Magsen Foundry,China
6.Seal	Natural cis1, 4 polyisoprene NR Supplier:Sinochem, China

Technical Drawings, Manufacturing Processes & Assembly

The technical drawings are an important step which communicate with manufacturing professionals' exact dimensions. The 3D cad models are given below of the components followed by the detail breakdown of all manufacturing processes.

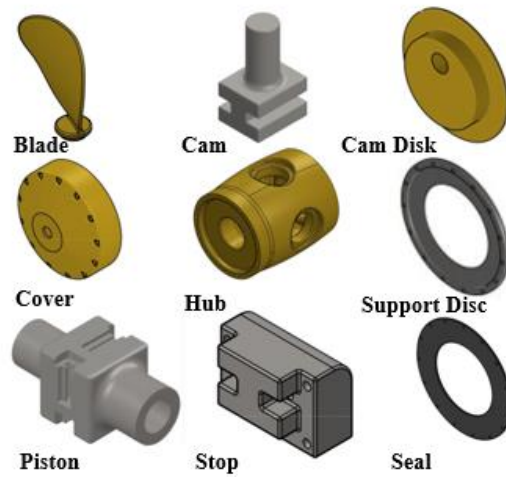
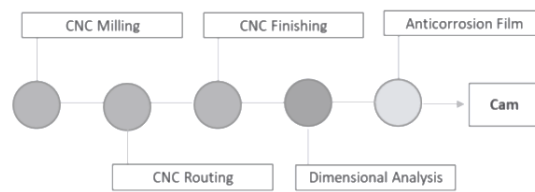


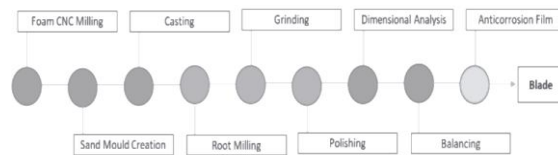
Figure 2. 3D CAD of Components

The manufacturing process route has defined for each part that is given below.

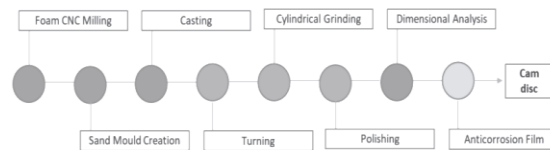
1. Cam



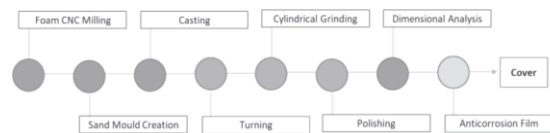
2. Blade



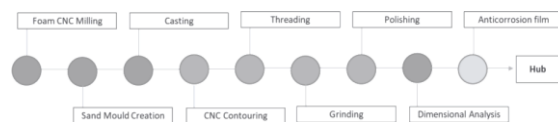
3. Cam Disc



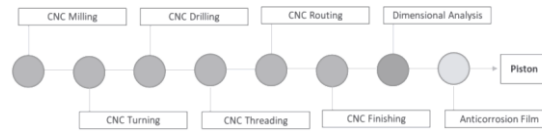
4. Cover



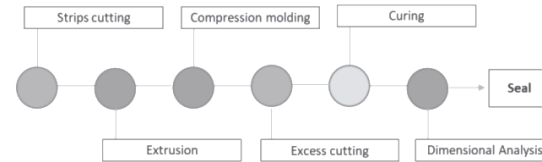
5. Hub



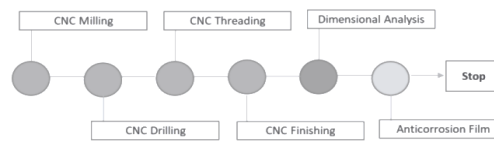
6. Piston



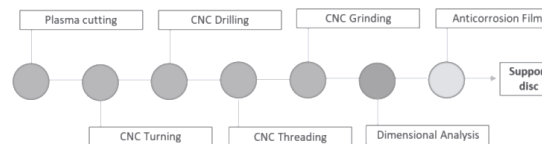
7. Seal



8. Stop



9. Support Disc



In the assembly process, the cam slides into the piston and is followed by the attachment of stops. Thread locking is applied to secure the stops. The piston is then assembled into the hub, and the cover is inserted and fastened with thread locking. Seals are positioned on the hub, and precise alignment of the cam disc is ensured. Support discs are added and secured with thread locking, followed by the attachment of blades to the cam disc, also using thread locking. The final step involves dynamic balancing to ensure optimal performance.

Table 5. *Equipment Cost & Supplier*

Manufacturing Processes	Equipment's Cost & Supplier
Casting	110000€, Induction Furnace-Dinhong electric
CNC Milling	130000€, CNC Milling, Haas.inc
CNC Turning	132000€, CNC Lathe, Haas.inc
Compression Moulding	45000€, Yizumi YL-V1000, Yizumi Co.
Anti-Corrosion electropainting	2000€, Electropainting machine, HCPC Equipment Co.

Eco-Audit Analysis

To conduct a carbon footprint analysis of materials and packaging, the "eco-audit" method introduced by Ashby was employed, using the Ansys Granta EduPack® software [12][13]. This approach facilitated

the quantification of Greenhouse Gas Emissions (GHE) across various phases, including material production, product manufacturing, transportation, and end-of-life disposal. Emission factors were applied by multiplying them with the average quantity of materials gathered per functional unit. Ansys Granta analysis is given below:

Materials Energy Consumption- CO₂-Footprint

Table 6. Materials Energy Consumption- CO₂-Footprint

Component	Material	Recycled content* (%)	Part mass (kg)	Qty.	Total mass processed** (kg)	Energy (MJ)	%	CO ₂ footprint (kg)	%
Hub	Brass, CuZn40Mn3Al2Fe2, C86550, cast (high-tensile manganese bronze)	Virgin (0%)	1,3e+04	1	1,4e+04	7e+05	43,0	4,8e+04	42,6
Piston	Stainless steel, austenitic, ASTM CE-30, cast, water quenched	Virgin (0%)	3,7e+03	1	8,9e+03	3,5e+05	21,4	2,5e+04	22,1
Cam	Stainless steel, austenitic, ASTM CE-30, cast, water quenched	Virgin (0%)	42	4	4,1e+02	1,6e+04	1,0	1,1e+03	1,0
Support disc	Stainless steel, austenitic, ASTM CE-30, cast, water quenched	Virgin (0%)	43	4	5,1e+02	1,8e+04	1,1	1,3e+03	1,1
Seal	Natural rubber (unreinforced)	Virgin (0%)	5	4	23	1,8e+03	0,1	44	0,0
Cam disc	Brass, CuZn40Mn3Al2Fe2, C86550, cast (high-tensile manganese bronze)	Virgin (0%)	2,2e+02	4	1e+03	4,9e+04	3,0	3,4e+03	3,0
Stop	Stainless steel, austenitic, ASTM CE-30, cast, water quenched	Virgin (0%)	40	4	2,8e+02	1,3e+04	0,8	9,3e+02	0,8
Blade	Brass, CuZn40Mn3Al2Fe2, C86550, cast (high-tensile manganese bronze)	Virgin (0%)	1,5e+03	4	6,6e+03	3,3e+05	20,0	2,2e+04	19,8
Cover	Brass, CuZn40Mn3Al2Fe2, C86550, cast (high-tensile manganese bronze)	Virgin (0%)	2,8e+03	1	3,2e+03	1,6e+05	9,6	1,1e+04	9,5
Total				27	3,5e+04	1,6e+06	100	1,1e+05	100

Manufacturing processes & Assemblies Energy Consumption & CO₂-Footprint

Table 9. Manufacturing processes & Assemblies Energy Consumption & CO₂-Footprint

Component	Process	% Removed	Amount processed	Energy (MJ)	%	CO ₂ footprint (kg)	%
Hub	Casting	-	1,4e+04 kg	1,2e+05	30,7	9,3e+03	31,0
Hub	Fine machining	12	1,7e+03 kg	6,1e+03	1,5	4,6e+02	1,5
Piston	Casting	-	8,9e+03 kg	1e+05	25,4	7,7e+03	25,6
Piston	Fine machining	58	5,2e+03 kg	3,2e+04	7,9	2,4e+03	8,0
Cam	Casting	-	4,1e+02 kg	4,7e+03	1,2	3,5e+02	1,2
Cam	Grinding	59	2,4e+02 kg	2,9e+03	0,7	2,1e+02	0,7
Support disc	Casting	-	5,1e+02 kg	5,8e+03	1,4	4,4e+02	1,5
Support disc	Grinding	66	3,3e+02 kg	3,9e+03	1,0	3e+02	1,0
Seal	Polymer molding	-	23 kg	3,7e+02	0,1	29	0,1
Seal	Cutting and trimming	12	2,7 kg	0,82	0,0	0,063	0,0
Cam disc	Casting	-	1e+03 kg	8,7e+03	2,2	6,5e+02	2,2
Cam disc	Fine machining	12	1,2e+02 kg	4,3e+02	0,1	32	0,1
Stop	Casting	-	2,8e+02 kg	3,2e+03	0,8	2,4e+02	0,8
Stop	Fine machining	42	1,2e+02 kg	7,1e+02	0,2	53	0,2
Blade	Casting	-	6,6e+03 kg	5,7e+04	14,3	4,3e+03	14,4
Blade	Grinding	12	7,9e+02 kg	5,3e+03	1,3	3,9e+02	1,3
Cover	Casting	-	3,2e+03 kg	2,8e+04	6,9	2,1e+03	6,9
Cover	Fine machining	12	3,8e+02 kg	1,4e+03	0,3	1e+02	0,3
Positioning	Construction	-	2,7e+04 kg	2,7e+03	0,7	2e+02	0,7
Fastening	Fasteners, large	-	61	4,3	0,0	0,32	0,0
Anti-corrosion coating	Electroplating	-	1,3e+02 m ²	1,2e+04	2,9	6,2e+02	2,1
Anti-fouling coating	Painting	-	1,3e+02 m ²	1,6e+03	0,4	1,3e+02	0,4
Total				4e+05	100	3e+04	100

Overall Analysis

Table 10. Overall Energy Consumption & CO₂-Footprint

Phase	Energy (MJ)	Energy (%)	CO ₂ footprint (kg)	CO ₂ footprint (%)	Cost (EUR)	Cost (%)
Material	1,64e+06	78,3	1,12e+05	77,0	1,59e+05	85,5
Manufacture	4,01e+05	19,2	2,99e+04	20,5	2,32e+04	12,5
Transport	3,78e+04	1,8	2,72e+03	1,9	3,43e+03	1,85
Use	0	0,0	0	0,0	0	0
Disposal	1,34e+04	0,6	937	0,6	144	0,0779
Total (for first life)	2,09e+06	100	1,46e+05	100	1,85e+05	100

Results & Conclusion

The analysis conducted using Ansys Granta Edupack (specifically the Eco-audit module) software package [14] provides a holistic view of a product's sustainability, considering energy use, ecological footprint, and financial implications. It reveals that 75% of the total CO₂ footprint (1.4×10^5 Kg) is attributed to raw material extraction, emphasizing the crucial role of material selection and management in environmental impact.

To enhance sustainability and reduce CO₂ footprint, strategies like recycling (which can cut emissions by 30%), adopting sustainable manufacturing techniques, and exploring eco-friendly materials can be implemented. Addressing the material aspect of sustainability allows businesses to take significant steps toward a greener future. Furthermore, this Cost, Energy, Environment (CEE) analysis can extend to evaluate the product's end-of-life potential (EoL).

Funding

The author conducted a portion of this independent work under two funding sources: the European Union's Horizon 2020 program with Marie Skłodowska-Curie grant agreement no. 10103442 and the Scientific and Technological Research Council of Türkiye (TUBITAK) with grant no. 120C158 for the A2M2TECH project under TUBITAK's 2236/B program.

References

- [1] Carlton, J. Marine Propellers and Propulsion, 2nd ed.; Butterworth-Heinemann: Oxford, UK, 2012.
- [2] Moreira, L.; Vettor, R.; Guedes Soares, C. Neural Network Approach for Predicting Ship Speed and Fuel Consumption. *J. Mar. Sci. Eng.* 2021, 9, 119.
- [3] DNV-GL. EEXI—Energy Efficiency Existing Ship Index. Available online: www.dnvgl.com/maritime/insights/topics
- [4] Bai, X., Ling, H., Luo, X. F., Li, Y. S., Yang, L., & Kang, J. C. (2023). Reliability and availability evaluation on hydraulic system of ship controllable pitch propeller based on evidence theory and dynamic Bayesian network. *Ocean Engineering*, 276, 114125.
- [5] Wärtsilä Controllable Pitch Propeller Systems, Available Online: wartsila.com/marine/build
- [6] Zhao, W., & Mercier, D. (2022). Materials Selection for a Heat Sink.
- [7] Michael F. Ashby. (2011). Materials Selection in Mechanical Design. <https://doi.org/10.1016/C2009-0-25539-5>
- [8] Ashby, M. F., Brechet, Y. J. M., Cebon, D., & Salvo, L. (2004). Selection strategies for materials and processes. *Materials & Design*, 25(1), 51-67.
- [9] Duriez, E., Azzaro-Pantel, C., Morlier, J., & Charlotte, M. (2023). A fast method of material, design and process eco-selection via topology optimization, for additive manufactured structures. *Cleaner Environmental Systems*, 9, 100114.
- [10] M.F. Ashby Materials Selection in Mechanical Design (4th ed.), Elsevier, Oxford, UK (2010)

- [11] de Oliveira, M. C. L., Ett, G., & Antunes, R. A. (2012). Materials selection for bipolar plates for polymer electrolyte membrane fuel cells using the Ashby approach. *Journal of power sources*, 206, 3-13.
- [12] M.F. Ashby *Materials and the Environment* Oxford, UK, Butterworth Heinemann (2013)
- [13] Baladés Ruiz, N., Remigio Carmona, P., Sales Lérída, D., Moreno Nieto, F. D., López, J. M., & Molina Rubio, S. I. (2023). Experimental and simulated study of 3D-printed couplings' suitability for industrial application.
- [14] Ansys. (2021). *Material Database: Ansys Granta EduPack Software*.

Synthesis of 2D MoS₂ Polycrystalline for Electro-optical Applications

Muhammad Adnan Saeed^{1,2,3}, Süleyman Özçelik³, Metin U. Salamci^{1,2}

1. Additive Manufacturing Technologies Application and Research Center, Ankara, Türkiye
2. Department of Mechanical Engineering, Faculty of Engineering, Gazi University, Ankara, Türkiye.
3. Photonics applications and research center, Gazi University, Ankara, Türkiye

Abstract

In this study, molybdenum disulfide (MoS₂) nanostructures were experimentally synthesized on Silicon and Sapphire Substrates. Some of the prepared samples were annealed at 900°C under argon gas in the chemical vapor deposition (CVD) furnace and others in the atmospheric oven for 60 min. The sulfurization of the Mo films was carried out at the Ar pressure of 3.4 mbar in a two-zone diffusion furnace by heating of 0.5 g sulfur powder to 250 °C in the first zone and by heating the precursor films to 900 °C in the second zone of the furnace. The heating rates of S and Mo precursor film zones were ~10 °C/min and ~20 °C/min, respectively. After preparing the samples, the samples were characterized by XRD, SEM, AFM, and Raman Spectroscopy. Both films exhibited uniform morphology with a polycrystalline structure as seen in top view SEM images.

Keywords: MoS₂, CVD, 2D Materials

Introduction

Two-dimensional materials such as MoS₂, MoSe₂, ReS₂, and WSe₂ have a crucial role in the manufacturing and performance of electron and optoelectronics devices. 2D-Materials Structured are based on layered materials. Van der Waals (vdWs) heterostructures composed of layered 2D materials got the attention of the researchers due to their excellent properties like smooth heterostructure interface, ultrafast carrier transport, and highly gate-tunable bandgap [1,2]. TMDCs exhibit the same structural properties but most of the properties like bandgap, thermoelectric conversion, and light-matter interaction are different. The stacked layers depict the difference in the photovoltaic properties, thermal transmission, elasticity, catalysis, etc. Like Graphene, TMDs are also layered materials with vdWs forces between their layers. Generally, MX₂ (X = S, Se, Te; M = Mo, W, Ta, etc.) is used to represent the typical formula of monolayer TMDs [3]. The assembling process of these crystal structures resulted in two different crystal structures, including an octahedral (1T) phase with metallic behavior and the other with trigonal prismatic (2H) phase to the P6₃/mmcc space group [4,5]. For WS₂ and MoS₂, the lattice constants of the WS₂ crystal are 0.315 and 0.312 nm, respectively. Comparing the 2H-MoS₂ and the 2H-WS₂, the 1T-MoS₂ and 1T-WS₂ phases exhibit higher conductivity, hydrophilicity, and a larger layer gap. However, the 2H phase is dominant and has good stability. The 1T phase is characterized by thermodynamic instability and will convert to the 2H phase even at room temperature [6]. TMDs can be easily exfoliated to single layers and be stacked to vdWs heterostructures on anticipated demand, which provides a thrilling prospect. The properties of MoS₂, similarly to those of other 2D materials, depend mainly on the vertical thickness of MoS₂ rather than its lateral size. The most important difference with respect to graphene is that 2D MoS₂ shows a direct bandgap of about 1.8 eV, making it an ideal candidate for applications in electronics, photonics, photovoltaics, energy storage, and catalysis. FETs with mobility up to 320 cm² V⁻¹ s⁻¹ and on/off ratio of 10⁸ at room temperature were realized [7,8], as well as inverters with gain up to 16. Several kinds of phototransistors, photosensors, and gas and biological sensors were demonstrated, and the mechanical properties of MoS₂ were exploited in the

realization of strain sensors [9]. to the continued evolution of additive manufacturing as a transformative force in modern industry. There are various methods which have been used to synthesize these materials but one of the most effective methods is CVD regarding the large area growth of crystals.

In this article. The MoS₂ thin films have been synthesized by a two-step CVD approach. The first step is the deposition of Mo precursor films on sapphire and SiO₂/Si substrates by the DC magnetron sputtering technique. The sulphurization of Mo films at high temperature by using Ar atmosphere in a CVD furnace with solid phase precursor. Various characterization like Xrd, AFM, SEM, and Raman spectroscopy has been done.

Materials and methods

In the standard horizontal configuration, a quartz tube about 1 m long with a diameter of 2–5 cm is used. The heating is provided by a resistance placed around the tube. The reaction for MoS₂ deposition requires a temperature in the 600–800 °C range, but in some cases, the supply of sulfur requires a second heating zone in the 100–200 °C range. In this case, to obtain better reproducibility and control, it is more convenient to separately and independently heat this additional zone (Figure 1.(a)) in which the sulfur precursor is placed. A standard routine to minimize the contamination from external air and O₂ in the reaction tube is to purge the system with inert gas several times before starting the growth, eventually evacuating the tube with a rotary pump, and then flushing with purified Ar or N₂ up to ambient pressure, repeating this procedure several times. X-ray diffraction (XRD) patterns of MoS₂ films were obtained by a APD 2000 PRO X-ray diffractometer in the 2θ range of 20 – 90 deg using CuKα radiation (λ = 1.54052 Å).

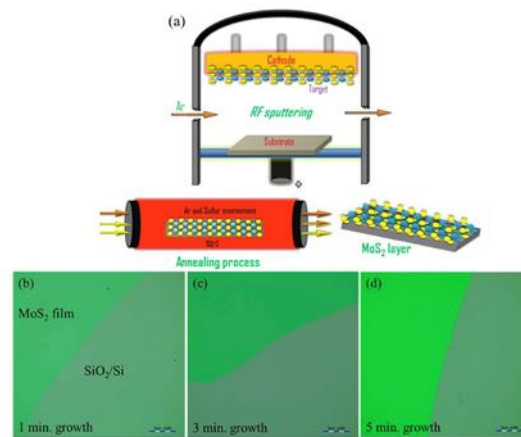


Figure 1. (a) schematic representation of the experimental set-up of MoS₂. The RF sputtering technique was used to prepare sputtered MoS₂ layer. To enhance crystalline quality post deposition annealing treatment was performed as sputtered MoS₂ under Ar and sulphur environment. Optical images of MoS₂ films has been grown on SiO₂/Si Substrate **b)** MoS₂ Sputtered for 1 min **c)** MoS₂ sputtered for 3 min **d)** MoS₂ spuetered for 5 min.

Results and discussions

Fig. 2 shows the XRD patterns of MoS₂ films grown on sapphire and SiO₂/Si substrates. The MoS₂ film grown on a sapphire substrate showed three sharp diffraction peaks at 14.39 deg, 32.81 deg, and 58.78 deg corresponding to (002), (100), and (110) planes of MoS₂, respectively. The films fabricated on SiO₂/Si substrates showed two diffraction peaks at 32.81 deg and 58.45 deg corresponding to (100) and (110) planes of MoS₂, respectively (JPDS Card 37-1492). In addition, two more peaks were observed at

41.70 deg and 69.16 deg which correspond to the reflection from (113) and (400) planes of sapphire and SiO₂/Si substrates, respectively. Some XRD parameters and calculated lattice constants of MoS₂ films were collected in Table 1.

Table 1. Structural parameters calculated from XRD

	hkl	2θ (°)	FWHM (°)	a (Å)	c (Å)	Grain size (nm)
Sapphire	002	14.39	0.68	-	12.30	20.42
	100	32.81	0.37	3.15	-	39.08
SiO ₂ /Si	100	32.81	0.19	3.15	-	74.62
	110	58.45	0.38	3.26	-	40.86

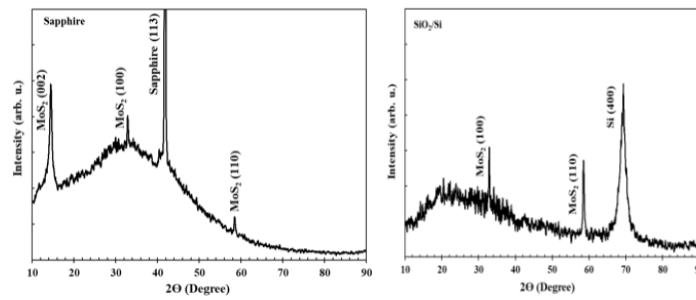


Figure 2. XRD results of MoS₂ grown on Sapphire and Silicon substrate

Raman spectra of the MoS₂ thin films for these substrates have been exhibited in the figure which shows the characteristics E_{2g}, E_{2g}¹ and A_{1g} Raman modes of MoS₂ hexagonal phase at around 288 cm⁻¹, 383 cm⁻¹ and 409 cm⁻¹, respectively. In addition, two peaks located at around 453 cm⁻¹ and 466 cm⁻¹ were attributed to 2LA (M) and A_{2u} modes.¹⁰

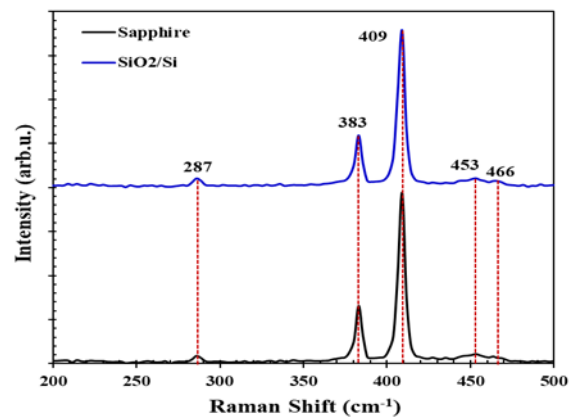


Figure 3. Raman Spectra of MoS₂ grown on Sapphire and Silicon

Table 2.

Raman Modes (cm ⁻¹) for MoS ₂ hexagonal phase							
	E _{2g}	E _{12g}	A _{1g}	2LA (M)	A _{2u}	$\Delta w =$ $w(A_{1g}) -$ $w(E_{12g})$	Ref.
Our samples	287	383	409	453	466	26	-
Bulk-MoS ₂	-	382	407	465	-	25	Frey GL et al., Pys. Rew. 1993
Platelet-MoS ₂	-	381	408	455	-	27	Frey GL et al., Pys. Rew. 1993
1 layer-MoS ₂	-	384.3	403	-	-	18.7	Li H. et al. Adv. Func. Mat. 2012

The surface topography of the films was investigated by AFM analysis. Fig shows 2D AFM and corresponding 2D grain boundaries images of the MoS₂ films. AFM measurements depict the high RMS roughness values of 27.04 nm and 19.02 nm for the films grown on sapphire and SiO₂/Si substrates respectively. The film grown on the SiO₂/Si substrate has less amount of grain boundaries with a larger grain size compared to the film grown on sapphire.

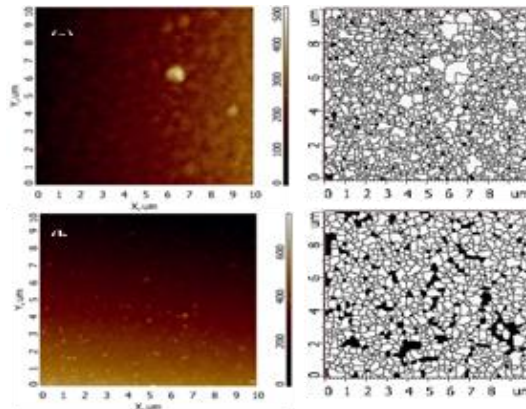


Figure 4. AFM images and 2D grain boundary images (10×10 μm²) of MoS₂ films grown on sapphire (a) and SiO₂/Si (b) substrates.

AFM measurements exhibited high RMS roughness values of 27.03 nm and 19.02 nm for the films grown on sapphire and SiO₂/Si substrates, respectively.

Conclusions and future work

MoS₂ films were grown by sulfurization of the precursor films at 900 °C in a two-zone CVD furnace. The results from XRD and Raman spectroscopy analysis depicted that the polycrystalline MoS₂ films were successfully grown on both substrates. They got nonstoichiometric as compared to MoS_{1.75} and MoS_{1.80}, respectively. The RMS roughness of the films on sapphire and SiO₂/Si substrates was found to be 27.04 nm and 19.03 nm, respectively. SEM results show the MoS₂ films have a uniform surface morphology and it has a packed columnar structure having no voids. The value of E_g of the film material on the sapphire substrate was calculated to be 1.58 eV by using a UV-Vis transmittance spectra graph. Experimentally both the films grown on sapphire and SiO₂/Si substrates resulted the *p*-type conductivity with hole mobility of 150 cm²/V·s and 1.24 cm²/V·s, respectively. Fabricated MoS₂ diodes have a good response under illumination. The resistivity of MoS₂ films was decreased under exposure to the gas. These results demonstrated that the fabricated films could be used in electro-optical devices as active materials.

References

- [1] Kuzmenko, I. Crassee, D. Van Der Marel, P. Blake and K. Novoselov, Phys. Rev. B: Condens. Matter Mater. Phys., 2009, 80, 165406
- [2] W. Xia, L. Dai, P. Yu, X. Tong, W. Song, G. Zhang and Z. Wang, Nanoscale, 2017, 9, 4324–4365.
- [3] S. Das, J. A. Robinson, M. Dubey, H. Terrones and M. Terrones, Annu. Rev. Mater. Res., 2015, 45, 1–27.
- [4] T. J. Wieting and M. Schlüter, Electrons and phonons in layered crystal structures, Springer Science & Business Media, 2012
- [5] F. Wypych and R. Schöllhorn, J. Chem. Soc., Chem. Commun., 1992, 1386–1388.
- [6] S. J. Sandoval, D. Yang, R. Frindt and J. Irwin, Phys. Rev. B: Condens. Matter Mater. Phys., 1991, 44, 3955.
- [7] Seravalli, L., & Bosi, M. (2021). A review on chemical vapour deposition of two-dimensional MoS₂ flakes. Materials, 14(24), 7590.
- [8] Lin, Y., Ling, X., Yu, L., Huang, S., Hsu, A. L., Lee, Y. H., ... & Palacios, T. (2014). Dielectric screening of excitons and trions in single-layer MoS₂. Nano letters, 14(10), 5569-5576.
- [9] R. Ganatra, Q. Zhang, ACS Nano 8, 4074 (2014).
- [10] Zhang, X., Han, W. P., Wu, J. B., Milana, S., Lu, Y., Li, Q. Q., ... & Tan, P. H. (2013). Raman spectroscopy of shear and layer breathing modes in multilayer MoS₂. Physical Review B, 87(11), 115413.

Funding

This work has received funding from, the European Union's Horizon 2020 research and innovation program under the Marie Skłodowska-Curie grant agreement No 101034425 for the project titled A2M2TECH. This study has also received funding from The Scientific and Technological Research Council of Türkiye (TUBITAK) with the grant No 120C158 for the same A2M2TECH project under the TUBITAK's 2236/B program.

Defect Analysis of Additively Manufactured AlSi10Mg Samples Using Different Process Parameters in a Single Specimen

Mussadiq Shah^{1,2}, Mutteb Butt^{1,3}, Nizami Akturk^{1,2}, Celal Sami Taufekci⁴, Metin U. Salamci^{1,2}

1. Additive Manufacturing Technologies Application and Research Center, Ankara, Türkiye
2. Department of Mechanical Engineering, Faculty of Engineering, Gazi University, Ankara, Türkiye.
3. Istanbul Technical University, Istanbul, Türkiye
4. Advanced Manufacturing Technologies Center of Excellence-URTEMM, Ankara, Türkiye

Abstract

Additive Manufacturing (AM) has emerged as a transformative technology in the realm of modern manufacturing. Its ability to fabricate complex structures and customize components has revolutionized various industries, including aerospace, automotive, and healthcare. However, the realization of the full potential of AM hinges on our ability to optimize the process parameters that govern its outcomes. This comprehensive research study embarks on a journey to explore the intricate relationship between layer-wise process parameters, porosity, microstructure, and mechanical properties in AM.

The primary goal of this study is to shed light on how variations in process parameters during the AM can significantly influence the quality, integrity, and performance of the final parts. We delve into the effects of specific parameters such as laser power, scan speed, and layer thickness on the resulting porosity, microstructure, and mechanical characteristics. Through an array of meticulously designed experiments and advanced characterization techniques, we seek to provide a nuanced understanding of these phenomena and establish a foundation for the optimization of AM processes. While this initial phase of our study has provided valuable insights into the defect profiles within the specimen using different process parameters, our research is far from complete. Moving forward, the focus will shift towards further characterizations and in-depth analyses.

Keywords: additive manufacturing, vibration analysis, process parameters, optimization.

Introduction

Additive Manufacturing (AM), often colloquially referred to as 3D printing, has emerged as a transformative and disruptive technology in the landscape of modern manufacturing [1]. Unlike traditional subtractive manufacturing methods that rely on the removal of material to achieve the desired shape, AM is a groundbreaking additive process. It builds intricate and complex structures layer by layer, offering unparalleled design freedom and customization capabilities [2]. This inherent flexibility, along with reduced material waste and accelerated production cycles, has propelled AM into the forefront of various industries, including aerospace, automotive, healthcare, and beyond.

In this era of innovation and technological advancement, AM has assumed a pivotal role in reshaping the way products are conceived, designed, and fabricated [3][4]. Its applications span from rapid prototyping and tooling to the production of highly specialized components with intricate geometries that would be challenging, if not impossible, to achieve through conventional manufacturing techniques.

AM has not only opened the door to new horizons in product development but has also introduced unprecedented opportunities for supply chain optimization, inventory management, and cost-effective production, further solidifying its position as a game-changer in the manufacturing landscape [5].

Central to the realization of the full potential of AM is the critical role played by the myriad of process parameters that govern the intricacies of the printing process. These parameters, which include laser power, scan speed, layer thickness, powder feed rate, and many others, are not merely variables; they are the conduits through which creativity is materialized into reality. They are the dials and levers that orchestrate the precise deposition and fusion of materials, thus dictating the ultimate form, quality, and functionality of the printed objects. However, the elegance and complexity of AM are juxtaposed with the challenges of process optimization [6]. For every degree of design freedom that AM offers, it demands an equivalent degree of expertise in process control and parameter optimization [7]. The successful implementation of AM requires a nuanced understanding of how these parameters interact, and how even subtle adjustments can lead to profound variations in the final product.

Few studies are available in the literature which have used similar ideas and correlate process parameter effect on porosity, microstructure, and mechanical properties. In a study by Wang et al., the authors studied the effect of process parameter (laser power, scanning speed) on porosity, microstructure, and mechanical properties [6]. The combination of parameters varied from bottom to top of the bar, with each combination repeating every eight layers. The hatch distance and layer thickness were set as constants at 100 μm and 20 μm , respectively. The process parameters varied cyclically, where the laser power (P) increased stepwise from 100 W to 210 W in twelve levels, and the scanning speed (v) fluctuated between 500 mm/s and 2000 mm/s in sixteen levels. In terms of porosity, the pore distribution varied along the z-axis, with six pore zones corresponding to the six low energy-input sets

Overall, with the increase of scanning speed or the decrease of laser power, the porosity fractions increase. In the porous zones, the melt pools are flat, thin, narrow and irregular, and their stacking is in disorder. In the middle, the melt pools are bigger, of regular bowl shape, and stacked in good order. The highly organized stack of melt pools from layer-to-layer exhibited stripes along the building direction. When the laser power is higher than 140 W and the scanning speed was slower than 1200 mm/s, it is the best zone with almost no porosity.

In another study by Xiang et al., varying scanning speed in the range of 500 mm/s to 1900 mm/s, and laser power in the range of 100 W to 200 W, were used from layer to layer in a cycle of 56 layers in a single. Similarly, high energy density led to sound regions with larger, orderly stacked melt pools and columnar grains. [8] While low energy density resulted in porous regions with smaller, mismatched melt pools, un-melted powder, and equiaxed grains with finer dendrites.

As such, the central objective of this comprehensive research study is to delve deep into this intricate and multifaceted relationship between layer-wise process parameters, porosity, microstructure, and mechanical properties in AM. It seeks to unravel the mysteries hidden within the layers of printed material, deciphering how variations in process parameters yield distinct outcomes. By doing so, we aim to not only advance the theoretical foundations of AM but also provide concrete insights that can be applied practically to optimize AM processes for a wide range of industrial applications.

The significance of this study extends beyond the confines of academia. It has direct implications for industries striving to harness the full potential of AM while maintaining rigorous standards of quality

and reliability. The knowledge gained here is poised to empower engineers, designers, and manufacturers to make informed decisions about process parameter selection, enabling them to unlock new possibilities in product development, and ultimately contributing to the continued evolution of additive manufacturing as a transformative force in modern industry.

Materials and methods

In the initial phase of this study, 10 tensile specimens and small cube samples were produced from AlSi10Mg powders using EOS Concept laser SLM machine. Random process parameters were selected for a single specimen as shown below in Table and Figure 1. These samples were manufactured under varying layer-wise process parameters to investigate the impact on the final part quality. Micro CT scans were conducted on one sample using ZEISS XRadia 510 Versa system. To examine internal porosity, revealing unexpected results. To further understand the phenomena, additional experiments and analyses will be carried out, including:

X-Ray Diffraction (XRD): XRD will be employed to investigate the crystalline structure and phase composition of the AM materials.

Electron Backscatter Diffraction (EBSD): EBSD will be used to characterize the microstructure and crystallography of the AM components, providing insights into grain boundaries and orientation.

Micro CT Scans: Micro CT scans will be performed on the remaining samples to assess porosity, void distribution, and defects in detail.

Fatigue and Vibration Testing: Fatigue tests will be conducted to evaluate the endurance of AM parts under cyclic loading conditions.

Tensile and Compression Testing: Mechanical properties, such as tensile strength and compressive strength, will be measured to understand the impact of process parameters on structural integrity.

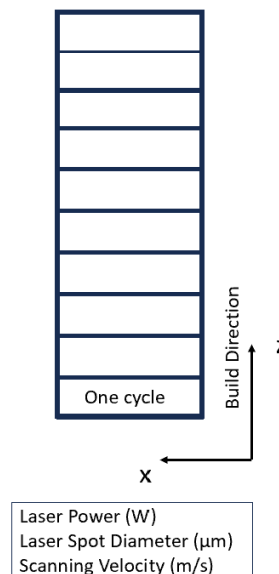


Figure 1. Graphical overview of 10 different process parameters in a single specimen

Table 1: Process parameters used in the study and their corresponding volume defects

No.	Laser Power (W)	Spot Dia (um)	Scanning velocity (m/s)	Max defect Volume (mm ³)
1	75	140	0.6	0.1354
2	225	140	1.4	0.0073
3	275	140	0.6	0.0815
4	350	140	1.1	0.0013
5	400	140	0.8	6.8117
6	110	150	0.8	0.0021
7	110	120	1.1	-
8	110	100	0.6	0.0255
9	110	75	1.1	0.0075
10	110	50	1.4	0.0056

Random Process Parameter Sequences:

1. 3, 4, 5, 10, 8, 1, 2, 6, 9, 7
2. 4, 5, 1, 8, 9, 6, 7, 2, 3, 10
3. 4, 5, 7, 6, 9, 10, 8, 1, 2, 3
4. 5, 7, 8, 10, 6, 1, 2, 3, 4, 9
5. 7, 8, 9, 3, 4, 1, 2, 6, 5, 10
6. 10, 1, 3, 6, 9, 2, 4, 5, 7, 8
7. 9, 3, 6, 7, 2, 4, 10, 1, 8, 5
8. 3, 5, 1, 2, 4, 6, 10, 8, 9, 7
9. 9, 1, 2, 3, 4, 5, 7, 8, 6, 10
10. 7, 2, 10, 4, 5, 1, 8, 9, 6, 3

Figure 2. Random process parameter selection for the study.

Results and discussions

We have performed XCT of each individual layer to study the effect of using different process parameters in each layer. In our ongoing research, we have undertaken an extensive examination of the impact of varying process parameters within each individual layer of our components using XCT. Just for now, only one sample has been examined and the rest will be done in due time. This analysis has allowed us to gain valuable insights into the presence, characteristics, and distribution of defects within each layer, as well as at the interfaces between them.

One of the key findings from our investigation is highlighted in the table provided, which illustrates the maximum defect volume detected in each layer. This data serves as a crucial reference point for assessing the quality and integrity of our layered components under different manufacturing conditions. By quantifying the defect diameter, volume, and density in each layer and at the interfaces and the corresponding energy density, a comprehensive understanding of how process parameters impact the structural properties of our components.

While this initial phase of our study has provided valuable insights into the defect profiles within our components, our research is far from complete. Moving forward, the focus will shift towards further characterizations and in-depth analyses. Specifically, it is aimed to establish correlations between the

observed defects and the mechanical response of these components. This future work will not only enhance our understanding of the relationship between process parameters, microstructure and component quality but also contribute to the development of optimized manufacturing processes and materials.

Conclusions and future work

This research study provides a comprehensive understanding of the impact of layer-wise process parameters on AM-produced parts. We anticipate several key findings based on preliminary data and existing literature:

A direct correlation between specific process parameter variations and the presence of porosity within the AM parts is expected to be observed. Microstructural analysis is likely to reveal variations in grain structure, crystallography, and defect density.

Variations in process parameters are expected to significantly affect the mechanical properties, fatigue and vibration performance of AM parts, including tensile strength, compressive strength, and fatigue resistance. We anticipate that certain parameter combinations will lead to improved mechanical performance, while others may result in reduced strength and durability.

Through a comprehensive analysis of the data, we aim to provide insights into the optimization of AM processes for specific applications. By identifying parameter sets that yield desired porosity levels, microstructures, and mechanical properties, we aim to contribute to the development of tailored AM processes for various industrial needs.

In conclusion, this study will act as a starting point for finding intricate relationships between layer-wise process parameters, porosity, microstructure, and mechanical properties in AM in a single specimen.

After the first batch of experiments, we can then print any mechanical metamaterial-based lattice structure on the optimized set of parameters obtained.

Also, using the same random parameters to study the effect of each set of parameters on metamaterial behavior (mechanical, fatigue etc.). We can then correlate the temperature profile with porosity and microstructure and understand the relation between them and can design the process for specific application requirements.

References

- [1] M. Shah, A. Ullah, K. Azher, A.U. Rehman, W. Juan, N. Aktürk, C.S. Tüfekci, M.U. Salamci, RSC Adv. 2023, 13, 1456.
- [2] P.M. Gopal, V. Kavimani, K. Gupta, D. Marinkovic, Micromachines (Basel) 2023, 14.
- [3] W.E. Frazier, J Mater Eng Perform 2014, 23, 1917.
- [4] Q. Han, R. Setchi, F. Lacan, D. Gu, S.L. Evans, Materials Science and Engineering: A 2017, 698, 162.
- [5] R.F. Vaz, A. Garfias, V. Albaladejo, J. Sanchez, I.G. Cano, Coatings 2023, 13.

- [6] X. Wang, J. Wang, J. Kang, T. Wang, P. Wu, T. Feng, L. Zheng, Y. Rong, *Mater Today Commun* 2021, 27, 102303.
- [7] J. Jue, D. Gu, K. Chang, D. Dai, *Powder Technol* 2017, 310, 80.
- [8] X. Wang, J. Kang, T. Wang, P. Wu, T. Feng, L. Zheng, *Materials* 2019, 12.

Funding

This work has received funding from, the European Union's Horizon 2020 research and innovation program under the Marie Skłodowska-Curie grant agreement No 101034425 for the project titled A2M2TECH. This study has also received funding from The Scientific and Technological Research Council of Türkiye (TUBITAK) with the grant No 120C158 for the same A2M2TECH project under the TUBITAK's 2236/B program

Corrosion Behavior in SLM-Produced AlSi10Mg Alloy: Evaluating Process Parameters Effect

Hossein Laieghi^{1,2,*}, Fahrettin ozturk^{3,4}, Hakan Yavas⁴, Burcu Arslan Hamat⁴, Peyman Ansari^{1,2}, Metin U Salamci^{1,2}, Elmas Salamci^{1,2}

1 Department of Mechanical Engineering, Gazi University, Ankara 06570, Türkiye

2 Additive Manufacturing Technologies Research and Application Center-EKTAM, Gazi University, Ankara 06560, Türkiye

3 Department of Mechanical Engineering, Ankara Yıldırım Beyazıt University, Ankara, Türkiye

4 Turkish Aerospace Industries, Inc., Ankara, Türkiye

Abstract

Al-Si alloys find extensive use in numerous applications due to their exceptional castability, corrosion resistance, and mechanical properties. The presence of large silicon particles limits the corrosion resistance of these alloys. Additive Manufacturing (AM) methods offer a promising solution to tackle these challenges. While there has been substantial research on the mechanical properties of samples produced through additive manufacturing (AM), the aspect of corrosion resistance has received comparatively less attention. This research aims to evaluate the impact of variations in the selective laser melting (SLM) process parameters on the microstructure of the SLM-AlSi10Mg alloy and, consequently, its electrochemical stability. Three sets of SLM-AlSi10Mg specimens were produced, each employing distinct combinations of SLM process parameters. The printed components demonstrated a reduction in surface roughness and porosity defects attributed to the optimized process parameter adjustments. The sample with the fastest cooling rate during solidification exhibited superior corrosion resistance and excellent stability of the passive film in a 3.5 wt. % NaCl electrolyte, which can be related to the finer Al-Si eutectic structure.

Keywords: Additive manufacturing, AlSi10Mg, Corrosion, powder bed fusion, microstructure

Introduction

Aluminum (Al) alloys containing silicon (Si) are widely employed due to their exceptional casting properties, minimal shrinkage, and relatively low melting point. Among these Si-containing alloys, AlSi10Mg stands out and finds extensive applications across various industries, including automotive, aerospace, and residential sectors. This popularity can be attributed to the alloy's advantageous characteristics, including its high specific strength, impressive mechanical properties (such as castability, weldability, hardenability, and corrosion resistance), and exceptional heat conductivity. The microstructure of the AlSi10Mg alloy, a multiphase material, comprises several key elements, including the α -Al phase, eutectic Si particles, and secondary phases like Mg₂Si, commonly known as the β -phase [1]. Because of its nearly eutectic composition, this alloy has a lower melting point (ranging from 555-600°C) than pure aluminum (660°C), enabling rapid solidification of all its constituent phases. Previous research indicates that achieving fast solidification with a cooling rate of up to 106 °C/s is a viable strategy for refining microstructure and achieving a uniform distribution of eutectic Si particles [2].

Nevertheless, the widespread utilization of Al-Si-Mg alloys has been hindered in more challenging conditions due to the time-consuming fabrication processes and the resulting microstructure of the alloy in its original state. These conventional manufacturing techniques, including casting, forging, and powder metallurgy, have imposed significant limitations on the rapid implementation of such alloys.

In recent decades, an increasing focus has been on engineering components characterized by complex designs and enhanced mechanical and electrochemical properties. These components are specifically designed to withstand extreme environmental conditions. Consequently, developing and using novel manufacturing processes have become imperative to meet these demands. Metal-based additive manufacturing is an emerging and dynamic fabrication technology that addresses the current limitations and shortcomings in design and manufacturing. It provides a flexible approach to creating complex components with enhanced performance and capabilities. Selective laser melting (SLM) is an additive manufacturing technique with notable benefits, including cost-effective production, the ability to fabricate intricate geometries with little material wastage, and reduced time to market when compared to conventional manufacturing methods. While SLM technology offers significant benefits to the manufacturing industry, it is essential to recognize that it is not a flawless fabrication method, much like other production processes. Specifically, when using this method with the AlSi10Mg alloy, various defects can manifest due to high laser power, rapid scanning rates, and challenges during the solidification process, such as balling defects. These imperfections commonly result in inconsistent microstructures, a notable presence of porosity, defects in the solidification microstructure, residual stresses within the printed component, and surface roughness after printing. The presence of defects stemming from the manufacturing process can adversely impact both the corrosion performance and mechanical properties of the printed components. To address these imperfections and improve the corrosion and mechanical properties of the components, various techniques have been employed. These methods encompass post-heat treatments, the utilization of different feedstock metal powder sizes, adjustments to SLM process parameters, and the implementation of post-printing surface treatments. Zakay et al. [3] found that heat treatment positively impacted the stress corrosion endurance of AlSi10Mg samples produced using SLM in Harrison solution. Slow strain rate testing revealed that specimens subjected to heat treatment at temperatures ranging from 200°C to 300°C exhibited a longer fatigue life than others. This enhancement in the mechanical properties can be attributed to the reduction of residual stress and the formation of a fine Si network within the α -Al matrix, which are outcomes of the rapid solidification process employed in SLM.

Table 1: Chemical composition of AlSi10Mg powder

Element	Al	C	Cu	Fe	Mg	Mn	Ni	O	Pb	Si	Sn	Ti	Zn
%	Bal.	< 0.005	< 0.03	0.13	0.38	< 0.03	< 0.03	0.114	< 0.03	10.3	< 0.03	< 0.03	< 0.03

Modifying various SLM processing parameters, including laser power, hatching distance, and scanning speed can significantly affect the density of internal defects, surface roughness, microstructure, and, in turn, the corrosion behavior of the resulting SLMed-AlSi10Mg components. Rafieazad et al. [4] systematically adjusted the printing process parameters while keeping surface roughness constant to investigate the impact of microstructural changes on the corrosion behavior of the L-PBF-AlSi10Mg alloy. Additionally, they delved into the effect of dissolved oxygen in a naturally aerated 3.5 wt.% NaCl solution on the corrosion of the L-PBF AlSi10Mg alloy. The findings indicated that samples with the fastest cooling rates during solidification exhibited a finer eutectic Si phase with more uniform granules.

Remarkably, the sample with the quickest cooling rate during solidification demonstrated the highest corrosion resistance among all the samples produced.

The objective of this work is to examine the impact of adjusting the SLM process parameters on the corrosion characteristics of the SLM- AlSi10Mg alloy. Electrochemical measurements were used to investigate the corrosion behavior of the AlSi10Mg alloy in a 3.5 wt% sodium chloride (NaCl) solution.

Materials and Methods

Material and Manufacturing Process:

The AlSi10Mg samples were fabricated using a Concept Laser- M2 CUSING type 3-D printer equipped with a 400-watt laser, powered by a continuous wave Ipg Ylr 400 ac y14 ytterbium fiber laser emitting at a wavelength of 1070 nanometers. The printer's build chamber is maintained within a controlled nitrogen environment, guaranteeing that the oxygen concentration does not surpass 0.4%.

Gas-atomized powders of the AlSi10Mg alloy, manufactured by Concept Laser, were employed in the manufacturing process. The composition of the AlSi10Mg alloy powder used in this study is provided in Table 1.

Samples of SLM- AlSi10Mg were divided into three groups, as detailed in Table 2, to investigate the impact of altering the fabrication process parameters on the corrosion characteristics of the samples. To minimize the influence of surface roughness, all specimens were subjected to grinding with abrasive paper of 4000 grit, followed by polishing with colloidal alumina particles measuring 0.3 μm in size. Additionally, before the commencement of the electrochemical experiments, all specimens underwent a degreasing process using acetone.

Table 2: SLM process parameters

No.	Laser Power (W)	Laser Spot Diameter (μm)	Scanning speed (m/s)
S1	400	140	0.6
S2	100	140	0.8
S3	140	100	1.1

Electrochemical measurements

Corrosion assessments were conducted on the smooth, finished surfaces of the SLM-fabricated samples. This was achieved using a three-electrode cell configuration with an IVIUM CompactStat Potentiostat in accordance with the ASTM G5 standard for anodic polarization measurements. In this experiment, a platinum rod served as the counter electrode (CE), while a saturated silver/silver chloride (Ag/AgCl) electrode acted as the reference electrode (RE). The specimens were positioned within an epoxy sample container, where a surface area of 0.196 cm^2 was exposed and utilized as the working electrode. All electrochemical experiments were carried out in a 3.5 wt% NaCl solution at a temperature of 25°C. To ensure stability, open circuit potentials (OCP) were monitored for an hour before initiating the corrosion tests. The OCP was employed for all anodic curve measurements, and a scanning rate of 0.125 mV/s was utilized. To ensure the repeatability of the results, all electrochemical measurements in this study were carried out multiple times, exceeding three repetitions.

Results and Discussion

The main objective of this research is to evaluate the influence of three distinct sets of process factors on corrosion behavior. It is well-recognized that surface roughness directly affects both corrosion behavior and mechanical properties. In their study, Leon et al. [5] presented evidence supporting the idea that the increased surface roughness observed in "as-built" samples reduced low-cycle corrosion fatigue compared to bulk samples. Furthermore, elevated surface roughness has been shown to promote pitting corrosion, a common form of corrosive attack in aluminum alloys produced through both forging and additive manufacturing [6].

However, an alternate perspective suggests that "as-built" specimens may initially exhibit higher corrosion distance compared to "bulk" conditions, possibly due to a thicker protective passive coating. Nevertheless, during an immersion period, the behavior of the "bulk" condition specimens undergo a complete transformation, displaying increased resistance compared to their initial state [7]. Therefore, utilizing "as-built" samples as the end-use for the alloy is not the most optimal choice. As a result, the samples underwent a polishing process in the current investigation.

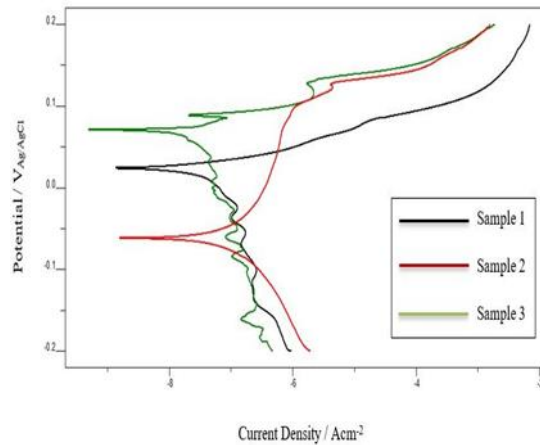


Figure 1: Representative polarisation curves for different sets of manufacturing parameters

Figure 1 illustrates the potentiodynamic polarization curves employed for validating the electrochemical processes for the samples immersed in a 3.5 wt% NaCl solution at ambient temperature. The results indicate that the corrosion behavior of all samples is similar. The interplay between the anodic and cathodic reactions determines the corrosion rate. Calculating the corrosion current densities involves integrating the anodic and cathodic branches of the potentiodynamic polarization curves. The current consensus in the field acknowledges that samples with lower corrosion current densities generally demonstrate better corrosion resistance and a reduced corrosion rate [8]. Consequently, it's apparent that the sample with the fast-cooling rate during solidification exhibited good corrosion resistance and stability of the passive film.

A conclusive resolution to this matter remains elusive. The existence of the passive range has been reported in various scholarly publications, and it has been attributed to alterations in the microstructure of dendrites, including changes in their shape and size distribution. These modifications ultimately impact the Si network [9]. In the current context, it appears to be linked to the refinement of the grain structure resulting from the optimization of process parameters and significant differences in porosity elimination that have been observed across various parameter configurations (see Figure 2). This

highlights the necessity of further research on the corrosion of materials produced using additive manufacturing, taking into account all the factors that influence the fabrication of components, both in terms of pre-processing and post-processing procedures.

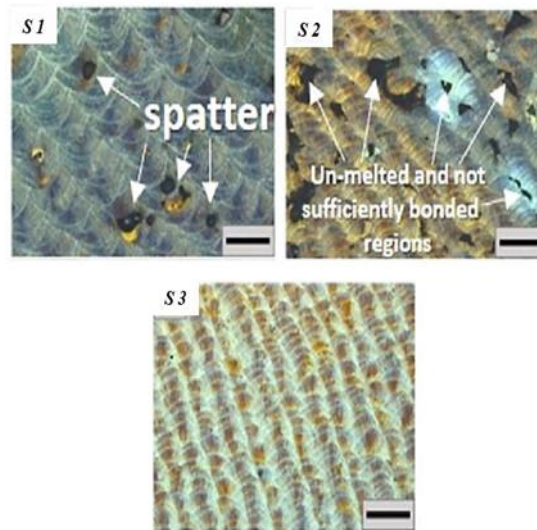


Figure 2: Optical micrographs of manufactured samples [10]. (Scale bar: 200(μ m))

Conclusions

This study delves into the influence of selective laser melting (SLM) process parameters on the microstructure and corrosion characteristics of AlSi10Mg components produced via SLM in a 3.5 wt. % sodium chloride (NaCl) solution.

The presence of residual porosity holds a critical role in ensuring the optimal performance of these components throughout their operational lifespan. It is evident that the processing conditions applied are effective in reducing porosity, resulting in a noteworthy reduction in the corrosion rate.

Specimen fabricated with the lowest volumetric energy density, leading to the formation of detrimental defects like pores and unbonded regions, displayed a notably low E_{corr} . The observed decrease in the E_{corr} value of the optimally processed sample, which underwent a higher cooling/solidification rate, can be linked to the diminished driving force for galvanic corrosion between the aluminum (Al) and silicon (Si) phases. This decrease is attributed to the production of a finer Al-Si eutectic structure.

Conflict of Interest

The authors declare no conflict of interest.

References

- [1] N. T. Aboulkhair, I. Maskery, C. Tuck, I. Ashcroft, and N. M. Everitt, "Improving the fatigue behaviour of a selectively laser melted aluminium alloy: Influence of heat treatment and surface quality," *Materials & Design*, vol. 104, pp. 174–182, 2016.

- [2] X.-H. Gu, J.-X. Zhang, X.-L. Fan, and L.-C. Zhang, "Corrosion behavior of selective laser melted alsil0mg alloy in NaCl solution and its dependency on heat treatment," *Acta Metallurgica Sinica (English Letters)*, vol. 33, pp. 327–337, 2020.
- [3] A. Zakay and E. Aghion, "Effect of post-heat treatment on the corrosion behavior of alsil0mg alloy produced by additive manufacturing," *Jom*, vol. 71, pp. 1150–1157, 2019.
- [4] M. Rafieazad, P. Fathi, M. Mohammadi, and A. Nasiri, "Effects of laser- powder bed fusion process parameters on the microstructure and corrosion properties of alsil0mg alloy," *Journal of The Electrochemical Society*, vol. 168, no. 2, p. 021505, 2021.
- [5] A. Leon and E. Aghion, "Effect of surface roughness on corrosion fatigue performance of alsil0mg alloy produced by selective laser melting (slm)," *Materials Characterization*, vol. 131, pp. 188–194, 2017.
- [6] C. Berlanga-Labari, M. V. Biezma-Moraleda, and P. J. Rivero, "Corrosion of cast aluminum alloys: a review," *Metals*, vol. 10, no. 10, p. 1384, 2020.
- [7] R. I. Revilla, D. Verkens, T. Rubben, and I. De Graeve, "Corrosion and corrosion protection of additively manufactured aluminium alloys—a critical review," *Materials*, vol. 13, no. 21, p. 4804, 2020.
- [8] C. Brito, T. Vida, E. Freitas, N. Cheung, J. E. Spinelli, and A. Garcia, "Cellular/dendritic arrays and intermetallic phases affecting corrosion and mechanical resistances of an al–mg–si alloy," *Journal of Alloys and Compounds*, vol. 673, pp. 220–230, 2016.
- [9] P. Fathi, M. Rafieazad, X. Duan, M. Mohammadi, and A. Nasiri, "On microstructure and corrosion behaviour of alsil0mg alloy with low surface roughness fabricated by direct metal laser sintering," *Corrosion Science*, vol. 157, pp. 126–145, 2019.
- [10] P. Ansari and M. U. Salamci, "On the selective laser melting based additive manufacturing of alsil0mg: The process parameter investigation through multiphysics simulation and experimental validation," *Journal of Alloys and Compounds*, vol. 890, p. 161873, 2022.

Funding

This work has received funding from the European Union's Horizon 2020 research and innovation program under the Marie Skłodowska-Curie grant agreement No 101034425 for the project titled A2M2TECH. This study has also received funding from The Scientific and Technological Research Council of Türkiye (TUBITAK) with grant No 120C158 for the same A2M2TECH project under the TUBITAK's 2236/B program.

Effect of Heat Treatment on The Energy Absorption and Ductility of The Imperfect BCC Lattice Structures

Muhammad Arslan Bin Riaz^{1,2}, Mustafa Güden¹, Hakan Yavaş³

1.Dynamic Testing and Modelling Laboratory, İzmir Institute of Technology, Türkiye

2.Eklemeli İmalat Teknolojileri Uygulama ve Araştırma Merkezi (EKTAM)

3.Turkish Aerospace Industries, Innovation Division, Ankara, Turkey

Abstract

Additive Manufacturing enables intricate geometries without extensive post-processing. It is a layer-by-layer buildup process in which the powder is melted by a powerful electron or laser beam. Ti6Al4V is known for its higher stiffness-to-weight ratio and is used in several advanced applications. The same alloy was manufactured using the Electron Beam Melting technique and was tested under quasi-static and dynamic strain rates. Different heat treatment schemes were employed to find the desired mechanical properties for energy absorption applications. The lattice samples were then printed with the same process parameters and were heat-treated according to the above study. Results showed that annealed samples had better ductility and energy absorption than untreated ones. This increase in strength was attributed to the rise in the α/α' and $\alpha+\beta$ boundaries. A novel method was used to figure out the brittle and ductile constitutive equations of the Ti6Al4V alloy, and the experimental results were compared to the numerical ones. A good correlation was found between both. The BCC lattice structure is known for its extended plateau region and can be used in both quasi-static and dynamic conditions for protective applications.

Keywords: constitutive equation, Ti6Al4V, heat treatment, energy absorption, body-centered cubic, lattice structure

Introduction

The Powder bed fusion (PBF) process manufactures complex geometries with interconnected networks. [1] In Additive manufacturing (AM), intense interaction of a high-powered laser/electron beam occurs, melting the metallic powder particles that are solidified rapidly. This abrupt solidification results in a sub-micron microstructure enriched with higher dislocation density [2]. This structure has higher yield strength and lower ductility in most AM-produced alloys [3]. A metastable α' martensitic phase is seen in the Ti6Al4V AM-produced alloys [4, 5], resulting in the effect mentioned previously. In most cases, annealing treatment and sometimes aging are required to negate the adverse effects of the higher cooling rates [6].

Conversely, un-melted powder particles, voids and different deformities form on the surface and act as stress raisers in AM fabricated parts [7-10]. For this, the numerical results with perfect solid models show higher strength than the experiments [11, 12]. A surface treatment is usually employed to smoothen the rough surfaces of these alloys [13]. Other experimental defects, such as strut waviness, under-sizing and thickness variations, can be seen in different studies and are somehow catered to by using different processing parameters [14-16]. The constitutive equations obtained for an alloy produced at certain

processing conditions and with or without a particular heat treatment are essential since they can help visualize how the material will behave for a specific loading condition. Therefore, a designer must correctly evaluate the material flow stress and damage constants. Especially at higher strain rates, the material response changes and the flow stress, failure strain and strain rate parameters become essential to predict and model the deformation and stress distributions correctly. [17]

Since previous methods to find the constitutive equations of a material are both time-consuming and expensive, in our earlier research, we devised a novel way to get the desired material properties with less direct effort. The mechanical testing of a defective strut directly under a compressive load was found to help predict the material behaviour. [17]

This study uses the same approach to determine the ductile and brittle constitutive equations for heat-treated and untreated samples. The in-depth microstructural analysis is included to select the reason for the brittleness induced inside the as-built samples. A comparison between the α -lathe thickness for both conditions is analyzed for the Ti6Al4V Electron beam melted (EBM) alloy. After evaluating the ductile and brittle constitutive models, the heat treatments were employed in the EBM-produced Body Centered Cubic (BCC) samples to assess the increase in ductility and the energy absorption of the alloy.

Theory / Experimental Set Up

The AP&C Grade 5 powders were melted in an ARCAM EBM machine to prepare cylindrical and 5x5 BCC lattice samples. The processing parameters used to print the samples can be seen in Table 1.

Table 1: Process parameters

Beam Current	15mA
Line Offset	0.2mm
Focus Offset	25mA
Manual Speed	4530 mm/sec
Grid Voltage	60000V

The as-built cylindrical ($\varnothing 12$ mm x 75 mm) and lattice samples can be seen in Figures 1 (a) and (b), respectively. The thickness of struts and face sheets of the lattice structure was 1 mm in diameter with a 10 mm unit cell.

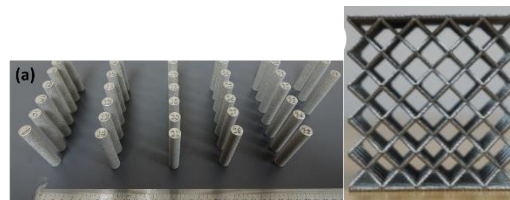


Figure 1: a) Cylindrical Samples [17] and b) BCC lattice sample

The as-built and mechanically tested lattice Ti64 specimens were microstructurally analyzed using an FEI Quanta 250 FEG SEM. A Kroll solution (3 ml HF + 6 ml HNO₃ + 100 ml H₂O) was used to etch the polished surfaces of mounted specimens. Half of the cylindrical samples were printed horizontally in the build direction to evaluate the effect of microstructure on the loading axis of the specimen. Furthermore, the cylindrical samples were used to manufacture notched samples required to evaluate damage parameters, as shown in Figure 2.

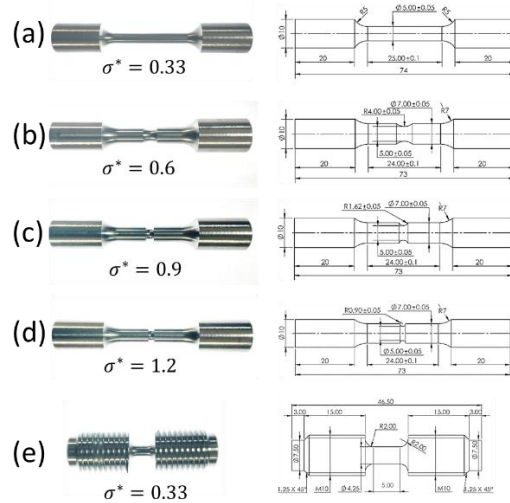


Figure 2: The standard and notched tensile test specimens used for quasi-static and high strain rate loadings with different stress triaxialities: (a) 0.33, (b) 0.6, (c) 0.9 and (d) 1.2 and (e) the SHTB test specimen with a stress triaxiality of 0.33 (Taken from [17])

Compression tests on the cylindrical samples and struts were performed according to the ASTM E9-19. The samples were compressed under a quasi-static strain rate (10^{-3} s $^{-1}$) using a SHIMADZU AG-300 kN testing machine to determine the flow stress parameters. The high strain-rate impact tests, XRD analysis and Vicker's hardness tests are yet to be performed. Furthermore, the μ CT will be used to build a solid model with imperfect strut surface and the same model will be used in the numerical simulations rather than a perfect solid model.

The heat treatment that is planned to be employed for our printed samples involves heating above β transus temperature and cooling at two different rates to compare and obtain a mix of higher Ultimate tensile strength and ductility, as can be seen in Figure 3. [18]

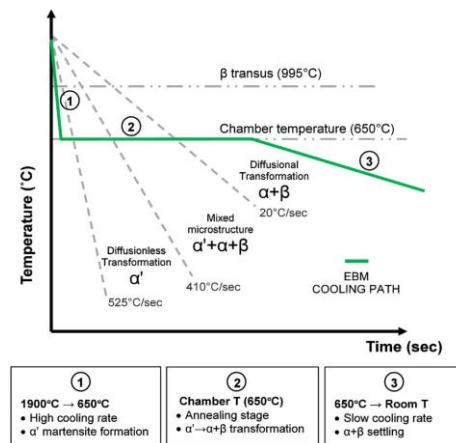


Figure 3: Cooling path and critical cooling rates for Ti-6Al-4V microstructure formation in the EBM process with a chamber temperature of 650°C [18]

Governing Equations / Numerical Model / Simulation / Methods / Use of Simulation Apps

The 5x5 lattices were compressed under a quasi-static load in the commercial software LSDYNA. The top and bottom compression platens were modeled as rigid steel elements with the following properties: $E=210\text{GPa}$, density= 7800kgm^{-3} , and Poisson's ratio=0.33. The faces, sheets, and struts were created with 8-node hexahedral brick components (Solid 164) and fully integrated S/R solids (0.35 mm). The mesh sensitivity analysis was used to choose S/R solid elements. For the hourglass, the Flanagan-Belytschko stiffness form was employed. Contact with struts was defined as SINGLE_SURFACE_CONTACT (Contact-1 in Figure 4), whereas contact with face sheets and compressive platens was defined as SURFACE_TO_SURFACE_CONTACT (Contact-2 in Figure 5). According to Figure 5, the model has three separate cell boundaries: the cell edge (where the 8-struts meet), the cell surface edge (where the 4-struts meet), and the cell surface sheet corner (4-strut connect with the face sheet). Mass scaling was applied to reduce the simulation time. The static and dynamic friction coefficients in the models were taken as 0.3 and 0.2, respectively.

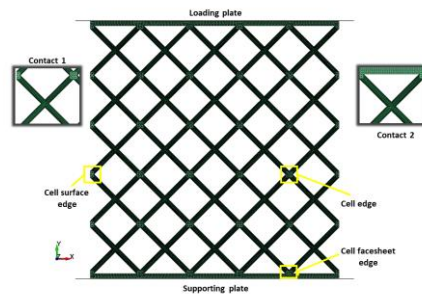


Figure 5: a) Facesheet with porosities and grinding marks b) Printed strut measurements c) Strut surface irregularities d) Facesheet surface roughness

The microstructure of Ti64 consists of needle-like α' enriched with titanium. As shown in Figure 6, the α' lathe thickness is shown in three different areas. The β -phase is also marked in Figure 6, which is in small amounts. The main reason for the formation of α' can be attributed to the rapid solidification of the alloy after melting in the build chamber.

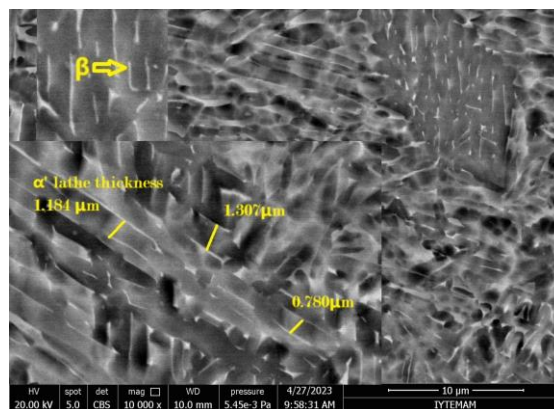


Figure 6: SEM image of the microstructure showing $\alpha+\beta$ and α' lathe thicknesses

The cross-section of the strut was also viewed to find the porosities and irregularities of the struts. The sharp valleys formed due to the unmelted powder particles act as stress concentrators. Figure 7(b) shows the voids formed due to the gas entrapment with spherical and elliptical shapes. Their sizes range from $5\mu\text{m}$ to $60\mu\text{m}$. A lack of fusion defects is also seen near the surface of the strut.

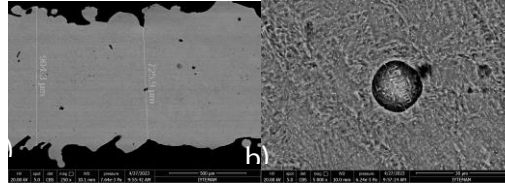


Figure 7: a) Cross-sectional view of the strut with porosities b) void formation and its size

Compression Behaviour

The lattice samples were compressed at 10-3s-1 until fracture. The initial peak stress shows the failure initiation of the cells. A sudden drop is seen in the stress values since the load is now distributed towards the other joints, such as the cell edges and cell face sheet edges. The lattice structure with 1mm strut dia and face sheet thickness failed after stress of 2.1 MPa. Until 0.5 failure strain, both lattice experiments show a good correlation. Whereas the flow stress parameters used from Table 2 from our previous study don't seem to work with this Ti64 lattice, urging a more detailed study into determining new parameters for this material.

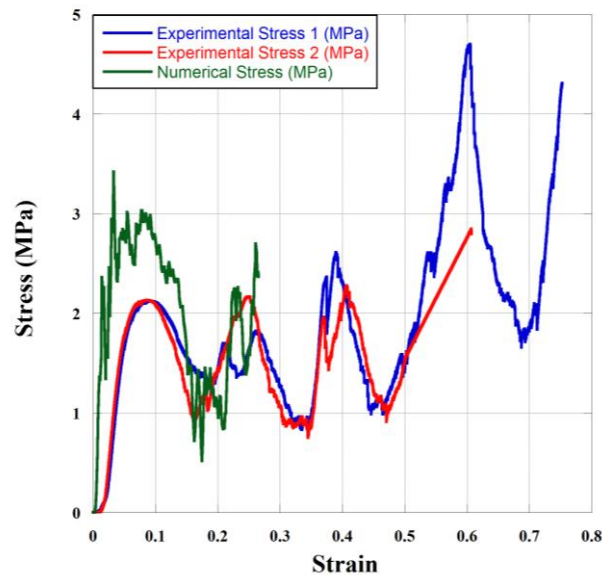







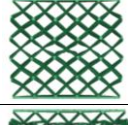

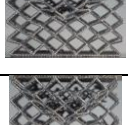


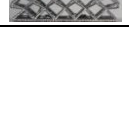

Figure 8: Quasi-static experimental and simulation results comparison

Table 2: Damage and flow stress parameters [17]

Flow stress eq	$\sigma_y(MPa)$	ϵ_{ep}
Strut Values	800 + 663 $\epsilon_{ep}^{0.49}$	D ₁ =0.1, D ₂ =0.142

Table 3 shows the comparison of the damage profile of the lattice structures as the tests proceed. Similar deformation and failure characteristics known as 45° shear failure can be seen in both lattices, where the initial buckling occurs at the bottom edges of the first unit cell followed by an inward series of collapse of the struts. Previous researchers have also studied the nature of failure for a BCC lattice. [17, 21]

Table 3: Comparison of damage profiles between Experimental and numerical results

Experiment 1	Experiment 2	Numerical
		
		
		
		

Conclusions

The microstructure of the BCC lattice shows the formation of narrow α' regions primarily due to the high cooling rate. The material in this condition seems to be brittle with higher peak stress and lower elongation to failure, which will be addressed through several heat treatment studies later. The deformation profile follows the trend from the literature, with a 45° failure being the leading cause.

References

1. Haghdadi, N., et al., Additive manufacturing of steels: a review of achievements and challenges. *Journal of Materials Science*, 2021. 56(1): p. 64-107.
2. Safdar, A., et al., Evaluation of microstructural development in electron beam melted Ti-6Al-4V. *Materials Characterization*, 2012. 65: p. 8-15.
3. Yin, Y.J., et al., Mechanism of high yield strength and yield ratio of 316 L stainless steel by additive manufacturing. *Materials Science and Engineering a-Structural Materials Properties Microstructure and Processing*, 2019. 744: p. 773-777.
4. Touri, M., et al., Additive Manufacturing of Biomaterials – The Evolution of Rapid Prototyping. *Advanced Engineering Materials*, 2019.
5. Wang, P., F. Yang, and J. Zhao, Compression Behaviors and Mechanical Properties of Modified Face-Centered Cubic Lattice Structures under Quasi-Static and High-Speed Loading. *Materials (Basel)*, 2022. 15(5).
6. Weiwei, H., et al., Research on preheating of titanium alloy powder in electron beam melting technology. *Rare Metal Materials and Engineering*, 2011. 40(12): p. 2072-2075.
7. Gong, H., et al. Defect Morphology in Ti-6Al-4V Parts Fabricated by Selective Laser Melting and Electron Beam Melting. 2013.
8. de Formanoir, C., et al., Improving the mechanical efficiency of electron beam melted titanium lattice structures by chemical etching. *Additive Manufacturing*, 2016. 11: p. 71-76.

9. Ladewig, A., et al., Influence of the shielding gas flow on the removal of process by-products in the selective laser melting process. *Additive Manufacturing*, 2016. 10: p. 1-9.
10. Grasso, M. and B.M. Colosimo, Process defects and *in situ* monitoring methods in metal powder bed fusion: a review. *Measurement Science and Technology*, 2017. 28(4): p. 044005.
11. Li, D., et al., Influence of processing parameters on AlSi10Mg lattice structure during selective laser melting: Manufacturing defects, thermal behavior and compression properties. *Optics & Laser Technology*, 2023. 161: p. 109182.
12. Li, C., et al., Crushing behavior of multi-layer metal lattice panel fabricated by selective laser melting. *International Journal of Mechanical Sciences*, 2018. 145: p. 389-399.
13. Yin, H., et al., Review on lattice structures for energy absorption properties. *Composite Structures*, 2023. 304.
14. Dallago, M., et al., On the effect of geometrical imperfections and defects on the fatigue strength of cellular lattice structures additively manufactured via Selective Laser Melting. *International Journal of Fatigue*, 2019. 124: p. 348-360.
15. Dong, G., Y. Tang, and Y.F. Zhao, A Survey of Modeling of Lattice Structures Fabricated by Additive Manufacturing. *Journal of Mechanical Design*, 2017. 139(10).
16. Mun, J., et al., Indirect additive manufacturing based casting of a periodic 3D cellular metal – Flow simulation of molten aluminum alloy. *Journal of Manufacturing Processes*, 2015. 17: p. 28-40.
17. Güden, M., et al., Investigation and validation of the flow stress equation and damage model parameters of an electron beam melted Ti6Al4V alloy with a martensitic phase. *Materials Science and Engineering: A*, 2023. 885: p. 145590.
18. Galarraga, H., et al., Effects of heat treatments on microstructure and properties of Ti-6Al-4V ELI alloy fabricated by electron beam melting (EBM). *Materials Science and Engineering: A*, 2017. 685: p. 417-428.
19. Johnson, G. and W.H. Cook. A constitutive model and data for materials subjected to large strains, high strain rates, and high temperatures in *Proc. 7th Int. Sympo. Ballistics*. 1983.
20. Johnson, G.R. and W.H. Cook, Fracture characteristics of three metals subjected to various strains, strain rates, temperatures and pressures. *Engineering fracture mechanics*, 1985. 21(1): p. 31-48.
21. Rodriguez-Nikl, T., G.A. Hegemier, and F. Seible, Blast Simulator Testing of Structures: Methodology and Validation. *Shock and Vibration*, 2011. 18(4).

Funding

This work has received funding from the European Union's Horizon 2020 research and innovation program under the Marie Skłodowska-Curie grant agreement No 101034425 for the project titled A2M2TECH. This study has also received funding from The Scientific and Technological Research

Council of Türkiye (TUBITAK) with grant No 120C158 for the same A2M2TECH project under the TUBITAK's 2236/B program.

Microstructural and Nano-mechanical Characterization of Gas Atomized IN738LC Powder

Aylin ŞAHİN KAHRAMAN¹, Müge AKDEMİR¹, Mertcan KIRAÇ², Yasemin KILIÇ¹, Deniz Sultan AYDIN¹, Hüseyin AYDIN¹

1. Materials Technologies Department, Metallic Materials Technologies Research Group, TUBITAK MRC, Kocaeli, Turkey.

2. Ermaksan, Bursa, Turkey.

Abstract

IN738LC is one of the most common superalloys in gas turbine hot-section components. In this study, IN738LC alloy powder was produced via vacuum induction melting and gas atomization method. The methodology used in this work includes an investigation of the physical, microstructural, and mechanical properties of gas-atomized IN738LC powder. To characterize and understand the powder efficiency, X-ray diffraction (XRD), optical and electron microscopy techniques, and nanoindentation (Nano-DMA) analysis were conducted. The aim of this study was to reveal the characterization of gas-atomized IN738LC powders in terms of microstructure, texture, and nano-mechanical properties.

Keywords: Additive manufacturing, nickel-base superalloys, IN738LC powder, microstructure, nanoindentation

Introduction

Over the last decade, additive manufacturing (AM) of nickel-based superalloys has been the center of attention for the aerospace industry. Selective laser melting (SLM) is one of the AM technologies that allows the fabrication of complex parts, improves components' performance, and decreases life-cycle and costs [1]. The gas atomization technique is widely used for achieving ultra-fine, spherical, and high-pack density metal powders for SLM [2-3]. There are a few studies about the influence of gas-atomized powder properties on the processability of SLM. In general, particle size distribution, flow properties, powder density, etc., have been researched before the application of AM process [4-6]. However, a few studies regarding the microstructure, texture, and nano-hardness of the gas-atomized powder have been published [7-8]. IN738LC is a typical non-weldable nickel-based superalloy that is preferred for its excellent high-temperature strength and hot corrosion resistance [9-10]. In the present study, gas-atomized IN738LC powder (produced for SLM process) was characterized. Step by step, starting from the particle size distribution, density, phase analysis (XRD), morphology and microstructure (SEM), followed by crystallographic orientation and texture (EBSD), and nano-mechanical properties (nanoindentation) of the powder were investigated. In this study, the characterization of gas atomized IN738LC powders will simply be discussed in another perspective.

Experimental Methods and Materials

Powder Production by Gas Atomization

IN738LC superalloy was cast by VIM (Vacuum Induction Melting) in TUBITAK MRC. Then, the vacuum inert gas atomization (VIGA) method was applied (in ERMAKSAN) to produce powder by using the as-cast IN738LC ingot. Process parameters of VIGA is given in Table 1.

Table 1. Process parameter of VIGA for IN738LC Powder

Parameter	Value
Molten metal temperature	1500-1600°C
Induction power	60kW
Casting pressure	20-30 bar
Ambient pressure	1 atm
Atomization gas	Argon

During the gas atomization process, molten metal was atomized and rapidly solidified; thus, IN738LC powders with spherical shape and cellular dendritic microstructure were achieved. Obtained powder particles were classified by an ultrasonic sieve system. Finally, 20 µm - 45 µm size fraction was chosen for characterization studies.

Characterization Methods

The gas-atomized IN738LC powders were characterized to identify the microstructural, chemical, physical, and mechanical features which are also believed to have significant effect on as-built materials.

Before atomization, the chemical composition of the as-cast alloy was determined by using OES (Optical Emission Spectrometry, Horiba) for primary elements and by elemental analyzers (Eltra and Horiba) for the minor elements (O, N, C, S). After atomization, particle size distribution (PSD) of the powders was conducted by using the Malvern Mastersizer-2000. X-ray diffraction (XRD) method was used for detecting the mineralogical phases present in the alloy powder using a RIGAKU SMARTLAB diffractometer with 9KW Cu-Kα radiation and operated at 40 kV and 20 mA. The scan rate was maintained at 1°/min and scan range was used from 30° - 100°.

Microstructural and morphological features of the gas-atomized powder were investigated using optical microscopy (Olympus BX53M) and electron microscopy (Hitachi SU7000, equipped with Oxford EDS and EBSD detectors) techniques. To identify morphological features of the powders, conductive carbon tape was used for SEM images. For EBSD and nanoindentation analysis, the powder was embedded in a conductive acrylic (with cold bakelite method), then mounted powder was polished with non-crystallizing colloidal silica by vibratory overnight.

To understand the mechanical properties of the powders, nanoindentation analysis was applied by Hysitron TI 980 TriboIndenter with Berkovich indenter. With this method, nano-hardness (GPa) and reduced elastic modulus (E_r) of the different areas of the microstructure can be calculated. The data obtained by nanoindentation belongs to the reduced elastic modulus, and its general formula is given below [11-12].

$$\frac{1}{E_r} = \frac{1 - \nu^2}{E} + \frac{1 - \nu_i^2}{E_i}$$

E: Elastic modulus of the sample

Ei: Elastic modulus of the indenter

Er: Reduced elastic modulus

N: Poisson ratio of the sample

vi: Poisson ratio of the indenter

Results & Discussion

The chemical composition of as-cast IN738LC is given in Table 2. The average particle size of the gas atomized powder is 33.34 μm and distribution is given in Figure 1. Physical properties of the powder were summarized in Table 3.

Table 2: Chemical composition of as-cast IN738LC

Ni %	Cr %	Co %	Mo %	W %	Ta %	Al %
Bal.	16.05	8.5	1.77	2.65	1.87	3.38
Ti %	Nb %	C %	S %	O ppm	N ppm	
3.33	0.83	0.11	0.0014	7.92	3.50	

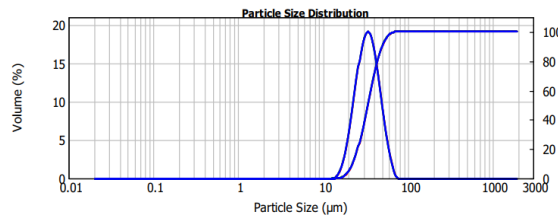


Figure 1. Particle size distribution (PSD) of gas-atomized IN738LC Powder

Table 3. Physical properties of gas atomized IN738LC Powder

d ₁₀ (μm)	d ₅₀ (μm)	d ₉₀ (μm)	Apparent density (g/cm^3)	Tapped density (g/cm^3)	Hausner ratio (-)
22.41	33.33	49.27	4.01	5.26	1.31

XRD pattern of the IN738LC alloy powder is given in Figure 2 which shows the presence of Ni-Cr ((a = 0.359 nm) phase at $2\theta=43.67$, $2\theta=50.86$, $2\theta=43.67$, $2\theta=74.77$, $2\theta=90.76$, $2\theta=96.05$ which correspond to the (111), (200), (220) and (311) planes of the single γ matrix.

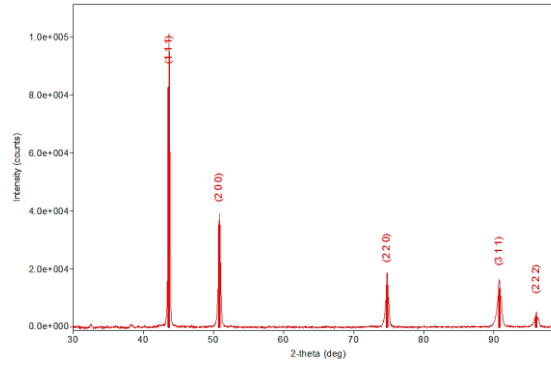


Figure 2. XRD pattern of the IN738LC alloy Powder

The general morphology of the gas-atomized IN738LC powder has a spherical shape. However, a few smaller satellite particles as well as a few irregular-shaped particles were observed attached onto the surface (Figure 3). Based on the SEM images, it was observed that the particle diameter varies from 3 μm to 44 μm .

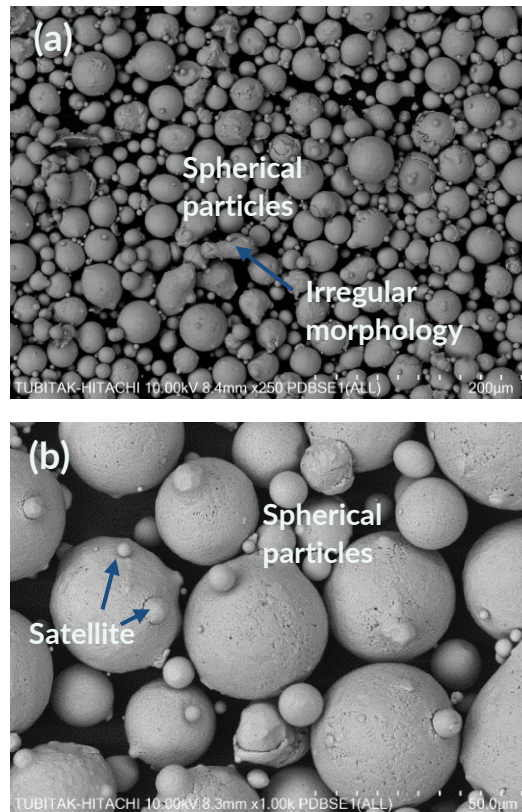


Figure 3. SEM images of gas-atomized IN738LC Powder

Dendritic microstructure of the powders formed during the solidification process of the atomization method. To understand grain orientation during solidification as well as atomized texture formation, EBSD studies were performed and pole figures (PF) of the gas atomized powders represented at respectively Figure 4 & Figure 5.

Dendritic microstructure with having randomly oriented grain boundaries were investigated with EBSD analysis (Figure 4). Moreover, columnar dendritic structure and different grains with random dendrite orientation is seen from the Figure 4-a. However, equiaxed grain distribution with random orientation was also distinguished from a few powders (Figure 4-b). This equiaxed grain boundaries can be seen from Figure 4-c. Moreover, it was noticed with EBSD analysis (Figure 4-d) that IN738LC powder composed of γ -gamma phase only as indicated by XRD phase identification.

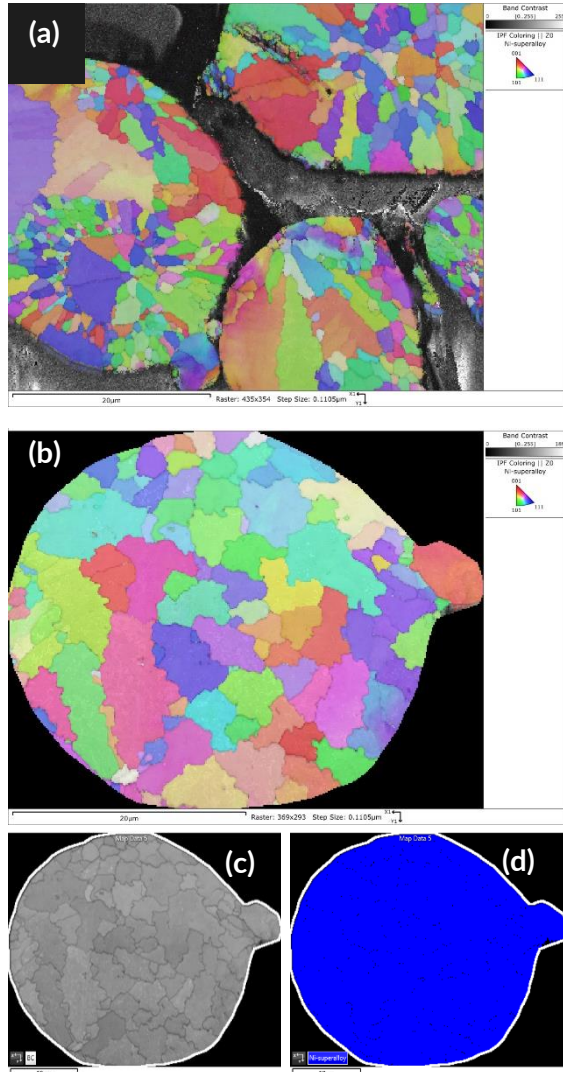


Figure 4. EBSD images of the powder (Oxford electron backscattered diffraction (EBSD) results): (a) Randomly oriented and (b) equiaxed dendritic structure with satellite particles, (c) band contrast, (d) phase color image of gas atomized IN738LC Powder

In Figure 5, pole figure (PF) map from EBSD measurements is shown that every individual powder particle has a polycrystalline structure.

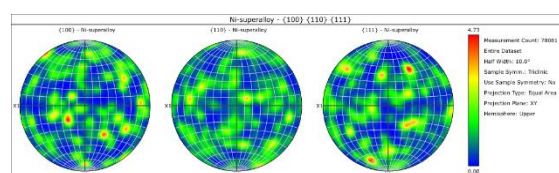


Figure 5. Pole figure results of the powder by EBSD analysis

Figure 6 and Figure 7 represent the nanoindentation scanned area ($20\mu\text{m}\times 20\mu\text{m}$) and nanoindentation curves, respectively. The nanoindentation load on the powder particle was applied at a maximum of $500\mu\text{m}$ for 3 seconds and with a loading/unloading speed of $100\mu\text{m}$. 15 different traces (with $5\mu\text{m}$ between them) were taken on this selected area.

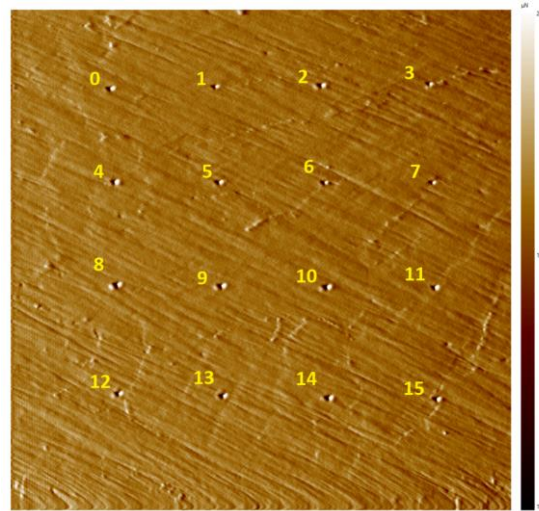


Figure 6. Nanoindentation traces on the powder particle (indent through dendrite core & dendrite arms)

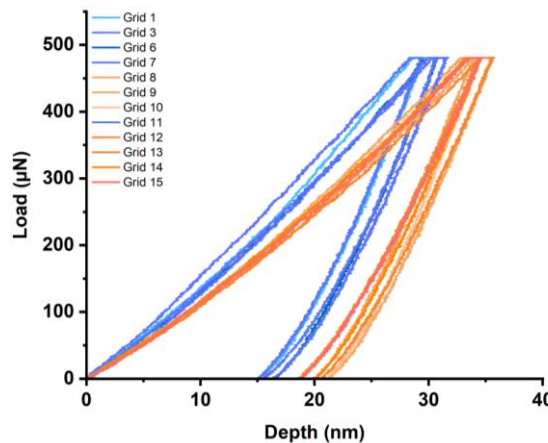
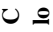


Figure 7. Nanoindentation curves of the Powder

When the results (Table 4) of these traces are compared, it was noticed that hardness and elastic modulus values are higher at the zone 1-3-6-7-11, but lower at the zone 8-9-12-13-14. It should be said that nano-hardness and reduced elastic modulus increased through the dendrite core. To correlate between microstructural features (orientation of dendrite & grains) and nano-hardness, some future studies are being carried out.

Table 4. Nanoindentation hardness and elastic modulus values of IN738LC Powder

Indents		hmax (nm)	Er (GPa)	H (GPa)
	Grid 1	29.67	216.73	13.00

	Grid 3	29.53	214.72	13.12
	Grid 6	30.88	205.64	12.34
	Grid 7	30.97	206.82	12.30
	Grid 11	31.75	190.31	12.20
	Mean	30.56	206.84	12.59
	STD	0.94	10.42	0.43
Further to dendrite core	Grid 8	35.66	178.18	10.01
	Grid 9	34.18	185.61	10.80
	Grid 12	34.55	164.78	11.12
	Grid 13	35.77	170.22	10.22
	Grid 14	34.73	176.25	10.63
	Mean	34.97	175.00	10.55
	STD	0.70	7.93	0.4.

Conclusions

In this study, IN738LC powder was produced nationally for the first time in Turkey. The as-cast ingot was produced by TUBITAK, while the powder was produced via VIGA from the as-cast ingot by ERMAKSAN. Then, microstructural, and nano-mechanical characterization of gas atomized IN738LC powder was performed:

- Spherical morphology having a few irregular and satellite particles was obtained by gas atomization manufacturing.
- EBSD analysis showed that gas atomized powders have randomly oriented dendritic microstructures with polycrystal grains.
- Nano-hardness on powder particles showed that dendrite cores have higher hardness (14.6 GPa) and higher Er (257 Ga) compared to dendrite arms.

A comparison of EBSD analysis before and after nano-indentation and XPM deviation according to different PF/IPF orientations are planned as the future studies

References

- [1] R. Engeli, T. Etter, S. Hövel, and K. Wegener, "Processability of different IN738LC powder batches by selective laser melting," J. Mater. Process. Technol., vol. 229, pp. 484–491, 2016, doi: 10.1016/j.jmatprotec.2015.09.046.
- [2] A. Mostafaei, C. Hilla, E. L. Stevens, P. Nandwana, A. M. Elliott, and M. Chmielus, "Comparison of characterization methods for differently atomized nickel-based alloy 625 powders," Powder Technol., vol. 333, pp. 180–192, 2018, doi: 10.1016/j.powtec.2018.04.014.

- [3] S. Chen, Lu, and G. Wang, “Undercooling and Microstructure of Gas Atomized Ni-based Superalloy Powders,” *Xiyou Jinshu Cailiao Yu Gongcheng/Rare Met. Mater. Eng.*, vol. 47, no. 12, pp. 3604–3609, 2018, doi: 10.1016/s1875-5372(19)30005-0.
- [4] Y. Li et al., “Microstructure, mechanical properties and strengthening mechanisms of IN738LC alloy produced by Electron Beam Selective Melting,” *Addit. Manuf.*, vol. 47, no. September, p. 102371, 2021, doi: 10.1016/j.addma.2021.102371.
- [5] Y. Li, X. Liang, G. Peng, and F. Lin, “Effect of heat treatments on the microstructure and mechanical properties of IN738LC prepared by electron beam powder bed fusion,” *J. Alloys Compd.*, vol. 918, p. 165807, 2022, doi: 10.1016/j.jallcom.2022.165807.
- [6] X. Zhang, H. Chen, L. Xu, J. Xu, X. Ren, and X. Chen, “Cracking mechanism and susceptibility of laser melting deposited Inconel 738 superalloy,” *Mater. Des.*, vol. 183, p. 108105, 2019, doi: 10.1016/j.matdes.2019.108105.
- [7] J. Xu, H. Gruber, D. Deng, R. L. Peng, and J. J. Moverare, “Short-term creep behavior of an additive manufactured non-weldable Nickel-base superalloy evaluated by slow strain rate testing,” *Acta Mater.*, vol. 179, pp. 142–157, 2019, doi: 10.1016/j.actamat.2019.08.034.
- [8] S. Bryer C, W. Caitlin E, J. Victor K Champagne, and C. Danielle L, “Initial Observation of Grain Orientation Dependent Nanoindentation Hardness of Al 6061 Gas-atomized Powder,” *Int. J. Metall. Met. Phys.*, vol. 5, no. 1, 2020, doi: 10.35840/2631-5076/9250.
- [9] O. M. D. M. Messé, R. Muñoz-Moreno, T. Illston, S. Baker, and H. J. Stone, “Metastable carbides and their impact on recrystallisation in IN738LC processed by selective laser melting,” *Addit. Manuf.*, vol. 22, no. May, pp. 394–404, 2018, doi: 10.1016/j.addma.2018.05.030.
- [10] Y. Li et al., “Microstructure, mechanical properties and strengthening mechanisms of IN738LC alloy produced by Electron Beam Selective Melting,” *Addit. Manuf.*, vol. 47, no. October, p. 102371, 2021, doi: 10.1016/j.addma.2021.102371.
- [11] A. C. Fischer-Cripps, *Factors Affecting Nanoindentation Test Data*. 2004. doi: 10.1007/978-1-4757-5943-3_4.
- [12] K. M. Mussert, W. P. Vellinga, A. Bakker, and S. Van Der Zwaag, “A nano-indentation study on the mechanical behaviour of the matrix material in an AA6061 - Al₂O₃ MMC,” *J. Mater. Sci.*, vol. 37, no. 4, pp. 789–794, 2002, doi: 10.1023/A:1013896032331.

Acknowledgements

This study was carried out within the scope of the project “TÜBİTAK 1004 - Yeni Nesil 3 Boyutlu Yazıcı İmalat Teknolojileri Platformu”. IN738LC as-cast ingot was produced by TUBITAK MAM Metallic Material Technologies Research Group. IN738LC powder used in this study was produced and supplied from Ermaksan. The authors wish to thank Metallic Materials Technologies Research Group in TUBITAK Marmara Research Center and Ermaksan for experimental infrastructure and studies.

Standardization of High Temperature Fatigue Tests for AM Metals

O.T. Gökgöz^{1,2}, H.K. Sezer²

1. Tr Mekatronik Inc., Düzce, Turkey.

2. Industrial Design Engineering Department, Gazi University, Ankara, Turkey.

Abstract

To fully harness the potential of Additive Manufacturing (AM), it is imperative that AM components are tested and verified for all service conditions. In contrast to typical testing scenarios conducted at room temperature, these components are often subjected to harsh real-world conditions. This research investigates the standardization of high-temperature fatigue tests, which is a part of an ongoing PhD thesis. Although there are some international standards governing fatigue testing, there is a notable absence of standards tailored specifically for AM parts, particularly those subjected to extreme conditions.

Keywords: Additive manufacturing, standardization, high temperature fatigue, extreme conditions.

Introduction

The primary aim of this research is to investigate the uncertainties of test standards concerning the evaluation of high-temperature fatigue characteristics in AM components. It is beneficial to note that this study confines its focus exclusively to the examination of test specimens, with the comprehensive analysis of full-scale functional components falling beyond the scope of this investigation. The initial phase of this study entails the execution of fundamental tests on coupon specimens, with the overarching objective being the assessment and enhancement of high-temperature fatigue performance exhibited by AM metal components.

Definition / Fatigue

Fatigue represents a progressive mechanism leading to sudden and non-reversible deterioration or structural failure in components subjected to cyclic loading conditions. A predominant proportion of structural failures can be attributed to fatigue-related phenomena. Consequently, it is inevitable to accord due significance to fatigue strength considerations as a crucial strategy for avoiding structural and component failures. In the context of AM, where components are frequently exposed to cyclic loading, meticulous attention must be devoted to designing AM parts with inherent fatigue resistance capabilities, especially in the context of their intended service conditions.

Standardization

“The benefits arising from the existence of standards for high temperature fatigue testing would include reduction in the duplication of testing and the removal of barriers to trade... This duplication of effort is attributable, in many cases, directly to the absence of an accepted standard and the consequent specification of 'customised' test procedures by each client organisation.” [1] The contemporary case for AM components is similar to the case in 80's for conventional components. There are some parameters should be standardized to ensure the compatibility of the results.

Discussion

In distinction to components fabricated via subtractive manufacturing techniques, AM counterparts exhibit a relatively inferior surface finish, which is known to exert an adverse impact on their fatigue performance. The vast majority of published fatigue tests for AM test coupons are conducted with machined and polished surfaces as suggested In ASTM Standards. [2] [3] [4] Notably, AM confers distinct advantages, such as the capacity for topology optimization, the creation of lattice structures and conformal cooling channels, features that are conspicuously challenging, if not impossible, to replicate using subtractive manufacturing methods. Consequently, it becomes imperative to underscore that even the as-built surfaces of AM components ought to possess resistance to fatigue-induced stresses. [5]

In the assessment of fatigue performance, due consideration must be allocated to the inherent surface roughness of as-built AM components. Moreover, it is suggested that forthcoming standards should specify and regulate parameters including but not limited to surface roughness, test temperatures, coupon geometry, the number of specimens, testing frequency, and the R-value.

Conclusions

AM contains great opportunities as a developing manufacturing technology. However, promoting AM to a mature state necessitates the establishment of testing standards to ensure its safe and reliable in industrial applications.

References

- [1] G. B. Thomas, «The Case for Standards in High Temperature Fatigue,» %1 içinde High Temperature Fatigue Properties and Prediction, London, Elsevier Applied Science, 1987, p. 261.
- [2] H. Kjellsson, «High Temperature Fatigue Performance of Electron Beam Powder Bed Fusion Manufactured Alloy 718,» Metallurgical and Materials Transactions A, pp. 2496-2514, July 2022.
- [3] S. Liu, «Additive Manufacturing of Ti6Al4V Alloy: A review,» Materials and Design, pp. 1-23, 2019.
- [4] E606-04 Standard Practice for Strain-Controlled Fatigue Testing, ASTM International, 2017.
- [5] A. Yadollahi, «Additive manufacturing of fatigue resistant materials: Challenges and opportunities,» International Journal of Fatigue, pp. 14-31, 2017.

Effect of The Orientation of The Trabecular Structure on The Comparison Strength of Bone for Future Studies

Ahmed JAWAD^{abd}, Arif BALCI^c, Yogendra Kumar MISHRA^d, Yusuf USTA^{ab}.

a Department of Mechanical Engineering, Gazi University, Ankara 06570, Turkey;

b Additive Manufacturing Technologies Research and Application Center-EKTAM, Gazi University, Ankara 06560, Turkey

c Mechanical Engineering Department, Kafkas University, Rektörlüğü, 36000 Kars Merkez/Kars, Türkiye.

d Smart Materials, NanoSYD, Mads Clausen Institute, University of Southern Denmark, Alsion 2, 6400, Sønderborg, Denmark

Abstract

The core of bones including trabecular bone, is a lattice-like structure built out of connected struts. Its high porosity helps the nutrition exchange and contains the bone marrow responsible for the desired generation of red blood cells. The trabecular bone exhibits a high surface area compared to the cortical bone and responds to mechanical stresses by refining its characteristics. It is less dense but stronger and stiffer because it contains concentrated minerals like calcium and phosphorus. Due to the efficient force distribution this particular bone tissue provides, it is resistant to compression, tension, and shear forces. Literature study reveals that the geometry of the metallic bone implant plays a significant role in enhancing mechanical and biocompatibility. In this study, the different orientations of the geometry on the bone-implant obtained were demonstrated using Trimetric software. Furthermore, ANSYS Structural Simulations will be performed on the geometries achieved through different orientations to examine the comparison strength for future studies.

Introduction

Porous metal scaffolds are essential in orthopedics, particularly for procedures involving prosthesis implantation, such as artificial joint replacements, and treating bone abnormalities caused by infections, trauma, or tumor removal. These scaffolds offer numerous advantages. One advantage is that its porous structure facilitates a robust bond between the bone and the implant by closely resembling the mechanical characteristics of bone. This reduces the risks associated with stress shielding [1]. This structure also facilitates nutrient transportation, bone cell ingrowth, and differentiation. In contrast, metal materials, such as titanium and its alloys, possess unique scaffold structures and well-balanced mechanical properties, rendering them more versatile for orthopedic implants compared to ceramics and polymers [2]. Titanium and its alloys are highly favored due to their biological compatibility, corrosion resistance, and affordability [3], [4].

The construction of bone scaffolds can involve either regular or irregular designs for their porosity. Regular porous structures can be generated by repeating a unit cell or a triply periodic minimum surface. The materials possess consistent unit structures, uniform pore sizes, and modifiable porosity. The mechanical behavior and biocompatibility of regular porous scaffolds are affected by these

characteristics. However, the human trabecular bone does not possess uniform local porosity or identical pore size and morphology [5], [6]. Consequently, the consistent structure of regular porous scaffolds may not elicit the desired cellular response, both in laboratory settings and within the body [7].

In contrast, the configuration and dimensions of irregular porous materials exhibit random variations. The diverse range of pore sizes, different pore shapes, and varying levels of local porosity in bone tissue engineering (BTE) can enhance the biocompatibility of porous scaffolds [8]. Research has shown that irregular porous structures resembling cancellous bone have advantages for cell development, thus emphasizing the benefits of this uneven architecture. Researchers have created numerous irregular porous scaffolds to achieve the desired characteristics of natural bone at different levels, such as mechanical properties, biological compatibility, mass transport, and microstructure geometry. These scaffolds are developed using image-based reverse modeling, mathematical modeling, or a combination of these approaches [5], [9][10]. Taniguchi et al. found that the size of the pores in bone implants is an essential factor in promoting bone regrowth [11]. Barack and his colleagues researched to examine the mechanical properties of different dimensions in a chimpanzee bone model created using micro-CT scanning. The researchers discovered that the average thickness of trabecular bone was too small to be accurately replicated using 3D printing technology. As a result, there were only minimal changes in the dimensions of the intended structure during the fabrication process [12]—Wood et al. employed micro-CT scanning to construct a model of the trabecular structure of sheep bones. The mechanical strengths of samples from various orientations within the same structure were analyzed, following their production through 3D printing [13]. In a study by Cheng et al. [14], the human femur was duplicated using Micro-CT. Subsequently, sample models with varying porosity levels (low, medium, and high) were created from Ti6Al4V Grade 5 powder using selective laser sintering. Mangano promotes the utilization of CAD/CAM technology in the production of dental bone implants [15].

Methodology and Cad Models

A. Balci achieved a duplicated trabecular structure based on bone samples obtained from a 22-month-old sheep's femur and vertebral regions. These bone samples were carefully excised for micro-CT imaging without significant damage and preserved in a 10% formaldehyde solution. Subsequently, the bone samples underwent scanning within a wet formaldehyde environment using a Bruker Skyscan 1272 machine. The settings included an 8-micron scanning pixel size, a 90 kV source voltage, 111 mA source current, and an Al 0.5 + Cu 0.038 mm filter [16].

The cross-sectional images in the horizontal slice plane, essential for creating 3D models, were generated using the NRecon software based on the obtained scanning data. The 3D computer-aided design (CAD) model was generated by identifying bone areas through grayscale distinctions using Mimics software. The complexity of the trabecular structure was affected by specific areas, such as damaged regions from bone cutting for Micro-CT and cortical bone, as well as disruptions caused by epiphyseal plaque, as illustrated in Fig. 1 [16].

Various designs of the bone implant were achieved using the identical model. At first, a cubic model, depicted in Fig. 2, was imported into Mimics 3-matics version 13.0. The object was subsequently reflected on various surfaces and positions in order to attain the most favorable thickness and other physical characteristics, including height and width. Subsequently, the solid entities were arranged and merged utilizing Boolean Union.

After attaining the desired physical parameters, cylindrical models were obtained by varying their orientations and axes.

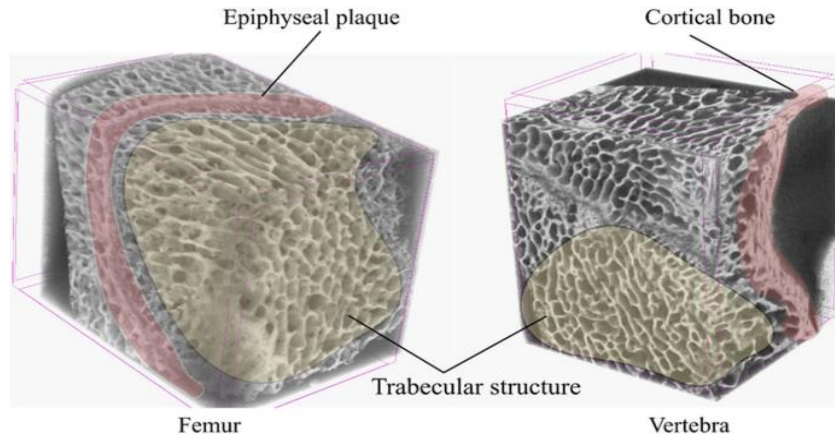


Fig. 1. Internal structure of trabecular bones scanned by micro-CT [16].

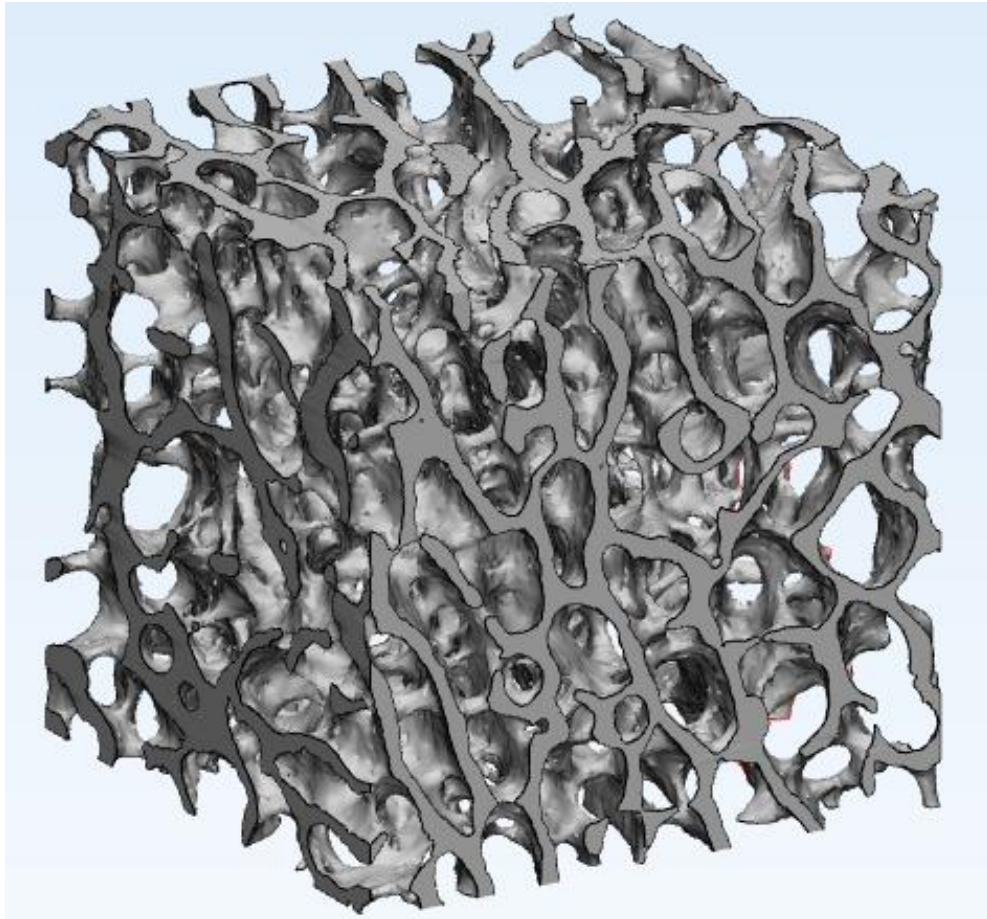
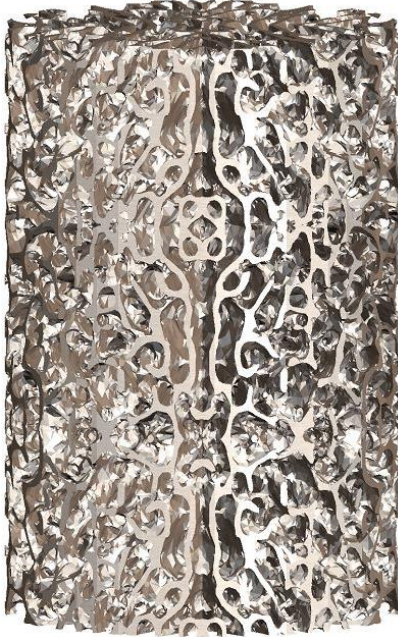



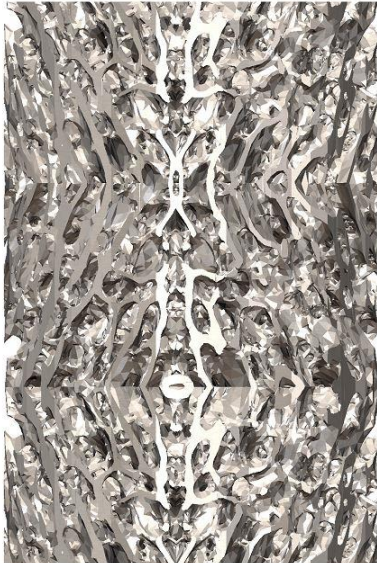

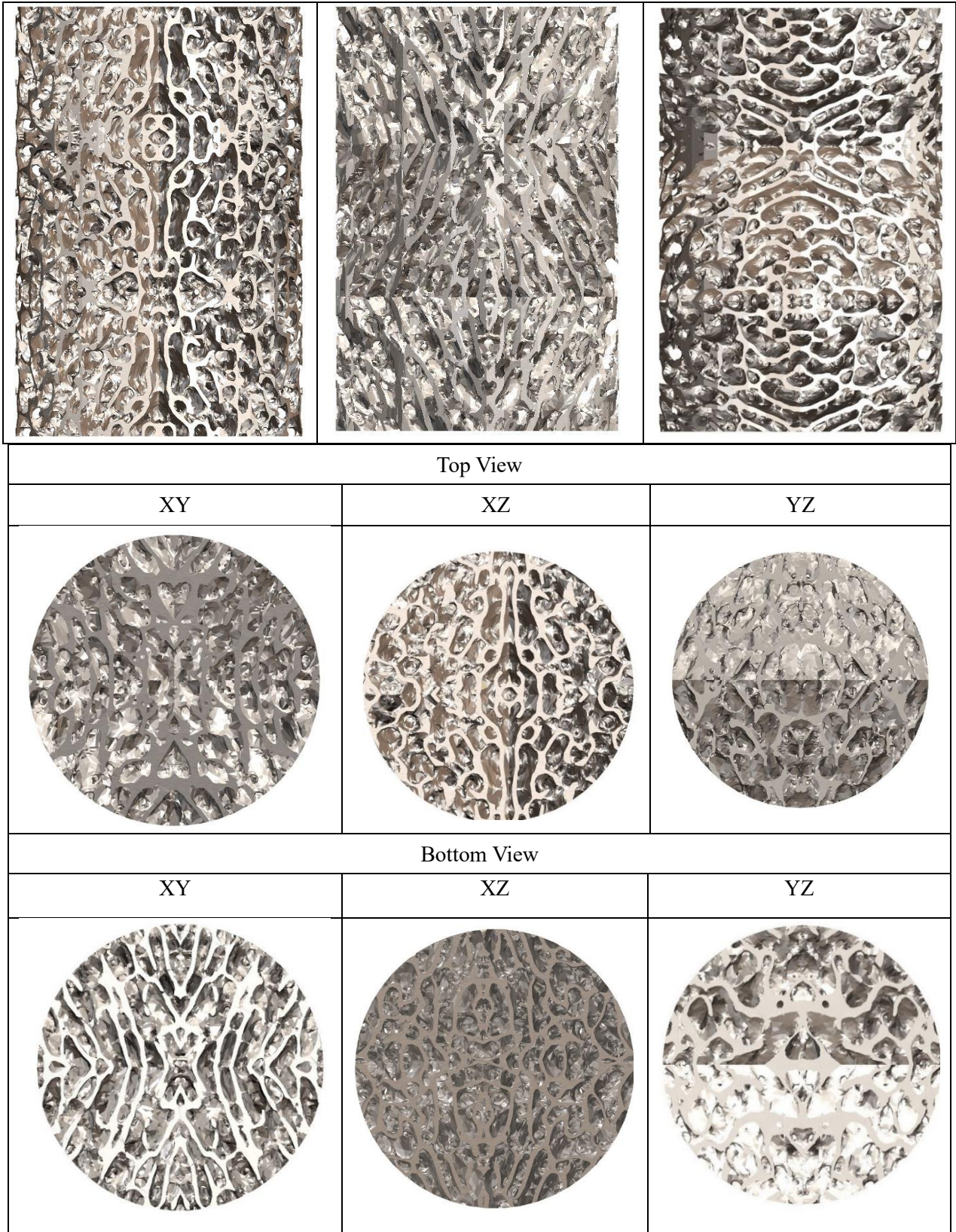


Fig. 2. Cubical CAD of the internal structure of trabecular bones

The cubical model was then converted into a cylindrical model from the different origins' axes. The axis was selected as XY, XZ and YZ. The obtained designs are shown in Table 1 below:

Table 1. Design of the trabecular structures for the analysis by Trimetric software

Isometric View		
XY	XZ	YZ
		
Front View		
XY	XZ	YZ
		
Back View		
XY	XZ	YZ



The porous nature of bone refers to the complex arrangement of minute cavities and openings within the bone tissue. These cavities are commonly known as "pores" or "porosity" and play a crucial role in several bodily functions, such as serving as a structure for blood vessels and bone marrow and contributing to the overall strength and flexibility of the bone. The porous nature of bone is essential for

its capacity to provide structural support to the body and endure mechanical pressures. It also functions as a mineral reservoir and a hub for bone cell activity.

The obtained designs reveal that different porosities and their structures were derived from various axes. These variations will influence the mechanical and biocompatibility properties, which arise from alterations in the pore structure and the thickness of the struts at multiple locations. Moreover, it is necessary to conduct future studies, including simulation and experimental studies, to determine the optimal design for the bone implant based on the obtained designs.

Conclusion

The central structure of bones, which includes trabecular bone, is essentially a lattice-like framework composed of interconnected struts. Its significant porosity facilitates the exchange of nutrients and houses the bone marrow responsible for generating red blood cells. Trabecular bone possesses a larger surface area than cortical bone, and it refines its characteristics in response to mechanical stresses. A review of existing literature demonstrates that the design of metallic bone implants plays a crucial role in improving their mechanical properties and biocompatibility. Arif replicated the trabecular bone structure using bone samples from a young sheep's femur and vertebral regions. The samples were carefully prepared for Micro-CT imaging and scanned with a Bruker Skyscan 1272 machine under specific conditions. Cross-sectional images were generated for 3D modeling. The trabecular structure was created using Mimics software. In this study, the same model was used to design various bone implants, optimizing their parameters. This approach demonstrates the potential for customizing bone implants based on natural bone structures. Future studies are needed to be carried out on these obtained customized designs to investigate mechanical properties such as shear, compression, and tensile strength at different angles and directions to observe whether the implant is isotropic or anisotropic in terms of strength to meet the optimal design for the bone implant.

Acknowledgment and Funding

This work has received funding from, the European Union's Horizon 2020 research and innovation program under the Marie Skłodowska-Curie grant agreement No 101034425 for the project titled A2M2TECH. This study has also received funding from The Scientific and Technological Research Council of Türkiye (TUBITAK) with the grant No 120C158 for the same A2M2TECH project under the TUBITAK's 2236/B program.

References

- [1] S. N. Parikh, "Bone graft substitutes in modern orthopedics," *Orthopedics*, vol. 25, no. 11, pp. 1301–1309, 2002.
- [2] T. W. Bauer and S. T. Smith, "Bioactive materials in orthopedic surgery: overview and regulatory considerations," *Clin. Orthop. Relat. Res.*, vol. 395, pp. 11–22, 2002.
- [3] P. Gubbi and T. Wojtisek, "5.2 - The role of titanium in implant dentistry," in *Woodhead Publishing Series in Biomaterials*, F. H. Froes and M. B. T.-T. in M. and D. A. Qian, Eds. Woodhead Publishing, 2018, pp. 505–529.

- [4] R. M. Mahamood, T.-C. Jen, S. A. Akinlabi, S. Hassan, and E. T. Akinlabi, “9 - Tribology of additively manufactured titanium alloy for medical implant,” in Elsevier Series on Tribology and Surface Engineering, P. Kumar, M. Misra, and P. L. B. T.-T. of A. M. M. Menezes, Eds. Elsevier, 2022, pp. 267–288.
- [5] C. Song et al., “Research progress on the design and performance of porous titanium alloy bone implants,” *J. Mater. Res. Technol.*, vol. 23, pp. 2626–2641, 2023, doi: 10.1016/j.jmrt.2023.01.155.
- [6] F. Li, J. Li, G. Xu, G. Liu, H. Kou, and L. Zhou, “Fabrication, pore structure and compressive behavior of anisotropic porous titanium for human trabecular bone implant applications,” *J. Mech. Behav. Biomed. Mater.*, vol. 46, pp. 104–114, 2015, doi: 10.1016/j.jmbbm.2015.02.023.
- [7] J. Y. Rho, L. Kuhn-Spearing, and P. Zioupos, “Mechanical properties and the hierarchical structure of bone,” *Med. Eng. Phys.*, vol. 20, no. 2, pp. 92–102, 1998, doi: 10.1016/S1350-4533(98)00007-1.
- [8] J. pu ZHENG, L. jian CHEN, D. yuan CHEN, C. sheng SHAO, M. fei YI, and B. ZHANG, “Effects of pore size and porosity of surface-modified porous titanium implants on bone tissue ingrowth,” *Trans. Nonferrous Met. Soc. China (English Ed.)*, vol. 29, no. 12, pp. 2534–2545, 2019, doi: 10.1016/S1003-6326(19)65161-7.
- [9] X. P. Tan, Y. J. Tan, C. S. L. Chow, S. B. Tor, and W. Y. Yeong, “Metallic powder-bed based 3D printing of cellular scaffolds for orthopedic implants: A state-of-the-art review on manufacturing, topological design, mechanical properties and biocompatibility,” *Mater. Sci. Eng. C*, vol. 76, pp. 1328–1343, 2017, doi: 10.1016/j.msec.2017.02.094.
- [10] W. Ming Peng et al., “Biomechanical and Mechanostat analysis of a titanium layered porous implant for mandibular reconstruction: The effect of the topology optimization design,” *Mater. Sci. Eng. C*, vol. 124, no. December 2020, p. 112056, 2021, doi: 10.1016/j.msec.2021.112056.
- [11] N. Taniguchi et al., “Effect of pore size on bone ingrowth into porous titanium implants fabricated by additive manufacturing: An in vivo experiment,” *Mater. Sci. Eng. C*, vol. 59, pp. 690–701, 2016, doi: 10.1016/j.msec.2015.10.069.
- [12] M. M. Barak and M. A. Black, “A novel use of 3D printing model demonstrates the effects of deteriorated trabecular bone structure on bone stiffness and strength,” *J. Mech. Behav. Biomed. Mater.*, vol. 78, no. September 2017, pp. 455–464, 2018, doi: 10.1016/j.jmbbm.2017.12.010.
- [13] Z. Wood, L. Lynn, J. Nguyen, M. Black, M. Patel, and M. Barak, “Are we crying Wolff? 3D printed replicas of trabecular bone structure demonstrate higher stiffness and strength during off-axis loading,” *Bone*, vol. 127, pp. 635–645, Aug. 2019, doi: 10.1016/j.bone.2019.08.002.
- [14] A. Cheng, A. Humayun, D. Cohen, B. Boyan, and Z. Schwartz, “Additively Manufactured 3D Porous Ti-6Al-4V Constructs Mimic Trabecular Bone Structure and Regulate Osteoblast Proliferation, Differentiation and Local Factor Production in a Porosity and Surface Roughness Dependent Manner,” *Biofabrication*, vol. 6, p. 45007, Oct. 2014, doi: 10.1088/1758-5082/6/4/045007.
- [15] C. Mangano et al., “Custom-made computer-aided-design/ computer-assisted-manufacturing (CAD/CAM) synthetic bone grafts for alveolar ridge augmentation: A retrospective clinical study with

3 years of follow-up,” *J. Dent.*, vol. 127, no. September, p. 104323, 2022, doi: 10.1016/j.jdent.2022.104323.

[16] A. Balcı, F. Küçükaltun, M. F. Aycan, Y. Usta, and T. Demir, “Reproducibility of Replicated Trabecular Bone Structures from Ti6Al4V Extralow Interstitials Powder by Selective Laser Melting,” *Arab. J. Sci. Eng.*, vol. 46, no. 3, pp. 2527–2541, 2021, doi: 10.1007/s13369-020-05145-7.

The Role of Dyes in Ceramic-Filled Acrylate Resin Composites for Ceramic Additive Manufacturing

B. Çetin¹, M. G. Seden¹, K.Ö. Yavuz¹, E. Özeren², A. Orhangül².

1. TUBITAK, Marmara Research Center, Chemistry Institute, 41470 Kocaeli, TURKEY

2. TEI, TUSAS Engine Industries Inc., 26210 Eskişehir, TURKEY

Abstract

The advent of 3D printing technology has ushered in a transformative era in manufacturing and various industries. 3D printing is a significant part of advanced manufacturing and builds products layer by layer. Additive Manufacturing (AM) enables design flexibility, the efficiency gains, having various application areas, reduce carbon footprints and where small businesses, startups, and individuals can compete on a level playing field with larger corporations. In addition in recent years, there has been significant interest in the advancement of photosensitive slurries for manufacturing ceramics with excellent mechanical properties [1]. The incorporation of ceramic fillers into UV-curable resin matrices is a promising approach to enhance the mechanical, thermal, and dielectric properties of UV-cured materials, making them suitable for a wide range of applications, including coatings, adhesives, and 3D printing. In this study, a binder system has been developed that can be a candidate as ceramic slurry for slurry-based AM technologies. This developed binder system was mixed with ceramic filler and different additives in varying concentrations by weight and turned into a slurry and characterized. Key aspects issues investigated in this study include the effect of the addition form of the dye (Sudan IV) and the effect of the amount of filler on the resulting composite materials.

Keywords: Ceramic Additive Manufacturing, UV Curable, Photopolimerization, Dye, Ceramic Powder, Ceramic Slurry

Introduction

Photopolymerization is a method by which a liquid monomer transforms into a solid polymer when exposed to ultraviolet (UV) light. This transformation generally occurs through polymerization initiated by free radicals generated by a photoinitiator [1]. When subjected to specific light wavelengths, these polymers chemically react and bond together, creating a solid structure. In contrast to conventional 3D printing techniques, which involve melting and extruding materials, often resulting in defects and the need for support structures, photopolymerization offers a cleaner and more precise alternative [2]. Therefore numerous industries, aerospace, medical, industrial manufacturing, and even consumer product applications, have embraced this technology, as it is well-suited for producing intricate and customized components with minimal waste.

So far, thanks to recent advances in both materials science and computer science, a wide variety of 3D printing methods have been created specifically for ceramic part production. Prior to printing, the raw material, depending on its form, can be broadly categorized into slurry-based, powder-based, and bulk solid-based methods [3]. Slurry-based 3D printing technologies for ceramics typically utilize liquid or semi-liquid systems containing finely dispersed ceramic particles as feedstock. These may be in the form of inks or pastes, with the choice depending on the solid loading and viscosity of the system [4].

Different additives were used along with the binder system and ceramics in the prepared slurry-based raw material systems. Ceramic selection and manufacturing process significantly affect the properties of the final composite material [4,5]. These systems are typically prepared by processes such as mixing, ultrasonication, and UV curing to ensure uniform distribution of ceramic particles. Dye additives, known for their versatile nature, have emerged as important players in customizing the performance and properties of these composites [6]. When dye absorbs UV light, it produces heat, which can help promote cross-linking and curing in areas where UV light intensity may be weaker or shadows are present. Additionally, when the dye absorbs UV light, it transfers energy to the photoinitiator, which can speed up the initiation of the curing process and shorten curing times. Hence, even challenging geometries and thick-layered coatings can be cured properly.

In this study, a binder system has been developed that can be a candidate for the 3D printing industry. This developed binder system was mixed with ceramic filler and different additives in varying concentrations by weight and turned into a slurry and characterized [7]. Sudan IV was used as the dye, and the effect of the addition method of the dye (liquid form) and the effect of the amount of ceramic filler on the composite materials obtained are included [8].

Experimental Procedure

The synthesis of ceramic-based acrylate resin composites involves mixing ceramic particles or fillers with acrylate-based resins.

Materials

Acrylate monomers and oligomers were used for the binder system. The oligomer percentage comprises approximately 80% of the binder system. TPO and Irgacure 819 were used as photoinitiators. Tween 80 was used as a surfactant, aiming to reduce surface tension and increase the compatibility of different components in the formulation. Additionally, Sudan IV dye was used as the building block of the article. The procedure for adding dye additives will be explained in detail. The amounts of substances in the binder system are summarized in Table 1.

Table 1. Binder system (BS) components

	Commercial Name	Weight [%]	Density [g/cm ³]
Monomers	HDDA	2-10	1.02
	2-HEA	2-10	1.01
	IBoA	5-15	0.99
	UM2380T	30-50	1.05-1.25
Oligomers	UM7200	30-50	1.05-1.25
	PAR	5-15	1.1-1.43
Photoinitiators	Irgacure 819	2-5	0.93
	TPO	2-5	1.12
Dye	Sudan IV	0,05-0,1	1.2
Surfactant	Tween 80	0,5-2	1.06

HDDA = 1,6-hexanediol diacrylate, 2-HEA = 2-hydroxyethyl acrylate, IBoA = isobornyl acrylate, PAR = polyester acrylic resin, Irgacure 819 = bis(2,4,6-trimethylbenzoyl)-phenylphosphineoxide, TPO = diphenyl(2,4,6-trimethylbenzoyl) phosphine oxide

Ceramic powders were prepared by ball milling. First, an optimized powder mixture was obtained. The aims here were to distribute the prepared ceramic powder homogeneously within the binder system, to increase the surface area and reactivity and to create a better powder quality. The powder mixture contained SiO₂, ZrO₂ and Al₂O₃. Ethanol was added to the powder mixture in the zirconia grinding bowl to reduce the solids content to 40%. To create a well-blended system, the mixture was subjected to the ball mill process at 300 rpm for a total of 6 hours. The material taken from the ball mill was dried in a vacuum oven at 50 degrees for 1 hour to prevent agglomeration and ensure stability. Finally, the dried material was ball milled again for 20 minutes. The average particle size of the resulting ceramic powder was measured with a mastersizer (Malvern Mastersizer-2000) as d(0.5):3.774 μ m.

Preparation of Liquid Dye Forms

Sudan IV were used as dye. Dye addition was carried out in liquid states. While preparing the liquid dye form, 15 ml of NVP, CB and Sudan IV were added to a balloon. The prepared solution was mixed with a magnetic stirrer in a balloon on a hot plate at 400 rpm at 80 °C for 4 hours. It was cooled to room temperature and used like that.

Preparation of Ceramic Filled Acrylate Resin Composites

We have two formulations of ceramic-based acrylate resin composites. These were without dye and liquid dye formulations, respectively. Ceramic filler was added to each of them at the rates of 40%, 50% and 60%. 1.5 ml of liquid dye solution was added to ceramic-based acrylate resin formulations. A total of 6 samples were prepared in this way. All prepared samples were mixed with a homogenizer for 5 minutes and then cured with Lithoz CeraFab System S65 Ceramic AM system Sample contents are summarized in Table 2.

Table 2. Ceramic-based acrylate resin formulations

Formulation Name	η	λ	CPF	TM
CP40/BS	5.67	420	SiO ₂ , ZrO ₂ , Al ₂ O ₃	115.5
CP50/BS	9.56	420	SiO ₂ , ZrO ₂ , Al ₂ O ₃	80.3
CP60/BS	16.89	420	SiO ₂ , ZrO ₂ , Al ₂ O ₃	73.3
CP40/BS-DYE	4.34	420	SiO ₂ , ZrO ₂ , Al ₂ O ₃	116.2
CP50/BS-DYE	8.21	420	SiO ₂ , ZrO ₂ , Al ₂ O ₃	79.8
CP60/BS-DYE	13.71	420	SiO ₂ , ZrO ₂ , Al ₂ O ₃	75.4

η = slurry viscosity @ 15 s-1 (Pa.s), λ = light wavelength (nm), CPF = ceramic powder formulation, TM = tensile modulus (MPa)

Results and Discussion

Characterization of the obtained composite materials was carried out using Infrared spectroscopy (FTIR), Thermogravimetric analysis (TGA), Differential scanning calorimetry (DSC). Additionally, scanning electron microscopy (SEM) was used to examine the surface morphology of the final product, the cured material. Tensile testing was used to characterize its mechanical properties. Moreover the

average particle size of the ceramic powder was measured using a mastersizer, and the viscosity and curing depth of the prepared composite materials were examined.

Infrared spectra of the prepared polymeric resins were measured to analyze their chemical structures. The acrylate resin system was measured with an infrared Spectrometer (Perkin Elmer Spectrum One). Transmission spectra (%T) were collected in the scanning range of 4000– 400 cm⁻¹.

Rheological properties of ceramic-filled acrylate resin-based slurries were determined using a Discovery HR 20 Rheometer (TA Instruments, New Castle, DE) at a constant temperature (40 °C). For each sample, a scan was first performed and average values were obtained by taking at least three measurements for the specified shear rate. The final viscosity results are reported in table 2.

The glass transition temperature (T_g) of cured ceramic-filled acrylate resin samples was analyzed using differential scanning calorimetry (DSC) Perkin Elmer Jade DSC. The sample was accurately weighed in an aluminum pan and heated to a temperature range of -30 to 300°C with a constant thermal ramp of 10°C/min under nitrogen flow.

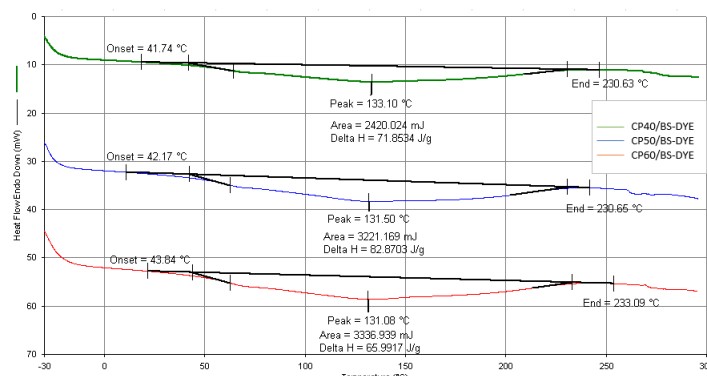


Figure 1. DSC thermograms of different ceramic-based acrylate resin formulations

Thermogravimetric analysis of cured ceramic-filled acrylate resin samples was performed on Perkin Elmer PYRIS 1 TGA devices under air atmosphere. Thermal analysis was monitored over a temperature range of 20 to 900°C with a constant thermal ramp of 10°C/min to measure the thermal stability and % ash content of different formulations. Thermal stability was critically evaluated using T1, T2 and T3. T1, T2 and T3 are the corresponding weight loss at 5%, 25% and 50%, Y% is the residue obtained at 900 °C (Table 3).

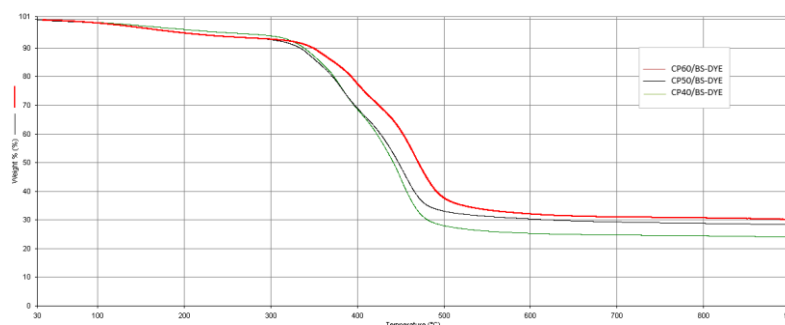


Figure 2. TGA curves of different ceramic-based acrylate resin formulations

Table 3. TGA results for ceramic-based acrylate resin

Formulation Name	T ₁ (°C)	T ₂ (°C)	T ₃ (°C)	%Y 900 °C
CP40/BS	256.5	342.9	490.5	23.96
CP50/BS	260.4	336.4	483.6	28.33
CP60/BS	247.8	356.9	481.9	30.12
CP40/BS-DYE	265.9	361.3	500.7	21.42
CP50/BS-DYE	261.2	349.5	492.6	26.41
CP60/BS-DYE	259.1	357.8	502.8	31.40

Tensile test samples were shaped into 1 mm square rectangular prisms in a teflon mold. The tensile strength was then calculated in one application using the universal testing machine (UTM) of Zwick Z250 5kN load cell and a speed of 2 mm/min. A pair of rotating clip jaws was used to clamp the sample. Tensile strength, % elongation and tensile modulus were then determined for four samples of each formulation and the average of the value was considered for analysis.

The most direct characterization of photopolymerization behavior is made by measuring the curing depth as a function of energy dose. This process can be done by exposing ceramic-filled acrylate resin slurry into to known doses of UV energy, removing the solidified layer and measuring the Cd with a micrometer. It requires careful cleaning of the cured layer after curing to obtain reliable measurements. While obtaining the curing depth data, measurements were taken at different points of the material and averaged. The cured layer must be carefully cleaned after curing to obtain reliable measurements.

Table 4. Depth of cure study results

Formulation Name	Energy Dose (mj/cm ²)	Cd (μ)
CP40/BS	200	565
CP50/BS	200	492
CP60/BS	200	469
CP40/BS-DYE	200	576
CP50/BS-DYE	200	539
CP60/BS-DYE	200	522

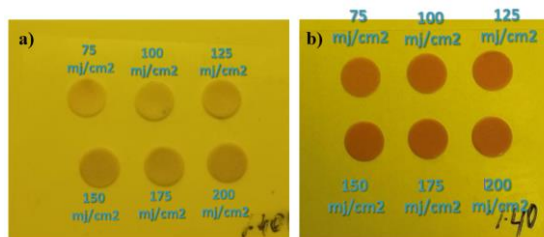


Figure 3. Post-curing images (a) CP40/BS; (b) CP40/BS-DYE

Conclusions

In this study, the preparation of ceramic-filled acrylate resin-based UV-curable slurries for 3D printing and the effects of the dye used as an additive on the resulting material were examined. In formulations prepared without the use of dye, the depth of cure decreased as the ceramic content increased. This is because as the amount of ceramic filling increases, homogeneous distribution becomes difficult and ceramic powders reduce the light transmittance. For this reason, partial curing occurs and the depth of

curing decreases. When the dye additive was added, the depth of cure decreased as the amount of ceramic filler increased. However, considering the obtained values, it was seen that the curing depth of slurries with added dye was greater than that of without dye slurries. Each sample obtained was observed for 1-2 days after curing and no shrinkage occurred in any sample. The results showed that the dye absorbed energy and increased polymerization during curing. Also since the amount of polymerization and curing are directly proportional, the depth of curing has increased.

References

- [1] Zhang, Jing, and Pu Xiao, 3D printing of photopolymers, *Polymer Chemistry* 9.13 (2018): 1530-1540
- [2] Mashouf G., Ebrahimi M., Bastani S., UV curable urethane acrylate coatings formulation: experimental design approach, 2014. Kim, Y. C., Hong, S., Sun, H., Kim, M. G., Choi, K., Cho, J., ... & Nam, J. D. (2017). UV-curing kinetics and performance development of in situ curable 3D printing materials. *European Polymer Journal*, 93, 140-147
- [3] Ozkan, Basar, et al. "Binder stabilization and rheology optimization for vat-photopolymerization 3D printing of silica-based ceramic mixtures." *Journal of the European Ceramic Society* 43.4 (2023): 1649-1662.
- [4] Kim, Y. C., Hong, S., Sun, H., Kim, M. G., Choi, K., Cho, J., & Nam, J. D. (2017). UV-curing kinetics and performance development of in situ curable 3D printing materials. *European Polymer Journal*, 93, 140-147
- [5] Ozkan, Basar, et al. "Hot ceramic lithography of silica-based ceramic cores: The effect of process temperature on vat-photopolymierisation." *Additive Manufacturing* 58 (2022): 103033
- [6] Chen, Z., Li, Z., Li, J., Liu, C., Lao, C., Fu, Y., ... & He, Y. (2019). 3D printing of ceramics: A review. *Journal of the European Ceramic Society*, 39(4), 661-687.
- [7] Borlaf, M., Serra-Capdevila, A., Colominas, C., & Graule, T. (2019). Development of UV-curable ZrO₂ slurries for additive manufacturing (LCM-DLP) technology. *Journal of the European Ceramic Society*, 39(13), 3797-3803.
- [8] Duran, C., Sato, K., Hotta, Y., Nagaoka, T., & Watari, K. (2008). Eco-friendly processing and methods for ceramic materials-A review. *Journal of the Ceramic Society of Japan*, 116(1359), 1175-1181.

Acknowledgements

The authors would like to thank TÜBİTAK for funding and PEGE GROUP and MCT CHEM (from Türkiye) for providing chemical support.

Process parameter optimization for directed energy deposition of Inconel 738LC using the response surface methodology

Hamidreza Javidrad^{1,2}, Mücteba Burak Karakaş³, Sertaç Alptekin⁴, Aylin Sahin Kahraman⁴, Huseyin Aydin⁴, Bahattin Koc^{1,2*}

1 Faculty of Engineering and Natural Sciences, Sabanci University, Istanbul, Turkey.

2 Integrated Manufacturing Technologies Research and Application Center, Sabanci University, Istanbul, Turkey.

3 ERMAKSAN MAKİNA SANAYİ ve Tic. A.Ş., Bursa, Turkey.

4 TUBITAK MAM, Metallic Materials Technologies Research Group, Turkey.

Abstract

Process parameter optimization is an initial requirement for additive manufacturing (AM) of any material. This short paper aimed at process parameter optimization of laser powder directed energy deposition (LP-DED) of Inconel 738LC. A design of experiment (DoE) was established based on the response surface methodology (RSM) to optimize single tracks. The desired responses were the geometrical attributes of single tracks including the bead height, bead width, and wetting angle. The results were regression models that can be used for predicting the geometrical properties of the single track according to the process parameters. These results will further be used for production of defect-free bulk samples.

Keywords: Metal additive manufacturing, process parameter optimization, RSM, nickel alloy.

Introduction

Additive manufacturing (AM) of nickel-based superalloys is challenging due to their susceptibility to cracking during the process. Inconel 738LC (IN738LC) is a non-weldable nickel-based alloy with excellent strength, corrosion and oxidation resistivity, and high thermal fatigue life with applications for high-temperature use such as turbine blades [1]. Non-weldability of IN738LC is related to the high content of Al and Ti (more than 6 wt.% in total), and more accurately the secondary phases that contain Ni₃(Al,Ti) γ' phase [2]. The microstructure of IN738LC consists of γ matrix, (γ' + γ) eutectic phase, γ' , and MC carbides [3].

The optimization of process parameters starts with producing defect-free single tracks with proper shape. Regardless of a few studies, the optimization of single-track deposition has not been fully addressed for IN738LC. Ramakrishnan et al. [4] investigated the effect of LP-DED process parameters on the deposition of defect-free thin-walled Inconel 738 structures. The results showed that a high scanning speed (720 mm/min) leads to delamination even though a laser power of 1000 W was used for the initial layer deposition. However, delamination can also be caused by incompatible substrate. Furthermore, their results showed that high applied energy causes cracks, especially in the vertical direction. On the other hand, it is known that in order to produce a porosity-free sample, the heat supplied must be sufficiently high. These conflicting requirements for producing high-quality Inconel 738 products result in significant problems with the processability of this alloy. The optimized process parameters in their

study were 400 W, 180 mm/min, and 3.4 g/min as laser power, scanning speed, and powder feed speed, respectively. Surprisingly, Zhang et al. [5] reported an even lower laser power (250 W) to obtain crack-free Inconel 738 using the LP-DED method. Sun et al. [3] proposed an average laser power of 500 W and a scanning speed of 250 mm/min to produce a crack-free bulk sample of Inconel 738. The linear energy density (P/v) and the powder density ($4P/\pi D^2$), where D was the nozzle diameter, were used as two indicators to design the process parameters.

This study aims to establish an optimal window of process parameters considering laser power, scanning speed, and powder feed rate, which are the most influential factors contributing to the quality of laser deposition processes.

The proposed model is based on analysis of variance (ANOVA) and response surface methodology (RSM). Geometrical attributes of a single track, such as track height, track width, and wetting angle, are important for determining other processing parameters including layer height and overlap value. Therefore, the properties mentioned were used to determine the suitability of the single tracks. The reliability of these models was evaluated using the linear regression coefficient and further verified through experiments.

Experimental Setup

IN738LC powder

The IN738LC powder was developed through vacuum induction gas atomization furnace process with a diameter range between 45 and 106 μm . The material composition is listed in Table 1.

Table 1: IN738LC powder composition.

Element	Wt%	Element	Wt%
Ti	3.20 – 3.70	Cr	15.70 – 16.30
Ta	1.50 – 2.00	Co	3.00 – 9.00
Al	3.20 – 3.70	Mo	1.50 – 2.00
B	0.007 – 0.012	Nb	0.60 – 1.10
C	0.09 – 0.13	Zr	0.03 – 0.012
Ni	Bal.	W	2.40– 2.80

LP-DED machine configuration

Single tracks were produced using the DMG Mori Seiki LASERTEC 65 DED Hybrid machine with a 1.6mm coaxial nozzle diameter with a 2.5kW diode laser. The substrate was a 10 mm thick C45 steel at room temperature. Argon gas with a flow rate of 5 and 3 L/min were used as the shielding gas, and carrier gas.

Table 2: The DoE of single-track deposition.

Sample No.	P (W)	S (mm/min)	PFR (gr/min)
1	700	400	7.5
2	900	400	7.5
3	700	800	7.5
4	900	800	7.5
5	800	600	7.5
6	700	600	6
7	800	400	6
8	800	800	6
9	900	600	6
10	800	400	9
11	800	800	9
12	700	600	9
13	900	600	9

Experimental Results

Figure 1 shows cross-sections of individual tracks. As observed, no delamination occurred in any of the jobs; therefore, the defined ranges for the process parameters were acceptable. However, in some cases, excessive deposition is observed. The porosity rate is influenced by the selection of process parameters. Laser power and scanning speed are the most influential factors that contribute to porosity formation. The experimental results showed that the laser power and scanning speed should be higher than 800 W and 600 mm/min to achieve the lowest porosity rate. The final porosity rate of a bulk sample is also influenced by the overlap ratio and thickness of the layer; accordingly, it would be more realistic to evaluate the porosity rate of bulk samples.

Figure 2(a) shows the main effect plots for bead height. According to the results, the laser power does not play an important role in determining the height of the individual deposited tracks. Taking into account a fixed amount of powder supplied, the laser power is responsible for fusing the material. Since the range of laser power examined melts the material sufficiently, there is no noticeable variation in the bead height. The scanning speed and powder feed rate affect the amount of powder delivered to the surface. Consequently, both parameters have a significant influence on the height of the deposited material. From Figure 2(a), it can be seen that increasing the scanning speed can significantly reduce the bead height as long as a smaller amount of powder is allocated every second. On the other hand, the powder feed rate has an inverse effect on the deposition height, which is indicated by a direct relationship in the third main effects plot. Several researchers combined these two parameters (F/v) and proposed a unified exponent [6]; However, this approach is not completely consistent with the main effect plots of the present study. Table 4 also shows the linear regression model for the bead height and the comparison between the experimental measurement and the model results. It can be seen that the regression coefficient is quite high, which indicates the accuracy of the model.

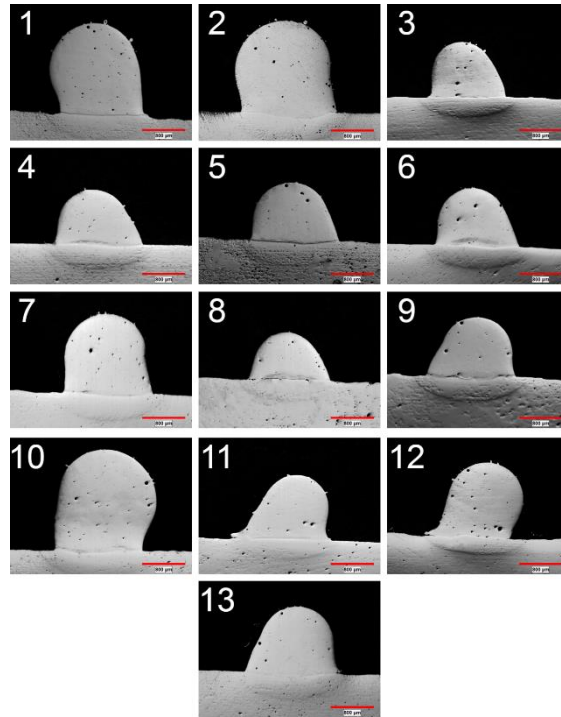


Figure 1. The optical micrographs from the cross-section of single tracks.

The width of the deposited material initially depends on the diameter of the nozzle; nonetheless, it effectively depends on the amount of heat supplied at a constant nozzle diameter. Figure 2(b) shows the main effect plots for the bead width, which is supported by the previous claims. As shown, laser power is the most influential process parameter due to its undeniable contribution to the heat input. By increasing the laser power from 700 to 900 W, the width of the deposited track increased from 1.51 to 1.69 millimeters. It is surprising that the minimum track width obtained was smaller than the nominal diameter of the nozzle, which is due to the insufficient material supply for deposition. A low laser scanning speed ensures longer exposure time and higher heat input; Therefore, reducing this process parameter can also increase the bead width. The effect of powder feed rate was first directly proportional and then inversely proportional to bead width. The reason for this strange behavior is that at high feed rates, the nozzle diameter restricts the distribution of the powder and instead forces the powder particles together, which is undesirable. It should be noted that the width of the track should not exceed the diameter of the nozzle, as this will lead to the lack of control of powder distribution, ball formation, and dimensional inaccuracy. Therefore, the optimal feed rate is close to the minimum value in the range. The bead width regression model is also shown in Table 3. The accuracy of the model is not as high as that of the bead height model due to the over-deposited samples; However, it can still give an idea of the width of the bead.

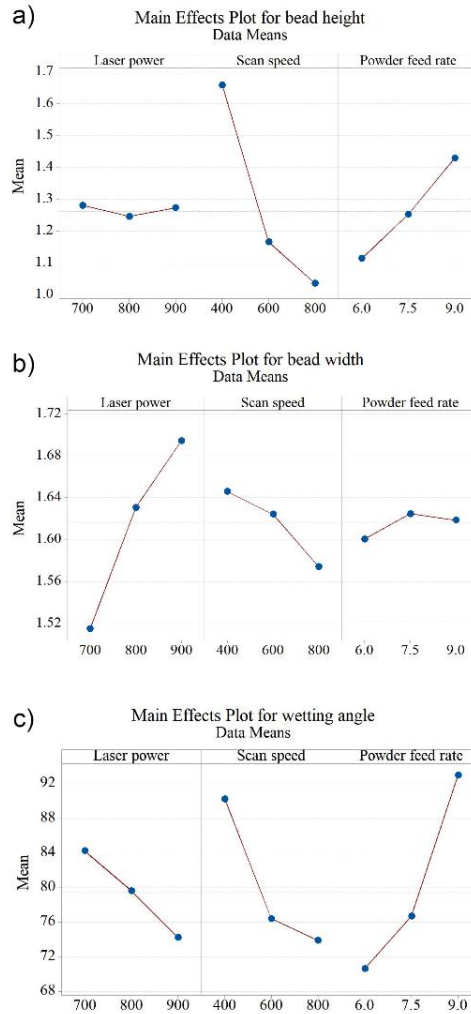


Figure 2. Main effect plot of the geometrical attributes: (a) Bead height, (b) bead width, and (c) wetting angle.

The wetting angle indicates the suitability of the entire bead shape. A suitable bead shape typically forms a 60 to 80-degree angle with the base plate, ensuring proper gap filling and material consolidation in successive laser tracks and stacking layers, ultimately resulting in a fully-densed component. Figure 2(c) shows the main effect analysis of the process parameters for the wetting angle. The influence of the process parameters on the wetting angle is more complex as it is influenced by all three parameters. Understandably, a higher powder conveying speed leads to a higher track height, which unfavorably increases the wetting angle. However, the influence of laser power and scanning speed requires further investigation. Surprisingly, several researchers had ignored the effect of laser power [7]. According to the first graph in Figure 2(c), increasing the laser power led to a decrease in the wetting angle, which can be explained by the effect of a more efficient melting cycle and the formation of a suitable bead shape. Furthermore, the wetting angle is directly related to the bead height, while it is inversely proportional to the bead width. Since the laser power has almost no influence on the bead height and has a positive effect on the bead width, the wetting angle decreases with increasing power. The high scanning speed limits the stacking of powder flow at any point, ensuring more uniform bead geometry and preventing balling. The linear regression model for the wetting angle was determined from the ANOVA results and showed acceptable accuracy (See Table 3).

Table 3: Regression models for each geometrical property.

Bead height = $5.8 - 0.00708 \times P - 0.007119 \times S + 0.1053 \times PFR + 4E-6 \times P^2 + 5E-6 \times S^2$ ($R^2=0.93$)
Bead width = $0.587 + 3.16E-3 \times P + 2E-5 \times S - 0.142 \times PFR - 3E-6 \times P^2 - 0.00822 \times PFR^2 + 3.07E-4 \times P \times PFR + 4.3E-6 \times S \times PFR$ ($R^2=0.829$)
Wetting angle = $90.6 + 0.14 \times P - 0.2484 \times S + 1.47 \times PFR + 1.51E-4 \times S^2 + 2.463 \times PFR^2 + 1E-4 \times P \times S - 0.033 \times P \times PFR - 7.17E-3 \times S \times PFR$ ($R^2=0.914$)

To determine the optimal configuration, the desirability function approach was adopted. The desirability function varies between 0 and 1 and should be as close to 1 as possible. Figure 3 shows the desired goals and the result obtained by the response optimizer as part of the RSM analysis. For this analysis, the previously defined areas for the process reactions were used. The optimal process parameter settings include a laser power of 746 W, a scanning speed of 590 mm/min and a powder feed rate of 7 g/min. The high desirability value (0.9781) shows the suitability of the optimal results according to the desired geometric values.

To verify the optimization result and the closeness of the predicted responses to the experimental measurements, the optimum set of process parameters were produced and measured. Table 4 shows the process parameters and the corresponding geometrical properties of the measurements. The overall error rate is less than 10%, reflecting the accuracy of the models.

Table 4: Experimental and RSM results of the geometrical properties.

Shape parameter	Experiment	RSM	Error (%)
Bead height (mm)	0.928	0.995	7.21
Bead width (mm)	1.51	1.6	5.96
Wetting angle (degree)	67	70	4.47

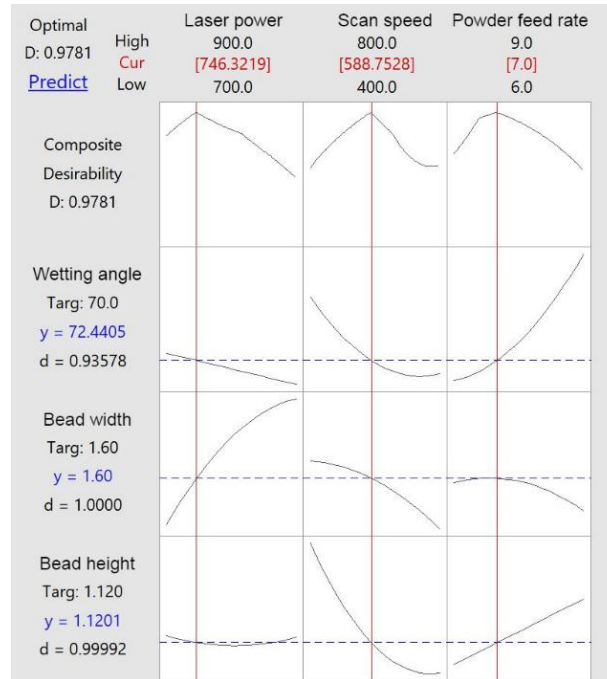


Figure 3. Desirability plot for wetting angle, bead height and width.

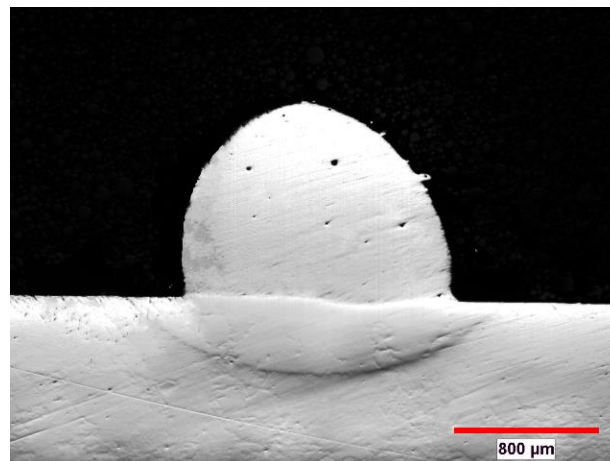


Figure 4. The cross section of the optimum single track.

Conclusions

The aim of the present study was to systematically investigate the influence of important process parameters on the geometric specifications of individual LP-DED IN738LC tracks. The ANOVA and RSM were used to determine the effect of each process parameter on the geometric shape of each bead. The results showed that the laser power has only a small influence on the track height. The bead width depends on all three parameters; however, the impact was less severe than the size of the bead height. The wetting angle was significantly influenced by the powder feed rate and scanning speed, as these parameters indicate the amount of powder delivered to the surface. The RSM was used to optimize the process parameters considering the bead height, width and wetting angle as responses. The obtained result was $P=750\text{W}$, $v=590\text{ mm/min}$ and $F=7\text{ gr/min}$. The optimum single track contained a few porosities that can be eliminated in bulk sample by selecting a proper layer thickness and step over value.

References

1. Gradl, P.R., S. Greene, and T. Wammen. Bimetallic Channel Wall Nozzle Development and Hot-fire Testing using Additively Manufactured Laser Wire Direct Closeout Technology. in AIAA Propulsion and Energy 2019 Forum. 2019.
2. Xu, J., et al., HAZ liquation cracking mechanism of IN-738LC superalloy prepared by laser solid forming. Metallurgical and Materials Transactions A, 2018. 49: p. 5118-5136.
3. Sun, H., et al. Direct laser deposition of Inconel 738 on directionally solidified Ni-base superalloy component. in Lasers in Material Processing and Manufacturing II. 2005. SPIE.
4. Ramakrishnan, A. and G. Dinda, Direct laser metal deposition of Inconel 738. Materials Science and Engineering: A, 2019. 740: p. 1-13.
5. Zhang, X., et al., Cracking mechanism and susceptibility of laser melting deposited Inconel 738 superalloy. Materials & Design, 2019. 183: p. 108105.
6. Alizadeh-sh, M., et al., Laser cladding of Inconel 718 powder on a non-weldable substrate: Clad bead geometry-solidification cracking relationship, J. Manuf. Process. 56(2020) 54–62. Manuf. Process, 2020.
7. Erfanmanesh, M., et al., An empirical-statistical model for laser cladding of WC-12Co powder on AISI 321 stainless steel. Optics & Laser Technology, 2017. 97: p. 180-186.

A Study on Beam Shaping Effects on The Mechanical Properties and Residual Stresses in Parts Processed Using Selective Laser Melting

Ahmad Reshad Bakhtari^{1,2}, Hüseyin Kürşad Sezer³, Olcay Ersel Canyurt^{1,2}

1. Mechanical Engineering, Gazi University, Ankara, Türkiye.
2. Additive Manufacturing Technology Application and Research Center (EKTAM), Gazi University, Ankara, Türkiye.
3. Industrial Engineering Design, Gazi University, Ankara, Türkiye.

Abstract

Selective Laser Melting (SLM) has emerged as an innovative technique for additive manufacturing, offering unparalleled freedom in design and precision in the fabrication of complex metallic components. An important aspect that influences the laser-material interaction and, eventually, the quality and performance of SLM-produced parts is the laser beam profile utilized during the process. In this study, COMSOL Multiphysics is employed to simulate the laser-material interaction in SLM, aiming to understand the effect of varying beam shapes on the generation of residual stresses in the fabricated components. The on-hand research begins with a comprehensive analysis of the physical processes involved in SLM, including laser energy absorption, heat transfer, and solidification dynamics. By varying the laser beam profile, such as the Gaussian to Top-Hat, the paper systematically explores their impact on laser-material interaction, melting and solidification, and, most importantly, the generation of residual stresses within the parts. The findings of this study are expected to provide valuable insights into optimizing SLM processes for improved mechanical performance and reduced defects in additively manufactured components. Understanding these effects is pivotal for optimizing SLM processes to enhance mechanical properties and reduce defects, bridging theory and practical applications in additive manufacturing.

Keywords: Selective Laser Melting, Residual Stresses, Beam Shaping, Beam Profile, Numerical Modelling.

Introduction

Additive manufacturing (AM) stands as a disruptive technology pivotal to realizing Industry 4.0 [1,2], revolutionizing traditional manufacturing methods by directly translating CAD models into components, reducing costs, time, and material waste [3]. Laser-Powder Bed Fusion (L-PBF), a key AM process, employs laser energy to melt metallic powders precisely, yielding custom components with fine grain structures and excellent mechanical properties [4]. However, the conventional Gaussian laser beam shape has inherent drawbacks, causing localized overheating, evaporation, and spattering during L-PBF due to its irradiance distribution [5,6]. As a result, it adversely affects melt pool dimensions, stability, and product quality [5,7].

To address these issues, researchers have explored alternative beam shapes from laser welding processes, known for their impact on weld quality and performance [8,9]. Insights from these studies offer promising strategies to enhance L-PBF [5–7]. In this context, the on-hand research aims to perform

thermomechanical modelling using COMSOL Multiphysics to analyze the effects of beam shaping on residual stress generation in the SLM process. It seeks to investigate how alternative beam shapes, developed initially for laser welding and related techniques, impact thermal and mechanical behavior within the SLM process. By simulating and comprehensively evaluating the resulting residual stresses, we aim to gain deeper insights into the potential benefits and challenges associated with adopting alternative beam shapes in L-PBF, contributing to the advancement of this transformative manufacturing technology.

Thermomechanical 3D FEM Model

In this study, a comprehensive continuum-based thermomechanical model was developed to investigate the effects of alternative beam shapes on the generation of residual stresses during the SLM process. The approach considers the powder layer, composed of discrete particles, as a continuum medium with equivalent properties, facilitating an accurate representation of thermal and mechanical behavior.

The domain considered for the 3D FEM model has a length of 5 mm, a width of 2.5 mm, and a layer thickness of 25 μm . In the model, the laser follows a bidirectional strategy for scanning the specified domain (see Figure 1). Furthermore, the model incorporates temperature-dependent material properties [10] to capture the evolving behavior of the Ti6Al4V alloy during the SLM process with precision. Specifically, consideration is given to temperature-dependent elasticity and plasticity, along with isotropic hardening, while kinematic hardening effects are disregarded. The mechanical properties of Ti6Al4V used in the simulation are taken from [11]. To accurately represent the phase change from powder to solid, the latent heat of fusion, phase change temperature, and temperature-dependent material properties are incorporated [12].

Table 1 shows the process parameters used for this study.

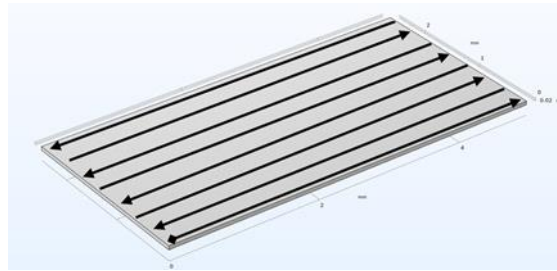


Figure 1. Thermomechanical 3D FEM model.

Table 1: Process parameters

Parameter	Value
Laser scanning velocity (v)	1100 mm/s
Laser power (P)	190 W
Absorption coefficient (A)	0.3 [13]
Laser spot radius (r)	50 μm
Hatch space (Hs)	50 μm
Emissivity (ϵ)	0.35 [14]
Optical penetration depth (δ)	65 μm [13]
convective heat transfer coefficient (h_c)	10 W/m ² K

Governing Equations, Initial and Boundary Conditions

The thermomechanical model consists of two governing equations: the heat balance equation for the transient thermal analysis and Hook's law for thermal stress analysis. The heat balance equation is expressed as follows:

$$\rho C_p \frac{\partial x}{\partial y} + \rho C_p u \nabla T = \nabla(k \nabla T) + Q \quad (1)$$

where ρ is density, C_p is specific heat capacity, k is thermal conductivity, u is the laser velocity, T is temperature, and Q is the heat absorbed (i.e., heat source). An exponentially decaying volumetric heat source, adapted from [15], is used and further modified to accommodate different beam shapes (e.g., Top hat and Donut).

$$Q(x, y, z) = \frac{2AP}{\pi \delta r^2} \exp\left(-\frac{2((x-ut)^2 + y^2)}{r^2}\right) \exp\left(-\frac{|z|}{\delta}\right) \quad (2)$$

A is absorption coefficient, P is laser power, r is laser spot radius, $|z|$ is the absolute value of the z -coordinate, and δ is the optical penetration depth of the laser for Ti6Al4v.

The whole domain is considered to be at ambient temperature (i.e., $T_0 = 293$ K at $t = 0$), and a heat loss due to convection and radiation at the surface of the domain takes place during the laser and material interaction and can be expressed as follows:

$$-k \frac{\partial T}{\partial n} = h_c(T - T_0) + \varepsilon \sigma(T^4 + T_0^4) \quad (3)$$

The $(-)$ sign shows the heat loss from the domain surface (n), h_c is the convective heat transfer coefficient, ε is the surface emissivity coefficient, and σ is the Stefan-Boltzmann constant.

For the thermal stresses analysis, Hook's law of elasticity considering an ideal elastic-plastic body, which goes under elastic and plastic deformation due to the cyclic loading behavior of the SLM process is used:

$$\{\sigma\} = [D]\{\epsilon^e\} \quad (4)$$

$$\{\epsilon^e\} = \{\epsilon\} - \{\epsilon^p\} - \{\epsilon^t\} \quad (5)$$

$\{\sigma\}$ is the stress vector, $[D]$ is the elasticity matrix, $\{\epsilon^e\}$ is the elastic strain vector, $\{\epsilon\}$ is the total strain vector, $\{\epsilon^p\}$ is the plastic strain vector, $\{\epsilon^t\}$ is the thermal strain vector.

Results and Discussion

In the SLM process, when the laser source scans the powder layer, a rapid increase in material temperature occurs, leading to quick melting. Subsequently, as the heat source passes, the material undergoes rapid solidification and cooling. This dynamic process introduces high thermal gradients to the material, resulting in the generation of tensile and compressive residual stresses in the final part. Preliminary results of the analysis indicate that altering the laser beam shape has a discernible impact on melt pool characteristics, cooling rate, and thermal gradients within the melt region. Specifically, as the laser beam profile is changed from Gaussian to Donut, the melt pool depth decreases, and its width increases. It is mainly attributed to the reduction of the peak irradiance at the center of the beam profile

[5,6,16]. A visual representation of the laser source with Donut beam profile during scanning is depicted in Figure 2.

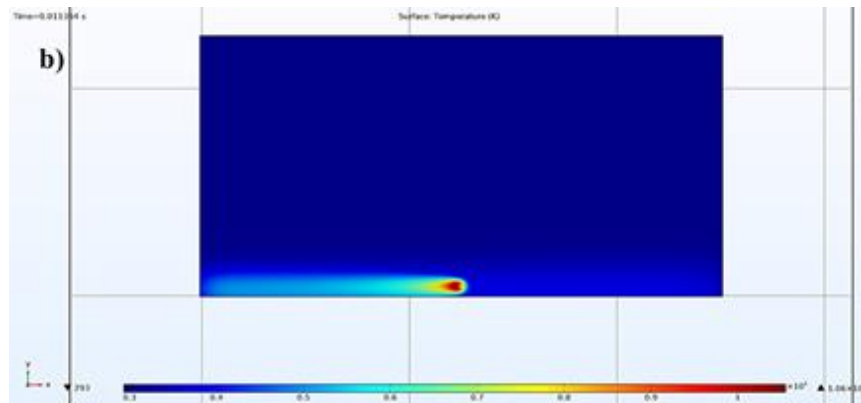


Figure 2. The laser source with a Donut profile.

The findings carry significant implications for the SLM process, suggesting that the manipulation of laser beam shape can be used to tailor the properties and quality of printed parts. This knowledge can aid in optimizing the SLM process for specific applications, potentially reducing the generation of residual stresses and enhancing the overall performance of the final part.

Conclusions

In conclusion, the SLM process, driven by the dynamic interplay of rapid material heating and cooling, gives rise to the development of complex residual stresses in the fabricated parts. The preliminary results presented in this study shed light on the potential for laser beam shape modification as a means to exert precise control over melt pool characteristics and thermal gradients. The transition from a Gaussian to a Donut beam profile was observed to bring about notable changes, notably reducing melt pool depth while increasing its width.

References

- [1] Bakhtari AR, Waris MM, Sanin C, Szczerbicki E. Evaluating Industry 4.0 Implementation Challenges Using Interpretive Structural Modeling and Fuzzy Analytic Hierarchy Process. *Cybern Syst* 2021. <https://doi.org/10.1080/01969722.2020.1871226>.
- [2] Dilberoglu UM, Gharehpapagh B, Yaman U, Dolen M. The Role of Additive Manufacturing in the Era of Industry 4.0. *Procedia Manuf* 2017;11:545–54. <https://doi.org/10.1016/j.promfg.2017.07.148>.
- [3] Gibson I, Rosen D, Stucker B. *Additive manufacturing technologies*. Springer; 2010.
- [4] Thijs L, Kempen K, Kruth J-P, Van Humbeeck J. Fine-structured aluminium products with controllable texture by selective laser melting of pre-alloyed AlSi10Mg powder. *Acta Mater* 2013;61:1809–19. <https://doi.org/10.1016/j.actamat.2012.11.052>.
- [5] Wischeropp TM, Tarhini H, Emmelmann C. Influence of laser beam profile on the selective laser melting process of AlSi10Mg. *J Laser Appl* 2020;32:022059. <https://doi.org/10.2351/7.0000100>.

- [6] Grünewald J, Gehringer F, Schmöller M, Wudy K. Influence of Ring-Shaped Beam Profiles on Process Stability and Productivity in Laser-Based Powder Bed Fusion of AISI 316L. *Metals* (Basel) 2021;11:1989. <https://doi.org/10.3390/met11121989>.
- [7] Gusarov A V., Grigoriev SN, Volosova MA, Melnik YA, Laskin A, Kotoban D V., et al. On productivity of laser additive manufacturing. *J Mater Process Technol* 2018;261:213–32. <https://doi.org/10.1016/j.jmatprotec.2018.05.033>.
- [8] Hansen KS, Kristiansen M, Olsen FO. Beam Shaping to Control of Weldpool Size in Width and Depth. *Phys Procedia* 2014;56:467–76. <https://doi.org/10.1016/j.phpro.2014.08.150>.
- [9] Rasch M, Roider C, Kohl S, Strauß J, Maurer N, Nagulin KY, et al. Shaped laser beam profiles for heat conduction welding of aluminium-copper alloys. *Opt Lasers Eng* 2019;115:179–89. <https://doi.org/10.1016/j.optlaseng.2018.11.025>.
- [10] Neira-Arce A. Thermal modeling and simulation of electron beam melting for rapid prototyping on Ti6Al4V alloys. PhD Dissertation. North Carolina State University, 2012.
- [11] Li Z, Xu R, Zhang Z, Kucukkoc I. The influence of scan length on fabricating thin-walled components in selective laser melting. *Int J Mach Tools Manuf* 2018;126:1–12. <https://doi.org/10.1016/j.ijmachtools.2017.11.012>.
- [12] Fu CH, Guo YB. Three-Dimensional Temperature Gradient Mechanism in Selective Laser Melting of Ti-6Al-4V. *J Manuf Sci Eng* 2014;136. <https://doi.org/10.1115/1.4028539>.
- [13] Fischer P, Locher M, Romano V, Weber HP, Kolossov S, Glardon R. Temperature measurements during selective laser sintering of titanium powder. *Int J Mach Tools Manuf* 2004;44:1293–6. <https://doi.org/10.1016/j.ijmachtools.2004.04.019>.
- [14] Yadroitsev I, Krakhmalev P, Yadroitsava I. Selective laser melting of Ti6Al4V alloy for biomedical applications: Temperature monitoring and microstructural evolution. *J Alloys Compd* 2014;583:404–9. <https://doi.org/10.1016/j.jallcom.2013.08.183>.
- [15] Liu S, Zhu H, Peng G, Yin J, Zeng X. Microstructure prediction of selective laser melting AlSi10Mg using finite element analysis. *Mater Des* 2018;142:319–28. <https://doi.org/10.1016/j.matdes.2018.01.022>.
- [16] Galbusera F, Caprio L, Previtali B, Demir AG. The influence of novel beam shapes on melt pool shape and mechanical properties of LPBF produced Al-alloy. *J Manuf Process* 2023;85:1024–36. <https://doi.org/10.1016/j.jmapro.2022.12.007>.

Funding

This work has received funding from the European Union’s Horizon 2020 research and innovation program under the Marie Skłodowska-Curie grant agreement No [101034425] for the project titled A2M2TECH. This study has also received funding from The Scientific and Technological Research Council of Türkiye (TUBITAK) with grant No [120C158] for the same A2M2TECH project under the TUBITAK’s 2236/B program.

Enhancing Dimensional Precision for Complex Geometries in Additive Manufacturing Post-Processing through Advanced Computing

Sultan Ullah^{1,2}, Arif MA¹, Ozkan Bulent¹

1. Department of Mechanical Engineering, Gazi University, Ankara, Turkiye

2. Eklemeli İmalat Teknolojileri Uygulama ve Araştırma Merkezi (EKTAM), Ankara, Turkiye

Abstract

This paper explores the critical challenge of achieving precise dimensional accuracy in additive manufacturing (AM) post-processing, with a specific focus on complex and intricate geometries. We emphasize the specific difficulties presented by such geometries and investigate how advanced computing solutions, including algorithms, simulations, and artificial intelligence, can be turned to address these challenges. Through empirical evidence and case studies, we demonstrate how these computational tools optimize print parameters, ensure component tolerances, and pave the way for superior dimensional precision in complex AM geometries. This research provides valuable insights for professionals and researchers seeking to improve dimensional accuracy in the context of challenging AM geometries.

Keywords: Complex geometry, dimensional accuracy, post-processing, advanced computing

Introduction

Post-processing is a critical step in manufacturing objects produced through various additive manufacturing techniques. While these technologies have revolutionized the way we create objects, they often leave behind undesired elements such as rough edges, support structures, or surface imperfections [1]. The need for post-processing arises from the desire to achieve the desired final quality and functionality of the manufactured parts. In this paper, we propose an approach and show the proof-of-concept to automatically generate trajectories for industrial robots for complex geometries. In the case of AM, some elements must be reinforced through the bottom in order to be entirely printed out. They are printed non-solid objects whose only purpose is to keep the upper layers from distorting owing to gravity. These support structures are fragile and simple to take down subsequently. These unwanted structures need to be taken out after the print is finished and the material has cooled in order to obtain the desired result. Those continue to manually carry out this time-consuming and unsafe removal operation during the post-processing step [2]. The technique used in this research is to create a robot trajectory for this task by automating the process and using only the already available data. The approach analyzes the difference between the two and then executes our experiment using the machine code and CAD data. In order to represent any type of three-dimensional object and modify the resolution based on the use case, we decided to use a voxel data structure. GPU-Voxels, an open-source framework for real-time data processing on graphics processing units, handles all voxel direction and calculation. Throughout all of the trajectory's execution, the actual object cannot sustain any adverse effects. To plan a collision-free path, the path planner makes use of a voxel representation of the robot and the tool as well as compacted surroundings. Consider that contact with the object's support structure is preferred, particularly while removing it. However, only within the support structures is contact between a tool and an item allowed. As a result, different structures are all addressed in different ways during path planning.

The voxel representation is updated during the execution of the computed trajectory based on the current joint values of the robot and the subsequent tool position. A robot-mounted tool's approach orientation in the object space is sampled in order to attain a high reachability. For the purpose of removing as much material as possible, the orientation that can reach the most target points is determined. After the initial iteration, if any unwanted material is still present, the procedure is restarted, and a new orientation is sampled. This paper will lead us on a complex getaway that combines academic understanding with real-world applications. We will present a wide range of illustrative examples to demonstrate the revolutionary potential of these computational tools. They optimize and improve print parameters as well as enforce the strict tolerances required to achieve excellent dimensional accuracy in the most complex AM designs [3-10].

Theory

Here is the theory of our study on using two robot arms to cooperate in post-processing parts with complex geometries in the context of additive manufacturing. We will acquire two robot arms equipped with end-of-arm tools suitable for post-processing operations. Ensure that these robots have the necessary sensors and control capabilities for precise and coordinated movements. Implement control software that can communicate with and control both robot arms simultaneously. This software should be capable of coordinating the motion of the two robots. Develop or use software for the control of AM processes and the generation of toolpaths for post-processing. Use of 3D scanning or other methods to obtain accurate digital representations of the parts produced by AM. This data will be used for planning and executing post-processing tasks. Develop a complex motion planning algorithm that can handle the specific geometries of the parts. This algorithm should optimize the movement of both robot arms to ensure efficient post-processing. Consider the hybrid position and force control strategy. Implement impedance control to account for interaction forces between the robot arms and the part being processed. Program the robot arms to work in tandem. While one robot arm manipulates the part, the other simultaneously performs the post-processing operation, such as grinding, polishing, or cutting. Ensure that both robot arms are aware of each other's movements to prevent collisions and to maintain a safe working environment. Implement feedback systems that provide real-time data on the progress of the post-processing operations. This includes data on the interaction forces, part surface quality, and any deviations from the planned trajectory. Develop safety protocols to ensure the safety of human operators and robots during the operation. This may involve emergency stop mechanisms and barriers to prevent accidents. Conduct iterative testing and refinement of the control algorithm and motion planning. Make adjustments based on the real-world performance of the robot arms. Validate the effectiveness of the proposed control algorithm and cooperative robot operation. Measure the quality and efficiency of the post-processing operations compared to conventional methods. Define performance metrics, such as processing time, surface finish quality, and accuracy. Collect data during the experiments, including time taken, the force exerted, and the quality of the processed parts. Analyze the data to assess the success of the cooperative robot operation in post-processing complex geometries.

Discussion

The utilization of robots in additive manufacturing (AM) post-processing offers a promising solution to address the challenges posed by complex geometric parts. In this study, we proposed and defined a route/novel control algorithm that enables two robot arms to collaborate effectively in post-processing operations. This section presents a comprehensive discussion of the key implications, limitations, and future directions of our research. This kind of study will demonstrate the cooperative operation of two

robot arms significantly enhances the efficiency of post-processing for complex geometries. Traditional methods often struggle to maneuver and manipulate tools in intricate and convoluted shapes. In contrast, the use of two robot arms allows for simultaneous manipulation and processing, leading to a remarkable reduction in processing time. One of the notable advantages of our approach is the ability to maintain a high level of quality and precision. By incorporating impedance control and real-time feedback mechanisms, the robot arms adapt to the varying topologies of the parts. The interactions between the arms and the workpiece will be carefully managed, resulting in smoother surfaces and fewer defects. The success of our research will present significant implications for various real-world applications. Beyond AM, this cooperative robot approach can be applied in industries that require precise post-processing of complex parts, such as aerospace, automotive, and medical device manufacturing.

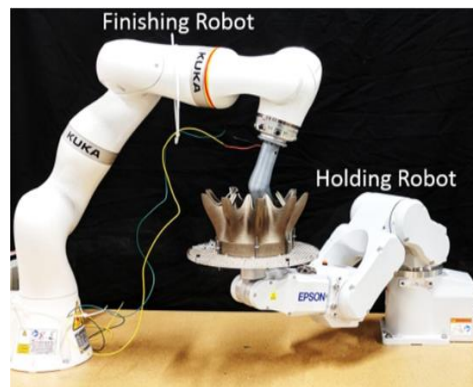


Figure 1. Multi degree of freedom robots for the post-processing of complex geometry (A.M Kabir 2018).

Conclusions

This research paves the way for several future directions. To further enhance the cooperative robot approach, future studies may explore advanced algorithms for better path planning, human-robot collaboration, and the integration of additional sensors for more precise feedback. Furthermore, research into cost-effective solutions for small and medium-sized enterprises could make this technology more accessible. In conclusion, our aim is to demonstrate using two robot arms to collaborate in post-processing complex geometric parts in AM offers significant advantages in terms of efficiency, quality, and safety. The successful implementation of this approach has the potential to revolutionize the post-processing phase in industries where precise and intricate work is required. Our research contributes to the ongoing efforts to optimize manufacturing processes and improve the quality of products in various industries.

References

- [1] P. Urhal, A. Weightman, C. Diver, and P. Bartolo, "Robot assisted additive manufacturing: A review," *Robot. Comput.-Integr. Manuf.*, vol. 59, pp. 335–345, 2019.
- [2] B. BACROIX, "Post-processing in Additive Manufacturing," *Addit. Manuf. Met. Alloys 2 Microstruct. Post-Process. Use Prop.*, pp. 99–161, 2023.

- [3] P. Becker, C. Eichmann, A. Roennau, and R. Dillmann, “Automation of Post-Processing in Additive Manufacturing with Industrial Robots,” in 2020 IEEE 16th International Conference on Automation Science and Engineering (CASE), 2020, pp. 1578–1583. doi: 10.1109/CASE48305.2020.9216955.
- [4] P. M. Bhatt, R. K. Malhan, A. V. Shembekar, Y. J. Yoon, and S. K. Gupta, “Expanding capabilities of additive manufacturing through use of robotics technologies: A survey,” *Addit. Manuf.*, vol. 31, p. 100933, 2020.
- [5] F. Chen, H. Zhao, D. Li, L. Chen, T. Chao, and H. Ding, “Contact force control and vibration suppression in robotic polishing with a smart end effector,” *Robot. Comput.-Integr. Manuf.*, 2019, doi: 10.1016/J.RCIM.2018.12.019.
- [6] W. Ji and L. Wang, “Industrial robotic machining: a review,” *Int. J. Adv. Manuf. Technol.*, vol. 103, pp. 1239–1255, 2019.
- [7] J. Li et al., “A high-bandwidth end-effector with active force control for robotic polishing,” *IEEE Access*, vol. 8, pp. 169122–169135, 2020.
- [8] I. F. Onstein, O. Semeniuta, and M. Bjerkeng, “Deburring using robot manipulators: A review,” in 2020 3rd international symposium on small-scale intelligent manufacturing systems (SIMS), IEEE, 2020, pp. 1–7.
- [9] X. Peng, L. Kong, J. Y. H. Fuh, and H. Wang, “A review of post-processing technologies in additive manufacturing,” *J. Manuf. Mater. Process.*, vol. 5, no. 2, p. 38, 2021.
- [10] J. Duro-Royo, L. Mogas-Soldevila, and N. Oxman, “Flow-based fabrication: An integrated computational workflow for design and digital additive manufacturing of multifunctional heterogeneously structured objects,” *Comput.-Aided Des.*, vol. 69, pp. 143–154, 2015.

Acknowledgements

“This work has received funding from the European Union’s Horizon 2020 research and innovation program under the Marie Skłodowska-Curie grant agreement No 101034425 for the project titled A2M2TECH. This study has also received funding from the Scientific and Technological Research Council of Türkiye (TUBITAK) with the grant No 120C158 for the same A2M2TECH project under the TUBITAK’s 2236/B program”.

Additive Manufacturing Design with Overhang Constraint Based on Reliability-Based Topology Optimization Approach

Fahri Murat^{1,2*} and İrfan Kaymaz^{1,2}

1. Department of Mechanical Engineering, Faculty of Engineering and Architecture, Erzurum Technical University, Erzurum, Turkey 25050

2. Biomechanics Research Group, Erzurum Technical University, Erzurum, Turkey 25050

Abstract

This study explores the integration of overhang constraints and Reliability-Based Topology Optimization (RBTO) within the realm of Additive Manufacturing (AM). While AM enables intricate component fabrication, it grapples with the challenge of support structures. By incorporating overhang constraints into topology optimization, the feasibility of self-supporting structures is enhanced. RBTO, on the other hand, addresses uncertainties associated with design variables, ultimately bolstering reliability. This research delves into solutions for the build direction parameter using both deterministic and RBTO algorithms. It evaluates topological properties, compliance, sensitivity, and density filters, alongside optimization techniques such as the Method of Moving Asymptotes (MMA) criterion and Optimal Criteria (OC). The findings contribute to the synergy of overhang constraints and RBTO within AM topology optimization, resulting in improved designs that account for uncertainties. The study not only advances computational efficiency but also stabilizes the optimization of build direction parameters, providing valuable insights for future applications of AM.

Keywords: Topology optimization, Reliability analysis, Additive manufacturing, Overhang constraint.

Introduction

Topology optimization is an advanced structural design method that can achieve the optimum structural configuration through the best material distribution under specific boundary conditions [1]–[3]. The use of Additive Manufacturing (AM) technology enables the creation of unique and innovative designs that cannot be achieved through traditional manufacturing methods in various industries [4]–[6]. To fully benefit from both topology optimization and AM, it is necessary to integrate design constraints into topology optimization [7]. Existing topology optimization approaches in the literature, to our knowledge, do not consider overhang angle limitations, resulting in optimized designs that often do not self-support and therefore cannot be produced independently of support structures [8].

Support structures are required to prevent overhang from collapsing during the AM process, and these supports are usually removed after manufacturing. Support structures used during manufacturing increase material consumption, post-processing time, and complexities [9], [10]. Therefore, it has been reported that the most significant problem limiting producibility in AM is support structures [11]. Consequently, one of the most prominent typical AM constraints for topology optimization is the overhang constraint [12].

In structural design, natural uncertainties often encompass design variables such as material parameters (e.g., elastic modulus, yield strength) and applied forces [13]. However, deterministic topology

optimization fails to account for the uncertainties of these random variables in the solution phase. Addressing these structural uncertainties within deterministic problems leads to more reliable designs. As a result, Reliability-Based Topology Optimization (RBTO) has emerged as a branch of optimization [14], [15]. RBTO aims to account for uncertainties in applied loads and other random variables during the solution process [16]–[20]. Using the RBTO model, different topologies are obtained depending on the targeted reliability levels, which are different from those obtained through deterministic topology optimization.

In this research, the build direction parameter used in additive manufacturing is solved by adapting it to both deterministic and RBTO algorithms. The comparison focuses on the topological characteristics and compliance of the intended design under four different direction parameters. The implementation of the solution was performed using 88 lines of MATLAB TO code on structures such as the Messerschmitt-Bolkow-Blohm (MBB) beam [21]. We conducted a comparative evaluation of sensitivity and density filters while obtaining the solution. As part of our optimization methodology, we used the MATLAB Optimization Toolbox's interior point algorithm to update design variables. For the example addressed in this research, a comparative analysis of the results was provided by considering both the Method of Moving Asymptotes (MMA) and the Optimal Criteria (OC) when addressing the RBTO problem.

Deterministic Topology Optimization

In this study, the focus is on the minimum compliance topology optimization algorithm, as illustrated in Equation 1. The objective here is to discover the material distribution (represented by ρ) throughout the design space that results in maximum stiffness while adhering to a specific volume constraint.

$$\begin{aligned} \min C(\rho) &= \mathbf{d}^T \mathbf{K} \mathbf{d} = \sum_{e=1}^N (\rho_e)^p d_e^T k_0 d_e \\ \text{subject to} \quad & \frac{V(\rho)}{V_0} \leq f \end{aligned} \quad (1)$$

$$\mathbf{K} \mathbf{d} = \mathbf{f}$$

$$0 < \rho_{\min} \leq \rho_e \leq 1$$

The vector ρ represents the design variables within the minimum compliance topology optimization algorithm. The stiffness matrix, displacement vector, and force vector are denoted by \mathbf{K} , \mathbf{d} , and \mathbf{f} , respectively. N refers to the number of elements that discretize the design area while d_e and k_0 are the displacement of an element and elemental stiffness matrix, respectively. The material volume and the design area volume are represented by $V(\rho)$ and V_0 , with f as a pre-determined upper limit in the volume fraction. ρ_{\min} is the minimum relative density used to prevent singularity in the model. When $\rho_e \cong 0$, it signifies that the corresponding element within the structure is considered empty, meaning it does not contribute to the physical attributes of the design.

Reliability Evaluation

Within the scope of topology optimization designs, the reliability criteria incorporate the uncertainties associated with random variables. This methodology is embedded within the optimization process to identify a dependable and ideal configuration for a structure in a specified area. In conducting a reliability analysis, a normalized vector of the random variable (u) and a reliability index (β) are introduced [22]. When dealing with a normal distribution, the expressions for u and β are defined as follows:

$$u_j = \frac{y_j - m_{y_j}}{\sigma_{y_j}}$$

$$\beta = \min(\sqrt{\mathbf{u}^T \mathbf{u}}) \quad (2)$$

where y_j is the j 'th random variable with a mean value of m_{y_j} and a standard deviation σ_{y_j} . The vector \mathbf{u} defines the relationship between random variables and design variables. Therefore, an RBTO (Reliability-Based Topology Optimization) problem, formulated by integrating the reliability analysis into the topology optimization problem, can be described as follows:

$$\begin{aligned} \min \quad & C(\boldsymbol{\rho}) = \mathbf{d}^T \mathbf{K} \mathbf{d} = \sum_{e=1}^N (\rho_e)^p d_e^T k_0 d_e \\ \text{subject to} \quad & \beta(\mathbf{u}) \geq \beta_t \\ & \frac{V(\boldsymbol{\rho}, \mathbf{y}, \mathbf{u})}{V_0} \leq f \end{aligned} \quad (3)$$

$$\mathbf{K}(\boldsymbol{\rho}, \mathbf{y}, \mathbf{u}) \cdot \mathbf{d}(\boldsymbol{\rho}, \mathbf{y}, \mathbf{u}) = \mathbf{f}(\mathbf{y}, \mathbf{u})$$

$$0 < \rho_{\min} \leq \rho_e \leq 1$$

Here, β and β_t represent the system's reliability index and target reliability index, respectively, and \mathbf{u} represents random variables described in the standard normal space.

AM filter concept

The frequently mentioned critical angle is approximately 45 degrees [23]–[25]. If a part has regions with overhang angles falling below this critical angle in the selected build direction, it cannot self-support and cannot be printed in its current state. The support region in this context refers to the three-square elements in the lower layer, as shown in Figure 1.

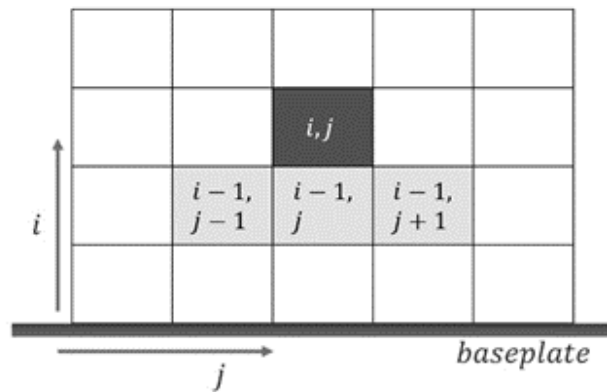


Figure 1. Definition of supporting regions for element i,j [26]

In this study, reliability analysis was adapted to the existing topology optimization approach, and an AM constraint was added to consider the direction of the printed part. Langelaar's suggested AM filter was incorporated into the well-known 88-line topology optimization code developed by [21], [27]. By default, this code uses an OC optimizer. In this procedure, an inner loop continuously evaluates the volume constraint, meaning the AM filter is called multiple times, leading to an increase in

computational time. As a result, modifications were made to the code to accommodate MMA [28] and interior point methods. We compared the Optimality Criteria (OC), Method of Moving Asymptotes (MMA), and interior point methods during the design iteration process. The assessment of the AM filter played a significant role in shaping our results. Equation 4 shows the modification of the AM filter to fit the RBTO problem:

$$\begin{aligned}
 &\min \quad C(\boldsymbol{\rho}) = \mathbf{d}^T \mathbf{K} \mathbf{d}(\mathbf{p}) \\
 &\text{subject to} \quad \beta(\mathbf{u}) \geq \beta_t \\
 &\quad \frac{V(\boldsymbol{\rho}, \mathbf{y}, \mathbf{u}, \mathbf{p})}{V_0} \leq f \\
 &\quad \mathbf{K}(\boldsymbol{\rho}, \mathbf{y}, \mathbf{u}, \mathbf{p}) \cdot \mathbf{d}(\boldsymbol{\rho}, \mathbf{y}, \mathbf{u}, \mathbf{p}) = \mathbf{f}(\mathbf{y}, \mathbf{u}, \mathbf{p}) \\
 &\quad 0 < \rho_{min} \leq \rho_e \leq 1, \\
 &\quad 0 < \mathbf{b} \leq 1
 \end{aligned} \tag{4}$$

Here, the variable \mathbf{p} governs the area of printed density, while the variable \mathbf{b} is responsible for controlling the blueprint area throughout the optimization procedure. The flow chart that outlines the formulation represented by Equation 4 is provided in Figure 2.

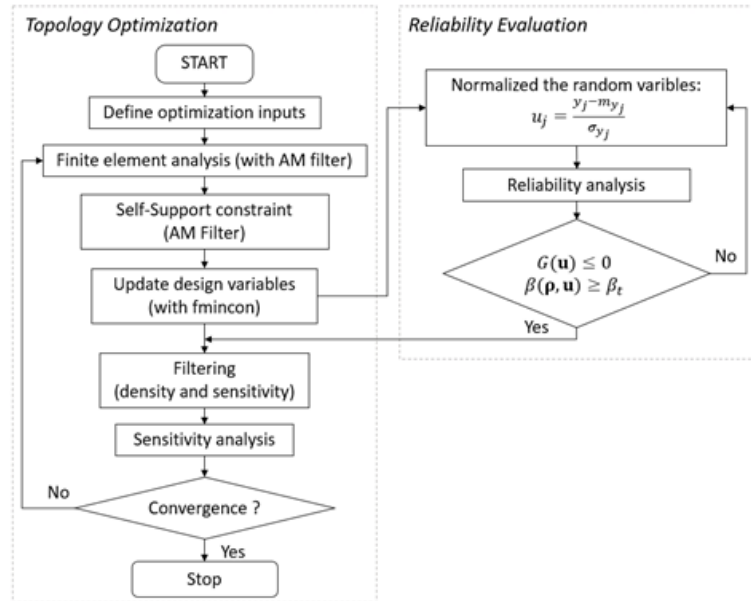


Figure 2. Flowchart for RBTO procedure using AM filter.

Numerical example: MBB beam

In the current research, the minimization of linear elastic compliance under volume constraints was achieved using the SIMP material interpolation technique [29], [30]. The study considered the Messerschmitt-Bölkow-Blohm (MBB) beam. Material properties with a symmetric beam and Young's modulus $E=100\text{GPa}$ and Poisson's ratio $\nu=0.3$.

The optimization process was performed in four different table layouts (West 'W', East 'E', North 'N', South 'S') using the 88-line TO code. A penalty factor of $p=3$ was applied to reduce the influence of medium-density (gray-colored) elements in topology optimization. Assumptions included an $r_{min}=1.2$ radius filter, $V_f=0.5$ volume ratio, and $\beta_t=3$ target reliability index.

For the MBB beam, design domains with dimensions of 30×20 and 180×60 , as shown in Figure 3, were utilized. The maximum number of iterations was limited to 300 for all scenarios evaluated. The results clearly demonstrated the influence of different build directions, leading to the emergence of different topologies. Most importantly, all resulting designs fully complied with the Additive Manufacturing constraint, which is a factor that considers a specific build direction.

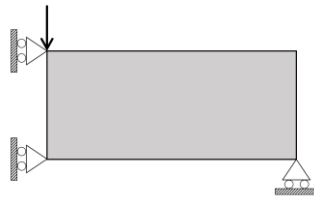


Figure 3. MBB symmetric beam and boundary conditions

Figure 4 depicts the deterministic Topology Optimization (DTO) results obtained for the MBB beam in four unique build directions (W, E, N, S) using the Additive Manufacturing (AM) filter applied in this research. As a result, a distribution was achieved that eliminates the need for support structures in the manufacturing direction. When the sensitivity filter ($ft=1$) was used in conjunction with the interior point algorithm, subsequent solutions were performed with the sensitivity filter due to the stability of the results compared to the density filter.

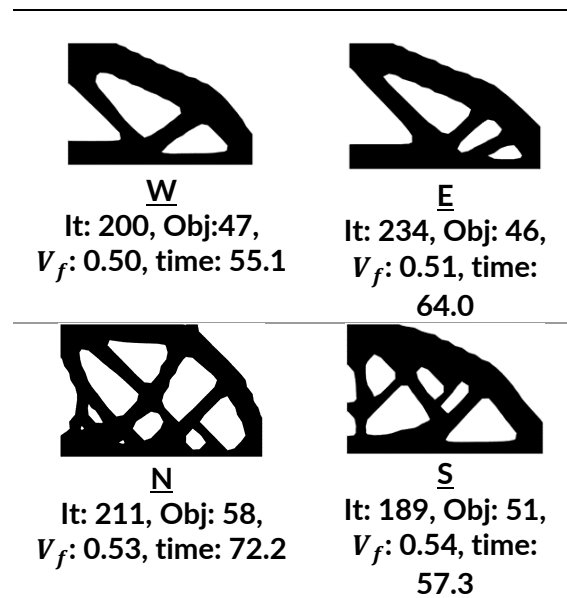


Figure 4. Deterministic topology optimization designs of 30×20 MBB beams employing the interior-point approach and AM filter in four different build directions, with the use of a sensitivity filter.

The West direction is preferred as it provides the necessary compliance without impeding performance. The North and South directions require additional material to support the structure, resulting in increased compliance. Small changes in the East and West designs lead to minor increases in compliance.

Figure 5 displays both the results of RBTO and RBTO with the AM filter. The layered manufacturing table highlighted in blue lines on the optimal figures represents the 'W' direction evaluated for minimum compliance, consistent with previous findings. Additionally, the defined optimal topologies were manufactured using a 3D printer (Crealty Ender-6, Shenzhen, China).







	30x20	90x60	3D Printing (90x60)
RBTO	 It: 87, Obj: 54, V_f : 0.5, time: 83.94	 It: 88, Obj: 62 V_f :0.50 time:954	 Total time: 71min Support time: 12min
AM- RBTO /W	 It: 29, Obj: 53, V_f : 0.51, time: 23	 It: 76, Obj: 53, V_f : 0.49, time: 752	 Total time: 58min Without support

Figure 5. RBTO design of MBB beam using interior-point with AM filter with sensitivity filter

Based on the presented results, the AM-RBTO/W algorithm consistently outperforms in structural design by achieving lower values for the objective function. Specifically, in the case of a 30x20 structure size, the AM-RBTO/W algorithm not only provides a lower objective function value but also delivers a faster solution compared to the RBTO algorithm. Even in the scenario where the objective function values are the same for a 90x60 structure size, the AM-RBTO/W algorithm reaches a solution more quickly, maintaining its advantage. When comparing 3D printing times, it was observed that the algorithm incorporating the AM filter completed the job 13 minutes faster.

These results collectively demonstrate the effectiveness of optimization in balancing material consumption against structural performance. A reduced objective function value indicates improved structural performance, while an increased volume ratio corresponds to using more material.

Conclusions

In this study, designs that consider reliability criteria in topology optimization were realized using the AM filter proposed by Langelaar (2017). Density-based topology optimization produces reliable designs based on the build direction in a typical powder-bed-based AM process. This eliminates parts that require support structures and cannot be printed from the design space. The proposed method was tested using a numerical example commonly used in the literature. In this context, it was observed that the topologies of reliability-based optimization problems differed from deterministic results. Similarly, analyses using the AM filter showed that additional material was unnecessary for self-supporting structures. To validate the accuracy of the results obtained from sample solutions, optimal topologies were 3D-printed and examined. As seen in the example, the use of the AM filter significantly reduced printing time and resulted in less material consumption. Furthermore, additional research is needed to adapt this method to three dimensions and address more complex engineering challenges.

References

- [1] O. Sigmund ve K. Maute, “Topology optimization approaches”, *Struct Multidisc Optim*, c. 48, sy 6, ss. 1031-1055, Ara. 2013, doi: 10.1007/s00158-013-0978-6.
- [2] M. Jalalpour ve M. Tootkaboni, “An efficient approach to reliability-based topology optimization for continua under material uncertainty”, *Struct Multidisc Optim*, c. 53, sy 4, ss. 759-772, Nis. 2016, doi: 10.1007/s00158-015-1360-7.
- [3] M. P. Bendsøe ve O. Sigmund, *Topology optimization: theory, methods, and applications*, 2. ed., corr. Printing. içinde Engineering online library. Berlin: Springer, 2004.
- [4] Z. Zhao ve X. S. Zhang, “Additive Manufacturing of Topology-Optimized Graded Porous Structures: An Experimental Study”, *JOM*, c. 73, sy 7, ss. 2022-2030, Tem. 2021, doi: 10.1007/s11837-021-04705-y.
- [5] O. Sigmund, “A 99 line topology optimization code written in Matlab”, *Structural and Multidisciplinary Optimization*, c. 21, sy 2, ss. 120-127, Nis. 2001, doi: 10.1007/s001580050176.
- [6] I. Kaymaz, F. Murat, İ. H. Korkmaz, ve O. Yavuz, “A new design for the humerus fixation plate using a novel reliability-based topology optimization approach to mitigate the stress shielding effect”, *Clinical Biomechanics*, c. 99, s. 105768, Eki. 2022, doi: 10.1016/j.clinbiomech.2022.105768.
- [7] J. Zhu, H. Zhou, C. Wang, L. Zhou, S. Yuan, ve W. Zhang, “A review of topology optimization for additive manufacturing: Status and challenges”, *Chinese Journal of Aeronautics*, c. 34, sy 1, ss. 91-110, Oca. 2021, doi: 10.1016/j.cja.2020.09.020.
- [8] Langelaar, “Topology optimization of 3D self-supporting structures for additive manufacturing”, *Additive Manufacturing*, c. 12, ss. 60-70, Eki. 2016, doi: 10.1016/j.addma.2016.06.010.
- [9] D. Walton ve H. Moztarzadeh, “Design and Development of an Additive Manufactured Component by Topology Optimisation”, *Procedia CIRP*, c. 60, ss. 205-210, Oca. 2017, doi: 10.1016/j.procir.2017.03.027.
- [10] S. C. Subedi, A. Shahba, M. Thevamaran, D. J. Thoma, ve K. Suresh, “Towards the optimal design of support structures for laser powder bed fusion-based metal additive manufacturing via thermal equivalent static loads”, *Additive Manufacturing*, c. 57, s. 102956, Eyl. 2022, doi: 10.1016/j.addma.2022.102956.
- [11] T. Miki, “Self-support topology optimization considering distortion for metal additive manufacturing”, *Computer Methods in Applied Mechanics and Engineering*, c. 404, s. 115821, Şub. 2023, doi: 10.1016/j.cma.2022.115821.
- [12] M. Mani, P. Witherell, ve H. Jee, *Design Rules for Additive Manufacturing: A Categorization*. 2017. doi: 10.1115/DETC2017-68446.
- [13] Y.-S. Eom, K.-S. Yoo, J.-Y. Park, ve S.-Y. Han, “Reliability-based topology optimization using a standard response surface method for three-dimensional structures”, *Struct Multidisc Optim*, c. 43, sy 2, ss. 287-295, Şub. 2011, doi: 10.1007/s00158-010-0569-8.

- [14] G. Kharmanda, A. Mohamed, ve M. Lemaire, "Integration of Reliability-Based Design Optimization within CAD and Finite Element Models", içinde Recent Advances in Integrated Design and Manufacturing in Mechanical Engineering, G. Gogu, D. Coutellier, P. Chedmail, ve P. Ray, Ed., Dordrecht: Springer Netherlands, 2003, ss. 453-462. doi: 10.1007/978-94-017-0161-7_44.
- [15] C. Kim, S. Wang, E. Kang, ve K. Lee, "New Design Process for Reliability-Based Topology Optimization of a Laser Scanned Model", s. 24, 2006.
- [16] S. Bobby, A. Suksuwan, S. M. J. Spence, ve A. Kareem, "Reliability-based topology optimization of uncertain building systems subject to stochastic excitation", Structural Safety, c. 66, ss. 1-16, May. 2017, doi: 10.1016/j.strusafe.2017.01.005.
- [17] K.-H. Cho, J.-Y. Park, S.-P. Ryu, J.-Y. Park, ve S.-Y. Han, "Reliability-based topology optimization based on bidirectional evolutionary structural optimization using multi-objective sensitivity numbers", Int.J Automot. Technol., c. 12, sy 6, ss. 849-856, Ara. 2011, doi: 10.1007/s12239-011-0097-6.
- [18] M. Jalalpour, J. K. Guest, ve T. Igusa, "Reliability-based topology optimization of trusses with stochastic stiffness", Structural Safety, c. 43, ss. 41-49, Tem. 2013, doi: 10.1016/j.strusafe.2013.02.003.
- [19] Kharmanda, N. Olhoff, A. Mohamed, ve M. Lemaire, "Reliability-based topology optimization", Struct Multidisc Optim, c. 26, sy 5, ss. 295-307, Mar. 2004, doi: 10.1007/s00158-003-0322-7.
- [20] C. Kim, S. Wang, K. Rae, H. Moon, ve K. K. Choi, "Reliability-based topology optimization with uncertainties", J Mech Sci Technol, c. 20, sy 4, s. 494, Nis. 2006, doi: 10.1007/BF02916480.
- [21] E. Andreassen, A. Clausen, M. Schevenels, B. S. Lazarov, ve O. Sigmund, "Efficient topology optimization in MATLAB using 88 lines of code", Struct Multidisc Optim, c. 43, sy 1, ss. 1-16, Oca. 2011, doi: 10.1007/s00158-010-0594-7.
- [22] A. M. Hasofer ve N. C. Lind, "Exact and Invariant Second-Moment Code Format", Journal of the Engineering Mechanics Division, c. 100, ss. 111-121, 1974.
- [23] J. Kranz, D. Herzog, ve C. Emmelmann, "Design guidelines for laser additive manufacturing of lightweight structures in TiAl6V4", Journal of Laser Applications, c. 27, sy S1, s. S14001, Şub. 2015, doi: 10.2351/1.4885235.
- [24] R. Mertens, S. Clijsters, K. Kempen, ve J.-P. Kruth, "Optimization of Scan Strategies in Selective Laser Melting of Aluminum Parts With Downfacing Areas", Journal of Manufacturing Science and Engineering, c. 136, sy 6, Eki. 2014, doi: 10.1115/1.4028620.
- [25] D. Wang, Y. Yang, Z. Yi, ve X. Su, "Research on the fabricating quality optimization of the overhanging surface in SLM process", Int J Adv Manuf Technol, c. 65, sy 9, ss. 1471-1484, Nis. 2013, doi: 10.1007/s00170-012-4271-4.
- [26] J. Zou, Y. Zhang, ve Z. Feng, "Topology optimization for additive manufacturing with self-supporting constraint", Struct Multidisc Optim, c. 63, sy 5, ss. 2341-2353, May. 2021, doi: 10.1007/s00158-020-02815-w.

- [27] M. Langelaar, “An additive manufacturing filter for topology optimization of print-ready designs”, *Struct Multidisc Optim*, c. 55, sy 3, ss. 871-883, Mar. 2017, doi: 10.1007/s00158-016-1522-2.
- [28] K. Svanberg, “The method of moving asymptotes—a new method for structural optimization”, *International Journal for Numerical Methods in Engineering*, c. 24, sy 2, ss. 359-373, 1987, doi: 10.1002/nme.1620240207.
- [29] M. P. Bendsøe ve N. Kikuchi, “Generating optimal topologies in structural design using a homogenization method”, *Computer Methods in Applied Mechanics and Engineering*, c. 71, sy 2, ss. 197-224, Kas. 1988, doi: 10.1016/0045-7825(88)90086-2.
- [30] G. I. N. Rozvany, M. Zhou, ve T. Birker, “Generalized shape optimization without homogenization”, *Structural Optimization*, c. 4, sy 3, ss. 250-252, Eyl. 1992, doi: 10.1007/BF01742754.

Acknowledgements

This study is supported by the Scientific and Technological Research Council of Turkey (TUBITAK) under the Project code TUBITAK-218M425. We would like to thank TÜBİTAK for their contributions.

Biodegradable Magnesium Bone Plates; Simulation Based Predictive Model for Controlled Degradation

Muhammad Usama ZAHEER¹, Cenk AKTAS³, Yogendra Kumar MISHRA², Mehmet Fatih AYCAN¹

1. Gazi University, Mechanical Engineering Department, Ankara, 06500, Turkey.

2. Mads Clausen Institute (MCI) University of Southern Denmark.

3. Multicomponent Materials, Institute of Materials Science, Faculty of Engineering, Kiel University, Kaiserstr. 2, 24143 Kiel, Germany

Abstract

Biodegradable materials have garnered significant attention in the field of orthopedics as an innovative solution for fracture fixation devices. Among these materials, magnesium (Mg) alloys have emerged as promising candidates due to their biocompatibility and mechanical properties closely resembling those of human bone. Additive manufacturing (AM) techniques, such as 3D printing, have revolutionized the production of biodegradable Mg bone plates, offering precise control over the geometry and structure of the implants.

However, one of the primary challenges associated with Mg implants is their fast degradation rate, which can compromise their structural integrity and performance. Corrosion, and Hydrogen Evolution are the main causes for fast degradation of Mg implants. Coatings play a crucial role in controlling the degradation rate of magnesium (Mg) implants. They act as protective barriers between the Mg implant and the surrounding physiological environment, slowing down the corrosion process and thereby influencing the overall degradation kinetics. Polylactic Acid (PLA) and Poly(lactic-co-glycolic acid) (PLGA), Hydroxyapatite (HA), Phosphate-Based Coatings, Hydroxyapatite-Polymer Composites, and Metallic Coatings, can offer both mechanical strength and controlled degradation characteristics.

In this current study we developed a simulation model to estimate the degradation behavior of Mg implants which can successfully predict their fast degradation rate and changes in the shape with respect to time. As this is ongoing work, in the later stage we will perform in-vitro tests after developing certain coatings on the bone implants and improve their degradation time. In addition, changes in the shape of the bone implant will also be predicted and problems with it will be rectified. This work aims to offer meaningful guidelines for researchers for future study.

Keywords: Mg Implant, Additive Manufacturing, Coatings, Degradation Simulation, Bone Plate

Introduction

Bioresorbable materials, particularly magnesium (Mg) alloys, have revolutionized the field of orthopedics and bone implant technology [1,2]. These innovative materials are designed to serve as temporary scaffolds or implants within the human body, gradually dissolving over time while facilitating bone healing and regeneration [2]. This groundbreaking approach eliminates the need for a second surgery to remove traditional metal implants and minimizes the risk of long-term complications [3]. Mg bone implants have gained significant attention due to their biocompatibility, mechanical properties, and

ability to support the body's natural healing processes [4]. In this context, they represent a promising avenue for improving patient outcomes and reducing the burden associated with permanent implants.[1]

However, the use of magnesium (Mg) bone implants can be restricted due to their early degradation in the human body [5]. This degradation may limit their application in scenarios where long-term implant stability is essential, such as load-bearing situations or cases requiring permanent implantation [6]. Mg implants are typically chosen for situations where temporary support aligns with the patient's healing process and where the implant's gradual dissolution is advantageous for bone healing and regeneration. In order to overcome this issue different coatings or hybrid implants or composite implants can be utilized to control the early degradation of the mg implants [7].

In this current work we developed a simulation model which can predict the different hybrid or pure Mg implants degradation under human body environment. The purpose of the study is to use different coating techniques in the future along with additive manufacturing technologies to delay mg degradation and make them adoptable for the orthopedic applications.

Materials and Methods

In this current work we employed materials and methods section from literature as the in vitro degradation of different Mg Alloys is already performed. We later simulated the results according to provided parameters. Three magnesium-based materials were employed in this research: Mg2Ag, Mg10Gd, and pure magnesium. These materials were cast at Helmholtz-Zentrum (HZG) in Gaeltacht, Germany. To carry out the casting process, high-purity materials were utilized, including magnesium (99.99%), gadolinium (99.95%), and silver (99.99%) [8].

For in vitro cell experiments, discs with a diameter of 10 mm and a height of 1.5 mm from extruded rods were fabricated [8].

To achieve the desired dimensions, the extruded rods of pure magnesium and Mg10Gd (with an initial diameter of 6 mm) were reduced to 1.6 mm through a turning process conducted with Ernst Wittner GesmbH in Vienna, Austria. On the other hand, the extruded Mg2Ag rods were transformed into wires using hardened steel drawplates with varying wire gauges and a drawing bench. This reshaped the metal and reduced the wire thickness. Subsequently, the wires underwent an annealing process at 300°C for approximately 45 minutes in a furnace between 1-3 wire drawing steps. The diameter of the Mg2Ag wires was ultimately reduced to 1.6 mm [8].

Following g production, all samples underwent sterilization through gamma radiation at a dose of 29.2 kGy, a procedure performed by BBF GmbH in Stuttgart Germany [8].

***In vitro* Test Results**

Even though gadolinium and silver is used, the degradation behavior of the mg was not significantly enhanced. Fig 1 and 2 provides the in vitro test results until 12 weeks in the hank solution of the Mg alloys.

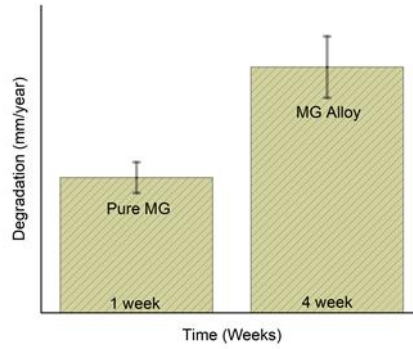


Figure 1. Degradation behavior of pure Mg in comparison to the MG alloys at 4 weeks

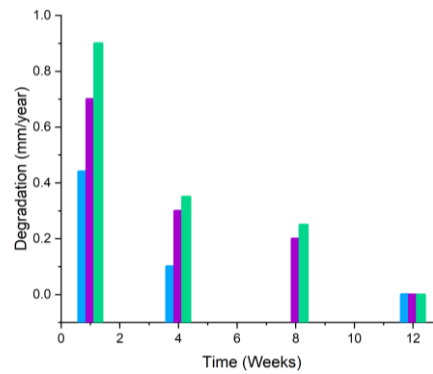


Figure 1. Degradation behavior of pure Mg, Gadolinium and Silver alloy

Abaqus Governing Equations; Degradation Simulation

Oblique or longitudinal fractures in the human usually take 4 months to completely heal. But as we know high strength metals causes stress shielding while there is always a risk of refracture for low strength materials. Biodegradable Mg implants are the best option for implantation.

Using the in vitro test results we given in the above figures we calibrated our model to provide complete degradation after 4 weeks while keeping degradation rate constant. Ficks law of diffusion is utilized as a hit a trial methos using Simulia Abaqus with Python subscribing to create a simulation for the degradation behavior. Ficks Law states that;

$$J = -D \frac{dC}{dx}$$

J represents the flux or the rate of diffusion (amount of substance passing through a unit area per unit time).

D is the diffusion coefficient or diffusivity, which quantifies how easily the substance can move through the medium. It depends on the properties of the substance and the medium.

dC/dx is the concentration gradient, which represents the change in concentration of the substance with respect to distance. It indicates how the concentration varies along the path of diffusion.

In our simulation whole bone plate model is divided into mesh sections and each element section is provided with the mechanical properties of the MG or MG alloy. As we know with degradation, stiffness

of the implant material must be reduced. We assumed that initial diffusion of the body fluids inside an element is 0 while it has its maximum Elastic Modulus E . As the amount of diffusion increases from 0 in an element and its value is multiplied with the E and the new E value is updated in the next iteration. While when the diffusion reaches 99.9 percent Abaqus removes the element as it becomes unable to support any kind of load hence it predicts the shape changes degradation. This iterative simulation continues for 12 weeks and final result provides the actual shape of the MG implant if it is emersed inside the human body. Figure 3 provides an overview of the simulation process.

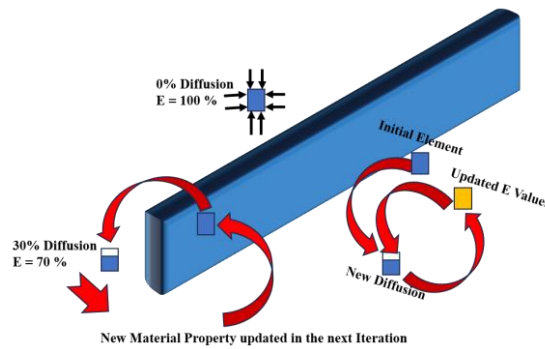


Figure 3. Simulation process for degradation simulation

Results and Discussion

It's interesting to note that developed Mg implants cannot be used without further processing as they will provide a destructive result in the biomedical implants for orthopedics.

We allowed diffusion from all the exposed sides of the implant including the screw holes but as the time passes screw holes also experience fast degradation, making the implants unreliable during early stages of implantation. Figure 4 provides the shape the degradation result of the MG implant.

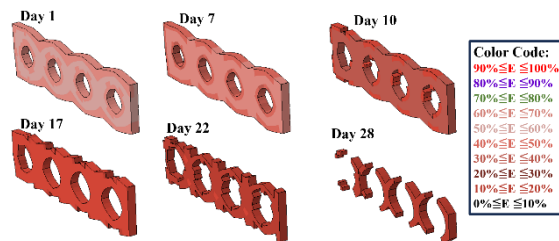


Figure 4. Results of the degradation of the Mg Implant

As it can be seen from the Figure 4 that even after 1st day degradation of the elements in contact with the medium is started to degrade while the screw holes got widen making it unusable for the rest of the time.

So we can predict that it is not worthy to be used in its initial condition while coatings or other processes applied over the surface to delay the degradation process.

Conclusion

It is safe to conclude that in order to use biodegradable MG implants extra processes must be employed. Coatings which can delay the healing process or the hybrid models with half biodegradable parts can be utilized as the future implants in this field.

As we are working in this area, performing in vitro tests and different coatings will be the future works for our group.

Funding

This work has received funding from, the European Union's Horizon 2020 research and innovation program under the Marie Skłodowska-Curie grant agreement No 101034425 for the project titled A2M2TECH. This study has also received funding from The Scientific and Technological Research Council of Türkiye (TUBITAK) with the grant No 120C158 for the same A2M2TECH project under the TUBITAK's 2236/B program.

Acknowledgements

We acknowledge TUBITAK and Marie Skłodowska-Curie for their generous help.

References

- [1] Tsakiris V, Tardei C, Clicinschi FM. Biodegradable Mg alloys for orthopedic implants—A review. *Journal of Magnesium and Alloys*. 2021;9(6):1884-1905.
- [2] Sekar P, Narendranath S, Desai V. Recent progress in in vivo studies and clinical applications of magnesium based biodegradable implants—a review. *Journal of Magnesium and Alloys*. 2021;9(4):1147-1163.
- [3] Wang JL, Xu JK, Hopkins C, et al. Biodegradable magnesium-based implants in orthopedics—a general review and perspectives. *Advanced science*. 2020;7(8):1902443.
- [4] Wang Y, Fu P, Wang N, et al. Challenges and solutions for the additive manufacturing of biodegradable magnesium implants. *Engineering*. 2020;6(11):1267-1275.
- [5] Uppal G, Thakur A, Chauhan A, et al. Magnesium based implants for functional bone tissue regeneration—A review. *Journal of Magnesium and Alloys*. 2022;10(2):356-386.
- [6] Bairagi D, Mandal S. A comprehensive review on biocompatible Mg-based alloys as temporary orthopaedic implants: Current status, challenges, and future prospects. *Journal of Magnesium and Alloys*. 2022;10(3):627-669.
- [7] Sarian MN, Iqbal N, Sotoudehbagha P, et al. Potential bioactive coating system for high-performance absorbable magnesium bone implants. *Bioactive Materials*. 2022;12:42-63.
- [8] Myrissa A, Agha NA, Lu Y, et al. In vitro and in vivo comparison of binary Mg alloys and pure Mg. *Materials Science and Engineering: C*. 2016;61:865-874.

Investigating the Impact of Recoater Speed on Micron-Sized Powder Dispersion on the Substrate in Selective Laser Melting (SLM) via DEM

Varma Kvvssn^{1,2}, Peyman Ansari^{2,3}, Metin U. Salamci^{2,3}, Elmas Salamci³, Hüseyin Kızıl¹

1. Department of Metallurgical and Materials Engineering, Istanbul Technical University, 34469, Istanbul, Türkiye

2. Additive Manufacturing Technologies Research and Application Center-EKTAM, Gazi University, Ankara 06560, Türkiye

3. Department of Mechanical Engineering, Gazi University, Ankara 06570, Türkiye

Abstract

Selective Laser Melting (SLM) within the realm of additive manufacturing is a dynamic and rapidly progressing field, marked by a multitude of parameters that exert substantial influence on the final properties of manufactured components. Ongoing research endeavors are dedicated to comprehensively unravel the intricate web of these influential factors, with particular emphasis on the pivotal role played by the powder spreading process. In the pursuit of this goal, our study harnessed the power of Discrete Element Method (DEM)-based simulations to shed light on the nuanced effects of spreader speed and shape on the dispersion of micron-sized powder particles upon the substrate. Our discerning observations unveiled that, as speed escalated to higher levels, the dispersion of the powder exhibited suboptimal characteristics, resulting in a looser distribution. Notably, a comparative analysis with prior research underscored the inferior performance of rectangular spreaders in contrast to their round counterparts, consequently, this led to a decrease in the compactness of powder dispersion.

Keywords: Additive manufacturing, Selective Laser Melting, Simulations, Discrete Element modelling

Introduction

The ASTM society defines additive manufacturing as a method of creating parts from 3D model data by joining materials, typically layer by layer [1]. Selective laser melting is a technique classified under the powder bed fusion category within ASTM characterization standards [1]. In this method, a layer of powder is initially spread onto the substrate, followed by laser melting the powder. The molten powder fuses with the previously solidified, and this layer-by-layer addition process culminates in the production of the desired shape. In this process, various parameters influence the final properties of the produced part. Therefore, it is imperative to comprehend the impact of these parameters on the end properties to optimize them and create a functional part that meets the specified requirements and withstands the anticipated working conditions throughout its service life. Numerous studies have been conducted to investigate the influence of process parameters, as demonstrated by Gyung Bae Bang et al. [2] for SUS316L, Jason Walker et al. [3] for nitinol, and Peyman Ansari et al. [4] for AlSi10Mg. Nevertheless, numerous other studies have also been undertaken to address existing knowledge gaps and gain a more comprehensive understanding of the selective laser melting (SLM) process, particularly in the context of various materials, with the goal of eliminating ambiguities and uncertainties. One property that significantly influences the final part's characteristics is the distribution of the powder as it compacts onto the substrate. Liu Cao [5] conducted a study to examine the effects of various spreading methods

and spreading speeds on the quality of the powder de- position. The research revealed that using a non-rotating roller for spreading achieved the highest powder compaction and the most uniform distribution. Furthermore, as the spreading speed increased, the compaction showed a linear decrease. In a similar vein, Eric J.R. Parteli and Thorsten Po"schel [6] developed a model to investigate the transport of powder particles using a roller as the coating system, and their findings emphasized the pivotal role of process speed in the packing characteristics of the applied powder.

In this study, we employ a modeling approach to conduct simulations with the aim of understanding how speed and the utilization of a rectangular shape spreader affect the behavior of powder distribution within a micron-sized range.

Theory of DEM

The Discrete Element Method (DEM) is founded on the fundamental assumption that particles are rigid bodies. Within the DEM framework, there are two primary models: the hard sphere model and the soft sphere model, each with distinct approaches to handling particle interactions and the associated fundamental equations. In the hard sphere model, particle collisions are treated as instantaneous events with negligible contact duration (contact duration is 0). This model does not consider deformation during contact. It relies on the equation of momentum exchange, where particle "overlap" is not permitted, and collision-induced momentum dissipation is determined by the coefficient of restitution. However, the hard sphere model encounters limitations when addressing scenarios involving multiple particles simultaneously in contact, referred to as the many- body contact problem. Conversely, the soft sphere model con- sider deformation during collisions, assuming that particles maintain the contact for a finite duration (contact duration is greater than 0). This model introduces a contact force model that allows for particle overlap to represent deformation. The contact forces and inertia derived from this model are used to calculate particle motion. Notably, the soft sphere model excels in addressing many-body contact problems where multiple particles are in simultaneous collision or contact. In this study soft sphere model was employed for the simulations, the equations utilized are provided. The force exerted between DEM particles can be described by equation 1 [7], which represents the combined effect of each component in both the normal and tangential directions. In the formula, the subscripts 'n' and 't' correspond to the particles 'i' and 'j,' representing the normal and tangential forces between them, respectively.

$$F_{ij} = F_n + F_t \quad (1)$$

$$F_n = -k\delta - \eta_n(u_{ij} \cdot n_{ij})n_{ij} \quad (2)$$

$$\delta = [L_{ij} - (r_i + r_j)]n_{ij} \quad (3)$$

$$u_{ij} = u_i - u_j \quad (4)$$

where, F_{ij} is the force that particle i receives from particle j, F_n is Normal component of the force that particle i receives from particle j, F_t is Tangent component of the force that particle i receives from particle j, k is Spring constant, η_n is Viscous coefficient of the dash pot.

The equation that expresses the contact force in the tangential direction F_t is the following [7]

$$F_t = -\eta_t(u_{ij} - (u_{ij} \cdot n_{ij})n_{ij}) \quad (5)$$

Particle equation of motion is [7]

$$\frac{du_i}{dt} = -\frac{1}{\rho_i} \nabla P + g + \beta(u - u_i)|u - u_i| \frac{\rho}{\rho_i} + \frac{F_i}{m_i} \quad (6)$$

where, u is Fluid flow velocity, P is Fluid pressure, ρ is fluid density. The subscript 'i' indicates that these variables pertain to the particle denoted as 'i.' Additionally, ' u_i ,' ' m_i ,' and ' d_i ' respectively denote the velocity, mass, and diameter of the individual particles marked as 'i.'

Time step for particle motion based on the stability limit shown below [7].

$$dt_{sub} = 0.25 \sqrt{\frac{m}{k}} \quad (7)$$

Simulation Setup

Flow-3D software was employed to perform the simulations. In this study, a model was created using a mesh size of 0.05 mm, and the substrate had a thickness of 40 microns, with a recoater of 0.05 mm, forming a rectangle shape as illustrated in Figure 1. Two different spreading speeds of 0.1 mm/sec and 50 mm/sec were selected to examine the substantial influence of spreader speed.

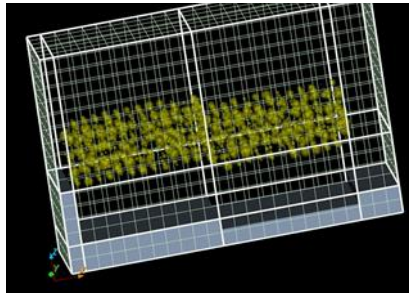


Figure 1. Model showcasing the substrate, spreader, and the generated powder before the powder laying process.

In this study, employed a powder size distribution with D10 at 5 microns, D50 at 26 microns, and D90 at 45 microns, following a Gaussian distribution and AlSi10Mg was used. To ensure a sufficient number of particles and achieve a closer approximation to the original behavior, Python code was developed that maintains the distribution's mean and deviation while providing the percentage concentration of particles at specific sizes. These size concentrations were then used to generate the particles in the Flow-3D software.

In the initial stage, the powder particles were created, followed by their layering and spreading using a spreader. The entire process was implemented within the software to replicate the original procedure. A larger-length substrate was subsequently employed to assess spreading across a broader surface at a speed of 50 mm/sec. Another simulation involved depositing powder solely on the source area, in contrast to the initial procedure where powder was spread both on the substrate and source area. This was done to investigate any deviations, as it emulates the initial powder spreading process on the substrate.

Results and Discussion

Figure 2 illustrates the powder deposited at both the supply place and on the substrate, while Figure 3 displays the powder exclusively laid at the supply place. Subsequently, a series of distinct simulations were conducted to investigate the behavior of powder spreading. Initially, simulations were carried out

for powder spreader speeds of 0.1 mm/sec and 50 mm/sec, considering powder deposition on both areas, given that it replicates the typical spreading behavior observed following the initial dispersion. The results for these simulations are presented in Figures 4 and 5, respectively.

Analysis of Figures 4 and 5 reveals a clear relationship between the increase in speed and powder spreading density. At very low speeds, the spreading exhibits compactness and even dispersion, while at higher speeds, there is a noticeable lack of powder at the starting area and increased compactness towards the end. It's important to note that these simulations focused on an initial small area to gain insight into powder dispersion. Notably, these simulation results are consistent with findings from other research works, as referenced in [5, 6]. Furthermore, the simulations indicate that the shape of the spreader, specifically the rectangular shape, has a significant impact on the spreading process it also consistent with research work as referenced in [5].

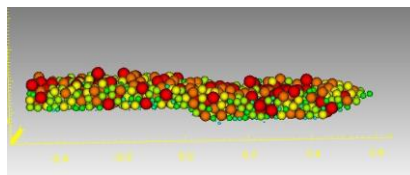


Figure 2. Laid the powder on both the substrate and supply area.

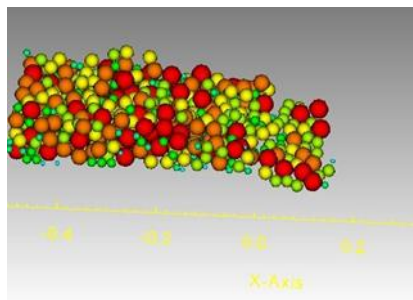


Figure 3. Model showcasing laid powder only on supply area.

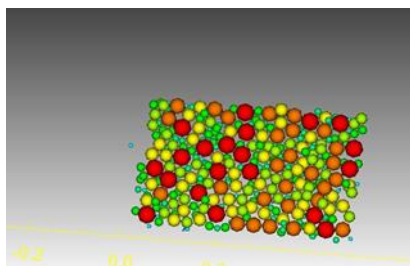


Figure 4. Simulation results for powder spread at 0.1 mm/sec after initially laying the powder on both the substrate and supply area.

Subsequently, simulations were conducted at a spreader speed of 50 mm/sec with the availability of powder at only supply section to replicate the initial spreading effect. Figure 6 illustrates the results, which clearly indicate a lack of consistency and compactness. It can be inferred that, due to the absence of obstacles from other particles, individual particles are capable of traveling longer distances, experiencing less loss of momentum over a given distance.

Subsequently, another simulation was conducted to assess the behavior of powder spreading on a larger-length substrate at a speed of 50 mm/sec. The results, presented in Figure 7, reveal that the spreading is even less effective compared to the smaller-length substrate shown in Figure 5. It appears that the rectangular-shaped spreader does not exert any additional force to compact the powder or reduce its momentum. Instead, the rectangular shape tends to disperse the powder over larger areas at higher speeds due to increased momentum.

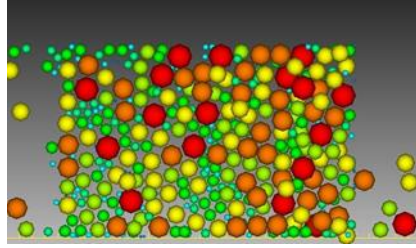


Figure 5. Simulation results for powder spread at 50 mm/sec after initially laying the powder on both the substrate and supply area.

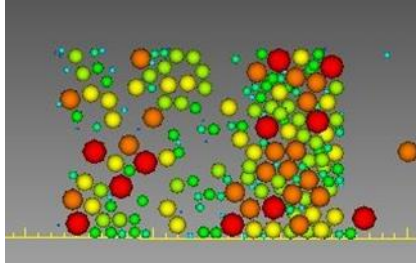


Figure 6. Simulation results for powder spread at 50 mm/sec after initially laying the powder only at supply area.

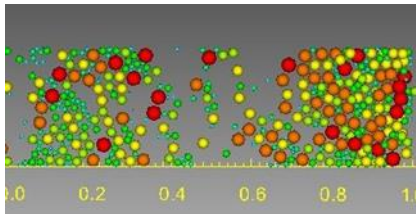


Figure 7. Simulation results for powder spread at 50 mm/sec over large substrate after initially laying the powder on both the substrate and supply area.

Conclusions

Selective Laser Melting (SLM) in additive manufacturing is a rapidly advancing field with a plethora of parameters influencing the final component properties. Research efforts are ongoing to achieve a comprehensive understanding of these influential parameters, including the powder spreading process. Our study employed DEM-based simulations to elucidate the effects of spreader speed and shape on micron-sized powder dispersion onto the substrate. Notably, our findings reveal that at higher speeds, powder dispersion was suboptimal, resulting in a looser distribution. Additionally, when compared to previous research [5], it became evident that the

rectangular shape was less effective than the round shape, contributing to the observed less compact spreading.

Conflict of Interest

The authors declare no conflict of interest.

Funding

This work has received funding from, the European Union's Horizon 2020 research and innovation program under the Marie Skłodowska-Curie grant agreement No 101034425 for the project titled A2M2TECH. This study has also received funding from The Scientific and Technological Research Council of Türkiye (TUBITAK) with the grant No 120C158 for the same A2M2TECH project under the TUBITAK's 2236/B program.

References

- [1] I. ASTM, "Astm 52900-21," Additive Manufacturing—General Principles—Fundamentals and Vocabulary. ASTM International: West Conshohocken, PA, USA, 2021.
- [2] G. B. Bang, W. R. Kim, H. K. Kim, H.-K. Park, G. H. Kim, S.-K. Hyun, O. Kwon, and H. G. Kim, "Effect of process parameters for selective laser melting with sus316l on mechanical and microstructural properties with variation in chemical composition," *Materials & Design*, vol. 197, p. 109221, 2021.
- [3] An Investigation of Process Parameters on Selective Laser Melting of Nitinol, vol. Volume 1: Development and Characterization of Multifunctional Materials; Modeling, Simulation and Control of Adaptive Systems; Integrated System Design and Implementation of Smart Materials, Adaptive Structures and Intelligent Systems, 09 2013.
- [4] P. Ansari and M. U. Salamci, "On the selective laser melting based additive manufacturing of alsi10mg: The process parameter investigation through multiphysics simulation and experimental validation," *Journal of Alloys and Compounds*, vol. 890, p. 161873, 2022.
- [5] L. Cao, "Study on the numerical simulation of laying powder for the selective laser melting process," *The International Journal of Advanced Manufacturing Technology*, vol. 105, pp. 2253–2269, 2019.
- [6] E. J. Parteli and T. Poßschel, "Particle-based simulation of powder application in additive manufacturing," *Powder Technology*, vol. 288, pp. 96–102, 2016.
- [7] I. Flow Science, FLOW-3D, Version 2023R1. Santa Fe, NM, 2023.

Application of Micro Computed Tomography (μ -CT) Method for Defect Detection in AlSi10Mg Parts Produced with SLM Technology

Zia Uddin^{1,2}, Huseyin Kizil¹

1. Department of Metallurgy and Materials Engineering Istanbul Technical University, 34469, Istanbul, Turkey

2. Additive Manufacturing Technologies Application and Research Centre-EKTAM Ghazi University, 06560, Ankara, Turkey.

Abstract

This conference article offers a comprehensive study aimed at determining the defects of AlSi10Mg alloy manufactured using Selective Laser Melting (SLM) technology. The investigation exclusively utilizes Micro-computed tomography (Micro-CT) imaging data. This work utilized non-destructive Micro CT analysis as a substitute for conventional testing methods, yielding significant findings regarding the defect characteristics and their relationship with the fatigue properties of the material. The analysis of micro-CT data was conducted on three samples to determine the diameter and volume of the most significant defects present in each sample. The process parameters (laser power) were utilized to determine the density of each sample. The study revealed that changes in laser power during the selective laser melting (SLM) procedure directly impacted the dimensions and magnitude of flaws present in the material. Furthermore, the determination of defect density was performed for each sample by previously known research findings. The defect density values for Sample 1, Sample 2, and Sample 3 were recorded as 22.32mm, 81.84mm, and 89.286mm, respectively. The findings suggest that a considerable quantity of defects is associated with a decrease in material density. The findings, as mentioned above, underscore the necessity of further refining the process parameters of selective laser melting (SLM) to improve material density and minimize the dimensions of the most significant defect. The optimization of additive manufacturing (AM) components is of utmost importance in enhancing their fatigue performance. The non-destructive XCT porosity analysis method presented in this study provides information on the internal defects that occur within the material in comparison to traditional methods. Further detailed investigation and digitalization of XCT results with simulations and computational tools are part of the ongoing research work.

Keywords: Computed tomography, Defects Energy, Density Selective laser melting.

Introduction

Additive manufacturing (AM) has become a well-established technology that has numerous possibilities for optimizing products. It is increasingly being utilized to design intricate structures at low cost and produce lightweight components. Selective laser melting (SLM) is one of the advanced additive manufacturing (AM) processes that utilize laser energy to melt powder material directly, producing three-dimensional objects. The powder material is subjected to selective scanning and melting by the desired component geometry provided by the Selective Laser Melting (SLM) system in the form of a three-dimensional design. This process is carried out layer by layer,

with each layer being sufficiently thin to allow for the melting of the powder material through the application of laser energy [1].

As a result, it has gained significant attention across several industries [2]. Nevertheless, the presence of porosity defects resulting from the printing process can negatively impact the mechanical properties and overall performance of components produced through additive manufacturing. This can pose considerable challenges to the dependability and reproducibility of this technology. The present progress in detection techniques has facilitated a more comprehensive and insightful investigation of porosity flaws. Nevertheless, the efficacy of a component constructed by AM is influenced by various factors, including the properties of the initial powder, the rate at which the scanning occurs, the thickness of each layer, and the intensity of the laser—SLM-fabricated alloys commonly exhibit porosity, which can arise from two main sources. The first source is the failure of the melted powder particles to fill gaps, resulting in pores known as lack of fusion pores. The second source is the entrapment of gases within the melt pool, leading to the formation of pores referred to as keyhole pores. Fusion holes deficient in their formation generally exhibit irregular shapes and tend to possess bigger dimensions compared to the more spherical keyhole pores.

To assess the suitability of the Selective Laser Melting (SLM) process for industrial and medical applications, the process must demonstrate a high level of reliability when subjected to cyclic loading[3]. Specifically, the fatigue performance of SLM parts must be comparable to that of materials produced by conventional manufacturing methods. Several factors influence fatigue performance, such as surface roughness, microstructures, and internal defects. These defects have a detrimental impact on the fatigue life of AM components. Several forms of faults that are inherent to the Selective Laser Melting (SLM) process and their impact on the mechanical properties of the material have been documented, as mentioned in the references[4], [5].

The utilization of traditional characterization approaches becomes challenging when dealing with complex structures, mostly due to the intricate nature of their development. Coordinate measurement machines (CMMs) have been employed as a dependable means of assessing quality. The control tool serves as a means of managing and regulating various aspects. Nevertheless, the identification and assessment of internal characteristics remain essential. The attainment of this outcome can only be realized through the use of a destructive cutting process.

X-ray computed tomography (CT) Tomography, specifically computed tomography (CT), offers a potentially effective method for assessing the interior composition of a component. This is achieved through the use of voxel-based volumetric mapping, which enables the reconstruction of the object's internal surfaces. CT measurements can be categorized into dimensional aspects. The topic of discussion pertains to the field of measuring and testing technology. Regarding the matter of dimensionality, the measurement process involves determining the dimensions of the pore. Indeed, it is crucial to ensure that the voxel resolution surpasses the dimensions of the smallest feature. It is necessary to have a requirement, whereas, for testing, only the detection is involved. When examining faults, it is of significance to consider the least detectable size of the defect. If the selected volumetric inspection size is adequate, it should be smaller. The partial volume effect contributes to the presence of contrast [6].

At present, there exists a limited number of studies that center on the utilization of computed tomography to characterize additive-produced components. The feasibility of detecting porosity in 316L stainless steel components produced using selective laser melting was examined by Ziolkowski et al.[7]. The pores size found was around 70 micrometers. In their study, Leuders et al.[8] employed computed tomography to identify and analyze the presence of pores in samples of Ti-6Al-4V that were produced. The process employed for fabrication was selective laser melting, which achieved a resolution of 22 micrometers. The process control of Direct Metal Laser Sintering (DMLS) has been investigated by Slotwinski et al.[9] The porosity of the material was assessed using various characterization techniques, including the Archimedes method, mass/volume measurements, and X-ray CT imaging. They reported that porosity detection by all of these techniques was in agreement.

It has been observed that the results obtained from all of these techniques were in concurrence in terms of porosity detection. The limited body of literature that has been documented thus far for computed tomography (CT) has been employed to detect porosity in additive manufacturing processes—the production of manufactured components. Several research have conducted comparisons between it and conventional manufacturing procedures and have found a consensus regarding the various techniques involved. It is imperative to conduct a comprehensive investigation of the impact of these factors.

The work aims to investigate the fatigue performances of additively manufactured AlSi10Mg specimens. These specimens are subjected to micro-CT scanning and analysis for the identification of the defects. Further, the present study will focus on stress concentration phenomena and their response under fatigue loading conditions. To analyze the influence of internal defects during mechanical loading, tomography files will be converted to solid models and reconstructed so that they can be analyzed using the finite element (FE) technique. Stress and strain distributions at pores and local stress concentration factors will be studied for their influence on the mechanical performance of parts.

Theory / Experimental Set Up

Al10SiMg samples were prepared from gas-atomized Al10SiMg powder (mean size 45-60 μm) using a selective laser melting (SLM) machine. The chemical composition of the powder has been presented in Table 1. The specimens were manufactured by melting the powder in a layer-by-layer manner according to the process parameters, as shown in Table 2.

Table 1. AlSi10Mg powder composition (wt. %) and SLM process parameters.

Si	Mg	Cu	Ni	Fe	Mn	Ti	Al
10	0.4	0.25	0.05	0.25	0.1	0.15	88

Table 11: SLM process parameters

Sample No.	Laser power (W)	Scan speed (m/s)	Spot size (μm)
1	75	0.6	140
2	275	0.6	140
3	400	0.8	140

Characterization

The micro-CT is a non-destructive experimental technique that allows the investigation of internal defects in specimens. Micro-CT inspections of the manufactured specimens were carried out in the additive manufacturing center EKTAM. The X-ray, in the form of a conical beam emitted by the X-ray tube, penetrates the test sample and is partially absorbed by it. As, during the measurement, the sample rotates by 3600, the detector captures numerous two-dimensional projected images from which a three-dimensional data set of volume elements (voxels) is reconstructed based on appropriate algorithms and high-performance computers. The schematic of micro-CT equipment is shown in Figure 1. The three-dimensional defect features were extracted from micro-CT results using the software VGSTUDIO MAX 3.5.

Various other characterizations will be carried out to understand in detail the defect and the effect of the defect on the fatigue damage behaviors. Along with simulation, fatigue testing will also be carried out to validate and compare the results.

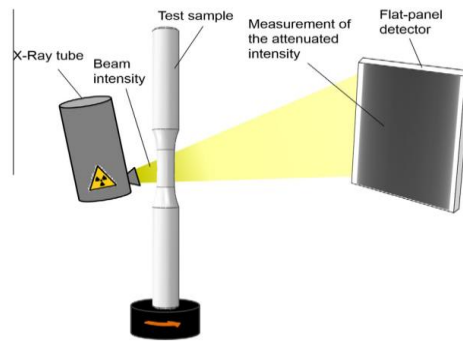


Figure 1. Schematic of micro-CT equipment

Experimental Results / Simulation Results / Discussion

This section highlights the feasibility of utilizing Micro CT data for assessing the fatigue life of AlSi10Mg alloy components produced through SLM. The non-destructive nature of Micro CT analysis offers a valuable alternative to traditional fatigue testing methods, reducing material and time requirements. This innovative approach provides essential insights into defect evolution, allowing for more accurate predictions of fatigue behaviors. Ultimately, this research contributes to advancing the understanding of fatigue in SLM-produced AlSi10Mg alloy components, with potential applications in quality control and design optimization.

Three specimens were subjected to micro-CT analysis to investigate defect characteristics, including size and quantity, with variations in laser power during fabrication. The parameters for each specimen are detailed in the table below. It was observed that altering the laser power had a direct impact on defect formation within the specimens. Lower laser power levels resulted in inadequate powder melting, while excessively high power levels led to evaporation and the formation of voids, compromising structural integrity.

Energy density $E = P/VDT$

Where, P: laser power, V: scan speed, D: Spot diameter

Density calculations for each specimen were performed using Equation 1, yielding defect density values of 22.32 mm, 81.84 mm, and 89.286 mm for Sample 1, Sample 2, and Sample 3, respectively. Additionally, micro-CT inspections determined the diameter of the largest defect in each specimen, measuring at 1.9205 mm, 1.9511 mm, and 1.8369 mm for Sample 1, Sample 2, and Sample 3, respectively.

Table 3. SLM Parameters and Energy Density

Laser power(W)	Scan speed (m/s)	Spot size(μ m)	The diameter of the largest Defect (mm)	The volume of the largest defect(mm)	Energy density $E = P/vdt$
75	0.6	140	1.9205	0.03	22.321
275	0.6	140	1.9511	0.084	81.845
400	0.8	140	1.8369	0.0709	89.286

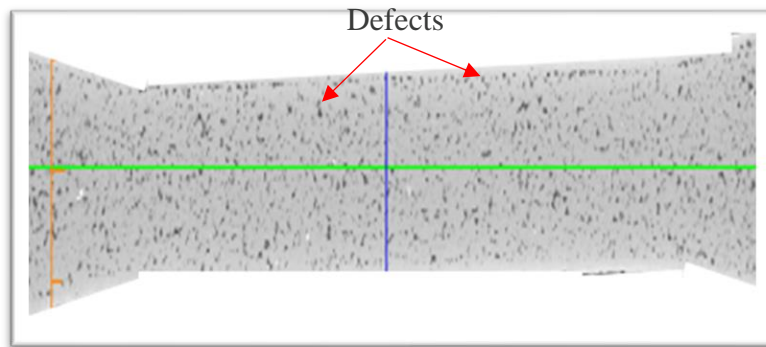


Figure 2. Picture showing the longitudinal section of the CT specimen

The energy density of faults present in CT data significantly influences the fatigue properties of additively manufactured (AM) components. In the present work, an examination was conducted on three independent samples generated using different laser powers, specifically 75, 250, and 400. Notably, discernible patterns were detected in the energy density of flaws. The first sample, generated with a power output of 75 watts, displayed a relatively low energy density value of 22, suggesting a greater prevalence of faults. In contrast, sample 2, which was produced with a power input of 250 watts, exhibited a slightly elevated energy density of 81, indicating a potentially improved equilibrium between energy density and defect levels. Sample 3, which was produced with a power output of 400 watts, exhibited the greatest energy density of 89. This value indicates an excessive amount of energy input and suggests the presence of potentially harmful faults. The results of this study highlight the significant significance of carefully choosing laser power in additive manufacturing (AM) processes. It is crucial to avoid excessive energy input, as it might result in a higher density of defects. This, in turn, can negatively impact the fatigue properties of the final components. Ideally, it is preferable to utilize a laser power of 250 watts that achieves a harmonious equilibrium between energy density and defect proportion. This choice aims to enhance fatigue performance and uphold the general integrity of the component.

Conclusions

In summary, this research utilized Micro CT analysis to provide significant findings regarding defect properties in AlSi10Mg alloy components manufactured using Selective Laser Melting. The results of our study highlight the importance of the size and volume of the biggest imperfections as critical determinants of material integrity. The investigation demonstrated a clear correlation between process parameters, defect density, and the quality of the component. A noticeable reduction in density was found at lower laser power settings, which can be attributed to an elevation in the presence of faults. Nevertheless, via the augmentation of laser power to 400 W from the original 75 W, a significant improvement in component density was attained, as seen by the computed values of 89.286, in contrast to the value of 22.32 observed at 75 W.

Moreover, although there were similarities in the size of the greatest defects observed in the samples, there were considerable variances in their numbers. This highlights the crucial influence of defect density on the fatigue life of components. The findings underscore the significant significance of optimizing process parameters to achieve defect-free additive manufacturing, hence improving the fatigue performance of crucial components.

In forthcoming times, additional insights will be extracted from the Micro CT data, with a particular emphasis on its conversion into STL files. The files above will be utilized as input for conducting finite element analysis through the implementation of Abaqus or any other software. This will provide a thorough investigation of the behavior of pores under various loading circumstances. The future work aims to examine the impact of pore size on damage mechanisms, with a particular focus on evaluating the development of plastic strain in different pores under varying load conditions. This investigation will help to develop a correlation between process parameters, defect features, and the fatigue performance of components produced by additive manufacturing techniques. Based on the data obtained by the XCT measurement analysis, it is possible to determine the course of the cracks and diagnose places that may be the point of crack initiation, especially fatigue.

References

- [1] T. S. Singhal et al., “A comprehensive comparative review: welding and additive manufacturing,” *International Journal on Interactive Design and Manufacturing*, vol. 1, no. 1, pp. 1–15, 2023, doi: 10.1007/s12008-022-01152-0.
- [2] V. Madhavadas et al., “A review on metal additive manufacturing for intricately shaped aerospace components,” *CIRP J Manuf Sci Technol*, vol. 39, pp. 18–36, 2022, doi: 10.1016/j.cirpj.2022.07.005.
- [3] R. Jones, “Fatigue crack growth and damage tolerance,” *Fatigue Fract Eng Mater Struct*, vol. 37, no. 5, pp. 463–483, 2014, doi: 10.1111/ffe.12155.
- [4] S. Afazov, A. Serjouei, G. J. Hickman, R. Mahal, D. Goy, and I. Mitchell, “Defect-based fatigue model for additive manufacturing,” *Progress in Additive Manufacturing*, vol. 1, no. 0123456789, pp. 1–8, 2022, doi: 10.1007/s40964-022-00376-6.
- [5] M. Khorasani, I. Gibson, A. H. Ghasemi, E. Hadavi, and B. Rolfe, “Laser subtractive and laser powder bed fusion of metals: a review of process and production features,” *Rapid Prototyp J*, vol. 1, no. 3, pp. 1–24, 2023, doi: 10.1108/RPJ-03-2021-0055.

- [6] S. Siddique et al., “Computed tomography for characterization of fatigue performance of selective laser melted parts,” *Mater Des*, vol. 83, pp. 661–669, Oct. 2015, doi: 10.1016/j.matdes.2015.06.063.
- [7] G. Ziółkowski, E. Chlebus, P. Szymczyk, and J. Kurzac, “Application of X-ray CT method for discontinuity and porosity detection in 316L stainless steel parts produced with SLM technology,” *Archives of Civil and Mechanical Engineering*, vol. 14, no. 4, pp. 608–614, Aug. 2014, doi: 10.1016/j.acme.2014.02.003.
- [8] S. Leuders et al., “On the mechanical behavior of titanium alloy TiAl6V4 manufactured by selective laser melting: Fatigue resistance and crack growth performance,” *Int J Fatigue*, vol. 48, pp. 300–307, 2013, doi: 10.1016/j.ijfatigue.2012.11.011.
- [9] J. A. Slotwinski and E. J. Garboczi, “Porosity of Additive Manufacturing Parts for Process Monitoring *.”

Funding

This work has received funding from the European Union’s Horizon 2020 research and innovation program under the Marie Skłodowska-Curie grant agreement No 101034425 for the project titled A2M2TECH. This study has also received funding from The Scientific and Technological Research Council of Türkiye (TUBITAK) with grant No 120C158 for the same A2M2TECH project under the TUBITAK's 2236/B program.

Conflict of Interest

There is no conflict of interest.

Numerical and Experimental Investigation of the Effect of Process Parameters on Mechanical Properties in Selective Laser Melting

Murat Yıldız^{1,3}, E. Kıvanç Sadak^{1,2}, Nureddin Dinler¹, Kadir Bilen², Peyman Ansari^{1,3}

1. Gazi University Department of Mechanical Engineering, Ankara, Türkiye

2. Ataturk University, Department of Mechanical Engineering, Erzurum, Türkiye

3. Additive Manufacturing Technologies Application and Research Center (EKTAM), Gazi University, Ankara, Türkiye

Abstract

Selective Laser Melting (SLM), an additive manufacturing method, is a method of obtaining 3D products by melting and solidifying each metal powder layer with a laser using certain process parameters. In this study, simulations were carried out using COMSOL Multiphysics software at selected process parameters for SLE method. In addition to numerical studies, experimental samples will be produced using the same process parameters and the dimensional distortions, cracks and fractures that occur in the part as a result of thermal stress will be tested and analysed with Micro-CT device in terms of microstructure. The relationship between energy density and pore volume is investigated. In this context, as a result of these analyses, the effect of process parameters on mechanical properties will be examined.

Keywords: Additive Manufacturing, Selective Laser Melting (SLM), Finite Element Analysis, COMSOL Multiphysics, Computed Tomography (CT), Porosity Analysis

Introduction

Selective laser melting (SLM), one of the metal additive manufacturing methods that have become widespread in recent years, has become a widely used production method for functional parts in industries such as aerospace, automotive and healthcare. Unlike conventional manufacturing methods, this method enables short production time, freedom of design and the ability to produce complex geometries [1]. The SLM process utilises a high intensity laser source to create a melt pool on a laid powder layer. The melt cools to the ambient temperature of the pool and solidifies. A new layer of powder is then laid down and the desired solid model is obtained by repeating this process [2]. During the SLM process, which is carried out in layers, thermal stress occurs due to high and sudden temperature changes and this causes dimensional distortions, cracks and fractures in the produced part. In addition, a poorly chosen combination of parameters can lead to inadequate powder fusion, keyhole formation and balling. High laser speed and insufficient laser power result in incomplete powder fusion, which leads to increased porosity. On the contrary, choosing too high a power for a given speed results in overheating and deeper laser penetration. This leads to the formation of pores known as keyholes [3].

Experimental studies are partly a trial and error approach, which requires time and cost. On the other hand, keeping the temperature of the melt pool within a range allowed by the applied process parameter sets and preventing temperature fluctuations during the process affects the stability of the production and thus the quality of the final product [4]. However, it is difficult to record the rapidly changing temperature history caused by the laser with an experimental method. Therefore, finite element analysis is used to model the SLM process and study its effects on the part [5].

Travis J. Black and Alexei F. Cheviakov developed a MATLAB code that fills a given volume with spherical powders for 316L stainless steel powder material, whose average powder radius was determined using different distributions. In addition, an example of numerical modelling of the interaction between the laser beam and the melted powder particles in the powder bed 3D printing process has been examined [6].

On the other hand, the process parameters used are the main factor that causes pore formation in the internal microstructure of the final product. The effect of process parameters on pore formation is determined by Micro-CT tests. Dimensional distortions, internal voids and cracks that occur in the sample due to thermal stress during production can be seen more clearly thanks to this non-destructive material inspection.

The aim is to analyse process-induced pores in selective laser melting (SLM), an Additive Manufacturing process. Porosity is one of the most problematic defects in SLM parts; it degrades part performance and yet is highly sensitive to the parameters of the SLM process itself. Detailed analysis of SLM pore formations can be performed using computed tomography (CT) technique to understand the level of porosity under different process conditions. There are different mechanisms of pore formation in SLM, especially the keyhole pore type caused by energy density is one of the most frequently encountered pore types. Computed tomography (CT) technique can clearly reveal the pores in SLM samples. From the CT scan and analysis results, it is seen that increasing the energy density increases the pore volume. [7]

The MATLAB code developed in this study was developed specifically for the material considered and the dust distribution was obtained in 3D. Then, it was transferred to the thermal model developed in COMSOL Multiphysics software and finite element analyses were performed.

With the process parameters considered in the analyses, experimental production will be carried out with CONCEPT Laser M2 Cusing SLM device and tested and analysed with Micro-CT device.

Material and Method

In this section, the metal powder layer was formed by considering the average radius value of AlSi10Mg metal powder for the numerical studies of the samples to be produced by SLM method. The MATLAB code created by Travis J. Black and Alexei F. Cheviakov was revised and spherical powders with a volume of 1 mm x 1 mm x 0.08 mm were randomly placed according to the weibull distribution.

Table 1. Material Properties of AlSi10Mg

Material property	Symbol	Value	Unit
Melting Temperature	T_m	867[23]	K
Melting Interval	δT	± 10	K
Evaporation Temperature	T_{ev}	2743[24]	K
Latent Heat of Melting	H_m	4.23×10^5 [23]	J/kg
Latent Heat of Evaporation	H_{ev}	1.07×10^7 [24]	J/kg
Density	ρ	2670[23]	kg/m ³
Thermal Conductivity	k	$113 + 1.06 \times 10^{-5}T$ [23]	W/m. K
Specific Heat Capacity	C_p	$536.2 + 0.035T$ [23]	J/kg. K
Marangoni Coefficient	$d\gamma/dT$	-0.35×10^{-3} [23]	N/m. K
Absorption Coefficient	A	0.6 (solid) – 0.3 (liquid) [5,23]	–

In addition, CT analysis parameters of the samples will be determined for experimental studies.

CT Scanning Method

CT (Computed Tomography), one of the non-destructive material testing methods, was used to evaluate the porosity of the samples. The examination of the finished samples was carried out with the ZEISS Xradia Versa 510 device (Figure 2). This device consists of the following main parts: X-ray source, rotary table, specimen holder and detector for recording 2D images. DragonFly software was used for scanning and data acquisition. X-ray scanning was performed according to the manufacturer's recommendations and the operator's skills [8]:

- Voltage 80 kV
- Power: 7 W
- Current 87 μ A
- Resolution: 1024 x 1024
- Objective: 0.4X
- Voxel Size: 22.64 μ m
- Binning: 2
- Projection Number: 2401
- Exposure Time: 1 s



Figure 1. Zeiss Xradia 510 Versa Device

The CT machine creates images based on the X-rays transmitted by the specimen. Where the sample absorbs more X-rays the image is darker and where it transmits more X-rays the image is brighter. Absorption increases with density and thickness and is generally higher for elements with higher atomic numbers in the periodic table. Magnification in CT instruments is typically achieved either by using a projection geometry with a point source (as in the Xradia Versa 510) or by using optical elements similar to a normal visible light microscope. In CT, the specimen is imaged from different angles over an angular range of 360°. A single image at a given angle is called a projection. Computer algorithms can be used to reconstruct the internal, 3-dimensional (3D) structure of the specimen from a series of projections. The reconstructed volume can be visualised in different ways, for example slice by slice (also called virtual sectioning) or by creating a 3D view of individual internal features. Figure 3 shows a schematic representation of the working principle of the CT method and the actual internal image of the device, the position of the specimen in the holder and the area where the specimen is scanned.

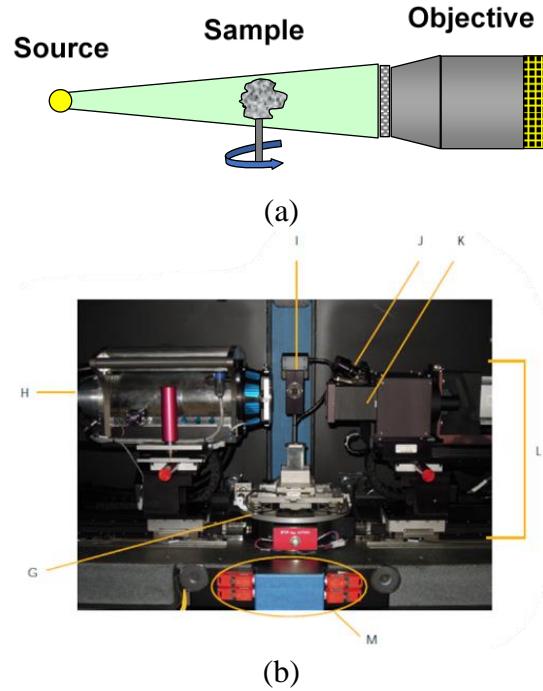


Figure 2. (a) Schematic representation of the working principle of the CT method, (b) Real interior view of the Zeiss Xradia 510 Versa device; (G) Sample section (H) X-ray source (I) Visual light camera (J) Objectives (K) 0.4X Objective (L) Detector assembly (M) Door safety locks

After reconstruction, the CT-scanned 3D models were evaluated in VGStudio Max 2022.1 software (Volume Graphics, Germany). The first step is surface determination to recognise the shape of the part. Porosity analysis was then used. This analysis shows the pores scanned in each part in terms of both size and location [8].

Simulation Results

AlSi10Mg alloy tensile specimens, CT scanned on Zeiss Xradia 510 Versa device, were analysed for porosity using VGStudio Max 2022.1 software. The effect of energy density on pore volume in the analysis results has been investigated and studies are ongoing.

References

- [1] Sing SL, Yeong WY, Laser powder bed fusion for metal additive manufacturing: perspectives on recent developments, Virtual Phys Prototypg (2020).
- [2] Zhao X., Iyer A., Promoppatum P., Yao S.C., Numerical modeling of the thermal behavior and residual stress in the direct metal laser sintering process of titanium alloy products, Elsevier (2017).
- [3] N. Ahmed, I. Barsoum, G. Haidemenopoulos, R.K. Abu Al-Rub, Process parameter selection and optimization of laser powder bed fusion for 316L stainless steel: A review, Elsevier (2022).
- [4] Peyman Ansari, Metin U. Salamci, On the selective laser melting based additive manufacturing of AlSi10Mg: The process parameter investigation through multiphysics simulation and experimental validation, Elsevier (2021).
- [5] Ansari J., Nguyen D., Investigation of SLM Process in Terms of Temperature Distribution and Melting Pool Size: Modeling and Experimental Approaches, MDPI (2019).

- [6] Black T. J., Cheviakov A. F., 3DRSP: Matlab-based random sphere packing code in three dimensions, Elsevier (2022).
- [7] Subin Shrestha, Thomas Starr, Kevin Chou Proceedings of the ASME 2018 International Mechanical Engineering Congress and Exposition IMECE2018, November 11-14, 2018, Pittsburg, PA, USA
- [8] Peter Pokorný, Štefan Václav, Jana Petru and Michaela Kritikos, Porosity Analysis of Additive Manufactured Parts Using CAQ Technology, MDPI (2021)

An Experimental Study on Ultrasonic Atomized 316L Stainless Steel Powder for Additive Manufacturing

Anıl Emiralioğlu¹, Eren Yağız Karaca¹, Nurettin Akın¹

1. Additive Manufacturing Technologies Application and Research Center (EKTAM), Gazi University, 06560 Ankara, Türkiye.

Abstract

With the increasing interest in additive manufacturing technology, which brings innovation to the manufacturing industry with its many advantages compared to traditional manufacturing methods, innovations have been needed, especially in the production of metal powders used in the SLM, EBM and DED methods. In contrast to powders produced by gas atomization methods, ultrasonic atomization method allows the production of powders with narrower particle size distribution and higher sphericity ratio. In this study, 316L stainless steel powders produced by ultrasonic atomization and gas atomization were compared in terms of particle size distribution and sphericity. Production was carried out with different values of electric current, which is one of the parameters used in the ultrasonic atomization method, and the results were presented graphically and CT images of the powders were given.

Keywords: Ultrasonic atomization; 316L stainless steel; additive manufacturing; powder production

Introduction

Additive manufacturing (AM) has been an area that has attracted the attention of many researchers in recent years due to the innovations and advantages it brings to the sector. The demand for high quality metal powders has increased with the development of metal AM. Metal powders used in AM methods must have physical and chemical characteristics such as particle morphology, particle size distribution (PSD), density, porosity, satellites etc. for a reliable final product [1]. Generally, gas atomization and plasma atomization methods use for the metal powders in the additive manufacturing methods. Ultrasonic atomization allows the production of metal powders with narrower particle size distribution and better sphericity compared other atomization methods [2]. In the ultrasonic atomization method, with the help of ultrasonic vibrations on a liquid material, metal droplets are formed uncontrollably with the principle of Rayleigh wave instability and become the desired powder with a rapid cooling rate [3].

This paper summarizes the comparison of ultrasonic atomized and commercially available 316L stainless steel metal powder in terms of particle size distribution and sphericity.

Methods

Within the scope of the study, stainless steel 316 L powders were analyzed. While the purchased powders produced by the vacuum inert gas atomization (VIGA) method are produced by melting the raw material in ingot form, the raw material of ultrasonic atomized powders is in wire form.

Ultrasonic Atomization

Capillary waves develop on the liquid's surface during the atomization process. The energy distribution, frequency amplitude, and physico-chemical characteristics of the molten metal affect

the wavelength. The density and surface tension of the liquid at the liquid-air contact are the most crucial elements. The capillary waves' peaks divide into droplets if the liquid starts to vibrate because of the ultrasonic frequency [4].

To produce metal powders with the desired quality and properties, the working principle of the ultrasonic atomization device must be understood well (Figure 1). Firstly, an electric arc is created between the sonotrode and the non-consumable tungsten electrode to melt raw material. Secondly, ultrasonic vibrations are transferred from the cold end of the sonotrode, where the ultrasonic transducer is located, to the hot end through the sonotrode. After that, raw material in the form of wire is continuously supplied into the pressurized atomization chamber. The raw material exposed to the electric arc melts as its temperature increases, creating a molten pool on the hot end of the sonotrode. Under the influence of surface tension, liquid metal droplets take a spherical shape and are thrown into the inert gas flow with the kinetic energy gained by ultrasonic vibrations. These droplets cool down and solidify by the convection and radiation processes occurring in the atomization chamber and are transported out of the atomization chamber under the influence of aerodynamic forces. Finally, metal powders accumulate in the powder chamber [5].

ATO LAB Plus ultrasonic atomization machine within EKTAM was used to produce the powders examined in the study. Electrical current values change between 120 A and 150 A. All other parameters that affect the production (ultrasonic frequency 35 kHz, amplitude 80%, wire diameter 1.2 mm and argon flow 20 l/min) are constant. Under these conditions, three different powders were produced. In addition to the powders produced by ultrasonic atomization, powders produced by the VIGA method were analyzed and named as in Table 1.

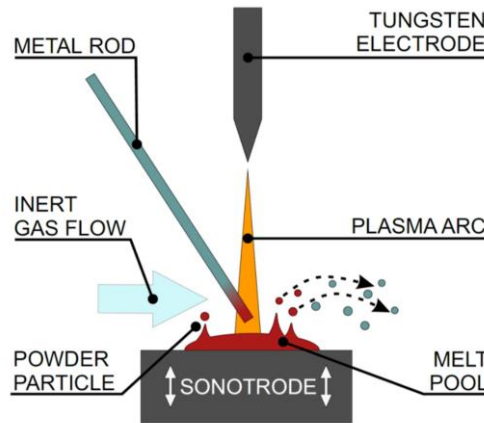


Figure 1. Scheme of Ultrasonic [6]

Table 1. Powders and Parameters

Powders	Electrical Current (Amp)
Powder-120	120
Powder-135	135
Powder-150	150
Powder-VIGA	-

Powder Property Analysis

Particle size distribution and sphericity measurements of the powders used in the study were analyzed using the laser diffraction method on the Microtrac MRB Flowsync particle characterization machine.

To confirm the sphericity analysis and to examine the gases trapped inside the powder grains, small amounts of samples taken from the powders were imaged on the Zeiss Xradia Versa 510 X-Ray Micro Computed-Tomography machine within EKTAM.

Results and Discussion

Particle Size Distribution

Particle size distributions of the powders used in the study are shown in Figure 2. Although the powder produced by the VIGA method has different sizes than the powders produced by ultrasonic atomization, it appears to have a wide size range. This situation confirms the phenomenon of a wide range of size distributions, which one of the main disadvantages of gas atomization methods [7]. The effect of the electric current value, which is another parameter, is seen more clearly in the D90 value of the produced powders. Table 2 shows that the D90 value of Powder-150 powder is 76.34, D90 value of Powder-135 is 83.65, while the D90 value of Powder-120 powder is 89.12. The fact that the D10 values of the powders are similar to each and the D90 values decrease with the increase in electric current shows that the increase in electric current causes the particle size distribution to narrow.

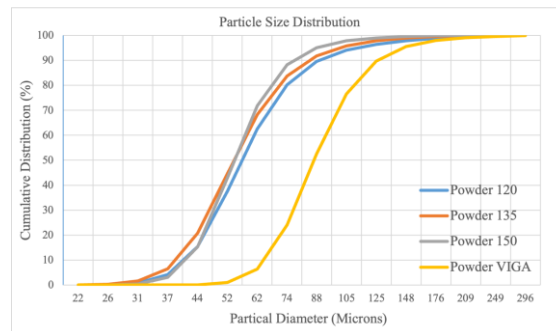


Figure 17. Particle Size Distribution

Table 2. D10, D50 and D90 Values (microns) of the Powders

	D10	D50	D90
Powder-120	41.22	56.92	89.12
Powder-135	39.11	54.29	83.65
Powder-150	41.70	54.46	76.34
Powder-VIGA	65.30	86.66	125.10

Sphericity

In powder bed additive manufacturing methods, proper laying of the powder forming the layer is one of the most important factors affecting production. The high sphericity ratio of the powder ensures that the layer is in the desired uniformity [8]. It can be seen in Figure 3 that the sphericity ratios of all powders produced by ultrasonic atomization method are dramatically higher than those of powders produced by VIGA. Considering the measured particle numbers, 60% of Powder-120,

56% of Powder-135, and 50% of Powder-150 are higher than 98%, which is a very good sphericity rate, only 2% of Powder-VIGA could reach this rate.

When the sphericity ratio distribution among the powders produced by the ultrasonic atomization method is examined, it is seen that sphericity decreases with the increase of electric current at high sphericity ratio values.

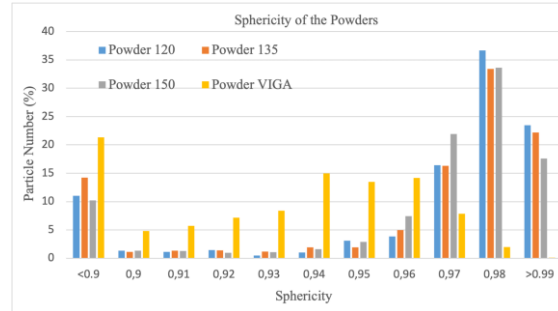


Figure 3. Sphericity of the Powders

A sample was prepared from the powders produced by two different methods used within the scope of the study (Powder-135 and Powder-VIGA) and Micro-CT images were analyzed (Figure 4).

At VIGA method, during solidification, the liquid metal can close on itself as the viscosity increases. It may cause inert gas porosity. By interacting the liquid metal with the inert gas, the inert gas is trapped inside the powder particles [9], [10]. While inert gas porosity was observed in Powder-VIGA, no gas porosity was observed in Powder-135. In addition, satellite formation, which disrupts the sphericity of the powders, is also quite common in Powder-VIGA.

Another aspect that we can clearly observe in Figure 4 is sphericity. While the particles in the image of Powder-135 are spherical, this is not the case in Powder-VIGA. It is an image that confirms our particle characterization measurements.

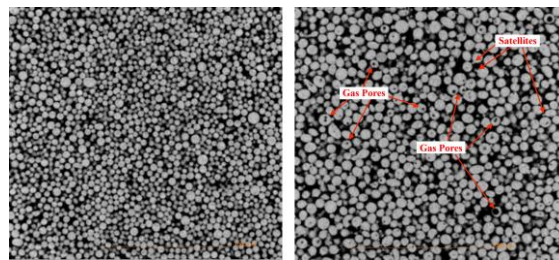


Figure 4. X-Ray Micro-CT images of the powders produced by ultrasonic atomization (left) and gas atomization (right)

Conclusions

This study discussed the effect of electric current on powders produced by ultrasonic atomization process and the comparison of powders produced by ultrasonic atomization and VIGA method. A summary of the results is as follows:

- 1- The powders produced by the VIGA method have a much wider particle size distribution than the powders produced by the ultrasonic atomization method.

2- When micro-CT images were analyzed, much more satellites and gas porosities were observed in VIGA powders. It is almost non-existent in ultrasonic atomization powders.

3- Ultrasonic atomization powders have much higher sphericity than VIGA powders.

4- As the electric current increases during the ultrasonic atomization process, the particle size distribution narrows, but the high sphericity of the powders decreases.

References

- [1] P. Moghimian et al., “Metal powders in additive manufacturing: A review on reusability and recyclability of common titanium, nickel and aluminum alloys,” *Additive Manufacturing*, vol. 43. Elsevier B.V., Jul. 01, 2021. doi: 10.1016/j.addma.2021.102017.
- [2] S. H. Alavi and S. P. Harimkar, “Ultrasonic vibration-assisted laser atomization of stainless steel,” *Powder Technol*, vol. 321, pp. 89–93, Nov. 2017, doi: 10.1016/j.powtec.2017.08.007.
- [3] B. Bałasz, M. Bielecki, W. Gulbiński, and Słoboda, “Comparison of ultrasonic and other atomization methods in metal powder production,” *Journal of Achievements in Materials and Manufacturing Engineering*, vol. 116, no. 1, pp. 11–24, Apr. 2023, doi: 10.5604/01.3001.0016.3393.
- [4] D. Halápi and L. Varga, “Ultrasonic Powder Atomization for Additive Manufacturing,” *International Journal of Engineering and Management Sciences (IJEMS)*, vol. 8, no. 2, 2023, doi: 10.21791/IJEMS.2023.2.8.
- [5] K. Grzelak et al., “A Comparative Study on Laser Powder Bed Fusion of Differently Atomized 316L Stainless Steel,” *Materials*, vol. 15, no. 14, Jul. 2022, doi: 10.3390/ma15144938.
- [6] F. Hinrichs et al., “Flexible powder production for additive manufacturing of refractory metal-based alloys,” *Metals (Basel)*, vol. 11, no. 11, Nov. 2021, doi: 10.3390/met11111723.
- [7] L. Haferkamp et al., “The influence of particle shape, powder flowability, and powder layer density on part density in laser powder bed fusion,” *Metals (Basel)*, vol. 11, no. 3, pp. 1–15, Mar. 2021, doi: 10.3390/met11030418.
- [8] C. Monti, M. Turani, K. Papis, and M. Bambach, “A new Al-Cu alloy for LPBF developed via ultrasonic atomization,” *Mater Des*, vol. 229, May 2023, doi: 10.1016/j.matdes.2023.111907.
- [9] I. E. Anderson, E. M. H. White, and R. Dehoff, “Feedstock powder processing research needs for additive manufacturing development,” *Current Opinion in Solid State and Materials Science*, vol. 22, no. 1. Elsevier Ltd, pp. 8–15, Feb. 01, 2018. doi: 10.1016/j.cossms.2018.01.002.
- [10] K. Kothari, R. Radhakrishnan, and N. M. Wereley, “Advances in gamma titanium aluminides and their manufacturing techniques,” *Progress in Aerospace Sciences*, vol. 55. Elsevier Ltd, pp. 1–16, 2012. doi: 10.1016/j.paerosci.2012.04.001.

Acknowledgements

This study is supported by The Scientific and Technological Research Council of Türkiye (TÜBİTAK) under the 1004 Program for the project number 20AG008.